1995

Computer study of a cavity bubble near a rigid boundary, a free surface, and a compliant wall

Mohammad Taghi Shervani-Tabar
University of Wollongong

COMPUTER STUDY OF A CAVITY BUBBLE NEAR A RIGID BOUNDARY, A FREE SURFACE, AND A COMPLIANT WALL

A thesis submitted in fulfilment of the

requirements for the award of the degree of

DOCTOR OF PHILOSOPHY

from

UNIVERSITY OF WOLLONGONG

by

MOHAMMAD TAGHI SHERVANI-TABAR

B.Eng., M.Eng.

Department of Mechanical Engineering

MARCH 1995

In the name of God, the merciful and compassionate

To my country, Islamic Republic of Iran, and its people

DECLARATION

This is to certify that the work presented in this thesis is carried out by the author in the Department of Mechanical Engineering of the University of Wollongong, Australia and has not been submitted for a degree in any other university or institution.

Mohammad Taghi Shervani-Tabar

ACKNOWLEDGMENTS

The author would like to express sincere gratitude and appreciation to his supervisor Dr. W. K. Soh for introducing him the most interesting field of computational fluid dynamics and especially the respective fields of bubble dynamics and interaction of a bubble with different boundaries and for his excellent guidance, supervision and encouragement during the course of this work.

The author also gratefully thanks the ministry of culture and higher education of the Islamic Republic of Iran for awarding him a scholarship and providing financial support to make this thesis possible. He also would like to extend his appreciation to Dr. M. Gezelayagh and Dr. M. H. Sorouraddin for their support and assistance.

Many thanks are due to Mr. Ali Akbar Karimi, Mr. Steven Harvey and Mr. Oliver Kennedy for their valuable comments. Thanks are also due to Mr. Des Jamieson for his valuable assistance in the use of computer facilities and to department's administrative staff.

The author acknowledges gratefully to his parents and his brothers and sisters for their support and encouragement.

Finally the author is extremely grateful to his wife and his son Navid for their constant support and encouragement and for their unending patience.

ABSTRACT

One of the main causes of the cavitation damage is due to the impingement of the micro-liquid jets of water generated by the collapse of the vapour bubbles. The impacts of micro-liquid jets give rise to a very high pressure pulse on the surface. These continuous impacts, initiated from many bubbles, will lead to surface fatigue and eventually fracture will occur.

In this research a boundary integral method is developed and applied to investigate the dynamics of the flow around a cavitation bubble and a bubble generated by a high local energy input in the following situations:

- a bubble in an infinite liquid domain;
- a bubble in the vicinity of a rigid boundary;
- a bubble beneath a free surface; and
- a bubble near compliant surfaces.

In the study of an isolated bubble, the behaviour of a constant pressure vapour bubble is investigated and is compared with the behaviour of a vapour bubble with a changing internal pressure and also with the behaviour of an ideal gas bubble with different polytropic indices.

The behaviour of a constant pressure vapour bubble and also a rebounding bubble is determined in the vicinity of a rigid boundary. The influence of the buoyancy

forces and the Bjerknes attraction force through the rigid boundary is discussed in detail.

In the study of a bubble beneath a free surface, the dynamics of a constant pressure bubble and also a rebounding vapour bubble is carried out under the influence of the Bjerknes force through the free surface. In this case the behaviour of the bubble by eliminating the influence of the buoyancy forces and also the behaviour of a buoyant bubble are investigated.

In the study of a vapour bubble near compliant surfaces the computation involves three domains: the vapour and/or non-condensable gases inside the cavity bubble, the flow of the surrounding water and the deformation of the compliant surface.

An unsteady non-linear equation relates the loading to the deformation of the compliant surface. It allows the dynamic loading on compliant surfaces to be evaluated.

This computer technique depicts various modes of bubble's collapses on compliant surfaces. Significant damping effects on the micro-liquid jet momentum is obtained.

TABLE OF CONTENTS

LIST OF FIGURES

LIST OF TABLES

LIST OF SYMBOLS

a_j^r, b_j^r, c_j^r, d_j^r	standard coefficients of the cubic spline functions of r with respect to the arc length of the bubble
a_j^z, b_j^z, c_j^z, d_j^z	standard coefficients of the cubic spline functions of z with respect to the arc length of the bubble
a_j^ϕ, b_j^ϕ, c_j^ϕ, d_j^ϕ	standard coefficients of the cubic spline functions of ϕ with respect to the arc length of the bubble
a_j^ψ, b_j^ψ, c_j^ψ, d_j^ψ	standard coefficients of the cubic spline functions of ψ with respect to the arc length of the bubble
B	flexural rigidity of the membrane
$c(p_i)$	function of the solid angle of the boundary at a point i
d	damping coefficient of the compliant surface
d_j	length of the j^{th} linear segment
$E(k)$	complete elliptic integral of the second kind
ESWL	extracorporeal shock wave lithotripsy
f	external forcing term
g	gravity acceleration

H	a pressure function defined in Section 4.7
H and G	influence matrices used in the boundary integral method
h	initial distance of the bubble centroid from the nearby boundary
K	spring constant of the compliant surface
k	polytropic index
$K(k)$	complete elliptic integral of the first kind
K*	non-dimensional spring constant of the compliant surface
l	arc length of the bubble boundary
L_j	length of jth cubic spline centre
l_j	length of the j^{th} cubic spline segment
M	number of the segments on the bubble surface
m	mass per unit area of the membrane
M*	non-dimensional mass per unit area of the membrane
M_{cs}	number of the segments on the compliant surface
m_l	mass of liquid in the proposed control mass
M_{rb}	number of the segments on the rigid boundary
M_w	number of the segments on the wall
N	number of the segments on the free surface

n	unit outward normal vector to the boundary
$(P_v)max$	maximum pressure inside the bubble
P	pressure inside the bubble
P(x)	a tabulated polynomial
P_b	total pressure inside a bubble containing a mixture of constant pressure vapour and ideal gas
P_c	saturated vapour pressure of the liquid
P_g	partial pressure of the ideal gas inside the bubble
P_g	pressure due to the ideal gas inside the bubble
P_i	initial pressure inside the bubble
p_i	application point of unit potential
P_{ig}	initial partial pressure due to the ideal gas inside the bubble
P_o	pressure on the free surface
P_{rozo}	pressure on the rigid boundary at (r=0, z=0)
P_v	internal pressure of the bubble or internal pressure of a vapour bubble
P_w	pressure on the wall
P_∞	pressure at infinity
Q	heat transfer

q	a point on the boundary of the liquid domain
q'	a point on the surface of the image of the bubble
Q(x)	a tabulated polynomial
R	non-dimensional radius of the bubble
$\ddot{R}$	non-dimensional acceleration of the bubble wall
$\dot{R}$	non-dimensional velocity of the bubble wall
R	radius of the bubble
r	non-dimensional radial cylindrical polar coordinate
r	radial cylindrical polar coordinate
R(x)	a tabulated polynomial
R_{CS}	non-dimensional radius of the compliant surface
R_{cs}	radius of the compliant surface
R_m	maximum radius of the bubble
R_{min}	minimum volume of an isolated bubble at the end of the collapse phase
R_O	initial minimum radius of the bubble
S	surface of the liquid domain
S(x)	a tabulated polynomial

S_b	surface of the bubble
S_{fs}	surface of the free surface
S_j	j^{th} segment
S_w	surface of the wall including compliant surface and rigid boundary
T	longitudinal tension of the membrane (used in *Chapter 7* in the equation of compliant surface)
T	temperature inside the bubble
T*	non-dimensional longitudinal tension of the membrane
T_{max}	maximum temperature inside an isolated bubble at the end of collapse phase
t_o	initial time that a constant pressure vapour bubble takes to grow from the inception to radius of R_o
u	velocity vector along the direction of r
u_g	specific internal energy of the gas
u_i	radial component of the velocity
u_l	specific internal energy of the liquid
u_v	specific internal energy of the vapour
V	bubble volume

v	velocity vector along the direction of z
v_i	vertical component of the velocity
V_{max}	maximum volume of the bubble
z	axial (vertical) cylindrical polar coordinate
z	non-dimensional axial (vertical) cylindrical polar coordinate

GREEK SYMBOLS

δ	a non-dimensional parameter which shows the strength of the buoyancy forces
δ_{ij}	Dirac delta function
Δt	time step
ε	strength parameter (a measure of the strength of the initial high pressure inside the bubble which drives the liquid motion)
Φ	non-dimensional velocity potential
ϕ	velocity potential
$\phi_0^R(R_0, t_0)$	initial velocity potential over the surface of an isolated bubble
Γ	boundary of Ω
Γ_∞	imaginary boundary at infinity
γ	non-dimensional initial distance of the bubble centroid from the nearby boundary

η	tangential component of the velocity of the boundary
η_i^j	y-displacement of the j^{th} segment compliant surface from its equilibrium position at the i^{th} time step (used in *Chapter 7*)
λ_n	zeroth of the zeroth-order Bessel function
θ	angular direction in the polar coordinate system
ρ	density of the liquid
ρ_v	density of the vapour
Ω	any general 3-dimensional domain
ξ	local coordinate
Ψ	non-dimensional normal component of the velocity of the boundary
ψ	normal component of the velocity of the boundary

LIST OF PUBLICATIONS

Shervani-Tabar, M.T. and Soh, W.K. (1993), "Dynamic loading on compliant layers due to the collapse of a vapour bubble", Thirteenh Australasian Conference on the Mechanics of Structures and Materials, Wollongong, Australia, pp. 793-800, July 1993.

Soh, W.K. and Shervani-Tabar, M.T. (1992a), "Computer study of unsteady flow around a cavity bubble", Computational Methods in Engineering; Advances and Applications, Singapore, pp. 529-534.

Soh, W.K. and Shervani-Tabar, M.T. (1992b), "Computer study on the rebound of a vapour cavity bubble", 11th Australasian Fluid Mechanics Conference, University of Tasmania, Hobart, Australia, pp. 199-202.

Soh, W.K. and Shervani-Tabar, M.T. (1994), "Computer model for a pulsating vapour bubble near a rigid surface", Computational Fluid Dynamics JOURNAL, Vol. 3, No. 1., pp. 223-236.

CHAPTER ONE

INTRODUCTION

1.1 THE IMPORTANCE OF THE CURRENT RESEARCH

The study of the dynamics of cavitation bubbles and bubbles generated by a high local energy input is extremely important in engineering, science and medicine. In engineering, it is important in the design of ship propellers, hydrofoils and all kinds of hydraulic machines. In medicine cavitation bubbles are becoming more important due to their role in the disintegration of kidney stones and gallstones by Extrocorporial Shock Wave Lithotripsy.

1.2 THE IMPORTANCE OF NUMERICAL INVESTIGATIONS IN BUBBLE DYNAMICS

Numerical techniques have many advantages in the simulation of the bubble dynamics in various situations. Experiments cannot provide more detailed information about the phenomenon. Although high speed photography with framing rates up one million frames per second, gives reliable data on bubble wall velocity, but it is not successful in the determination of bubble wall velocities at the actual instant of collapse.

Analytical solutions for spherically symmetric bubbles are not valid due to the significantly deformed shape of the bubble at the later stages of its collapse.

It is accepted that only numerical methods are capable of simulating the bubble dynamics in the final stages of collapse.

1.3 BUBBLE DYNAMICS NEAR DIFFERENT BOUNDARIES

The dynamics of a cavitation bubble, or a bubble generated by a high local energy input, in the vicinity of a rigid boundary, a free surface and compliant walls is extremely important and has been one of the important research fields during recent decades.

During the last decade the boundary integral method was successfully applied on the dynamics of a cavitation bubble in the vicinity of a rigid boundary and near a free surface and provided more information about the phenomena. In 1987 Blake and Gibson in their review entitled "cavitation bubble and boundaries", suggested that the current challenge was to develop a robust numerical model that can cope with mixed boundary conditions provided by a surface coating with inertia, damping and stiffness.

In 1991 Duncan and Zhang calculated dynamics of a cavitation bubble in the vicinity of the Kramer-type compliant walls, by ignoring the effects of damping and flexural rigidity. They considered a cavitation bubble collapsing from its initial maximum spherical volume.

1.4 SCOPE OF THESIS

In this work a boundary integral method is developed and applied to the dynamics of a cavitation bubble and a bubble generated by a high local energy input. The behaviour of a bubble in the following situations is investigated:

- in an infinite liquid domain;
- in the vicinity of a rigid boundary;
- beneath a free surface; and
- near compliant walls.

The influence of condensation and vaporisation through latent heat is modelled by using the first law of classical thermodynamics for a control mass, and included in the analysis of the behaviour of a vapour bubble.

The dynamics of a rebounding bubble, generated by a high local energy input beneath a free surface, is investigated.

The growth phase of the bubble from its initial minimum volume is considered in the case of a bubble generated by a high local energy input near compliant surfaces.

1.5 THESIS ORGANISATION

This thesis is organised in eight chapters as follows:

In chapter one the significance of bubble dynamics and numerical investigations on the bubble dynamics, scope of the thesis, thesis organisation and a brief list of

contributions of this work to the fields of the bubble dynamics and the boundary integral method is presented.

In chapter two the historical background of the current research is discussed.

In chapter three the boundary integral method, developed throughout this research, is presented and discussed in detail. A new numerical technique to approximate the geometry of the bubble boundary and the distribution of the velocity potential over the surface of the bubble, Cubic Spline Geometry - Constant Physical Function is introduced.

In chapter four the dynamics of an isolated bubble, a bubble in an infinite liquid domain, is carried out and is discussed in detail.

In chapter five the dynamics of a constant pressure vapour bubble, the dynamics of a rebounding bubble generated by a high local energy input and dynamics of an ideal gas bubble with different polytropic indices is carried out in the vicinity of a rigid boundary.

In chapter six dynamics of a constant pressure vapour bubble, and also the dynamics a rebounding bubble generated by a high local energy input, beneath a free surface is determined.

In chapter seven the dynamics of a constant pressure vapour bubble, and also the dynamics of a rebounding vapour bubble collapsing from their initial maximum spherical volume, in the vicinity of compliant surfaces is carried out. In this chapter the dynamics of a rebounding bubble generated by a high local energy input is also determined. In this case the rebounding bubble is initially at its minimum volume and the initial growth rate of the bubble is considered.

In the conclusion presented in chapter eight the achievements of this research are assessed and discussed. In this chapter directions for future research are outlined.

The list of references follow chapter eight.

1.6 BRIEF LIST OF CONTRIBUTIONS

- Introducing the numerical model of "Cubic Spline Geometry - Constant Physical Function" and applying it to the dynamics of a vapour bubble in the vicinity of different boundaries.

- Determining the volume and radial velocity of an isolated bubble by numerical solution of the Rayleigh equation by the Mathematica software package and comparison with the corresponding values obtained by the boundary integral method.

- Determining the temperature inside an isolated rebounding vapour bubble and comparison with the temperature inside an ideal gas bubble with different polytropic indices .

- Determining the saturated vapour mass inside an isolated rebounding vapour bubble by considering the effects of condensation and vaporisation.

- The dynamics of an ideal gas bubble with different polytropic indices in the vicinity of a rigid boundary is carried out and the results are compared with the results of the behaviour of vapour bubble by considering the effect of condensation and vaporisation.

- Determining the critical value of $\gamma\delta$ as a criterion for the direction of the high speed liquid jet for a rebounding bubble containing a mixture of a constant pressure vapour bubble and ideal gas bubble.

- Investigating the effects of the Bjerknes force through the rigid boundary and the buoyancy forces on the developing of an annular liquid jet around a rebounding bubble, which cause necking and splitting of the bubble.

- Simulating the dynamics of a rebounding bubble generated by a high local energy input beneath a free surface.

- It is found that during the rebound phase of a bubble beneath a free surface, a stagnation point and a point of maximum pressure exist between the free surface and the bubble. In this case the stagnation point and the point of maximum pressure do not coincide.

- Simulating the dynamics of a rebounding vapour bubble collapsing from its initially maximum volume near a compliant surface.

- Determining the behaviour of a rebounding bubble generated by a high local energy input in the vicinity of a compliant surface. In this case the bubble is initially assumed to be in its minimum volume and the initial growth phase of the bubble is considered.

CHAPTER TWO

LITERATURE SURVEY

2.1 HISTORICAL BACKGROUND

Liquid under appropriate conditions may sustain considerable tension. If the tension subjected to a liquid is large enough the liquid fractures. The fracture of the liquid under high tension is known as cavitation. The name cavitation is given to the phenomenon because of the production of voids and clouds of bubbles in the liquid. This phenomenon is of great importance in both pure and applied science. In engineering it is related to the design of ship propellers and hydrofoils and all kinds of hydraulic machines because of the possible occurrence of cavitation damage and reduction of efficiency. In the design of nuclear reactors, the cavitation properties of the liquid coolant are of the utmost importance from the safety point of view. In medicine, cavitation is of great importance because it occurs in the human body. A rapid drop in the pressure of an aircraft cabin pressure at high altitude will cause cavitation in the blood. In Extracorporeal Shock Wave Lithotripsy (ESWL), cavitation bubbles play an important role in the fragmentation of kidney stones and gallstones [Zhong and Chuong (1993), Zhong, Chuong and Preminger (1993), Vakil, Gracewski and Everbach (1991) and Kitayama *et al.* (1987)].

The foundation of this important subject was laid by scientists in the eighteenth century. In about 1730 the mathematicians Jean and Daniel Bernoulli were

developing their idea about the relationship between pressure and velocity in a liquid flow. Leonard Euler was the first one who described mathematically the relationship between pressure and velocity in a fluid flow in 1754. The result of his achievement is known today as the Bernoulli equation, after Daniel Bernoulli, although it was first derived by Euler [Trevena, (1987)]. Euler showed that in a moving liquid where the liquid velocity increased the pressure decreased. If the velocity increases sufficiently the liquid may cavitate because of the large pressure drop.

In the nineteenth century the screws of steamships had the problem of losing their hold on the water under certain circumstances, and this had mystified the engineers. Reynolds in 1873 after investigating the problem by a series of experiments with a model boat concluded that the admission of air behind the blades of a propeller will reduce the ability of the propeller to supply itself with water [Reynolds (1873)]. The performance of the destroyer HMS Daring, in 1893, was a famous case where she sailed well below her design speed of 27 knots. Barnaby and Parsons (1897) found that the reduction of the speed of the destroyer was because of the poor propeller performance due to the formation of water vapour bubbles on the blades. When the first turbine ship, the Turbinia, met similar difficulties, Parsons (1906) realised that:

> *The excessive slip of the propellers beyond the calculated amount and their inefficiency, indicated a want of sufficient blade area upon which the thrust necessary to drive the ship was distributed - in other words, the water was torn into cavitation behind the blades. These cavities contained no air only vapour of water, and the greater portion of the power of the engine was consumed in the formation and maintenance of these cavities instead of the propulsion of the vessel.*

Parsons' experience with the Turbinia trials led him to building of a small closed water tunnel with a side window which was the first ever made for testing propellers. It is still in existence at the Department of Naval Architecture and Shipbuilding at the University of Newcastle upon Tyne.

Parsons developed a satisfactory wide-bladed propeller design. Nine such propellers were required to drive the Turbinia, three on each of the three shafts and consequently (as the result) a speed of 32 knots was attained.

The first time that the word "cavitation" appeared in the literature was in a paper by Barnaby and Thornycroft in 1895 describing the trials of a new destroyer [Trevena, (1987), Hutton (1972) and Young (1989)]. Barnaby and Thornycroft in their paper concluded that the propellers were not developing sufficient thrust because of the production of voids and clouds of bubbles in the water when the pressure near the blades fell to a negative value (tension) of about a half of an atmosphere. They described this effect by the term "cavitation" and this was suggested by R. E. Froud to the authors. Since then the term "cavitation" has been universally used to describe the formation of bubbles in liquids when the pressure fell to a sufficiently low value.

2.2 CAVITATION DAMAGE

Cavitation can damage almost any solid surface. Cavitation damage has been produced on very strong materials such as stainless steel, tungsten, carbides, glass concrete and quartz as well as soft materials such as Bakelite, rubber and plastic. It was found that the cavitation damage in various fluids such as the liquid metals, sodium, lithium, lead-bismuth alloy and organic fluids is of similar nature to that obtained with water [Hammitt (1966), Robinson and Hammitt (1967), Thiruvengadam *et al.* (1965), Garcia and Hammitt (1966), Garcia *et al.* (1967) and Wheeler (1960)].

For clarifying the mechanism of the cavitation damage, chemically inert liquids have been used in place of water in situations that water might cause chemical attack [Wheeler (1956 and 1960)]. These tests show that cavitation damage also occur in such dielectric liquids. Knapp *et al.* in their valuable book have concluded that [Knapp *et al.* (1970)]:

> *The fact that cavitation damage is produced by water on dielectrics as glass, quartz and Bakelite and that metals have been damaged by cavitation in dielectric liquid shows that electrical or electrochemical effects cannot be responsible for all cavitation damage. Also the fact that these combination of liquids and solids were not only dielectric but chemically inert shows that chemical attack is not a necessary factor in the damage process. It must be concluded, therefore, that one of the major factors that cause cavitation damage is purely mechanical and this factor is always present. ... However, it is certainly true that other*

factors such as chemical and corrosive effects are also important in some cases.

2.3 CAVITATION EROSION

Turbines, bearings and mechanical seals, as well as many other marine devices such as hydrofoils, struts, torpedoes, sonar domes and stabilisers may suffer cavitation problems [Pearsall (1972)]. The material may be eroded so rapid as to require the replacement of a ship's propeller after a voyage or a pump's impeller after a few weeks.

To minimise cavitation, an optimum design can be found for most of these devices with the aid of theory or model experiments. Erosion damage in these devices because of cavitation can be alleviated by proper material selection. Also significant attention has been made to use of protective coatings of soft material, such as rubber and plastics, or hard material such as stainless steel. In this particular field satisfactory adhesion of the coating to the parent surface is an important problem which should be solved properly.

2.4 MECHANISMS OF CAVITATION DAMAGE

A cavitation bubble during its collapse produces pressure and thermal shock waves, and high speed liquid micro-jets. These intense local forces will damage the material in the vicinity of the collapsing bubble. Cavitation damage starts as pitting and may become large holes [Young (1989)]. So it would appear that there are two mechanisms responsible for the damage caused by a bubble collapse:

a) the damage caused by the impact of the high speed liquid microjet on the surface,

b) the effect of the radiated shock wave hitting the surface.

Lush and his coworkers have given a remarkable theoretical analysis of a surface damage because of both high speed liquid microjet and shock wave [Lush *et al.* (1983) and Lush (1983)]. They have analysed the cavitation damage by two model; the microjet model and the shock wave model.

2.4.1 The microjet model

In this model a cylindrical liquid micro-jet of radius a with a conical tip is considered. The conical tip of the liquid micro-jet strikes a solid surface with a velocity v. The result is a conical pit of depth d and radius a in the solid. In this model the liquid micro-jet radius and pit radius are assumed to be equal. By means of this model a theoretical value for the ratio $\frac{d}{a}$, which is the average surface slope of the pit, can be obtained.

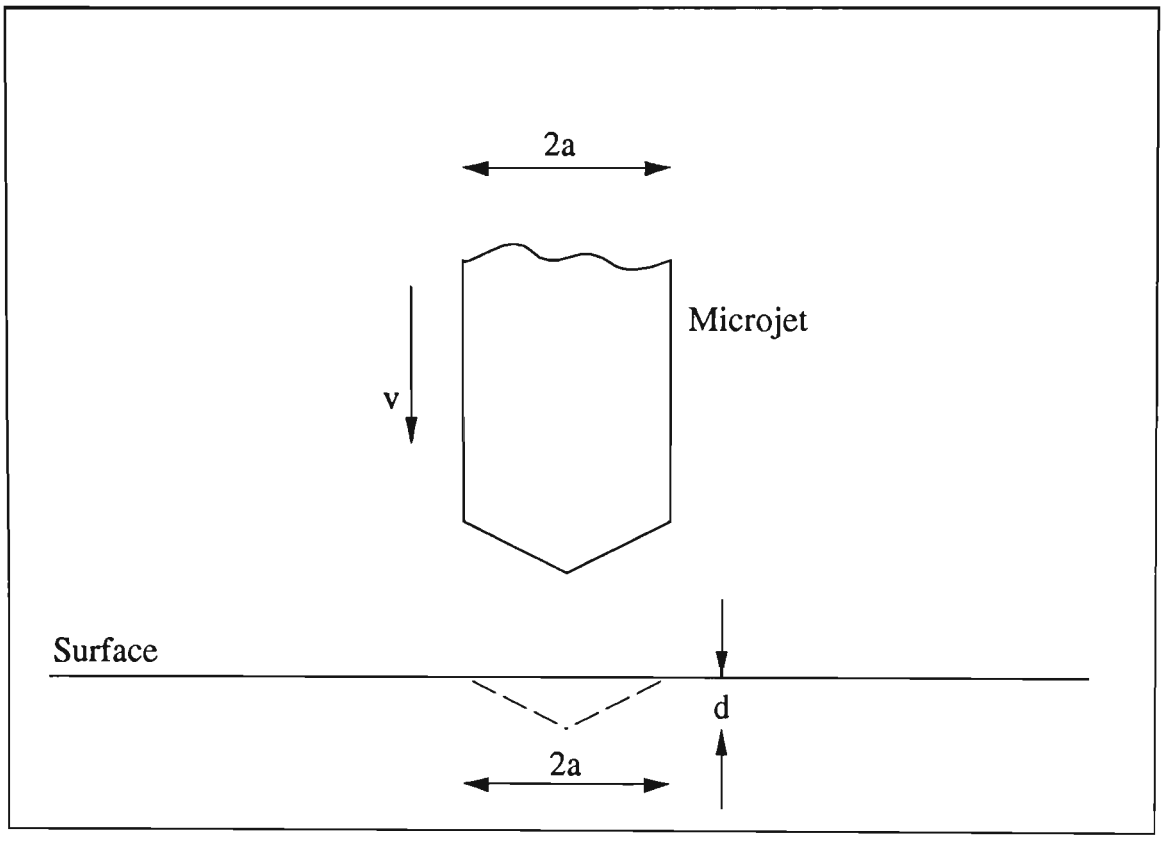

Figure 2.1A liquid micro jet just before it impinges upon the solid surface. The conical pit which is created after the liquid microjet impact is shown by a dashed line [Lush *et al.* (1983)].

2.4.2 The shock wave model

In this model a spherical shock wave radiating from the centre of a collapsing bubble at a distance h from the surface is considered. At a later stage of the collapse a saucer-shape pit is created in the surface. The maximum depth of this saucer-shaped is d and its edge is a circle with radius a on the solid surface. By using this model a theoretical value for the average surface slope, $\frac{d}{a}$, can be calculated.

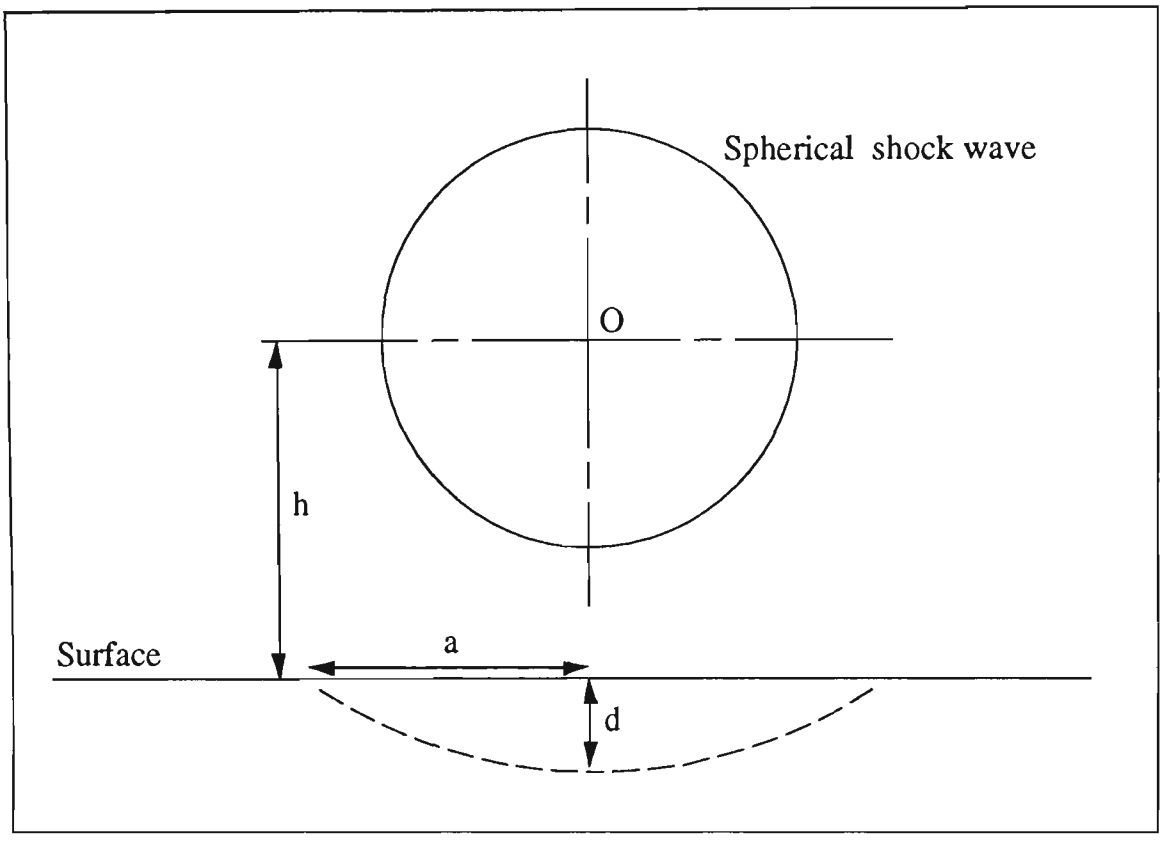

Figure 2.2 A spherical shock wave approaching the solid surface. The saucer-shaped pit which is formed after the impact of the shock wave on the slid surface is shown by a dashed line [Lush *et al.* (1983)].

2.5 EXPERIMENTAL STUDIES ON CAVITATION EROSION

Koutny (1987) [see also Sedlacek (1992)] has presented characteristics of the cavitation effect which is based on the data of some published experiments, Table 2.1. From these data it is obvious that there is no material that could permanently resist cavitation effects.

Table 2.1 Characteristics of cavitation effects [Koutny (1987)]

Parameter	Range of common values
Initial common crack diameter	$30-5000\ \mu m$
Decay time	$10^{-6}-10^{-3}\ s$
Maximum pressure in bubble	$(1-30)\times10^{3}\ Pa$
Maximum temperature in bubble	$(1-4)\times10^{3}\ ^{o}C$
Microbeam (microjet) diameter	$1-50\ \mu m$
Microbeam (microjet) velocity	$50-1500\ m.s^{-1}$
Loading frequency	$10-100\ Hz$
Pit diameter	$0.1-500\ \mu m$
Pit depth / pit diameter ratio	$0.02-1$
Involved layer thickness	$50-150\ \mu m$

2.6 STUDIES ON BUBBLE DYNAMICS

It is obvious that cavitation usually occurs as the production of clouds of bubbles in a cavitating liquid domain. But it has proven more profitable to study the growth and collapse of a single bubble. A vast array of literature exists on the topic of bubble investigation, both experimental and theoretical. The earliest study on this

topic is traced back to the work by Besant [Besant (1859)]. He explained the problem in his book as follow:

> *An infinite mass of homogeneous incompressible fluid acted upon by no forces is at rest, and a spherical portion of the fluid is suddenly annihilated; it is required to find the instantaneous alteration of pressure at any point of the mass, and the time in which the cavity will be filled up, the pressure at an infinite distance being supposed to remain constant.*

Besant used the equation of the fluid and solved this problem.

Rayleigh, in 1917, considered the same problem by assuming a vapour-filled cavity in a liquid domain. He found an elegant solution for the velocity of the bubble boundary and the time of bubble collapse. In this model the pressure inside the bubble is considered constant and the vapour bubble collapses under the influence of a constant pressure in the liquid at infinity. Although this is the simplest possible model for the collapsing of a spherical bubble, it is a remarkably good model of a bubble collapse and is still used by many researchers.

The basic Besant-Rayleigh differential equation for bubble collapse can be expressed as [Hammitt (1980)]:

$$R\ddot{R} + \left(\frac{3}{2}\right)\left(\dot{R}\right)^2 = \frac{1}{\rho}\left(P - P_\infty\right), \tag{2.1}$$

where

R = radius of the bubble measured from its centre,

ρ = liquid density,

P_∞ = pressure in the liquid at infinity,

P = pressure in the liquid at the bubble wall.

It should be noted that upon application of this theory an initially spherical cavitation bubble at its maximum volume collapses to a small fraction of its initial size and generates a high local pressure. Equation (2.1) is also known as the Rayleigh equation [Plesset and Prosperetti (1977)], extended Rayleigh equation [Hammitt (1980)] and Rayleigh-Plesset equation [Young (1989)].

Equation (2.1) can be modified to include both the surface tension and the effect of internal gas in addition to vapour pressure [Hammitt (1980)]:

$$R\ddot{R} + \frac{1}{2}\dot{R} = \left(\frac{P_1 - P_\infty}{\rho}\right), \tag{2.2}$$

where

$$P_1 = P_V - \frac{2\sigma}{R} + \frac{NT}{R^3}, \tag{2.3}$$

N = constant incorporating the gas properties,

T = absoloute temperature,

σ=*surface tension,*

P_V=*vapour pressure.*

Plesset and Prosperetti in their review article on the topic of "bubble dynamics and cavitation", (1977), have pointed out that for a spherical bubble, viscosity effects appear only on the boundary conditions so that the relationship between pressure

inside the bubble, P_i, and the pressure in the liquid at the bubble boundary, $P(R)$, is given by:

$$P(R) = P_i - \frac{2\sigma}{R} - \frac{4\mu}{R}\dot{R}. \tag{2.4}$$

The surface-tension constant and the coefficient of the liquid viscosity are indicated by σ and μ respectively. By using Equation (2.3), they give a generalised Rayleigh equation for bubble dynamics as:

$$R\ddot{R} + \frac{1}{2}\dot{R} = \frac{1}{\rho}\left(P_i - P_\infty - \frac{2\sigma}{R} - \frac{4\mu}{R}\dot{R}\right), \tag{2.5}$$

where the pressure in the gas at the bubble boundary, P_i, may be a function of time, and the pressure at infinity, P_∞, may also be a function of time.

It should be noted that the surface-tension term, which has always a stabilising effect, is important only for very small bubbles.

2.6.1 Dynamics of a vapour bubble near a rigid surface

The effect of a rigid boundary on the dynamics of a collapsing bubble in its neighbourhood is explained by Plesset and Prosperetti (1977):

> *We have seen that, in principal, deviations from the spherical shape for a bubble in an unbounded liquid can take place only through the amplification of preexisting small perturbations. No such initial perturbations, however, are necessary for the occurrence of the deformations of a bubble near a boundary, because the asymmetry of the flow that the boundary itself introduces is sufficient to give rise to highly distorted bubble shapes.*

The formation of liquid jets on the collapse of bubbles near a solid surface was first suggested by Kornfel and Suvorov in 1944. According to their theory cavitation damage is due to the formation of high speed liquid jets during the collapse of bubbles near a solid surface. The idea that liquid microjets could be responsible for cavitation damage was not explored any further, and the large pressure associated with the later stages of the bubble collapse, as suggested by Rayleigh in 1917, remained an accepted explanation for cavitation damage. In 1961 Naude and Ellis undertook the first experiment on the formation of a high speed microjet.

Gibson (1968) in his landmark article entitled "Cavitation adjacent to plane boundaries" reported the results of his experimental investigations into the collapse of cavities in the vicinity of three types of plane boundary:

- a rigid surface,
- a free surface,
- a flexible foam plastic surface.

Gibson used an experimental apparatus having the important feature of being able to remove the effect of gravity during the life time of a vapour cavity. This was possible by mounting a perspex box, where a single cavity was generated by an electrical discharge, on a platform which was able to fall freely between two vertical guide rails through the view field of a drum camera. The results of his experiments on a bubble near a rigid boundary suggested that jet-impact is a potent damage mechanism. Gibson divided his experimentally observed cavities into two broad categories:

a) those which became attached to the boundary during the expansion,

b) those which did not attach to the boundary until they were toroidal.

After an electrical spark discharg a cavity of category (a) initially expanded spherically until it made contact with the rigid boundary when its side attached to the boundary became distorted from the spherical form. During the last stages of collapse all bubbles of category (a) deformed in a similar manner. A dimple appeared on the side of the bubble far from the rigid boundary, then rapidly grow into a liquid jet. The liquid jet threaded the bubble along its axis of symmetry and impinged on the rigid boundary. A cavity belonging to category (b) remained almost spherical during its expansion, whereas during the initial stages of collapse it deformed into a prolate form. Then the cavity kept its prolate form for the greater part of the collapse and finally became toroidal and moved rapidly towards the rigid boundary. Gibson found that the average value of the jet velocity, $\overline{V}_J$, for the 15 cavities that had shown direct impingement, might be represented with an equation such as:

$$\overline{V}_J = 7.6\left(\frac{P_\infty - P_c}{\rho}\right), \tag{2.6}$$

where P_C is the saturated vapour pressure of the liquid.

Equation (2.6) found that the average jet impact speed for bubbles collapsing under a pressure of one atmosphere in water was about 76 m/s (250 ft/s). Therefore the corresponding impact pressure of the liquid jet could be found by using the water hammer equation:

$P_1 = 1.7\times10^4$ lb./in.^{2}.

Gibson concluded that the pressure of the liquid jet impact was well in excess of the yield stress of the aluminium boundaries which had been used by Naude and Ellis

(1961). Thus his results provided support to the conclusion had been made by Naude and Ellis that the cavitation damage which they had observed was due to the liquid jet impingement.

Analytical treatment of the problem of bubble collapse in the neighbourhood of a rigid boundary is extremely complex. Rattray, in 1951, predicted the possibility of jet formation and also predicted the elongation of the bubble in a direction perpendicular to the rigid boundary in the early stages of bubble collapse. The first theoretical analysis of the collapse of an empty bubble in the vicinity of a rigid boundary was given by Plesset and Chapman in 1971, who successfully treated the problem by a numerical method. They assumed the bubble to be spherical and at rest at the initiation of the collapse, and neglected any other extraneous asymmetric effects such as gravity. The work of Plesset and Chapman was the first numerical work which successfully simulated the collapse of a vapour bubble close to a solid surface. It is therefore worthwhile to review their original work in more detail. The assumptions made in their numerical method are:

1) The liquid is incompressible;

2) The flow is non-viscous;

3) The vapour pressure is uniform throughout the bubble interior;

4) The ambient pressure and the vapour pressure are constant with time;

5) The bubble contains no permanent gas; and

6) Surface tension effects are negligible.

Only the first three assumptions were essential to the method of simulation that they developed. The last three assumptions were made to keep the essential features of

the problem defined. Results of their calculations showed that the solid wall influenced the bubble early in the collapse by reducing the upward motion of the lower part of the bubble. By reducing this upward motion, the bubble elongated in a direction normal to the wall. This fact had been previously predicted by Rattray in 1951. Their calculations predicted the formation of the liquid jet in the upper portion of the bubble. They pointed out that after the formation of the liquid jet, the speed of its tip remained fairly constant. They found that in the case of a bubble initially attached to the a wall, the liquid jet speed was 130 m/s. However in the case ofthe initial distance from the centroid of the bubble to the solid wall being 1.5 times initial radius of the bubble, the jet speed was 170 m/s. These values of jet speed were obtained when the pressure difference driving the bubble collapse was about one atmosphere. They wrote:

> *As general conclusion we may say that it appears very likely that cavitation damage with collapsing vapour bubbles is caused by the impact of the jet produced by the presence of the adjacent solid wall. Further, it appears reasonable to say that only those cavitation bubbles quite near the solid boundary can produce damage whether by a jet or by any radiated shock.*

They used the water hammer equation to obtain the pressure produced by liquid jet of speed v directly striking the solid wall,

$$P_{WH} = \rho_L c_L v \left(\frac{\rho_s c_s}{\rho_L c_L + \rho_s c_s} \right), \tag{2.7}$$

where c is the sound speed, while L and s subscripts refer to the liquid and the solid, respectively. Since $\rho_s c_s$ is large compared to $\rho_L c_L$, Equation (2.7) reduces to

$$P_{WH} = \rho_L c_L v. \tag{2.8}$$

Plesset and Chapman used Equation (2.5) to determine that for a liquid jet of speed 130 m/s the "water-hammer" stress was about 2000 atm. They concluded that:

> *While this is a most impressive impact stress, it is not obvious that it is the important mechanism since the duration of this stress is so short. We can estimate this duration as being no longer than the time for the impact signal to traverse the radius of the jet.*

Lauterborn and Boll in 1975 experimentally confirmed the numerical results of Plesset and Chapman (1971). Figure 2.3 illustrates a comparison of their experimental results, with the numerical results of Plesset and Chapman for the collapse of an initially spherical cavitation bubble in the vicinity of a rigid boundary. The initial distance, b, of the centroid of the bubble from the rigid boundary is 1.5 times the initial radius of the bubble.

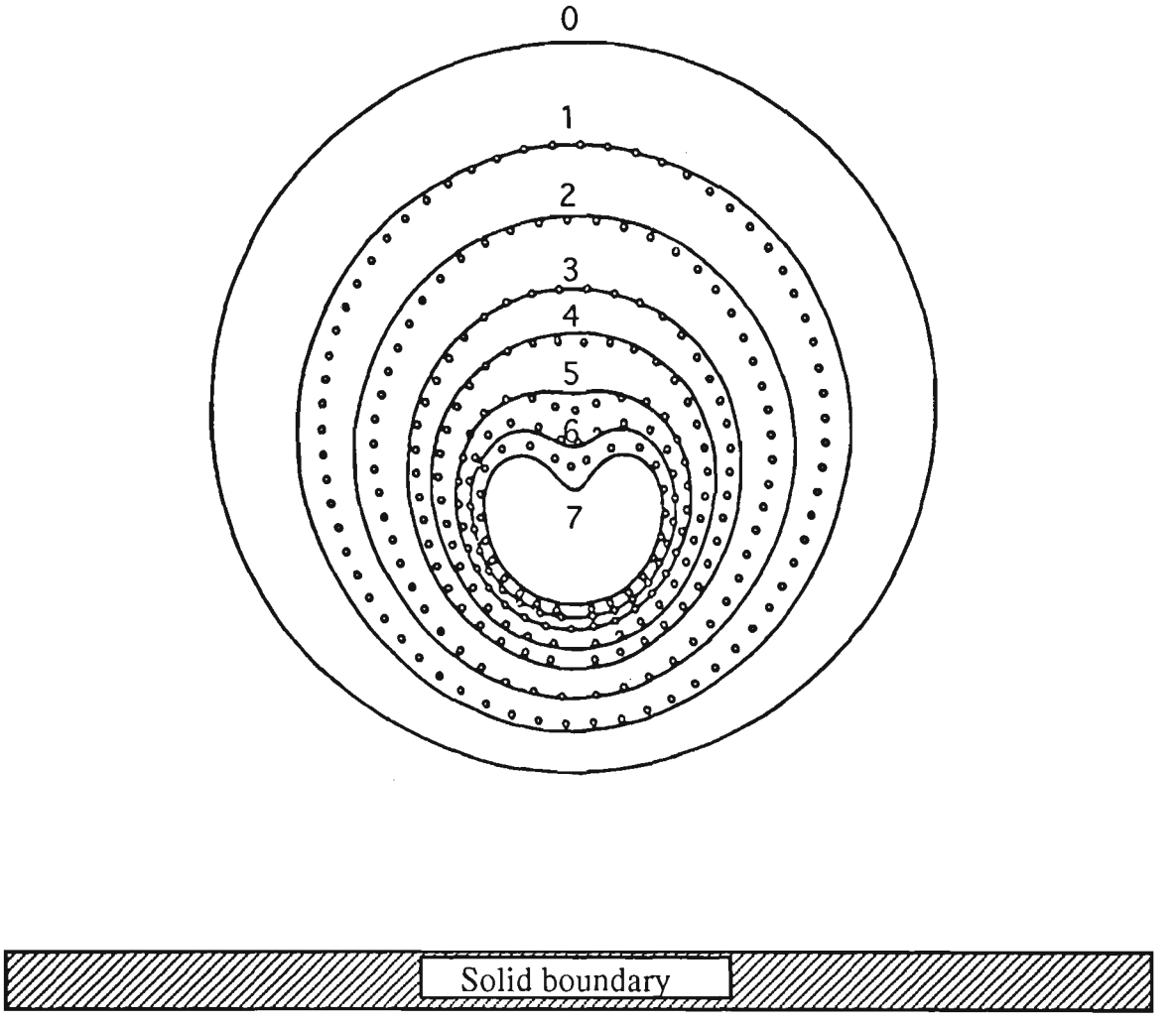

Figure 2.3 Comparison between experimentally obtained bubble shapes (open circles) during the collapse of a spherical bubble near a rigid boundary and the theoretical results (continuous line) of Plesset and Chapman (1971). The framing rate is 300000 frames/s, the maximum bubble radius R_{max}=2.6 mm, the initial distance from the bubble centroid to the wall b=3.9 mm and b/R_{max}=1.5 [from Lauterborn and Boll (1975)].

Table 2.2 presents the time and jet velocity for several selected shapes of the bubble during its collapse which is shown in Figure 2.3 by the continuous line and is calculated by Plesset and Chapman under a collapse driving pressure of one

atmosphere. It also shows the measured time and jet velocity for several selected shapes of the bubble shown in Figure 2.3 by open circles and measured by Lauterborn and Boll experimentally. It should be noted that the bubble shapes indicted by 8, 9 and 10 in Table 2.2 are not shown in Figure 2.3, because it was not possible for Lauterborn and Boll to capture the shapes of the bubble at these later stages of collapse. However, they are included in the table to show that after the liquid jet initiates, its velocity (first) remains nearly constant and then decreases very slightly as it approaches the opposite side of the bubble.

Table 2.2 Comparison between the numerical results obtained by Plesset and Chapman (1971) and the experimental results obtained by Lauterborn and Boll (1975)

Bubble Shape	Numerical Results Plesset & Chapman (1971)		Experimental Results Lauterborn & Boll (1975)
	Time $R_m\left(\frac{\rho}{P_\infty - P_c}\right)^{\frac{1}{2}}$	Velocity m/s	Time $\left[R_m\left(\frac{\rho}{P_\infty - P_c}\right)^{\frac{1}{2}}\right]$
0	0	0	0
1	0.63	7.7	0.725
2	0.885	19	0.825
3	0.986	42	0.961
4	1.013	65	0.991
5	1.033	100	1.016
6	1.048	125	1.028
7	1.066	129	1.036
8	1.082	129	---
9	1.098	128	---
10	1.119	128	---

Lauterborn and Boll pointed out that even by using a high speed photography at the framing rate of 300000 frames/s, the instant of collapse cannot be determined precisely. They measured a maximum jet velocity of 120 m/s at a framing rate of 250000 frames/s with a value of $\frac{b}{R_{max}} = 3.8$, where b and R_{max} are the initial distance of the bubble centroid from the solid wall and the maximum radius of the bubble respectively.

Lauterborn (1980) in the introduction to his paper, grouped the quite different types of cavitation systematically. According to his scheme cavitation may be brought about by two mechanism, either a tension in the liquid or a local deposit of energy. Figure 2.4 illustrates his classification scheme for different kinds of cavitation.

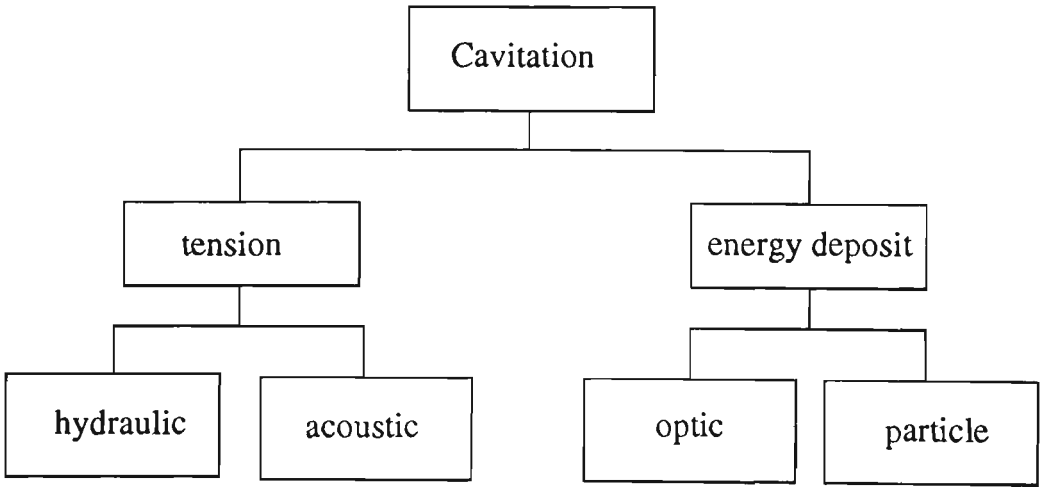

Figure 2.4 Classification scheme for different kinds of cavitation [from Lauterborn, (1980)]

He investigated the collapse of a vapour bubble in the neighbourhood of a solid boundary by using a high speed camera with a framing rate of 75000 frames/s. He

observed that in the case of a bubble with maximum radius of 1.1 mm and generated with $b = 4.5$ mm a liquid jet developed at the end of the first collapse and during the first rebound. He predicted that the diameters of such jets lie in the range of $10-100\ \mu$m and that their maximum velocities are in the range of $100-200$ m / s.

Lauterborn and Timm (1980) studied bubble collapse by high speed photography at one million frames per second. They observed that a spherical laser produced bubble, far from any boundaries, collapsed to a very small spherical bubble, and at the end of the collapse a shock wave was radiated from the bubble in the liquid domain. They noticed that during the rebound the vapour bubble deviated from sphericity. Their study showed that in the case of a vapour bubble in the neighbourhood of a boundary, the collapse was not as strong as for the infinite liquid case. In the case of a bubble near a rigid boundary they observed that a weaker shock wave radiated into the liquid domain at the end of the collapse and just after commencement of the rebound.

Blake *et al.*, (1986) investigated the growth and collapse of a vapour bubble near a rigid boundary in the presence of buoyancy forces and stagnation-point flow by using a boundary integral method. They were the first researchers who numerically simulated the bubble behaviour during both its growth and collapse phases and found that the growth phase had important effect on the behaviour of the bubble during its collapse. They pointed out that while a rigid boundary always attracted a pulsating cavitation bubble through the Bjerknes effect, buoyancy forces and stagnation-point flow might either attract or repel a bubble depending on their orientation and strength. They used the Kelvin impulse technique to analyse buoyant vapour bubbles and obtained a criterion for determining the direction of bubble migration and the subsequent liquid jet formation. They found that the

value of $\gamma\delta = 0.442$ was critical in determinig the direction of bubble migration and development of the liquid jet, where γ determined the initial location of the bubble, and δ indicted the relative importance of the buoyancy forces. They concluded that in the case of $\gamma\delta < 0.442$ the vapour bubble, located above a rigid boundary, was attracted to the rigid boundary with a liquid jet directed towards the boundary. In the cases of $\gamma\delta > 0.442$ the vapour bubble migrated upward with a liquid jet away from the boundary. For more information about the boundary integral equation technique used by Blake *et al.*, the reader is referred to the work of Taib (1985).

Blake and Gibson (1987), in their review on the topic of cavitation bubbles near boundaries, presented the history of the subject in great detail and concentrated on developments in the field that had been achieved since the first review of this subject by Plesset and Prosperetti in 1977. They discussed the bubble behaviour in the vicinity of a rigid boundary, near a free surface, close to an interface between two fluids of different density and in the neighbourhood of composite and flexible materials. Their discussion and comments in the case of a bubble near a compliant surface is discussed in *Section (2.6.4)* of the present work.

Vogel and Lauterborn (1988) experimentally studied the flow around cavitation bubbles during their collapse near a solid wall. In their study bubbles were produced by focusing pulses from a passively Q-switched ruby laser into a cuvette with distilled water. They tracked the unsteady flow generated by a cavitation bubble by combining particle image velocimetry and high speed photography. As a result of their study, they found the path line trace of the flow around a collapsing bubble near a rigid wall which confirmed the numerical calculations of Kucera and Blake (1988). This is shown in Figure 2.5.

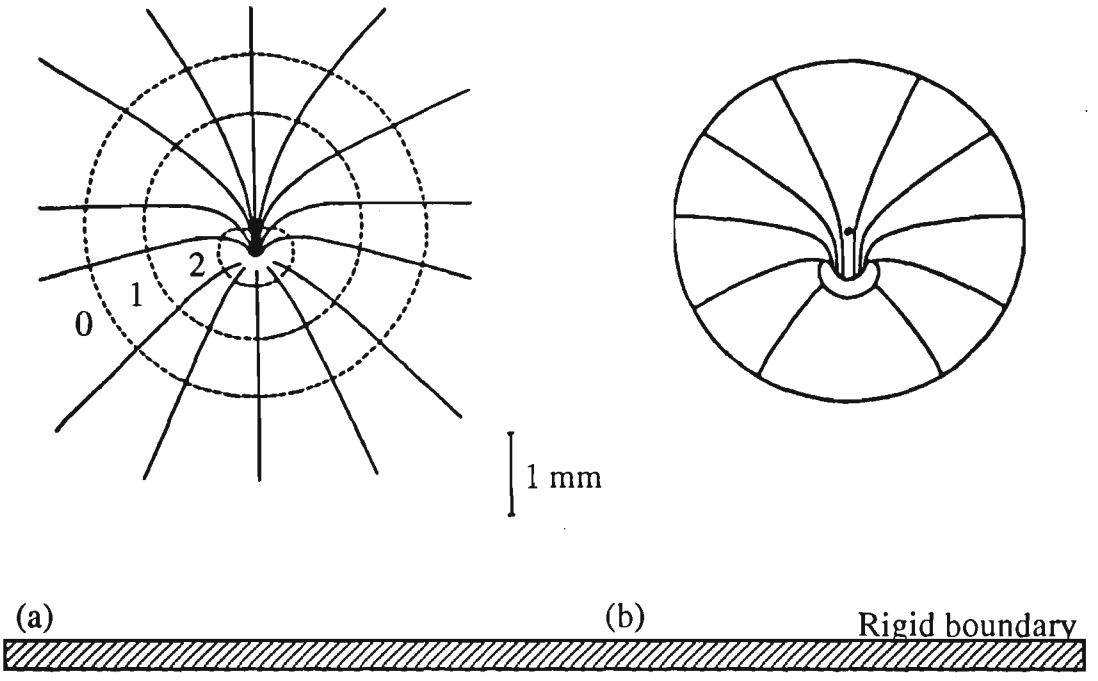

Figure 2.5 (a) Experimentally obtained path line trace of the flow around a collapsing bubble near a solid wall at $\gamma = 2.4$. Bubble shape 0 represents the bubble at maximum expansion, shape 1 corresponds to $t = 1.85$ and shape 2 $t = 2.08$, while t is the time non-dimensionalised by $R_m\left(\frac{\rho}{P_\infty - P_c}\right)^{\frac{1}{2}}$. (b) Calculated pathline trace for $\gamma = 2.4$ from Kucera and Blake (1988) for several points on the wall of a collapsing bubble. The dots in (a) and (b) indicates the location of bubble inception [from Vogel and Lauterborn (1988)].

2.6.1.1 Dynamics of a rebounding bubble

The numerical studies on the dynamics of a vapour bubble discussed previously assume the vapour bubble to have a constant vapour pressure inside. It has been shown that the assumption of constant vapour pressure inside the bubble is accurate

enough for studying the first cycle of the bubble's growth and collapse. Experimental observations [Lauterborn (1980), Wong *et al.* (1989) and Soh and Yu (1992)] show that an electrical spark generated vapour bubble often undergoes more than one cycle of growth and collapse. This fact indicates the building up of pressure inside the vapour bubble produced by a high local energy input. It is obvious that building up of pressure inside the vapour bubble in most cases causes rebounding of the bubble.

Best (1991) studied the dynamics of underwater explosion bubbles by assuming the non-condensable bubble contents to be an ideal gas. He successfully simulated the rebound of an explosion bubble after its collapse phase. Best was the first researcher to successfully simulate the dynamics of a toroidal bubble after the liquid jet had reached the opposite side of the bubble.

Soh and Shervani-Tabar (1992a, 1992b and 1994) simulated the dynamics of a vapour bubble by a semi empirical approach and obtained bubble rebound by using the vapour properties from steam tables. They made a detailed comparison between the dynamic nature of a rebounding vapour bubble and ideal gas bubbles with different polytropic indices.

Zhang and Duncan (1994) studied the dynamics of a cavitation bubble by considering an internal gas pressure inside the bubble which was a function of the bubble volume. They also generated the bubble's motion after its transformation to a toroidal shape by using the same method as used by Best (1991).

For more details on the dynamics of a vapour bubble near a rigid boundary one can also refer to the work of Ellis and Benjamin (1966), Shima and Nakajima (1977), Prosperetti (1980), Prosperetti (1982), Hirose *et al.* (1983), Tomita and Shima (1986), Kucera and Blake (1988), Blake (1988), Vogel *et al.* (1989), Tomita and

Shima (1990), Best and Kucera (1992), Best (1993), Kumar and Brennen (1993), Philipp *et al.* (1993) and Zhang and Duncan (1993).

2.6.1.2 The effect of heat transfer on the dynamics of a bubble

The effect of heat transfer on the behaviour of a vapour bubble has been studied numerically and theoretically during the last two decades. Prosperetti (1991), as one of his more informative papers, concluded that in bubbly liquids thermal damping in nearly isothermal or nearly adiabatic cases was small. According to Prosperetti, in the nearly isothermal case, since the thermal penetration was large compared to the radius, the temperature in a bubble deviated little from its equilibrium value, while in the nearly adiabatic case most of the gas in the bubble was insulated from the liquid. He proved that thermal damping, in the nearly isothermal case, resulted in a term with the same mathematical structure as viscous damping.

Fujikawa and Akamatsu (1980) in their original paper considered the effect of heat conduction inside a bubble and in the surrounding liquid. They also considered the effects of compressibility and viscosity of the liquid, non-equilibrium condensation of the vapour and the temperature discontinuity at the phase interface.

Karimi and Soh (1994a, 1994b) have recently studied the effect of heat transfer in the dynamics of a spherical vapour bubble in an infinite fluid. They used the dual reciprocity boundary element method to solve the energy equation in the liquid. In their work the liquid motion is simulated by the flow field of a sink or source, with the properties of the vapour found from thermodynamic tabulations. The non-condensable contents are assumed to behave as an ideal gas. They concluded that

their formulation is a suitable method for the study of changes of vapour mass, partial pressure of vapour and non-condensable gas, temperature of the bubble contents, bubble wall velocity and volume of the bubble. It was also pointed out that the reduction of amplitude of the pulsations, which were numerically obtained, demonstrate that heat transfer has a damping effect on the dynamics of a pulsating bubble. This fact was previously observed by Wong *et al.* (1989) experimentally.

2.6.1.3 Bubble dynamics under oscillatory ambient pressure

Sato *et al.* (1994) investigated the dynamics of a gas bubble near a rigid boundary numerically by using a boundary integral method. They found that the period and amplitude of the bubble oscillation are related not only to the nature of the time dependent pressure in the liquid but also to the location of the bubble with respect to a rigid boundary. Their results illustrated that once the pressure inside the bubble became larger than the surrounding pressure, the bubble collapse motion changed to growth motion. They noticed that the bubble motion tended to have a short period with small amplitude due to the relatively large frequency of the surrounding oscillatory pressure. They explained that:

> *Therefore, we understand that the effect of the rigid boundary on the bubble motion becomes weaker as the frequency of the pressure oscillation is increased. ... This result suggested that if the bubble is subjected to high-frequency pressure oscillations, the resultant bubble motion is strongly affected by the pressure oscillation while very little bubble migration occurs.*

For more details on the dynamics of a spherical bubble under oscillatory ambient pressure one also can refer to the work of Forbes (1994).

2.6.1.4 Vapour bubble collapse near moving rigid structures

The dynamics of a vapour bubble near a finite rigid body is of great interest in the fields of engineering and science. It is obvious that the size and the geometry of the rigid body is an important parameter which affects the fluid flow around a pulsating vapour bubble in its vicinity. The behaviour of a vapour bubble with a comparable size to the rigid body will be significantly different from the case of a vapour bubble collapsing near a rigid boundary. A few experimental and numerical studies have been done which provide very general insight to the problem.

Soh and Yu (1993) studied the dynamics of a vapour bubble near a fixed submerged perspex sphere experimentally by using a high speed camera. Their results showed that the vapour bubble migrates towards the perspex sphere and collided with it.

Harris (1992) studied the motion of a bubble close to a fixed rigid structure. He utilised a fully three dimensional boundary element method to determine the migration of the vapour bubble and the direction of the liquid jet which was developed during the bubble collapse near a rigid structure. Harris analysed the motion of the bubble close to a fixed rigid structure in the cases of a weak gravity field and a strong gravity field. Harris later extended his work and considered the motion of a bubble close to a moving rigid structure [Harris (1993)]. He showed that the growth and collapse of an explosion bubble led to significant changes in the

pressure distribution on the nearby structure. He concluded that changes in the pressure could be an important mechanism for damage to the structure.

2.6.1.5 Dynamics of a column of bubbles near a rigid surface

Lauterborn (1980) investigated cavities collapsing near each other and near a solid wall by using a high speed camera with a framing rate of 75000 frames/s. His experimental results showed strong jet formation in the case of two equally sized cavities collapsing simultaneously. Obviously the configuration of the bubbles was equivalent to the collapse of a cavity in the vicinity of a rigid boundary at half the distance between the cavities. Consequently both of the cavities developed a liquid jet directed to each other. This fact had also been observed in the experimental works of Lauterborn (1974) and Timm and Haimmitt (1971). Lauterborn observed distinctly different phenomena when the cavities were of different sizes. A very small cavity near a big one developed a jet directed away from the big cavity. A comparable size cavity developed a liquid jet towards the big one. The intermediate case between the above two cases displayed very interesting behaviour. In this case the smaller bubble developed two jets simultaneously opposite to each other , one directed towards the larger cavity and the other directed away from it. He investigated the collapse of two bubbles near a solid wall and concluded that:

> *It is found that the jet is now inclined both to the boundary and to the other cavity. The issue is that another cavity can deflect the jet away from the boundary . This is an important fact as jet formation is believed to be at least one source of damage to solids from cavitation. The observation that jets are deflected away from the boundary suggests that dense cloud cavities as often encountered in hydraulic as*

well as acoustic cavitation may have less damage capabilities than loosely distributed ones.

Blake *et al.* (1993) studied the dynamics of two bubbles close to a rigid surface experimentally and numerically by using the boundary integral method and assuming the bubbles to have constant internal vapour pressure. Comparison between experimental and numerical results were favourable with regard to both the bubble shape history and centroidal motion. They emphasised that nearby bubbles are equally as important as the presence of a rigid boundary in determining the behaviour of bubbles. Their study revealed a wide range of bubble responses and clearly indicated the significance of including the dynamics of bubble interaction in any large-scale two phase flow. They studied the behaviour of two approximately equally sized bubbles near a rigid boundary. They found that during the growth and collapse phase of a bubble close to the rigid boundary there was no liquid jet directed towards the rigid boundary as had been observed in the case of a single bubble under the same conditions. Their experimental results showed that the bubble close to the rigid surface was elongated during its collapse phase. This phenomenon was due to the fact that bubble close to the rigid surface was subjected to strong interactions with both the rigid surface and the bubble above it. They put emphasis on the behaviour of two bubbles with similar sizes and different sizes and with different distances between the lower bubble and the rigid boundary. They concluded that when bubbles were close together their mutual interactions could dominate over the influence of a rigid boundary. They also clarified that although the axisymmetric case was only likely in very special circumstances, it highlighted the importance of the interactions with the nearest bubble or boundary.

Kucera (1994) investigated the dynamics of axi-symmetric multiple bubbles near a rigid surface. The bubbles contained saturated vapour with constant vapour

pressure. As in his previous works [Kucera and Blake (1988)] he used boundary integral method and employed cubic splines to represent the geometry of the elements and velocity potential on the elements. He used a simple Euler scheme to calculate the evolution of the bubble. Kucera studied the dynamics of a bubble near a rigid boundary and as expected observed a high speed liquid jet directed toward the rigid boundary at the end of the collapse phase. He also studied the dynamics of two equally sized bubbles in an infinite liquid domain and observed, as expected, a high speed liquid jet at the end of the collapse phase in both of the bubbles directed to each other. His numerical investigations on the dynamics of two equally sized bubbles near a rigid boundary showed that the closest bubble to the rigid boundary remained almost at its maximum volume whereas the bubble further away from the rigid boundary collapsed with a high speed liquid jet directed toward the trapped bubble. His numerical results on the dynamics of three equally sized bubbles in an infinite liquid domain showed that the bubble between other two bubbles remained approximately at its maximum volume. The other two bubbles collapsed with a high speed liquid jet directed toward the bubble trapped between them and consequently directed toward each other. He also showed that in the case of three equally sized bubbles near a rigid boundary, the bubble further away from the rigid boundary collapsed with a high speed liquid jet directed toward the two other bubbles and consequently toward the rigid boundary. However the other two bubbles remained approximately at their maximum volume.

2.6.1.6 Vapour bubble collapse between narrow parallel plates

Information on the dynamics of a vapour bubble between two parallel plates is relatively scarce. Shima and Sato (1980, 1984) investigated the behaviour of a

bubble between two parallel plates and close to one of the wall by using a variational method. Momose *et al.* (1983) studied the phenomenon in the case that the vapour bubble was attached to one of the walls. Brujan (1994) studied an initially spherical bubble between two parallel plates in a viscous incompressible fluid. He assumed the flow field to be axially symmetric and neglected the effect of heat and mass transfer as well as surface-tension forces. He also assumed the pressure inside the bubble to be uniform throughout the bubble interior. Brujan used a finite difference method and solved the problem by assuming various distances between two parallel walls and also by assuming the vapour bubble to be in different locations with respect to the walls. He summarised the results of his studies as follows:

a) The collapse time of the bubble increases with decreasing the distance between the walls and the dimensionless parameter $\mathrm{Re} = \dfrac{R_o\left(\dfrac{P_\infty}{\rho}\right)^{\frac{1}{2}}}{\upsilon}$.

b) When the bubble is located between two parallel walls the jet velocity is diminished in comparison with the case of a single bubble; and

c) The liquid jet is not formed in the case when the bubble is located equally distant from the walls.

It should be noted that, according to Brujan, the dimensionless parameter $\mathrm{Re} = \dfrac{R_o\left(\dfrac{P_\infty}{\rho}\right)^{\frac{1}{2}}}{\upsilon}$ is a measure of viscous forces, R_o is the initial radius of the bubble, P_∞ is the ambient pressure of the liquid, ρ is the liquid density while υ indicates kinematic viscosity.

2.6.2 Dynamics of a vapour bubble beneath a free surface

The dynamics of a vapour bubble near a free surface has been one of the more interesting fields in the study of bubble dynamics. Chahine and Bovis (1980) investigated the dynamics of a vapour bubble beneath a two-liquid interface experimentally (i.e. bubble located in the denser liquid). They used a high speed camera to capture the behaviour of the vapour bubble. They reduced the ambient fluid pressure to increase the life time of the bubble and thus to facilitate the usage of the high speed camera. They found that the bubble migrated away from the interface when its distance from the interface was closer than a critical distance and migrated towards the interface when it was further away. Blake and Gibson (1981) in their experimental and theoretical study on the dynamics of an electrical spark generated vapour bubble near a free surface observed a liquid jet directed away from the surface. They found that during the growth phase the upper part of the bubble close to the free surface elongated and the free surface rose up as the vapour bubble approached its maximum volume. Their experiments showed that when the vapour bubble was relatively far from the free surface the deformed free surface at the end of the growth phase of the bubble collapsed together with the collapse of the vapour bubble. They observed that an interesting phenomenon occurred in the case of a bubble located very close to the free surface. In that case during the collapse phase of the bubble with a liquid jet directed away from the free surface the deformed free surface continued its movement upward and developed a spike moving away from the bubble. The experimental and theoretical study on the dynamics a vapour bubble near a free surface by Blake and Gibson was followed by the works of a few other researchers which added more detailed information to the literature in this field.

Ceron and Blake (1984) showed that in the case of a bubble collapsing near a rigid boundary, in the absence of buoyancy forces the bubble motion and the liquid jet were directed towards the boundary. However in the case of the bubble collapsing near a free surface the bubble motion and the liquid jet developed during the bubble collapse were directed away from the free surface. Neglecting of the buoyancy forces enabled Ceron and Blake to put emphasis on the different influences of a free surface and a rigid boundary on the dynamics of a vapour bubble. Blake *et al.* (1984) in their experimental, analytical and numerical studies on the dynamics of a vapour bubble near a free surface concluded that there were two opposing mechanisms which influenced on the migration of the bubble. One is the effect of the free surface which repelled the bubble away from it. The other was the buoyancy forces which caused the migration of the bubble towards the free surface.

Taib (1985) investigated the dynamics of a vapour bubble near a free surface by considering different initial distances of the centroid of the bubble from the free surface. He showed that in contrast to the case of a bubble near a rigid boundary the lifetime of the bubble was shortened when it was collapsing nearer to a free surface. His numerical results showed that the centroid of the vapour bubble migrated towards the free surface in the early stages of the expansion phase but it moved away before the expansion phase concluded. The movement of the bubble centroid away from the free surface increased rapidly during the collapse phase.

Numerical investigations of Taib (1985) and theoretical calculations of Blake and Ceron (1982), showed that in the absence of buoyancy forces the vapour bubble was always repelled by the less dense fluid. Thus the case when the bubble was located in the denser liquid and migrated toward the two-liquid interface as it was observed by Chahine and Bovis (1980) could be due to the buoyancy forces.

2.6.3 Dynamics of a vapour bubble in shallow waters

The study of a vapour bubble in shallow waters is of great importance because of the effects of both a rigid boundary and a free surface on the dynamics of the bubble. In this case the vapour bubble lies between a free surface and a horizontal rigid boundary. This phenomenon has been investigated numerically and experimentally by a few researchers. Best (1991) and Soh (1990,1992,1994) studied bubble dynamics in shallow waters by assuming the vapour bubble as a point source and considering an infinite number of bubble images which are reflected with respect to both the free surface and the rigid boundary. Soh (1994) explained that in such a configuration the boundary condition on the free surface was linearised so that the requirement for constant pressure on the free surface could be approximated by making the horizontal velocity component zero. He emphasised that for a bubble far away from the free surface, the linearised boundary condition was a reasonable approximation. The boundary condition on the rigid boundary was zero normal velocity. The principal image set in this configuration which illustrates one set in the series of bubble images is shown in Figure 2.6.

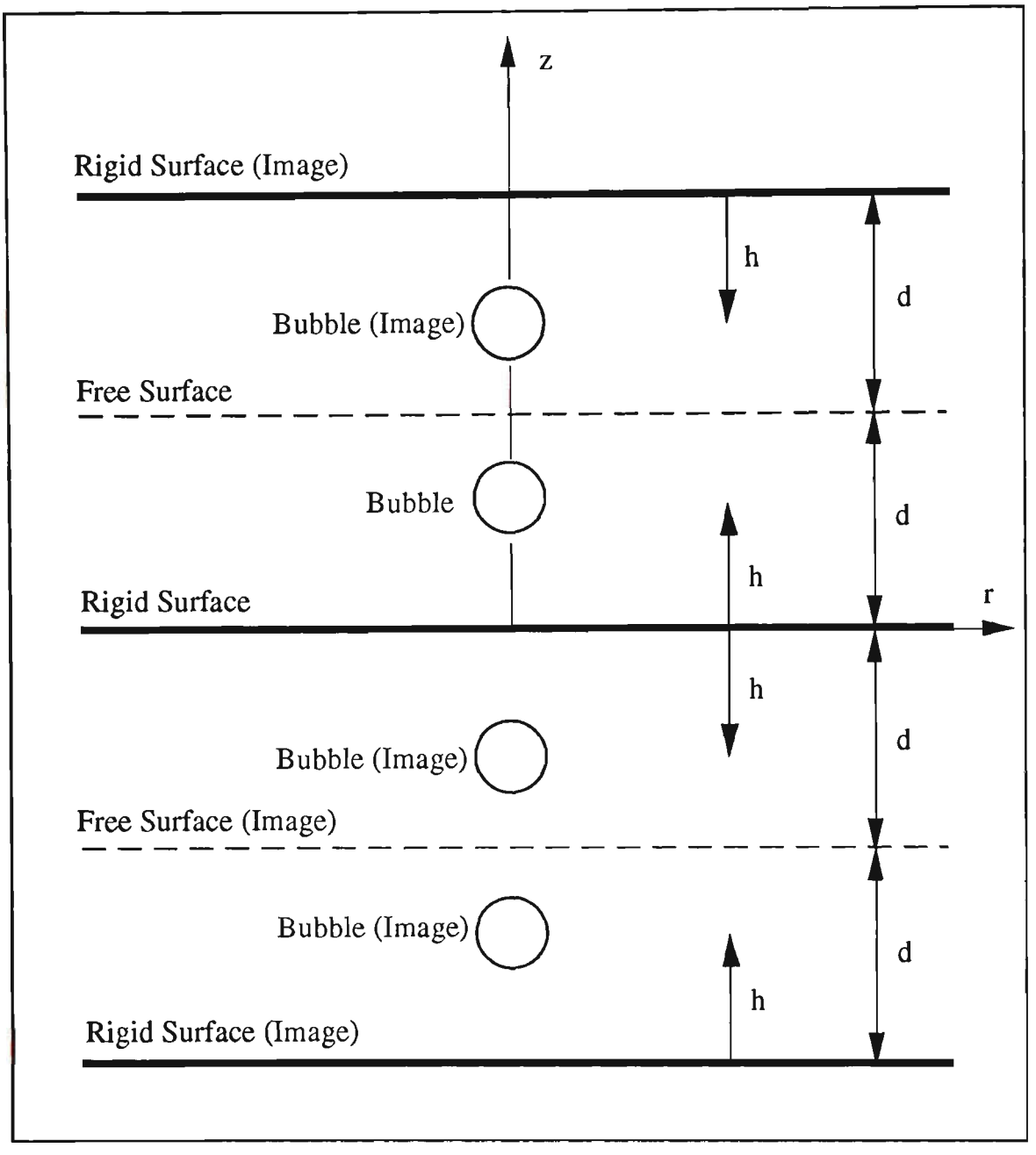

Figure 2.6 Schematic diagram showing one set in the series of the bubble images [from Soh (1994)].

According to Soh (1994) the flow in the liquid domain generated by the volume rate of change of a vapour bubble is assumed to be as a source (or sink) which has a

strength equal to this rate of volume change. Thus the assumption of a series of bubbles as illustrated in Figure 2.6 provides a series of positive and negative images of point sources (or sinks). The kinetic energy of the flow is given by an integration from the radius of the bubble to infinity:

$$KE = \frac{\rho}{2}\iint_s \Phi \frac{\partial \Phi}{\partial r}\, ds, \tag{2.9}$$

Soh found that by assuming the surface of the bubble remained spherical the result of the integration was:

$$KE = \frac{\rho}{2}\,\frac{\left(\dot{V}\right)^2}{4\pi}\left[\frac{1}{R(t)} + \frac{\pi}{2d}\cot\left(\frac{\pi h}{d}\right)\right]. \tag{2.10}$$

It should be noted that in Equation (2.10) $R(t)$ is the radius of the spherical bubble and h and d are the distance of the bubble centroid from the rigid surface and the depth of the water respectively.

Experimental observations of Soh and Yu (1992) and Yu and Soh (1992), showed that the shape of an electrical spark generated bubble remains nearly spherical in its first pulsation if it was far from the free surface and is located at a distance greater than $2R_m$ from the rigid boundary, where R_m is the maximum radius of the bubble.

It is obvious that in the situations that the vapour bubble is close to either the free surface or the rigid boundary the deformation of the bubble from its initially spherical shape is significant because of the strong Bjerknes forces through the free surface or the rigid boundary. Obviously in the case of a vapour bubble (in extremely shallow water) where the vapour bubble grows and collapses inside a relatively thin layer of liquid over a flat horizontal rigid surface the approximation of spherical shape of the bubble during its growth and collapse is not valid longer

and the point source theory cannot be applied. Thus a robust numerical technique is needed to solve the problem in the very complex cases that the vapour bubble or both the vapour bubble and the free surface are highly deformed.

2.6.4 Dynamics of a vapour bubble near compliant surfaces

Gibson (1968) experimentally studied the behaviour of a bubble adjacent to a flexible boundary. He observed that a small local displacement of the flexible boundary, typically 0.1 R_m peak to peak, could completely change the form of the collapse of an adjacent bubble. Gibson generated a cavity at a distance of 0.6 in. from the compliant boundary, under a pressure difference of 3.5 mm Hg. The maximum average radius of the cavity was 0.85 in.. It is obvious that a cavity generated at this distance from a rigid boundary would attach to the boundary during the expansion phase, and the subsequent collapse would conclude with the development of a liquid jet on the side of the bubble far from the boundary and its impingement upon the rigid boundary. Gibson explained that:

> *The cavity under discussion behaved in a similar manner to its counterpart adjacent to a rigid boundary during the first half of its expansion. However, it was then observed to lift off the boundary and its lower surface became involute, so that the jet was seen to thread the cavity away from the boundary. The cavity then commenced to collapse, and a wave was seen to pass up its interface. This wave caused a cylindrical extrusion of the cavity along its "axis of symmetry" in the concluding stage of the collapse.*

Gibson and Blake (1988, 1982) conducted a series of experiments to study the behaviour of a vapour bubble in the vicinity of deformable surfaces. Their aim was to estimate the type of compliant coating that could repel a collapsing bubble in its neighbourhood. Figure 2.7 illustrates the results of their extensive study of bubble dynamics near a compliant surface.

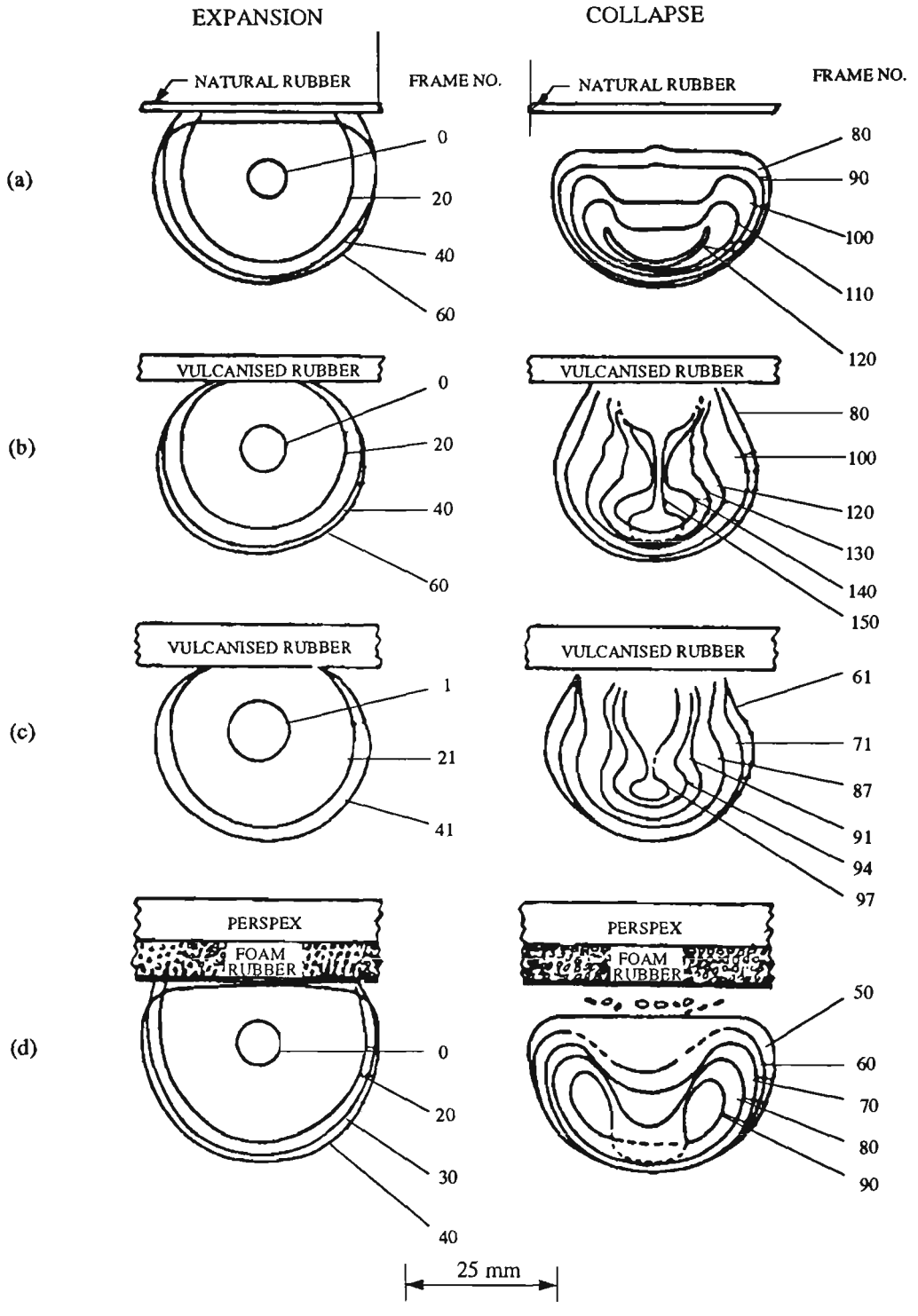

Figure 2.7 A range of responses for bubbles near different compliant boundaries. All bubbles were generated at frame zero. Camera speeds (frames / ms) were; (a) 11.7, (b) 13.5, (c) 12.9, and (d) 12.3 [from Gibson and Blake (1982)].

Figure 2.7 shows that the behaviour of a bubble near a compliant surface can be significantly affected by a wide range of deformable surfaces over a wide range of experimental conditions.

Gibson and Blake (1987) in their review on the topic of "cavitation bubbles and boundaries" expressed that:

> *The challenge now is to develop a robust numerical model that can cope with the mixed boundary conditions provided by a surface coating with inertia, damping, and stiffness.*

Later they concluded that:

> *Numerical models based on the motion of an incompressible inviscid liquid are accurate when programmed to account for the correct nonlinear velocity and pressure boundary conditions imposed by adjacent surfaces. The effects of mean flow and imposed pressure gradients cannot be ignored when modelling cavitation. It is therefore important that future studies seek to introduce flow effects in a more realistic fashion, and that a systematic investigation may be undertaken of the growth and collapse of bubbles in the vicinity of deformable surface coatings. This last work should be a computer study because the parameter space that needs to be covered is too great for an experimental search, at least in the initial stages.*

Duncan and Zhang (1991) investigated the behaviour of an initially spherical bubble near a compliant surface numerically. They assumed the fluid as a potential flow and used a boundary integral method to solve Laplace's equation for the velocity

potential. They modelled the compliant wall as a circular membrane with a spring foundation which was located in a rigid surface. Duncan and Zhang assumed that at the interface between the fluid and the membrane, the pressure and vertical velocity in the liquid were matched with the pressure and vertical velocity of the membrane. They considered the initial cavity size, the initial distance of the cavity centroid from the compliant surface, the fluid density and the pressure driving the collapse as parameters which described the flow. They also considered the mass per unit area, membrane tension, spring constant and coating radius as parameters which described the compliant wall. Their calculations showed that when the wall was rigid the bubble collapse was characterised by a liquid jet directed towards the wall. They found that by changing the properties of the compliant wall, the behaviour of the vapour bubble was greatly affected. Their numerical results illustrated that by choosing a proper compliant surface, the vapour bubble could be made to collapse spherically, as if the bubble were in an infinite liquid domain or with the liquid jet away from the compliant wall, as if the bubble were adjacent to a free surface.

CHAPTER THREE

BOUNDARY INTEGRAL METHOD

3.1 INTRODUCTION

Analytical studies of non-spherical bubbles are very complicated and in most situations impossible. Experimental investigations, although laying significant role in the understanding of bubble dynamics, are not suitable for exploring many features of the phenomenon. A major reason for this is that the duration of the bubble collapse in its later stages is so short that makes experimental investigations very difficult. Thus only numerical methods are suitable for theoretical studies on the dynamics of non-spherical bubbles. Since the early work of Plesset and Chapman (1971), who successfully used a finite difference method to simulate the collapse of an initially spherical bubble, a number of different approaches have been put forward for the numerical study of bubble dynamics. For a quick review one can refer to the methods of Variational Formulation by Shima and Nakajima (1977), Modified Marker-and Cell Technique by Mitchell and Hammitt (1973), Perturbation by Chahine and Bovis (1983), Finite Element Method by Nakajima and Shima (1977)and also Kumar and Booker (1991a, 1991b), Approximate Integral Equation by Blake and Gibson (1981), Method of Images by Kucera and Blake (1990) and Boundary Integral Method was by Blake, Taib and Doherty (1986a, 1986b). Among these numerical techniques the Boundary Integral

Method, which was first successfully applied in the study of bubble dynamics by Blake, Taib and Doherty (1986, 1987), has been proven to be the most accurate and reliable method. Following the early work of Blake , Taib and Doherty (1986) the Boundary Integral Method employed by other researchers in the study of bubble dynamics. In this respect one can refer to the works of Kucera and Blake (1988), Best *et al.* (1989), Duncan and Zhang (1991), Best and Kucera (1992), Soh and Shervani-Tabar (1992a, 1992b), Blake *et al.* (1993), Best (1993), Zhang *et al.* (1993), Soh and Shervani-Tabar (1994), Zhang and Duncan (1994) and Sato *et al.* (1994).

In the current work a highly accurate Boundary Integral Method is developed to study the dynamics of an axisymmetric vapour bubble in an infinite liquid domain and near various boundaries.

3.2 EXTERIOR PROBLEM

Consider a bubble which is located in an infinite liquid domain. As it is illustrated in Figure 3.1, the inner surface of the liquid domain is its interface with the vapour bubble and the outer surface is a sphere with an infinite radius. In this case the liquid domain and its interface with the vapour bubble are called an open domain and internal surface respectively [Brebbia and Dominguez (1989)]. This case is known as an exterior problem.

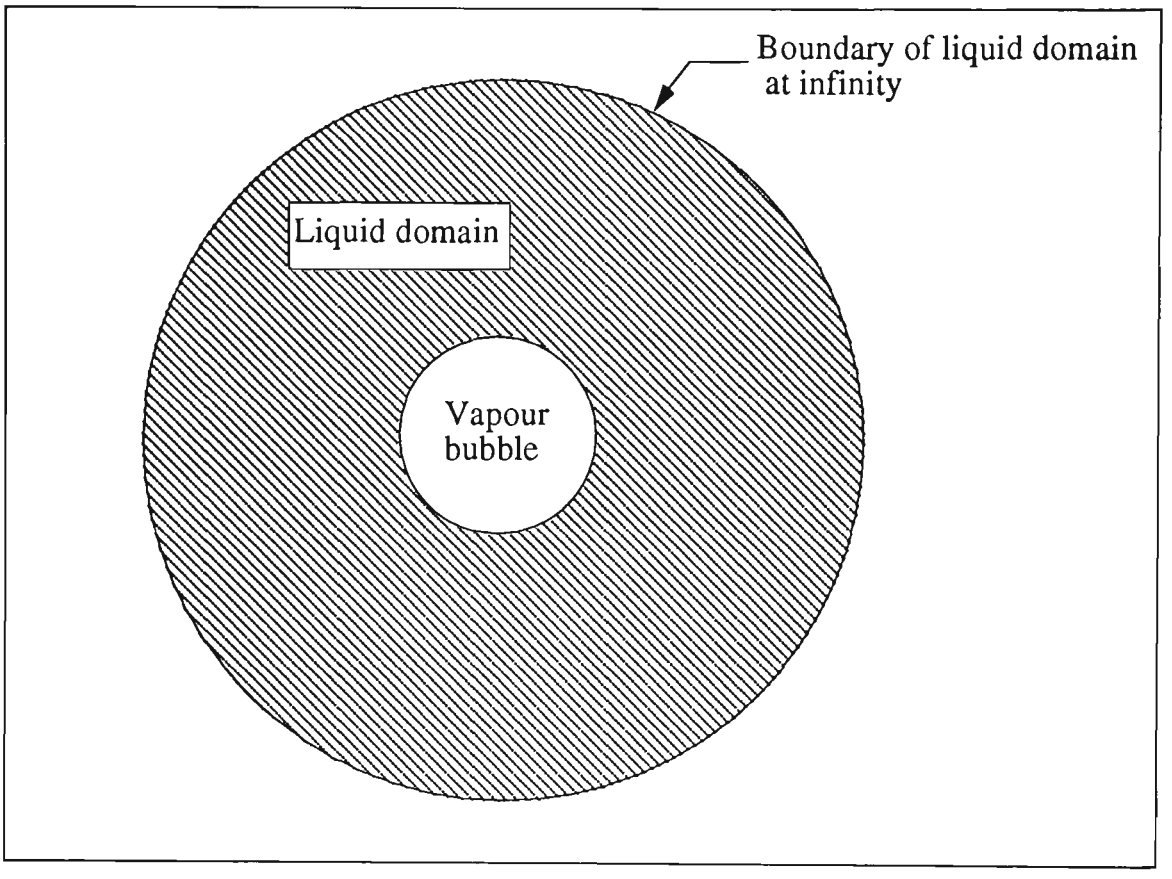

Figure 3.1 Schematic representation of the liquid domain extended to infinity as an OPEN DOMAIN and its interface with a vapour bubble as an internal surface. This case is known as an EXTERIOR PROBLEM.

3.3 BOUNDARY ELEMENT FORMULATION FOR POTENTIAL PROBLEMS

Brebbia in 1978 formulated potential problems, which are governed by Laplace's equation, for the boundary element method in the form of the integral equation:

$$c_i U_i + \int_\Gamma Q^* U d\Gamma = \int_\Gamma U^* Q d\Gamma, \qquad (3.1)$$

where U represents potential, Γ is the boundary of the domain under consideration and $Q = \dfrac{\partial U}{\partial n}$ indicates the normal derivative of the potential over Γ. Also in Equation (3.1) c_i is a function of the solid angle of the boundary at a point i, U^* is the fundamental solution and $Q^* = \dfrac{\partial U^*}{\partial n}$ is its normal derivative. The fundamental solution of the three dimensional Laplace's equation which represents a concentrated unit potential at a point i is given by Kellog (1929) as:

$$U^* = \frac{1}{4\pi R}, \tag{3.2}$$

where $R = \left[(x - x_i)^2 + (y - y_i)^2 + (z - z_i)^2\right]^{\frac{1}{2}}$ indicates the distance between the application point (x_i, y_i, z_i) of the unit potential and the point under consideration (x, y, z).

3.4 AXISYMMETRIC POTENTIAL PROBLEMS

By representing the potential by ϕ and the application point of the unit potential as p and any point under consideration on the surface of the domain as q, Equation (3.1) becomes:

$$c(p)\phi(p) + \int_S \phi(q) \frac{\partial}{\partial n}\left(\frac{1}{|p-q|}\right) dS = \int_S \frac{\partial}{\partial n}(\phi(q)) \frac{1}{|p-q|}\, dS, \tag{3.3}$$

where S is the surface of the domain Ω and

$$\begin{cases} c(p) = 2\pi & \text{when} \quad p \in S, \\ c(p) = 4\pi & \text{when} \quad p \in \Omega. \end{cases}$$

Equation (3.3) is known as Green's integral formula and the term $\frac{1}{|p-q|}$ is called the Green's function.

The Green's function in three dimensional cylindrical coordinates (r,θ,z) can be written in the form:

$$\frac{1}{|p-q|}=\frac{1}{\left[r^2+r_i^2-2rr_i\cos(\theta-\theta_i)+(z-z_i)\right]^{\frac{1}{2}}}. \tag{3.4}$$

In the case of axisymmetric problems, all quantities are independent of the angle of revolution θ, thus in Equation (3.3) one integration can be performed in advance. As described by Wrobel and Brebbia (1981) and Gipson (1987), this is equivalent to using ring potentials as a fundamental solution.

If θ is substituted for $\theta-\theta_i$, then Equation (3.4) can be written as:

$$\frac{1}{|p-q|}=\frac{1}{\left[(r+r_i)^2+(z-z_i)^2-4rr_i\cos\left(\frac{\theta}{2}\right)\right]^{\frac{1}{2}}}. \tag{3.5}$$

By parametrising the surface S by the variable ξ, the integral on the right hand side of Equation (3.3) becomes

$$\int_S\frac{\partial}{\partial n}(\phi(q))\frac{1}{|p-q|}dS=\int_0^1\frac{\partial}{\partial n}(\phi(q))r(\xi)\left[\left(\frac{\partial z}{\partial\xi}\right)^2+\left(\frac{\partial r}{\partial\xi}\right)^2\right]^{\frac{1}{2}}d\xi$$
$$\int_0^{2\pi}\frac{d\theta}{\left[(r(\xi)+r_i)^2+(z(\xi)-z_i)^2-4r(\xi)r_i\cos\left(\frac{\theta}{2}\right)\right]^{\frac{1}{2}}}. \tag{3.6}$$

In the axisymmetrical case the integration over the angle of revolution can be calculated explicitly in terms of the complete elliptic integral of the first kind $K(k)$. Thus Equation (3.6) becomes [Wrobel and Brebbia (1981) and Taib (1985)]:

$$\int_S \frac{\partial}{\partial n}(\phi(q))\frac{1}{|p-q|}dS = \int_0^1 \frac{\frac{\partial}{\partial n}(\phi(q))r(\xi)\left[\left(\frac{\partial z}{\partial \xi}\right)^2+\left(\frac{\partial r}{\partial \xi}\right)^2\right]^{\frac{1}{2}}K(k)}{\left[\left(r(\xi)+r_i\right)^2+\left(z(\xi)-z_i\right)^2\right]^{\frac{1}{2}}}d\xi, \quad (3.7)$$

where

$$k = k(\xi) \text{ and } k^2(\xi) = \frac{4r(\xi)r_i}{\left(r(\xi)+r_i\right)^2+\left(z(\xi)-z_i\right)^2}. \quad (3.8)$$

The unit normal, $\tilde{n}$, and $\nabla\frac{1}{|p-q|}$ can be written as:

$$\tilde{n} = \frac{1}{\left[\left(\frac{\partial z}{\partial \xi}\right)^2+\left(\frac{\partial r}{\partial \xi}\right)^2\right]^{\frac{1}{2}}}\left(\frac{\partial z}{\partial \xi}\cos(q),\ \frac{\partial z}{\partial \xi}\sin(\theta),\ -\frac{\partial r}{\partial \theta}\right), \quad (3.9)$$

$$\nabla\frac{1}{|p-q|} = \frac{-\left(r(\xi)\cos(\theta)-r_i,\ r(\xi)\sin(\theta),\ z(\xi)-z_i\right)}{\left[\left(r+r_i\right)^2+\left(z-z_i\right)^2-4rr_i\cos\left(\frac{\theta}{2}\right)\right]^{\frac{1}{2}}}. \quad (3.10)$$

Thus the integral on the left hand side of Equation (3.3) becomes:

$$\int_S(\phi(q))\frac{\partial}{\partial n}\left(\frac{1}{|p-q|}\right)dS = \int_0^1 \frac{(\phi(q))r(\xi)}{\left[\left(r(\xi)+r_i\right)^2+\left(z(\xi)-z_i\right)^2\right]^{\frac{1}{2}}}$$

$$\left\{\left[\frac{\partial z}{\partial \xi}\left(r(\xi)+r_i\right)-\frac{\partial r}{\partial \xi}\left(z(\xi)+z_i\right)-\frac{2}{k^2(\xi)}\frac{\partial z}{\partial \xi}r_i\right]\frac{E(k)}{1-k^2(\xi)}+\frac{2}{k^2(\xi)}\frac{\partial z}{\partial \xi}r_iK(k)\right\}d\xi, \quad (3.11)$$

where $E(k)$ is a complete elliptic integral of the second kind. Details of this integration can be found in the work of Taib (1985).

An approximation for the complete elliptic integral of the first and second kind are given by Hastings (1955) as:

$$K(k) = P(x) + Q(x)\ln\left(\frac{1}{x}\right), \tag{3.12}$$

$$E(k) = R(x) + S(x)\ln\left(\frac{1}{x}\right), \tag{3.13}$$

where

$$x = 1 - k^2, \tag{3.14}$$

with

$0 \leq k < 1,$

and $P(x)$, $Q(x)$, $R(x)$ and $S(x)$ are tabulated polynomials.

3.5 APPROXIMATION OF SURFACE GEOMETRY AND PHYSICAL FUNCTIONS

In the boundary integral method the geometry of the boundary and the potential and its normal derivative, which are called physical functions, are represented by approximate models. It should be noted that these approximations can be independent to some extent. The three dimensional axisymmetric surface is represented by its two dimensional interface with a plane section taken through the axis of symmetry. It is obvious that by rotation of this two dimensional interface

about the axis of symmetry the three dimensional axisymmetric surface is recovered. In the following sections the approximate model of "Linear Surface Geometry-Constant Physical Functions" is explained. Then a highly accurate approximate model of "Cubic Spline Surface Geometry-Constant Physical Functions", which is developed throughout this research, is introduced and discussed.

3.5.1 Linear Surface Geometry-Constant Physical Functions

In this model the boundary is approximated by a set of M linear segments and the potential and its normal derivative are assumed to be constant on each segment. The collocation points are located at the midpoint of each linear segment, and the collocation form of the boundary integral equation, Equation (3.3), is written as:

$$2\pi\,\phi(p_i)+\sum_{j=1}^{M}\phi(q_j)\int_{S_j}\frac{\partial}{\partial n}\left(\frac{1}{|p_i-q_j|}\right)dS=\sum_{j=1}^{M}\frac{\partial}{\partial n}\left(\phi(q_j)\right)\int_{S_j}\frac{1}{|p_i-q_j|}\,dS, \tag{3.15}$$

for $i=1,2,\ldots,M$.

By denoting $\frac{\partial\phi}{\partial n}$ as ψ, Equation (3.15) can be written in matrix form as:

$$2\pi\,\phi_i+\sum_{j=1}^{M}\hat{H}_{ij}\phi_j=\sum_{j=1}^{M}G_{ij}\psi_j\,. \tag{3.16}$$

where $\hat{H}_{ij}$ and G_{ij} are the integration terms in Equation (3.15) and are integrated over a straight segment.

By defining $H_{ij}=\hat{H}_{ij}+2\pi\delta_{ij}$, Equation (3.16) may be written as:

$$\sum_{j=1}^{M} H_{ij}\phi_j = \sum_{j=1}^{M} G_{ij}\psi_j . \qquad (3.17)$$

Figure 3.2 illustrates the linear representation of a bubble boundary with constant physical functions on each linear segment which are located at the midpoints. The variables z_j and r_j represent the cylindrical axisymmetric coordinates of the bubble boundary, while the z axis is the axis of symmetry. It is obvious that in this model r and z vary linearly along each element.

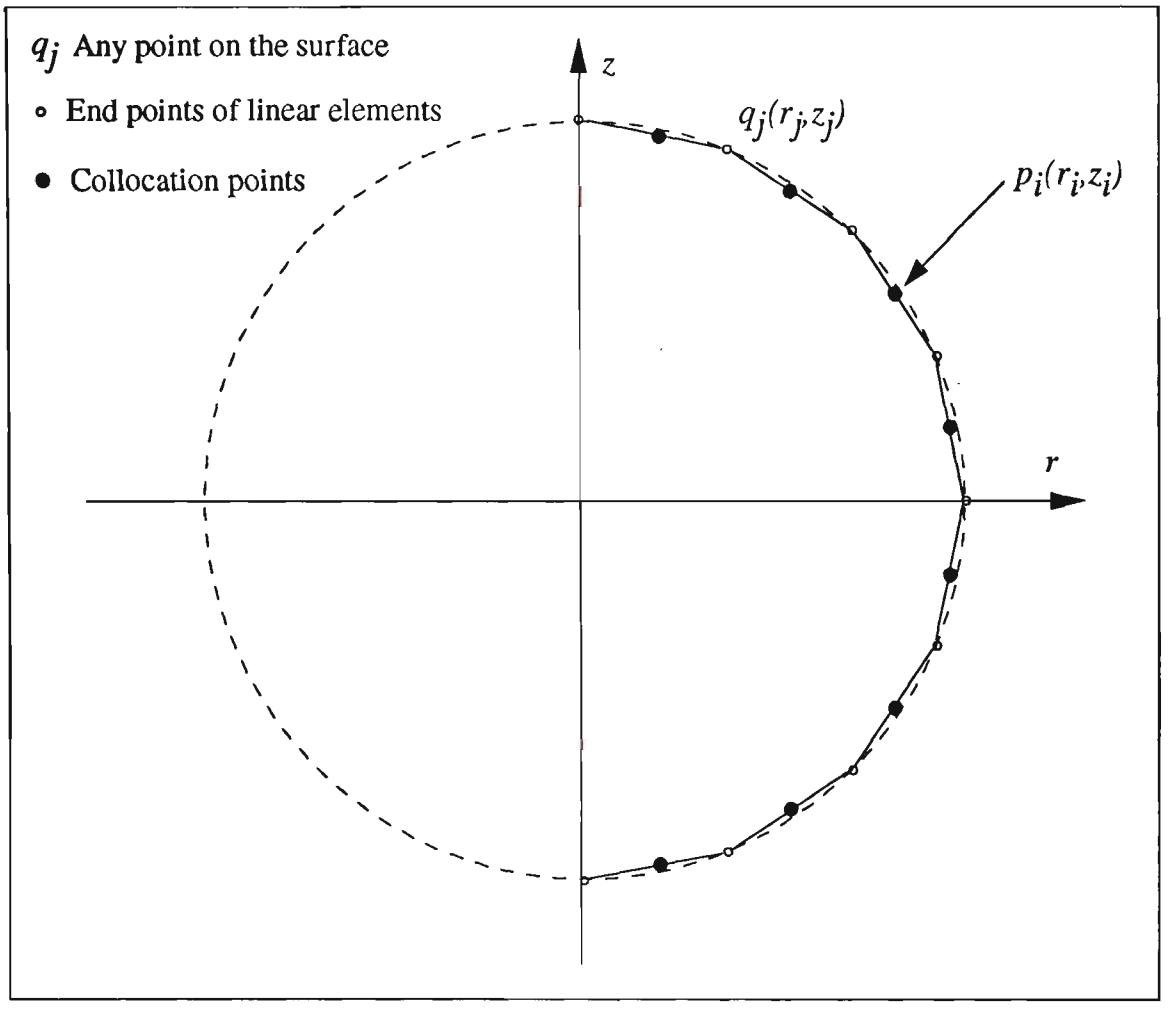

Figure 3.2 Linear representation of a bubble boundary with collocation points at the mid of linear segments. The dashed line (_ _ _) represents the actual surface of the bubble and the solid line (_____) represents its approximation by linear elements. $p_i(r_i,z_i)$ represent collocation points whereas $q_j(r_j,z_j)$ indicates any point on the surface of the bubble.

3.5.1.1 Evaluation of tangential velocity

From a given distribution of the velocity potential, ϕ, the tangential velocity, $\eta_j = \left[\frac{\partial \phi}{\partial S}\right]_j$, is approximated by the formula

$$\eta_j = \left[\frac{\partial \phi}{\partial S}\right]_j = \frac{(\phi_j - \phi_{j-1})(d_j + d_{j+1})^2 + (\phi_{j+1} - \phi_j)(d_{j-1} + d_j)^2}{\frac{1}{2}(d_{j-1} - d_j)(d_j + d_{j+1})(d_{j-1} + 2d_j + d_{j+1})}, \quad (3.18)$$

where d_j is the length of the segment S_j.

3.5.2 Cubic Spline Surface Geometry-Constant Physical Functions

It is obvious that in the case of linear elements representing the geometry of the bubble boundary, the functions of r and z are not differentiable at the end points of elements and this fact affects the accuracy of the solution. For the purpose of increasing the accuracy of the solution, cubic splines are used to construct a more smooth and continuous boundary. Figure 3.3 illustrates the cubic spline representation of a bubble boundary with constant physical functions located at the midpoints of each segment.

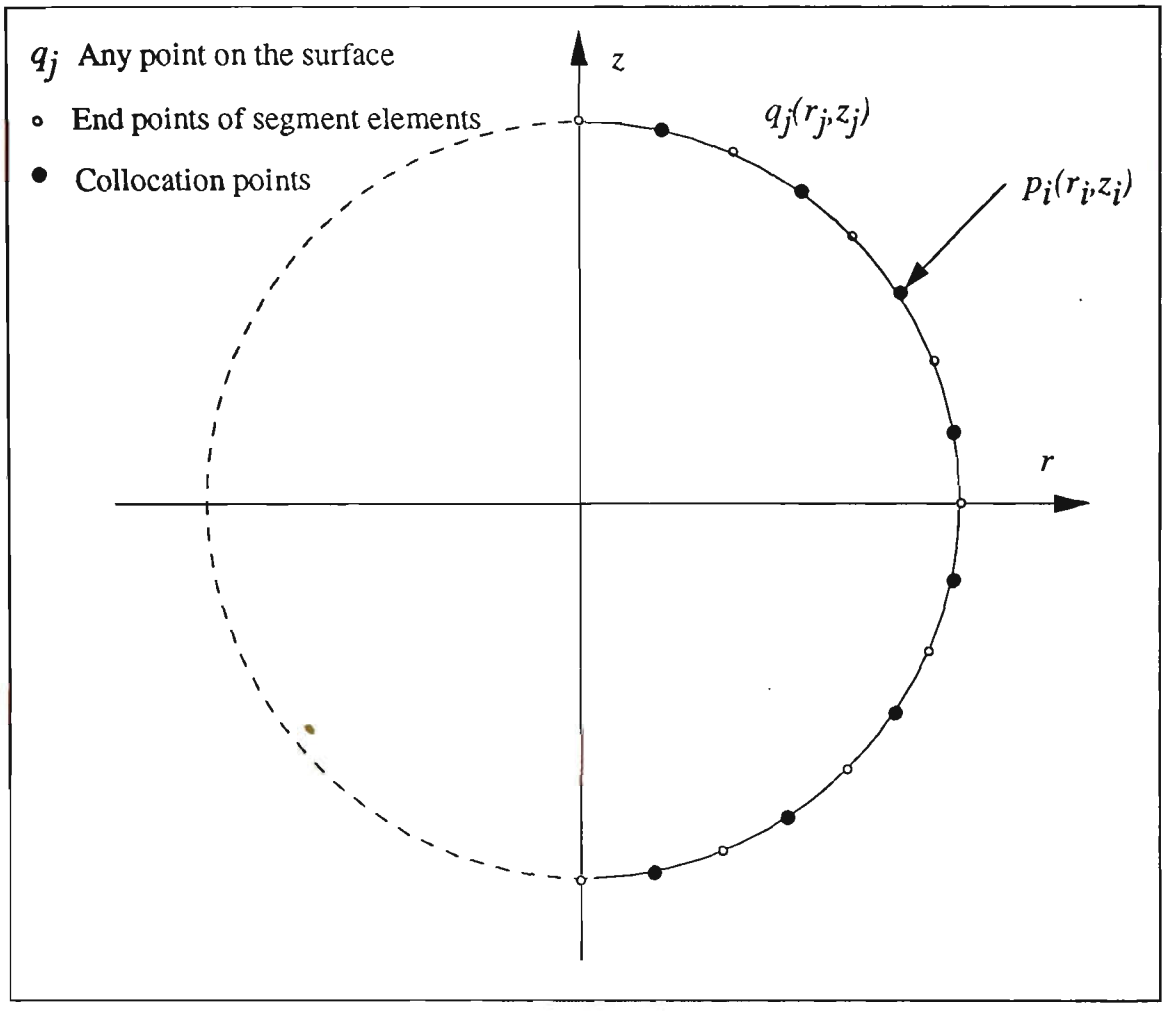

Figure 3.3 Cubic spline representation of a bubble boundary with collocation points at the midpoints of each segment. the dashed line (- - -) represents the actual surface of the bubble and the solid line (——) represents its approximation with a cubic spline. $p_i(r_i,z_i)$ represent collocation points whereas $q_j(r_j,z_j)$ indicates any point on the surface of the bubble.

Equations (3.19) and (3.20) represent the cubic spline functions of r and z with respect to the arc length of the bubble boundary, l, which is used as the parameter for the cubic splines.

$$r(l) = a_j^r + b_j^r\left(l - l_j\right) + c_j^r\left(l - l_j\right)^2 + d_j^r\left(l - l_j\right)^3, \tag{3.19}$$

$$z(l) = a_j^z + b_j^z\left(l - l_j\right) + c_j^z\left(l - l_j\right)^2 + d_j^z\left(l - l_j\right)^3, \tag{3.20}$$

with

$l_j < l < l_{j+1}$

for

$j = 1,2,...,M$

where M is the number of segments and l_j's are the progressive arc lengths as illustrated in Figure 3.4. The clamped end conditions are:

$$\frac{dr}{dl} = +1 \text{ and } \frac{dz}{dl} = 0, \text{ at } l_j = l_1, \tag{3.21}$$

and

$$\frac{dr}{dl} = -1 \text{ and } \frac{dz}{dl} = 0, \text{ at } l_j = l_{M+1}. \tag{3.22}$$

The constant parameters a_j^r, b_j^r, c_j^r and d_j^r, $j = 1,2,...,M$ are the standard coefficients of the cubic spline functions of r with respect to the arc length of the bubble boundary, l, which are obtained in terms of $r_j; j = 1,2,...,M+1$ and $l_j; j = 1,2,...,M$.

In a similar manner a_j^z, b_j^z, c_j^z, and d_j^z, $j = 1,2,...,M$ are the standard coefficients of cubic spline functions of z with respect to the arc length of the bubble boundary which are obtained in terms of $z_j; j = 1,2,...,M+1$ and $l_j; j = 1,2,...,M$.

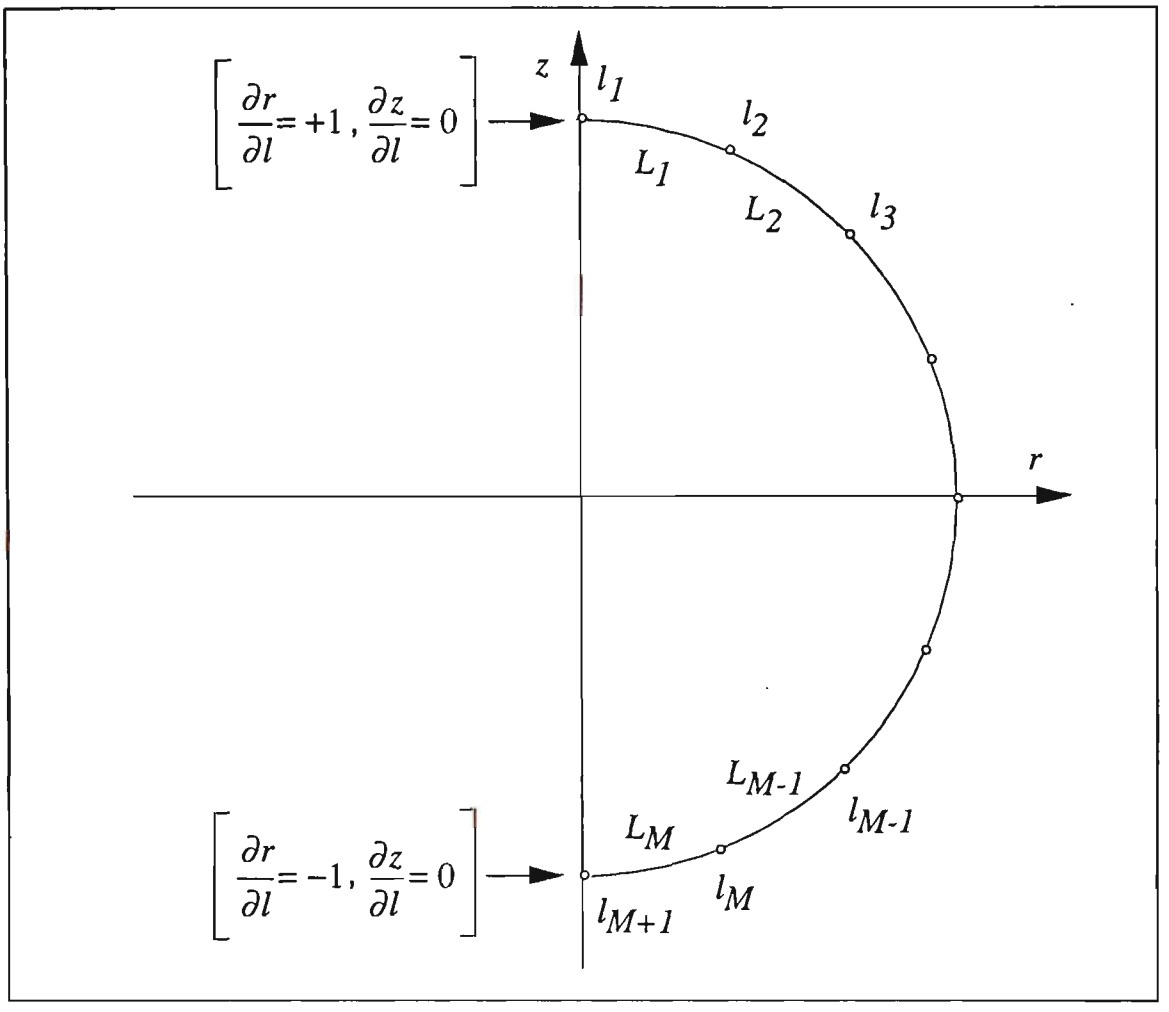

Figure 3.4 The discretization and node labelling used on the bubble surface. l_j's , $j=1,2,...,M+1$, are the progressive arc lengths while $L_j = l_{j+1} - l_j$, $j=1,2,...,M$, indicate the length of each segment.

The length of each segment is denoted by L_j and is given as

$$L_j = l_{j+1} - l_j. \tag{3.23}$$

For more details on the calculations of the standard spline coefficients one can refer to Burden and Faires (1993).

The arc length along the spline is not known, *a priori*. In order to parametrize the splines good approximations to the length of individual segments are required. To overcome this problem Kucera has introduced an iteration scheme starting off with the Euclidean distance between the nodes as the zeroth order approximation to the individual segment lengths

$$L_j^{(0)} = \left(\left(r_{j+1} - r_j \right)^2 + \left(z_{j+1} - z_j \right)^2 \right)^{\frac{1}{2}}, \tag{3.24}$$

where $L_j^{(0)}$ indicates the zeroth order approximation to the length of *jth* segment. The higher order approximations are calculated by the following integration along the length of the segments

$$L_j^{(k+1)} = \int_{l_j}^{l_{j+1}} \left[\left(\frac{\partial r^{(k)}}{\partial l} \right)^2 + \left(\frac{\partial z^{(k)}}{\partial l} \right)^2 \right]^{\frac{1}{2}}, \tag{3.25}$$

$k = 0,1,2,\ldots$

where $r^{(k)}$ and $z^{(k)}$ indicate the approximate spline functions of r and z of order k. Integration of Equation (3.25) is performed numerically using the appropriate order of Gaussian quadrature. Kucera found that a highly accurate representation of the cubic spline arc length is achieved after two or three iterations of Equation (3.25) [Best (1991) and Best and Kucera (1992)].

In this model the discretised form of Equation (3.3) with collocation points in the middle of each segment yields the following set of linear equations:

$$2\pi\phi_i + \sum_{j=1}^{M} A_{ij}\phi_j = \sum_{j=1}^{M} B_{ij}\psi_j, \tag{3.26}$$

where A_{ij} and B_{ij} are obtained from Equations (3.11) and (3.7) respectively and where

$$A_{ij} = \int_{l_j}^{l_{j+1}} \frac{r(\xi)}{\left[\left(r(\xi)+r_i\right)^2+\left(z(\xi)-z_i\right)^2\right]^{\frac{1}{2}}} \left\{\left[\frac{\partial z}{\partial \xi}\left(r(\xi)+r_i\right)-\frac{\partial r}{\partial \xi}\left(z(\xi)+z_i\right)-\frac{2}{k^2(\xi)}\frac{\partial z}{\partial \xi}r_i\right]\frac{E(k)}{1-k^2(\xi)}+\frac{2}{k^2(\xi)}\frac{\partial z}{\partial \xi}r_i K(k)\right\} d\xi, \tag{3.27}$$

$$B_{ij} = \int_{l_j}^{l_{j+1}} \frac{r(\xi)\left[\left(\frac{\partial z}{\partial \xi}\right)^2+\left(\frac{\partial r}{\partial \xi}\right)^2\right]^{\frac{1}{2}} K(k)}{\left[\left(r(\xi)+r_i\right)^2+\left(z(\xi)-z_i\right)^2\right]^{\frac{1}{2}}} d\xi. \tag{3.28}$$

3.5.2.1 Evaluation of tangential velocity

The velocity potentials are known at the midpoint of each segment. The progressive arc length of the surface at the midpoints of segments are obtained by Equations (3.19) and (3.20) and the iteration of Equation (3.25). Thus a cubic spline representation of velocity potential over the bubble surface with respect to the arc length can be constructed. The cubic spline functions of velocity potential are of great importance in calculating an accurate tangential velocity on the bubble surface. It is also useful in rediscretising the deformed surface of the bubble into equally sized segments elements during its non-spherical collapse.

The velocity potentials are at the midpoint of segment elements and are calculated at every time step by the Lagrangian form of the unsteady Bernoulli equation, as is discussed later in *Section (3.5.2.2)*. Thus the velocity potential at the first and end points of the axisymmetric half of the bubble boundary, both located on the axis of symmetry, are not known, *a priori*. The combination of an accurate approximation to the velocity potential at the first and end points of the axisymmetric half of the bubble boundary and the clamped end conditions results in construction of a highly accurate cubic spline function of velocity potential with respect to the arc length of the bubble boundary.

To calculate an accurate approximation of the velocity potential at the first and end points of the axisymmetric half of the bubble boundary the following procedure is employed. Since the number of the segments on the half of the bubble is equal to M, then L_1 and L_{2M} indicate the arc length of the first and last segments of the whole of the bubble boundary. Obviously these two segments are symmetric about the z axis. Consider the larger part of the whole of the bubble boundary with end points midway along L_1 and L_{2M}. A cubic spline representation of the velocity

potentials are constructed by parametrising with respect to the arc lengths between every two subsequent mid points of the segments. The conditions at the end points are found by determining the second derivatives of the functions by extrapolation. This extrapolation is performed by using the second derivatives of the functions on the mid points of the other two segments next to each of the end points. This assumption , as with every other arbitrary assumption, affects the shape of the polynomial near the end points but its effects diminish rapidly towards the middle of the data [DeBoor (1979)]. Then the velocity potential at the mid of the large part of the bubble which is located on the axis of the symmetry can be obtained very accurately. The velocity potential at the other end of the axisymmetric half of the bubble boundary located on the axis of symmetry is found in a similar manner.

Natural conditions or free end conditions which result from the second derivative of the spline functions at the end points being equal to zero, in spite of the positive sounding name, is of little use to theoretical point of view. Setting the second derivative of the spline functions at the end points equal to zero arbitrarily produces $o\left(|l|^2\right)$-error, unless the actual second derivative of the cubic spline functions at the end points are equal to zero, and so dramatically reduces the overall rate of convergence of the interpolation method [DeBoor (1979)].

Now the velocity potentials on the axis of symmetry and at the mid points of each segment are known and the accurate arc length of each cubic spline segment are also known by the iteration of Equation (3.25). Thus, a cubic spline representation of the velocity potentials over the surface of the bubble with respect to the arc length of the bubble boundary can be constructed.

As is illustrated in Figure 3.5, l'_j indicates the progressive arc length of the bubble boundary between the points on the axis of symmetry and the midpoints of the

segments. Thus the cubic spline representation of the velocity potential over the bubble boundary becomes:

$$\phi(l) = a_j^{\phi} + b_j^{\phi}\left(l - l_j'\right) + c_j^{\phi}\left(l - l_j'\right)^2 + d_j^{\phi}\left(l - l_j'\right)^3, \tag{3.29}$$

with

$l_j' < l < l_{j+1}'$

for

$j = 1,2,\ldots,M+2$

The clamped end conditions are:

$$\frac{d\phi}{dl} = 0, \text{ on } l_j' = l_1' \text{ and } l_j' = l_{M+2}'. \tag{3.30}$$

Conditions given by Equation (3.30) are obtained by consideration of simple continuity theory.

The constant parameters a_j^{ϕ}, b_j^{ϕ}, c_j^{ϕ} and d_j^{ϕ}, $j = 1,2,\ldots,M$ are the standard spline coefficients which are obtained in terms of velocity potentials on the knots and progressive arc lengths l_j', $j = 1,2,3,\ldots,M+2$.

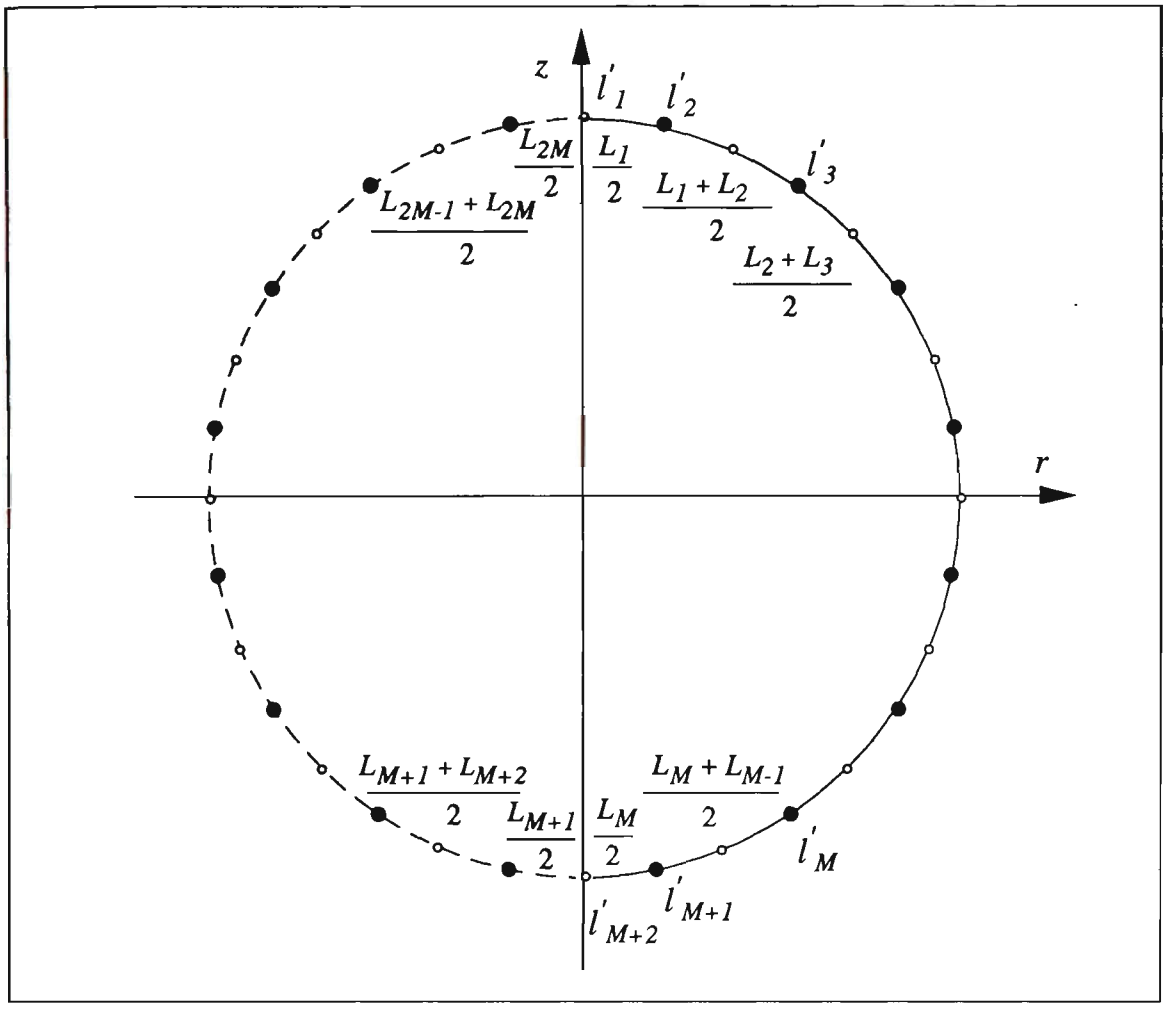

Figure 3.5 Progressive arc lengths of l'_j, $j = 1,2,3,\ldots,M+2$, which are used as parameters for constructing a cubic spline representation of Velocity potential, ϕ, over the bubble surface.

The cubic spline functions of the velocity potentials with respect to the arc length as constructed above give the highly accurate values of the tangential velocity, $\eta(l)$, at every point of the bubble boundary, where:

$$\eta(l'_j) = \frac{\partial \phi(l'_j)}{\partial l} = b_j^{\phi} + 2c_j^{\phi}(l - l'_j) + 3d_j^{\phi}(l - l'_j)^2 . \qquad (3.31)$$

3.5.2.2 Evolution of the bubble

By solving the linear set of Equation (3.17) normal velocities on the collocation points at the midpoint of the segments are obtained. Thus a cubic spline representation of the normal velocities over the bubble surface can be constructed in the same manner as discussed in section (3.5.2.1):

$$\psi(l'_j) = a_j^{\psi} + b_j^{\psi}(l - l'_j) + c_j^{\psi}(l - l'_j)^2 + d_j^{\psi}(l - l'_j)^3, \tag{3.32}$$

with

$l'_j < l < l'_{j+1}$

for

$j = 1,2,...,M+2$

The clamped end conditions are:

$$\frac{d\psi}{dl} = 0, \text{ on } l'_j = l'_1 \text{ and } l'_j = l'_{2M}. \tag{3.32}$$

The constant parameters a_j^{ψ}, a_j^{ψ}, c_j^{ψ} and d_j^{ψ}, $j = 1,2,...,M$ are the standard spline coefficients which are obtained in terms of normal velocities on the knots and progressive arc lengths l'_j, $j = 1,2,3,...,M+2$.

Equations (3.31) and (3.32) give the tangential and normal velocity at every point over the bubble surface. The radial and vertical components of the fluid velocity at the bubble surface are evaluated respectively as:

$$u(l) = \eta\frac{\partial r}{\partial l} + \psi\frac{\partial z}{\partial l}, \tag{3.33}$$

$$v(l) = \eta\frac{\partial z}{\partial l} - \psi\frac{\partial r}{\partial l}. \tag{3.34}$$

It should be noted that the outward normal to the liquid domain on the bubble surface and directed inside the bubble and is given by $\left(\frac{\partial z}{\partial \xi}, -\frac{\partial r}{\partial \xi}\right)$ [see Equation (3.9)]. By evaluating Equations (3.34) and (3.35) at the end points of the segments and by using an Euler integration scheme, the position of the end points of the segments after a small time step, Δt, can be determined. Thus

$$r_i(t+\Delta t) = r_i(t) + u_i(t)\Delta t + 0(\Delta t)^2, \tag{3.36}$$

$$z_i(t+\Delta t) = z_i(t) + v_i(t)\Delta t + 0(\Delta t)^2, \tag{3.37}$$

and the velocity potentials at the midpoint of the segments become:

$$\phi_i(t+\Delta t) = \phi_i(t) + \left[\frac{D\phi}{Dt}(t)\right]_i \Delta t + 0(\Delta t)^2. \tag{3.38}$$

In Equation (3.38) $\frac{D\phi}{Dt}$ indicates the rate of change of the velocity potential with respect to time:

$$\frac{D\phi}{Dt} = \frac{\partial \phi}{\partial t} + |\nabla \phi|^2, \tag{3.39}$$

where $\frac{\partial \phi}{\partial t}$ can be obtained using the Bernoulli equation which is discussed in *Chapter four.*

Thus the position of the end points of the segments and the value of velocity potentials at the collocation points at the midpoint of the segments are known at time $t+\Delta t$. This is the complete set of computations for one time step. These calculations are repeated at every time step, in order to generate the evolution of the bubble.

3.6 NUMERICAL INTEGRATION

The terms of the matrices H and G in Equation (3.17) are calculated numerically. Gauss Legendre quadrature is used, and is an adequate scheme for calculating such non-singular integrals. In the case that the collocation point p_i is within the segment S_i, the integrand is singular and must be treated specially.

The singular integrals are calculated by subtracting the logarithmic term to remove the singularity. In this scheme the singular integral is transformed into two integrals; one integral contains no singularity which can be integrated by standard Gauss Legendre quadrature while the other integral contains an explicit logarithmic singularity. The integral containing the explicit logarithmic singularity can be integrated by a special quadrature scheme tabulated by Stroud and Secret (1966) for the integral:

$$\int_0^1 f(x)\ln\left(\frac{1}{x}\right)dx. \qquad (3.40)$$

The details of the special treatment of singular integrals, discussed above, can be found in the work of Taib (1985).

For further information about special schemes for treating singularities one can refer to the works of Wrobel and Brebbia (1981), Pina *et al.* (1981),Telles (1987), Hayami and Brebbia (1988), Niessner (1989), Sato *et al.* (1989), Hayami and Brebbia (1989) and Hall (1989).

3.7 EVALUATION OF DIAGONAL ELEMENTS

The diagonal terms of the H matrix in the system of Equations (3.17) can be calculated implicitly. As is described by Brebbia and Dominguez (1989), by considering a uniform potential over the whole boundary, the normal derivative of the potential must be zero. Then by defining I as a vector with a unit potential for all collocation points, it can be show that:

$$[H]\,[I]=0. \tag{3.41}$$

Thus the satisfaction of Equation (3.41) requires

$$H_{ii}=-\sum_{j=1}^{M} H_{ij} \qquad (for\, j\neq i), \tag{3.42}$$

which gives the diagonal elements of the H matrix in terms of the rest of its elements. For closed domains or interior problems the above considerations are strictly valid. But it must be noted that for exterior problems, infinite or semi-infinite domains, Equation (3.42) must be modified.

In the case of exterior problems, by prescribing a unit potential the integral

$$\int_{S_\infty} \frac{\partial}{\partial n}\left(\frac{1}{4\pi|p-q|}\right)dS, \tag{3.43}$$

over the external boundary S_∞ at infinity is zero. Since $\dfrac{\partial}{\partial n}\left(\dfrac{1}{4\pi|p-q|}\right)$ is due to a unit source, this integral must be

$$\int_{S_\infty} \frac{\partial}{\partial n}\left(\frac{1}{4\pi|p-q|}\right)dS=-1. \tag{3.44}$$

Thus the diagonal terms of Equation (3.17), applied to an infinite region, are [see also Taib (1985)]:

$$H_{ii} = 4\pi - \sum_{j=1}^{M} H_{ij} \qquad (for\ j \neq i). \tag{3.45}$$

More details on the integration of (3.44) can be found in Brebbia and Dominguez (1989).

CHAPTER FOUR

DYNAMICS OF AN ISOLATED BUBBLE

4.1 INTRODUCTION

Vapour cavity bubbles such as those formed in cavitational flows, are generated in the liquid when the pressure drops below the vapour pressure. These cavities are carried by the fluid flow and collapse violently in the regions where the surrounding liquid pressure is higher than the saturated vapour pressure. Vapour bubbles can also be generated by local boiling of the liquid due to a high energy input such as the case of an underwater explosion. In this case the growth of the bubble is followed by its rapid collapse. Experiments [Lauterborn (1980), Wong *et al.* (1989) and Soh and Yu (1992)] show that the collapse of a bubble generated by a high local energy input is followed by subsequent rebounds.

Many of the computational and analytical studies on the dynamics of vapour bubbles are based on the assumption that either a constant vapour pressure exists inside the bubble [Blake, Taib and Doherty (1986 and 1987), Kucera and Blake(1988)] or that the pressure changes according to a simple gas law [Kumar and Brooker (1991), Vokurka (1985) and Best and Kucera (1992)].

These assumptions do not include the process of energy transfer arising from latent heat. The release and absorption of latent heat will affect the pressure and

temperature in the vapour and consequently the growth and collapse rates of the bubble, and the hydrodynamics of the flow around the bubble. In this case the thermodynamic process inside the bubble cannot be ignored.

An energy equation [Soh and Shervani-Tabar (1994)] derived from the first law of thermodynamics for a control mass has been formulated in such a manner as to include the process of vaporisation and condensation and thus includes the effect of the latent heat .

It should be noted that throughout this work a bubble containing vapour with constant pressure during its growth and collapse is referred to as a constant pressure vapour bubble. However a bubble in which the vapour pressure changes by considering the energy transfer through latent heat is termed a vapour bubble. It is obvious that an ideal gas bubble refers to a bubble with an ideal gas inside which follows a simple gas law.

In this chapter the boundary integral method, which is discussed in *Chapter three*, is employed to simulate the dynamics of a bubble in an infinite liquid domain for cases of

- a constant pressure vapour bubble;
- an ideal gas bubble; and
- a vapour bubble.

It should be noted that a bubble in an infinite liquid domain is also called an isolated bubble.

The dynamic characteristics of a bubble resulting from each of these assumptions will now be compared.

4.2 CONSTANT PRESSURE VAPOUR BUBBLE

In this case it is assumed that the bubble contains saturated vapour and the pressure inside the bubble remains constant equal to the saturated vapour pressure of the surrounding liquid. The temperature of the surrounding liquid is assumed to be constant during the lifetime of the bubble.

4.2.1 Initial conditions for a constant pressure vapour bubble

For a constant pressure vapour bubble at its minimum volume the initial conditions may be found in terms of the initial radius and the initial velocity potential over the surface of the bubble. This was first derived by Gibson and Blake (1980) and is given by the formula

$$\phi_0^R(R_0,t_0) = R_0\left[\frac{2}{3}\left(\frac{P_\infty - P_C}{\rho}\right)\left\{\left(\frac{R_m}{R_0}\right)^3 - 1\right\}\right]^{\frac{1}{2}}, \qquad (4.1)$$

where R_m is the maximum radius of the bubble, P_∞ is the ambient pressure in the liquid domain in the initial position of the bubble centroid and in the absence of the bubble, P_C is the saturated vapour pressure of the liquid, while ρ is the density of the fluid. The maximum radius of the bubble is controlled by P_∞, P_C and the initial kinetic energy of the fluid.

The initial time, t_0, that a constant pressure vapour bubble takes to grow from inception to radius R_0 may be determined by the incomplete beta function

$$t_0 = 3R_m\left(\frac{3\rho}{P_\infty - P_C}\right)^{\frac{1}{2}}\beta_a\left(\frac{5}{6},\frac{3}{2}\right); \qquad a = \left(\frac{R_0}{R_m}\right)^3. \tag{4.2}$$

For further information about Beta functions one can refer to Abramowitz and Stegun (1965).

4.3 IDEAL GAS BUBBLE

An ideal gas bubble contains an ideal gas which follows the simple gas law

$$P_V = P_i\left(\frac{V}{V_i}\right)^k, \tag{4.3}$$

where k is the polytropic index, P_V indicates the pressure inside the bubble, V is the volume of the bubble while P_i and V_i are the initial pressure inside the bubble and the initial volume of the bubble respectively.

From Equation (4.3) it is obvious that the pressure inside an ideal gas bubble decreases during the expansion phase of the bubble and increases during its collapse phase. The building up of pressure during the collapse phase is believed to cause bubble rebound which has been observed experimentally [Lauterborn (1980), Wong *et al.* (1989) and Soh and Yu (1992)].

4.4 VAPOUR BUBBLE

In this case the complicated process of a vapour-liquid mixture in the bubble is simplified by using a 'lumped system' approach in the framework of classical thermodynamics [Soh and Shervani-Tabar (1994) and Soh (1994)]. In this

analysis, since the liquid is considered as to be water, properties of the vapour-liquid mixture can be determined from steam tables.

It is assumed that the vapour cavity is surrounded by a very thin thermal boundary layer. For simplicity, heat transfer between the thermal boundary layer and the surrounding water is also assumed to be negligible. The vaporisation and condensation is restricted to a control volume which includes the vapour cavity and a fixed narrow region of the surrounding liquid, which contains the thermal boundary layer. Thus energy transfer occurs through vaporisation and condensation.

4.4.1 The energy equation for a vapour bubble

Within the framework of classical thermodynamics, the energy equation (First Law for a control mass) for vapour within a bubble is given by:

$$P_V dV + \rho_V V du_V(P_V) - dm_L\left[u_V(P_V) - u_L(T)\right] = Qdt, \qquad (4.4)$$

where

$P_V dV$ is the work done by the bubble;

$\rho_V V du_V(P_V)$ is the change in internal energy of the vapour;

$dm_L\left[u_V(P_V) - u_L(T)\right]$ is the change in the internal energy due to the condensation and vaporisation; and

Qdt is the heat conduction into the bubble.

The conservation of mass demands that

$$dm_L + d(\rho_V V) = 0, \qquad (4.5)$$

and the assumption of no heat transfer requires that the temperature of the surrounding liquid remains constant, thus

$$P_V dV + d\left\{\rho_V V\left[u_V(P_V) - u_L(T)\right]\right\} = 0. \qquad (4.6)$$

Equation (4.6) governs the thermodynamics process in the bubble.

It should be noted that the energy transfer through vaporisation and condensation between the vapour and a narrow region of the surrounding liquid is excluded from the heat transfer term.

4.5 THE HYDRODYNAMIC EQUATION

The liquid outside of the bubble is considered to be a potential flow domain. Thus the hydrodynamic process in the liquid domain is governed by Green's integral formula [see *Chapter three*, Equation (3.3)]

$$C(p)\phi(p) + \int_S \phi(q)\frac{\partial}{\partial n}\left[\frac{1}{p-q}\right]dS = \int_S \frac{\partial}{\partial n}\left[\phi(q)\right]\left(\frac{1}{p-q}\right)dS, \qquad (4.7)$$

where ϕ is the velocity potential, S is the surface of the bubble that is piece-wise smooth, p is any given point in the domain, q is a point on S and $C(p)$ is 4π except that it is 2π when p is on S.

Equation (4.7) is used for a bubble in an infinite liquid domain, i.e., an isolated bubble.

The dynamic condition on the surface of the bubble is determined by equating the pressure inside the bubble to the pressure of the liquid domain at its interface with the bubble

$$P_V = P_\infty - \rho\frac{\partial\phi}{\partial t} - \frac{1}{2}\rho|\nabla\phi|^2 + \rho g(z - z_0), \tag{4.8}$$

where P_∞ is the pressure at infinity, P_V is the vapour pressure inside the bubble and ρ is the liquid density.

Thus the unsteady Bernoulli equation, in Lagrangian form, is given by

$$\frac{D\phi}{Dt} = \frac{P_\infty - P_V}{\rho} + \frac{1}{2}|\nabla\phi|^2 + g(z - z_0), \tag{4.9}$$

Equations (4.7) and (4.9) form the basis of a boundary integral method for the solution of the flow potential.

4.6 DISCRETIZED APPROXIMATION OF THE HYDRODYNAMIC EQUATION

The boundary integral method developed on the basis of Green's integral formula for potential flows can be applied to simulate the dynamics of an isolated bubble. The surface of the bubble is discretized into M segments that are cut along planes normal to the axis of symmetry. Let S_j represents the j^{th} segment. For a point p_i on the surface of the bubble, the discretized form of Equation (4.7) is given by:

$$2\pi\phi(p_i) + \sum_{j=1}^{M}\left\{\phi(q_j)\int_{S_j}\frac{\partial}{\partial n}\left[\frac{1}{p_i - q_j}\right]dS\right\} = \sum_{j=1}^{M}\left\{\frac{\partial}{\partial n}\left[\phi(q_j)\right]\int_{S_j}\left[\frac{1}{p_i - q_j}\right]dS\right\}, \tag{4.10}$$

for

$i = 1, 2, \ldots, M$.

The surface integrations are carried out analytically where p_i, chosen as a collocation point, is located at the middle of the i^{th} segment (see *Chapter three*). Thus Equation (4.10) becomes a system of linear equations of the form

$$2\pi\phi(p_i)+\sum_{j=1}^{M} H_{ij}\phi(q_j)=\sum_{j=1}^{M} G_{ij}\psi(q_j), \tag{4.11}$$

for

$i=1,2,...,M$.

In Equation (4.11) ψ indicates the velocity component normal to the surface of the bubble, H_{ij} and G_{ij} are the integration terms in Equation (4.10) which are integrated over a segment. Therefore H_{ij} and G_{ij} in the case of an isolated bubble are

$$H_{ij}=\int_{S_j}\frac{\partial}{\partial n}\left[\frac{1}{|p_i-q_j|}\right]dS, \tag{4.12a}$$

and

$$G_{ij}=\int_{S_j}\frac{1}{|p_i-q_j|}dS. \tag{4.12b}$$

4.7 DISCRETIZATION OF THE ENERGY EQUATION FOR A VAPOUR BUBBLE

A pressure function $H(P_V,T)$ is defined so that

$$H(P_V,T)=\rho_V\left[u_V(P_V)-u_L(T)\right]. \tag{4.13}$$

The discretization of Equation (4.6) gives:

$$\Delta H(P_V,T) = -\frac{\Delta V}{V}\left[P_V + H(P_V,T)\right]. \tag{4.14}$$

This enables the pressure function to be computed for every increment of ΔV, i.e.,

$$H(P_V + \Delta P_V,T) = H(P_V,T) + \Delta H(P_V,T). \tag{4.15}$$

Known tabulations of H with respect to P_V allow the vapour pressure to be interpolated from the current value of H.

4.8 EVOLUTION OF THE BUBBLE

From a given distribution of velocity potential, ϕ, the normal velocity, ψ, on the bubble surface is evaluated by Equation (4.11).

It is obvious that the tangential velocity on the surface of a spherical vapour bubble in an infinite liquid with no buoyancy forces and in the absence of other pressure gradients is zero. But in the case of two or more bubbles or a buoyant vapour bubble in an infinite liquid, the tangential velocity over the surface of the bubble can be calculated by Equation (3.18) or Equation (3.31) depending on the approximation model for the bubble surface.

The discretized form of Bernoulli's equation for calculating the velocity potential allows the velocity potential to be time-marched over a time increment of Δt:

$$[\phi_i]_{t+\Delta t} = [\phi_i]_t + \Delta t\left\{\frac{P_\infty - P_V}{\rho} + \frac{1}{2}|\nabla\phi|^2 + g(z - z_0)\right\}. \tag{4.16}$$

The collocation points, p_i, are the position vectors in an axisymmetrical cylindrical coordinates system (r_i, z_i) and are time-marched according to the Euler formula:

$$r_i(t+\Delta t) = r_i(t) + u_i \Delta t + 0(\Delta t^2), \tag{4.17}$$

$$z_i(t+\Delta t) = z_i(t) + v_i \Delta t + 0(\Delta t^2). \tag{4.18}$$

Here the velocity vectors (u_i, v_i), along the direction of r and z are derived from the velocity components that are normal to the bubble surface, ψ_i, and tangential to it, η_i.

In the case of rebounding bubbles a large variation of the normal velocity occurs over an extremely short period of time. In order to capture the rebound instant a fourth order Runge-Kutta method is employed as the integration scheme over the time.

4.9 OUTLINE OF SOLUTION

An isolated bubble with no buoyancy forces and in the absence of any other pressure gradients remains spherical in its growth and collapse phases. In numerical calculations, the initial growth phase has no effect on the shape of the bubble during its collapse. Thus for the purpose of simplicity the computations are initiated by considering a spherical bubble collapsing from its initial maximum volume.

The velocity potential on the surface of the bubble at its initial maximum volume is zero. The normal velocity, although initially zero, is found from Equation (4.11). The tangential velocity, as mentioned before, over the surface of a bubble in an infinite liquid domain with no buoyancy forces and in the absence of any other pressure gradients is zero.

A variable time step, Δt, is employed according to the expression

$$\Delta t = \min_i \left(\frac{\Delta\phi}{\frac{P_\infty - P_C}{\rho} + \frac{1}{2}|\nabla\phi_i|^2} \right), \tag{4.19}$$

where $\Delta\phi$ is an assigned constant which limits the velocity potential increment in each time step and i indicates collocation points. It should be noted that the variable time step determined by Equation (4.19) is adequate for the case of a constant pressure vapour bubble and provides accurate results by using a simple Euler scheme. But in the case of a rebounding bubble, at the later stages of the collapse the pressure inside the bubble increases and exceeds the ambient pressure. Thus in this case the variable time step is given by

$$\Delta t = \min_i \left(\frac{\Delta\phi}{\frac{P_\infty + P_V}{\rho} + \frac{1}{2}|\nabla\phi_i|^2} \right). \tag{4.20}$$

The velocity potential and the coordinates of the collocation points are advanced in time by applying Equations (4.16), (4.17) and (4.18).

In the case of an ideal gas bubble or a vapour bubble the pressure inside the bubble has to be evaluated at the end of each time step. The pressure inside an ideal gas bubble can be simply determined by Equation (4.3) at every time step. In the case of a vapour bubble Equation (4.15) yields the updated value of the pressure function $H(P_V, T)$; the pressure P_V, is interpolated from a tabulation of H versus P_V, which is constructed from steam tables [UK Steam Tables in SI Units (1970)]. Note that the function H is related to vapour density and internal energy as shown in Equation (4.13).

4.10 NON-DIMENSIONALISING OF THE SOLUTION

The maximum radius of the bubble, R_m, the pressure difference driving the bubble collapse, $P_\infty - P_C$, and the liquid density, ρ, are chosen as the basic parameters for non-dimensionalising the numerical results. Based upon these parameters the terms chosen for non-dimensionalising are

- R_m, as the length scale,
- $R_m\left(\frac{\rho}{P_\infty - P_C}\right)^{\frac{1}{2}}$, as the time scale,
- $R_m\left(\frac{P_\infty - P_C}{\rho}\right)^{\frac{1}{2}}$, as the scale for velocity potential,
- $\left(\frac{P_\infty - P_C}{\rho}\right)^{\frac{1}{2}}$, as the scale for velocity.

4.11 NUMERICAL RESULTS

An analysis of the dynamics of an isolated bubble can be carried out numerically for the cases of

- a constant pressure vapour bubble;
- an ideal gas bubble (with the different polytropic indices of 1.4, 1.2 and 1.15); and
- a vapour bubble.

The initial conditions for all of these cases are chosen as

- P_∞ = pressure at infinity = 35000 Pa,
- temperature of the surrounding liquid = 25°C,
- pressure inside the bubble at its maximum volume = 3166 Pa (equal to the surrounding liquid saturated vapour pressure),
- R_m = maximum radius of the bubble = 0.0249 m,
- buoyancy forces are not considered.

4.11.1 Numerical results on the dynamics of a constant pressure vapour bubble

Figure 4.1 shows the radius of a constant pressure vapour bubble in an infinite liquid domain, collapsing from its initial maximum volume, with respect to time. In this figure empty squares show the numerical results obtained by the boundary integral method, while solid line indicates the results of the Rayleigh equation [see Equation (5.11)] which is solved numerically by Mathematica ["Mathematica; a system for doing mathematics by computer", Wolframe (1992)]. Figure 4.1 demonstrates a very good agreement between the results obtained by the boundary integral method and the results obtained by the numerical solution of the Rayleigh equation by Mathematica.

Figure 4.2 illustrates the normal velocity of the bubble boundary with respect to time. This figure shows that in the case of a constant pressure vapour bubble the normal velocity of the bubble boundary increases very sharply at the later stages of

collapse. In this case the normal velocity of the bubble boundary approaches infinity while the volume of the bubble approaches zero.

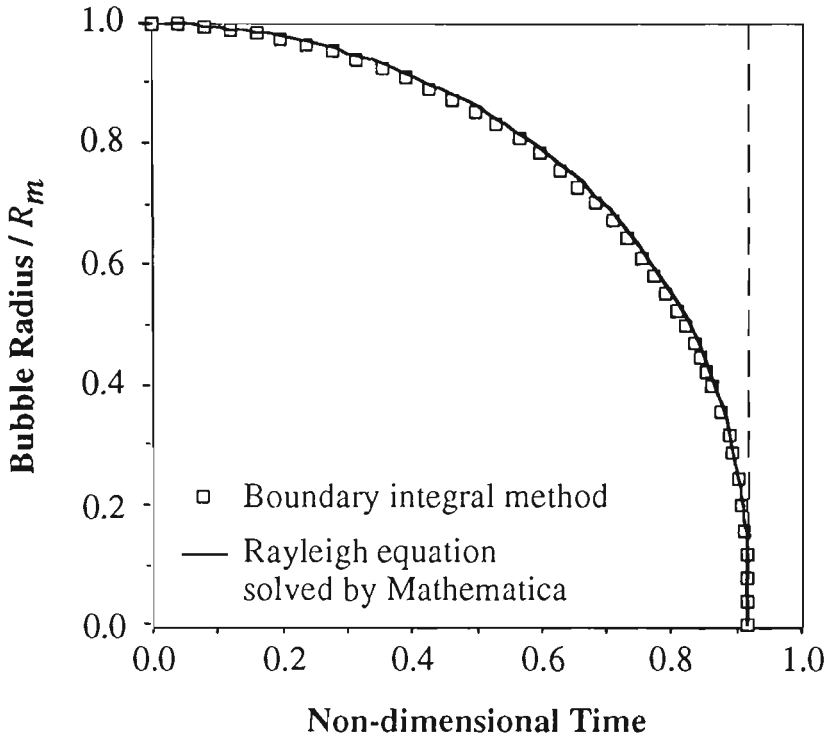

Figure 4.1 Radius of a constant pressure vapour bubble against time obtained by the boundary integral method and by the numerical solution of the Rayleigh equation by Mathematica.

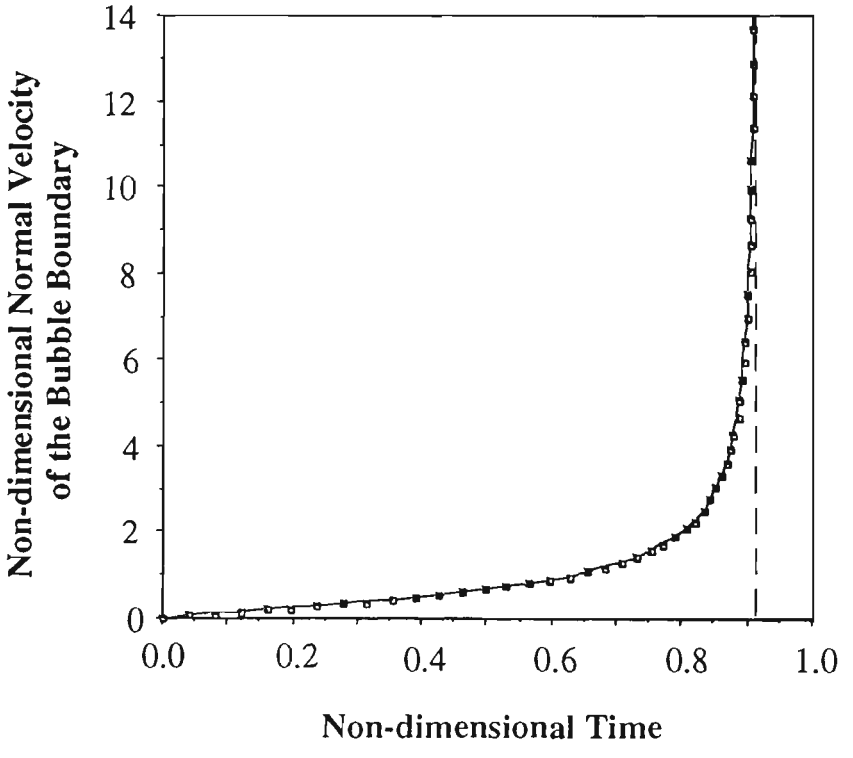

Figure 4.2 Normal velocity of the bubble boundary for the case of a constant pressure vapour bubble.

According to Rayleigh (1917), the total collapse time for a spherical constant pressure vapour bubble is [see also Plesset and Chapman (1971)]

$$t_{collapse} = 0.915 R_m \left(\frac{\rho}{P_\infty - P_C} \right)^{\frac{1}{2}}.$$

Table 4.1 presents bubble collapse time obtained by three different methods;

- the boundary integral method;
- Rayleigh equation solved by Mathematica; and
- analytical solution.

As shown in the Table 4.1, in comparison with the results of the analytical solution, the collapse time obtained by the boundary integral method is more accurate than the collapse time obtained by the numerical solution of the Rayleigh equation by Mathematica.

Table 4.1 Comparison between collapse times of a spherical constant pressure vapour bubble calculated by three different methods

METHOD OF SOLUTION	COLLAPSE TIME OF THE BUBBLE
Boundary integral method	$0.91486 R_m \left(\frac{\rho}{P_\infty - P_C} \right)^{\frac{1}{2}}$
Rayleigh equation solved by Mathematica	$0.91467 R_m \left(\frac{\rho}{P_\infty - P_C} \right)^{\frac{1}{2}}$
Analytical solution	$0.915 R_m \left(\frac{\rho}{P_\infty - P_C} \right)^{\frac{1}{2}}$

4.11.2 Numerical results on the dynamics of an ideal gas bubble

Numerical results reveal same interesting features about an isolated ideal gas bubble having a polytropic index k of 1.4 and collapsing from its maximum volume. Figure 4.3 shows the bubble radius the normal velocity of the bubble boundary with respect to time. This figure illustrates two complete cycles of the bubble pulsations. Figure 4.3 shows that an ideal gas bubble collapses to a very small volume and then rebounds. The rebound of an ideal gas bubble is due to the building up of pressure inside the bubble during its collapse phase as illustrated in Figure 4.4.

Figure 4.3 also shows that the normal velocity of the bubble boundary increases during the collapse phase and at the later stages of the collapse drops sharply to zero normal velocity at the rebound instant of the bubble. Then the normal velocity changes its direction and increases sharply and approaches the same maximum magnitude as that of that of the collapse phase. At this point the bubble grows up to its initial maximum volume and the normal velocity decreases to zero. The recovery of the bubble volume to its initial maximum value at the end of the rebound in the absence of energy dissipation indicates the accuracy of the solution.

Figure 4.4 shows that the pressure inside an ideal gas bubble increases very slightly during the early stages of the bubble collapse. This figure also illustrates that the pressure inside the bubble increases very sharply during the later stages of the bubble collapse and reaches a peak pressure to a maximum at the rebound instant and then drops very sharply during the very early stages of the bubble rebound.

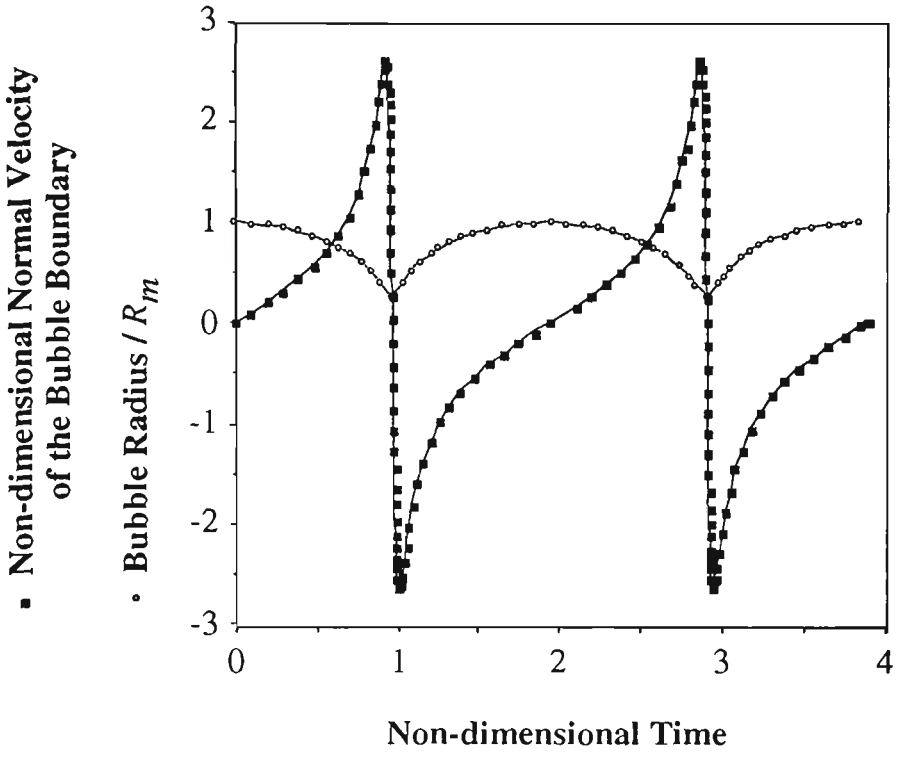

Figure 4.3 Normal velocity of the bubble boundary and bubble radius against time in an ideal gas bubble (k=1.4) during two cycles of its pulsations.

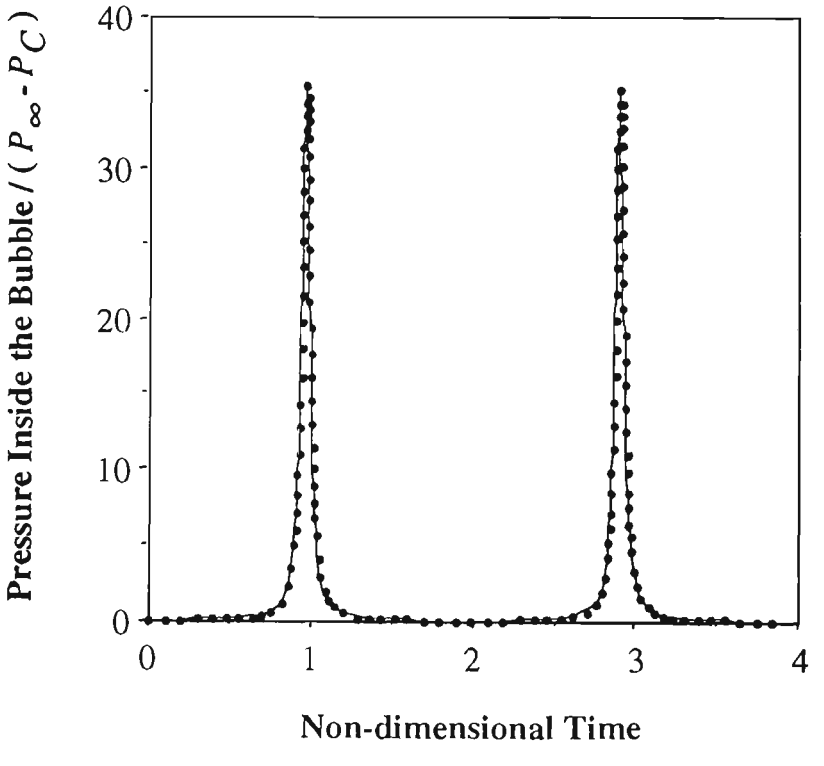

Figure 4.4 Pressure inside the ideal gas bubble used for Figure 4.3.

It is obvious that in the framework of energy conservation the consequent bubble pulsations have the same magnitude as the first collapse and rebound phases of the bubble without any damping effects. This fact is clearly shown in Figures 4.3 and 4.4 for the second cycle of bubble pulsations.

It should be noted that according to the boundary integral formulation (see *Chapter three*) the normal velocity of the bubble boundary is positive during the collapse of the bubble and is negative during its rebound.

4.11.3 Numerical results on the dynamics of a vapour bubble

Numerical calculations show that the effects of energy transfer due to latent heat during vaporisation and condensation in a vapour bubble (see *Section 4.4*) are the cause of bubble rebound. This fact indicates that in contrast to the case of a constant pressure vapour bubble, the effects of energy transfer through latent heat causes a building up of pressure inside the vapour bubble during its collapse. The dynamic character of an isolated vapour bubble is discussed in more detail in the next section on numerical results in comparison with the dynamic character of an ideal gas bubble with different polytropic indices and also a constant pressure vapour bubble.

4.12 COMPARISONS AND DISCUSSION

In this section a detailed comparison is made between the dynamic character of a bubble in the cases of

- a constant pressure vapour bubble;
- an ideal gas bubble (with different polytropic indices of k = 1.4, 1.2 and 1.15); and

- a vapour bubble.

Figure 4.5 shows that a constant pressure vapour bubble collapses to zero volume while an ideal gas bubble collapses to a minimum volume and then rebounds to its initial maximum volume. Figure 4.5 also illustrates that the collapse time of a constant pressure vapour bubble is less than the time that an ideal gas bubble with polytropic index k of 1.4 takes to collapse from its initially maximum volume to its minimum volume at the end of collapse and just before rebound.

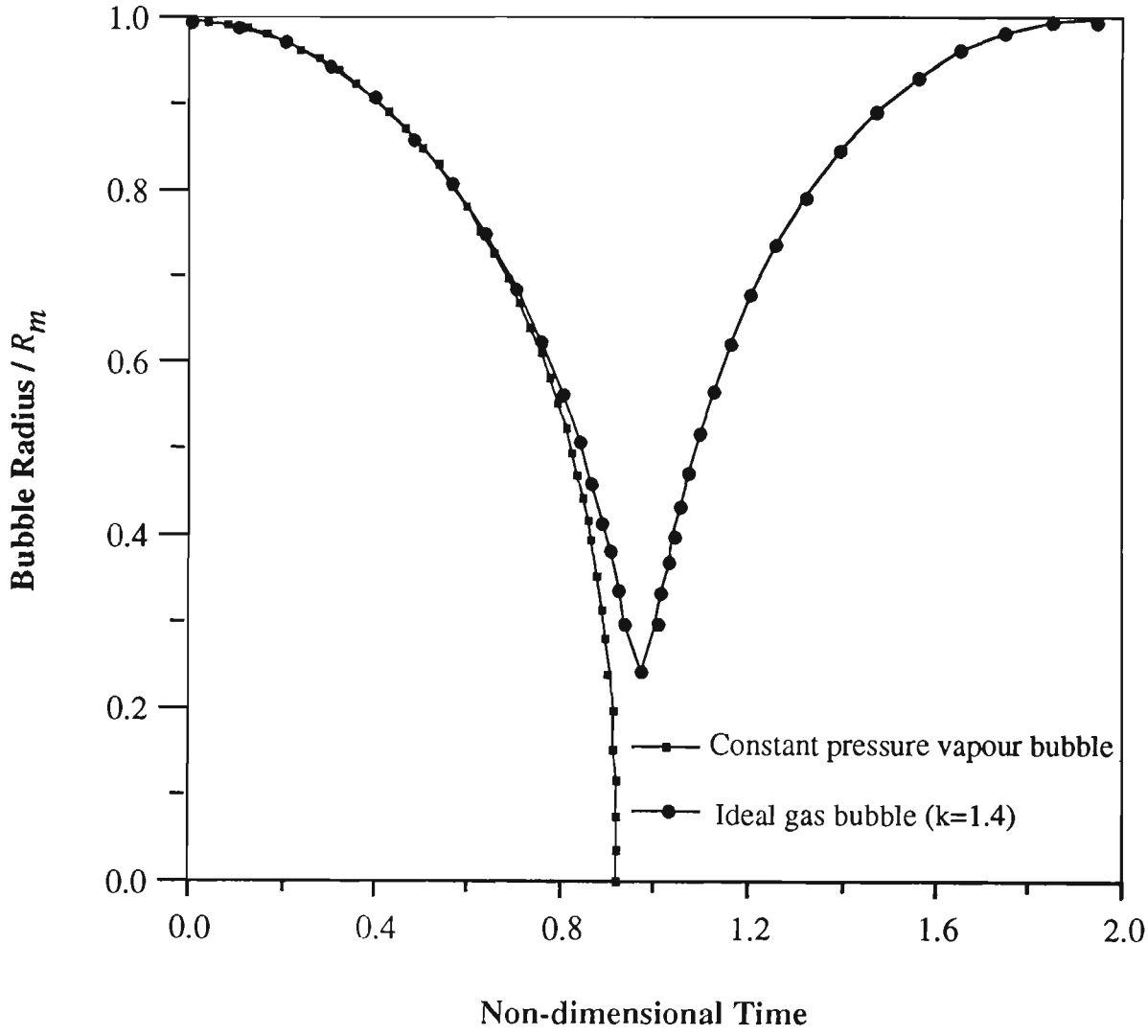

Figure 4.5 Comparison between the collapse rate of a constant pressure vapour bubble during its collapse with the collapse rate of an ideal gas bubble (k=1.4) during its collapse and rebound.

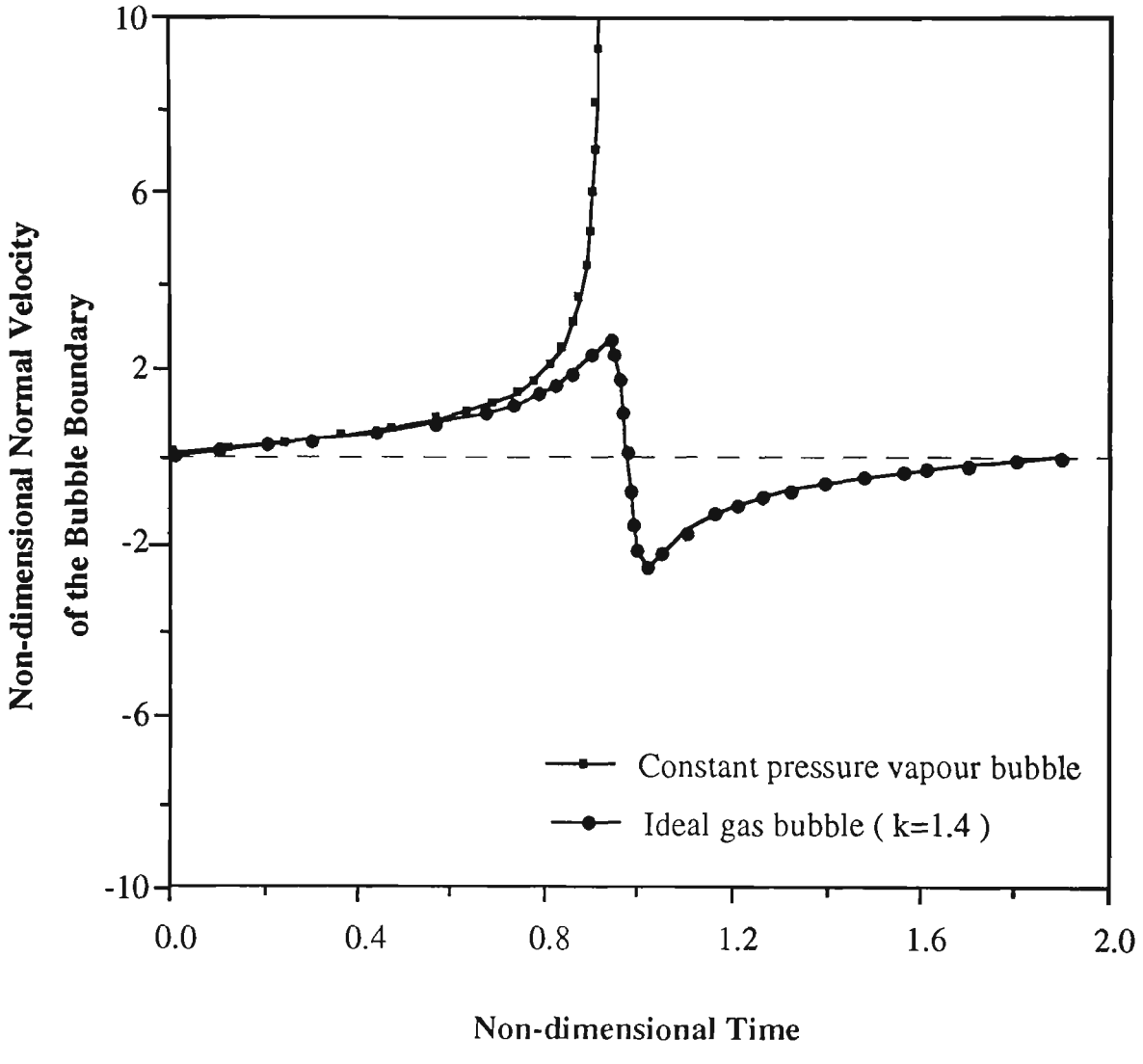

Figure 4.6 Comparison between the normal velocity of a constant pressure vapour bubble during its collapse with the normal velocity of an ideal gas bubble (k =1.4) during its collapse and rebound.

Figure 4.6 shows the normal velocity of the bubble boundary for an constant pressure vapour bubble in its collapse phase and for an ideal gas bubble with the polytropic index k of 1.4 during one collapse and rebound cycle.

Figure 4.7 illustrates the collapse and rebound times of isolated bubbles for different cases. This figure shows that the collapse time of a constant pressure vapour bubble is less than the time that an ideal gas bubble or a vapour bubble takes

to collapse from their initially maximum volume to their minimum volume at the end of collapse and just before rebound. Figure 4.7 also indicates that the collapse time of an ideal gas bubble, which undergoes an isentropic process, from its initially maximum volume to its minimum volume at the end of collapse and just before rebound is greater than the corresponding values for the case of ideal gas bubbles with polytropic indices of 1.2 and 1.15. This figure also illustrates that the minimum volume at the end of the collapse phase in the case of an ideal gas bubble with polytropic index of 1.4 is greater than corresponding values of the minimum volume for the case of ideal gas bubbles with polytropic indices of 1.2 and 1.15.

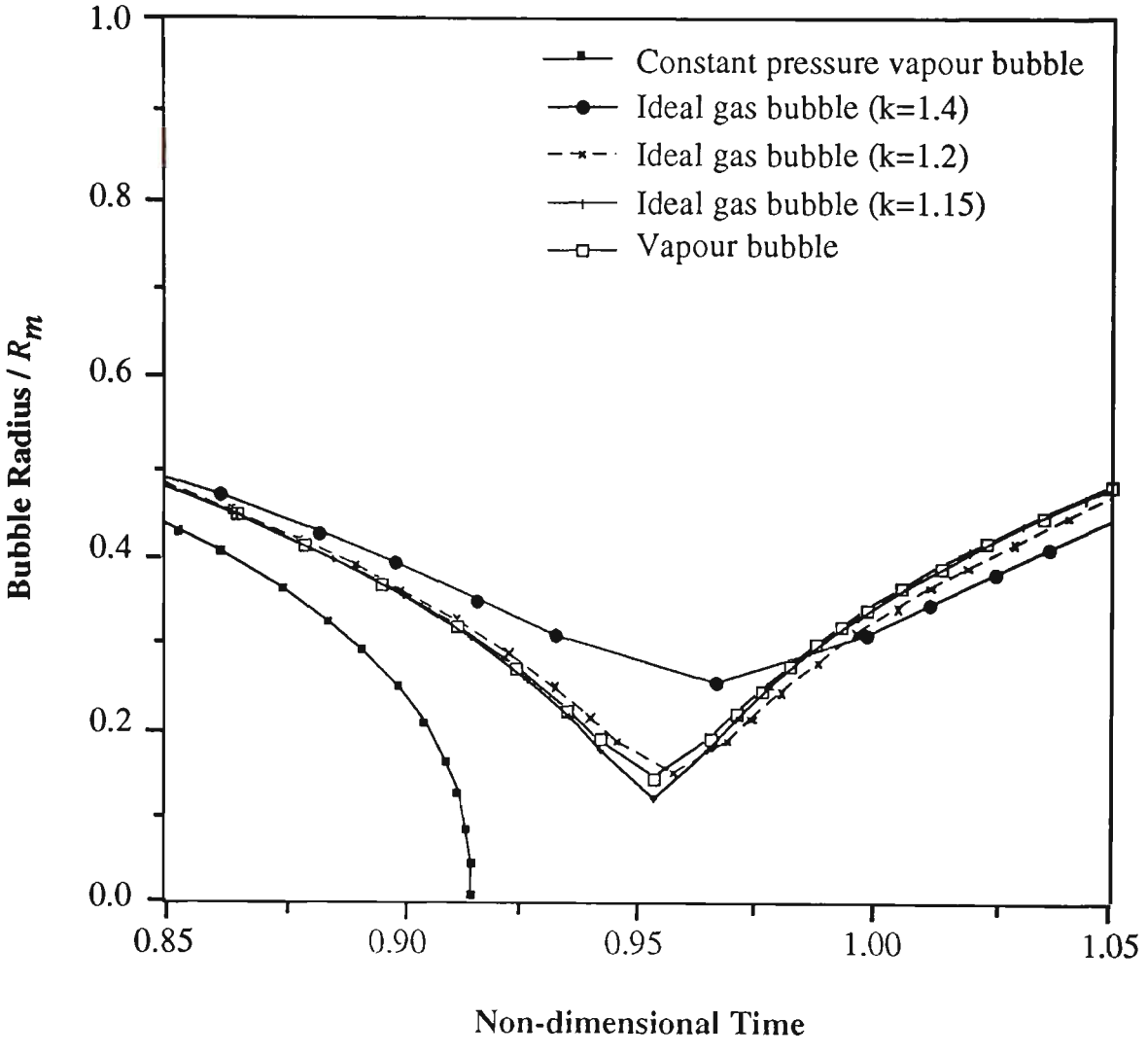

Figure 4.7 Comparison between the collapse rate of a constant pressure vapour bubble, the collapse rate of ideal gas bubbles with polytropic index k of 1.4, 1.2 and 1.15 and the collapse rate of a vapour bubble.

In Figure 4.7 it is shown that the time for one collapse phase of a vapour bubble is nearly equal to the time for one collapse phase of an ideal gas bubble having a polytropic index k of 1.15. The minimum volume of a vapour bubble at the end of the collapse phase is nearly equal to the minimum volume of an ideal gas bubble having a polytropic index k of 1.2.

From the physical point of view it can be concluded that an ideal gas bubble with smaller polytropic index collapses more violently and consequently has a stronger rebound.

Figure 4.8 shows the values of pressure inside the bubble at the later stages of collapse and early stages of rebound. Figure 4.9 illustrates the corresponding values of normal velocity of the bubble boundary.

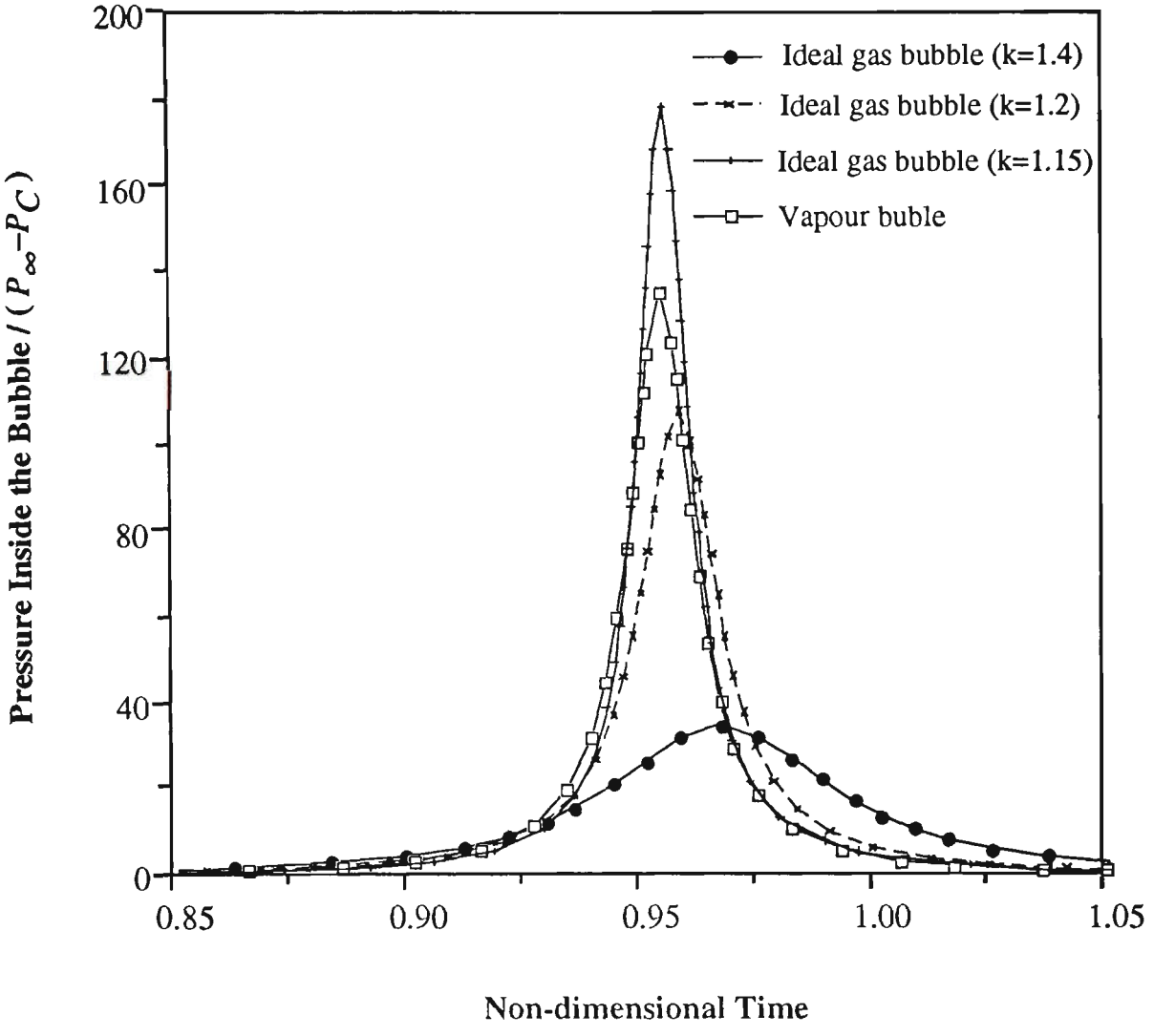

Figure 4.8 Comparison between the pressure inside ideal gas bubbles with polytropic indices k of 1.4, 1.2 and 1.15 and a vapour bubble.

Figures 4.8 and 4.9 indicate that an ideal gas bubble which undergoes an isentropic process has the lowest peak pressure inside the bubble with the smallest maximum normal velocity of the bubble boundary and greatest minimum volume at the end of collapse phase. An ideal gas bubble having a polytropic index of 1.15 has the highest peak pressure inside the bubble with the greatest normal velocity of the bubble boundary and smallest minimum volume at the end of its collapse phase. From these two figures it can be seen that the peak pressure inside the vapour

bubble at the end of the collapse phase and its maximum normal velocity are located between their corresponding values for the cases of ideal gas bubbles with polytropic indices k of 1.2 and 1.15.

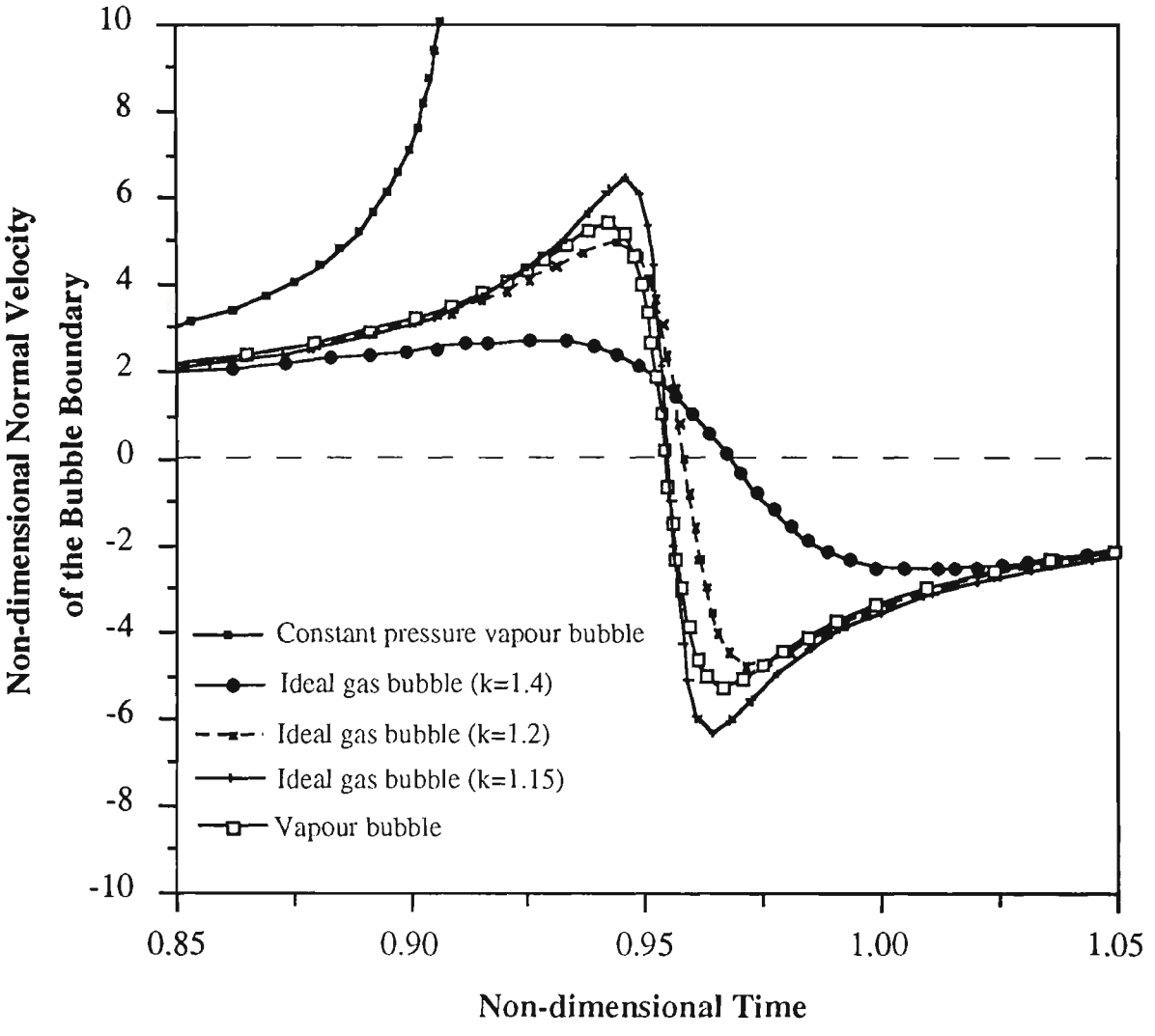

Figure 4.9 Comparison between the normal velocity of the bubble boundary in the case of a constant pressure vapour bubble, the normal velocity of the bubble boundary for the cases of ideal gas bubbles with polytropic indices k of 1.4, 1.2 and 1.15 and in the case of a vapour bubble.

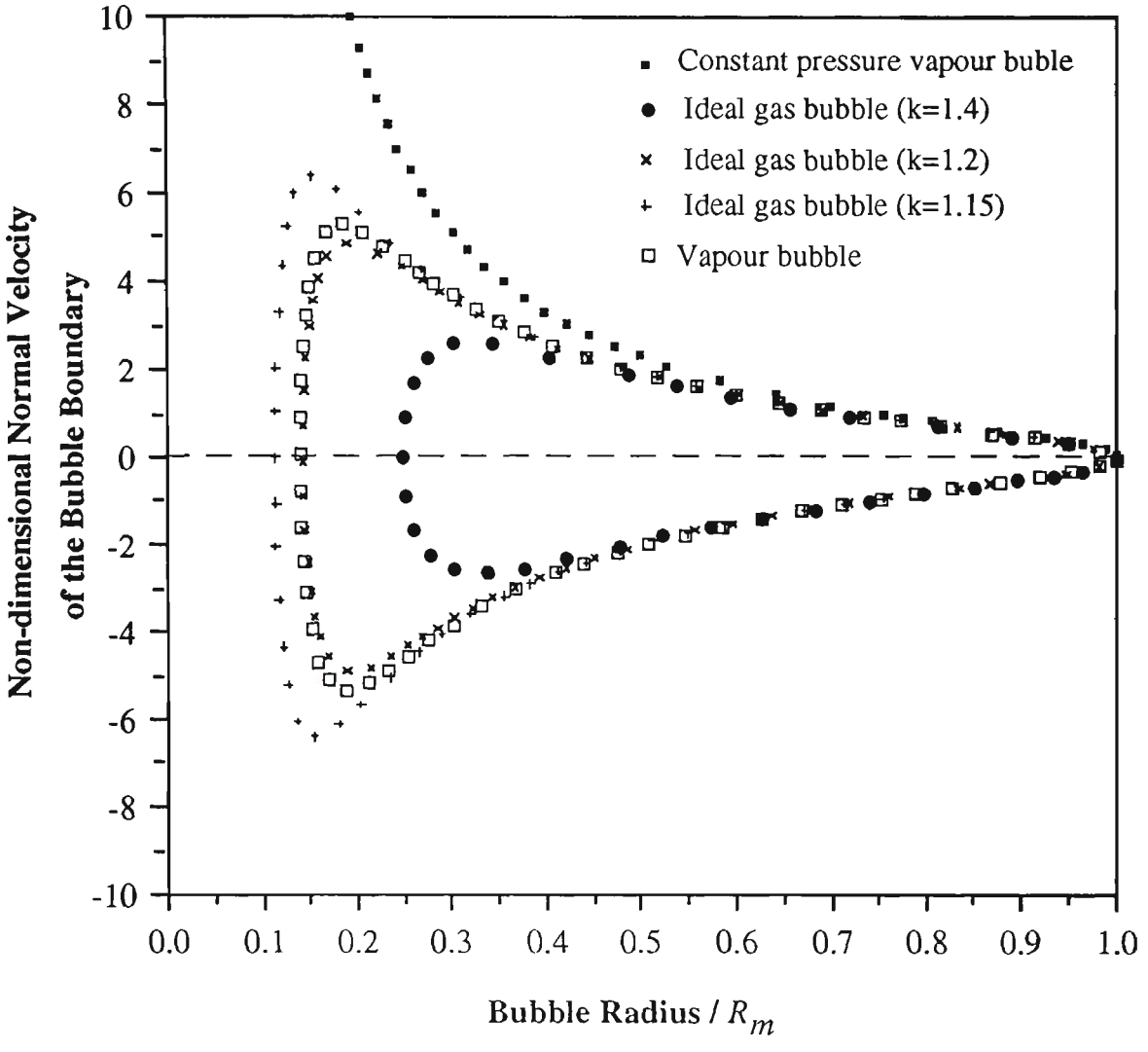

Figure 4.10 Comparison between the normal velocity of the bubble boundary against bubble radius for the cases of ideal gas bubbles having polytropic indices k of 1.4, 1.2 and 1.15 and a vapour bubble.

Figure 4.10 illustrates the normal velocity of the bubble boundary against the bubble radius. It can be seen that the bubble has zero normal velocity at its maximum volume and as the bubble collapses the normal velocity of the bubble boundary increases and reaches its maximum value at the later stages of the collapse. Then the normal velocity of the bubble boundary sharply drops to zero at the minimum volume of the bubble. It then increases sharply in the opposite direction at the very early stages of the bubble rebound and reaches the same

magnitude of maximum normal velocity as that of the collapse phase. The normal velocity of the bubble boundary, then, decreases to zero as the bubble recovers to its initial maximum volume at the end of the rebound phase which completes one cycle of bubble collapse and rebound. The radius of the bubble at its minimum volume for different cases can be easily compared in Figure 4.10.

Figure 4.11 illustrates the normal velocity of the bubble boundary against the pressure inside the bubble during one cycle of its collapse and rebound for the different cases.

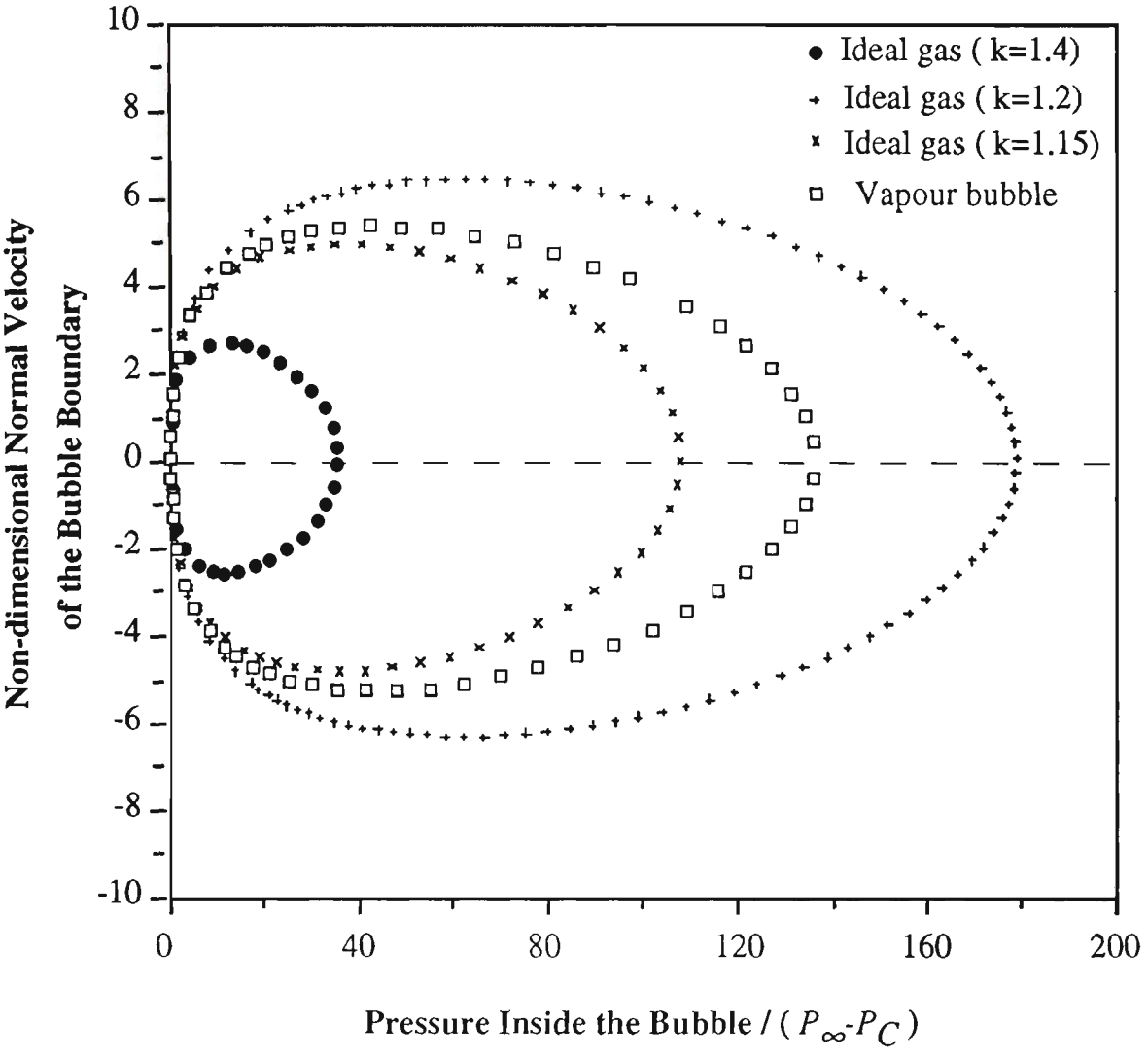

Figure 4.11 Normal velocity of the bubble boundary against pressure inside the bubble for the cases of ideal gas bubbles with polytropic indices k of 1.4, 1.2 and 1.15 and a vapour bubble during their one cycle of collapse and rebound.

Figure 4.12 illustrates the temperature inside the bubble for the different cases. It should be noted that the temperature inside the bubble is assumed to be uniform at every time step. Figure 4.12 indicates that the temperature inside an ideal gas bubble and a vapour bubble increases during the collapse phase of the bubble and reaches a maximum value at the end of collapse phase and then decreases as the bubble rebounds. It should also be noted that the temperature inside a constant pressure vapour bubble remains constant during the lifetime of the bubble.

It can be seen that the maximum value of the temperature inside an ideal gas bubble which undergoes an isentropic process is higher than in the cases of an ideal gas bubble that has polytropic indices k of 1.2 and 1.15.

It is shown that the temperature inside a vapour bubble during its collapse and rebound is less than the temperature inside the ideal gas bubble with polytropic index of 1.15. This fact may be explained in terms of mass conservation: In a polytropic process the mass in a bubble is constant, whereas in the process modelled in *Section 4.4*, there is mass interchange between vapour and liquid during condensation and vaporisation.

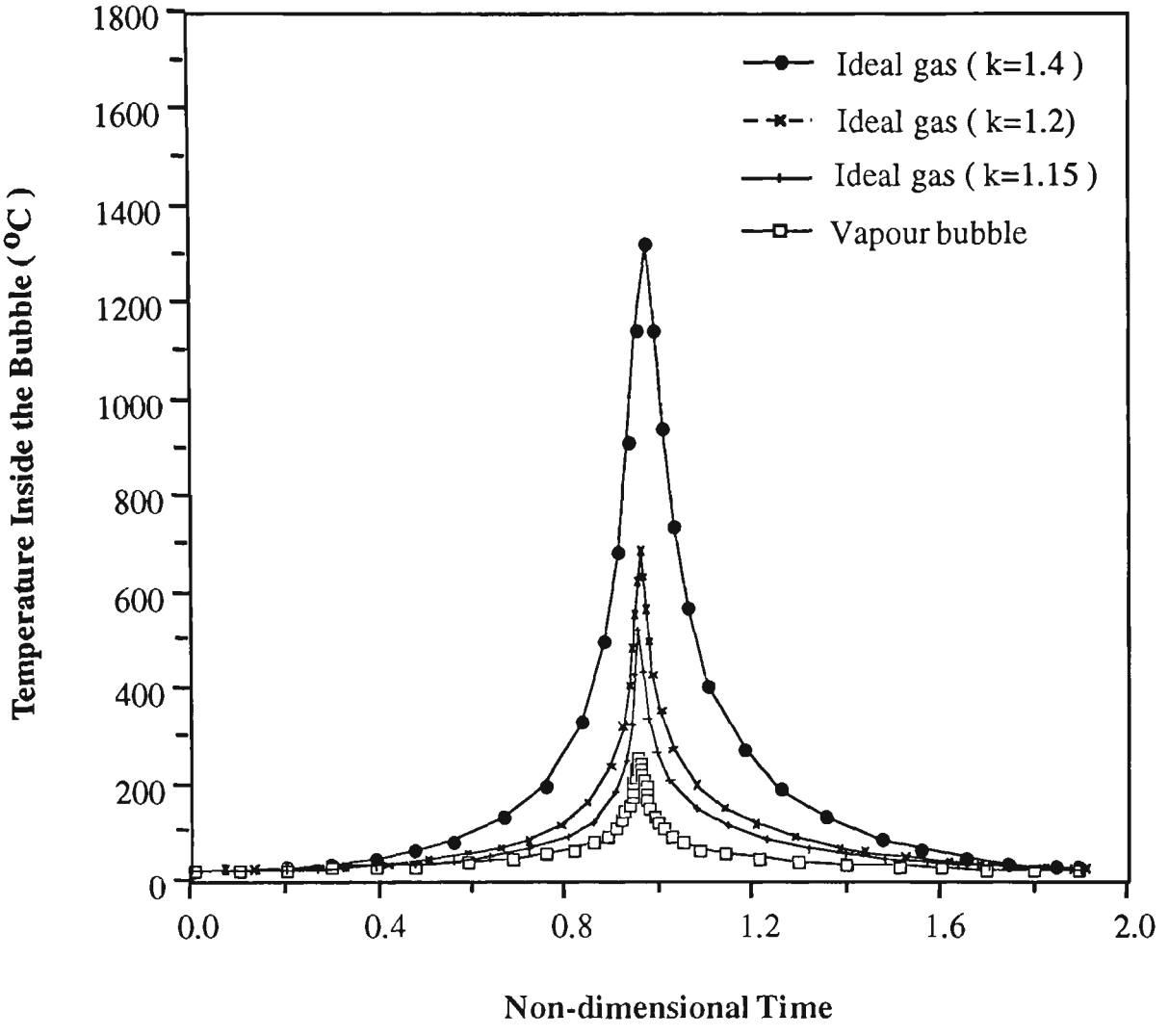

Figure 4.12 The temperature inside the bubble for the cases of ideal gas bubbles with polytropic indices of 1.4, 1.2 and 1.15 and a vapour bubble.

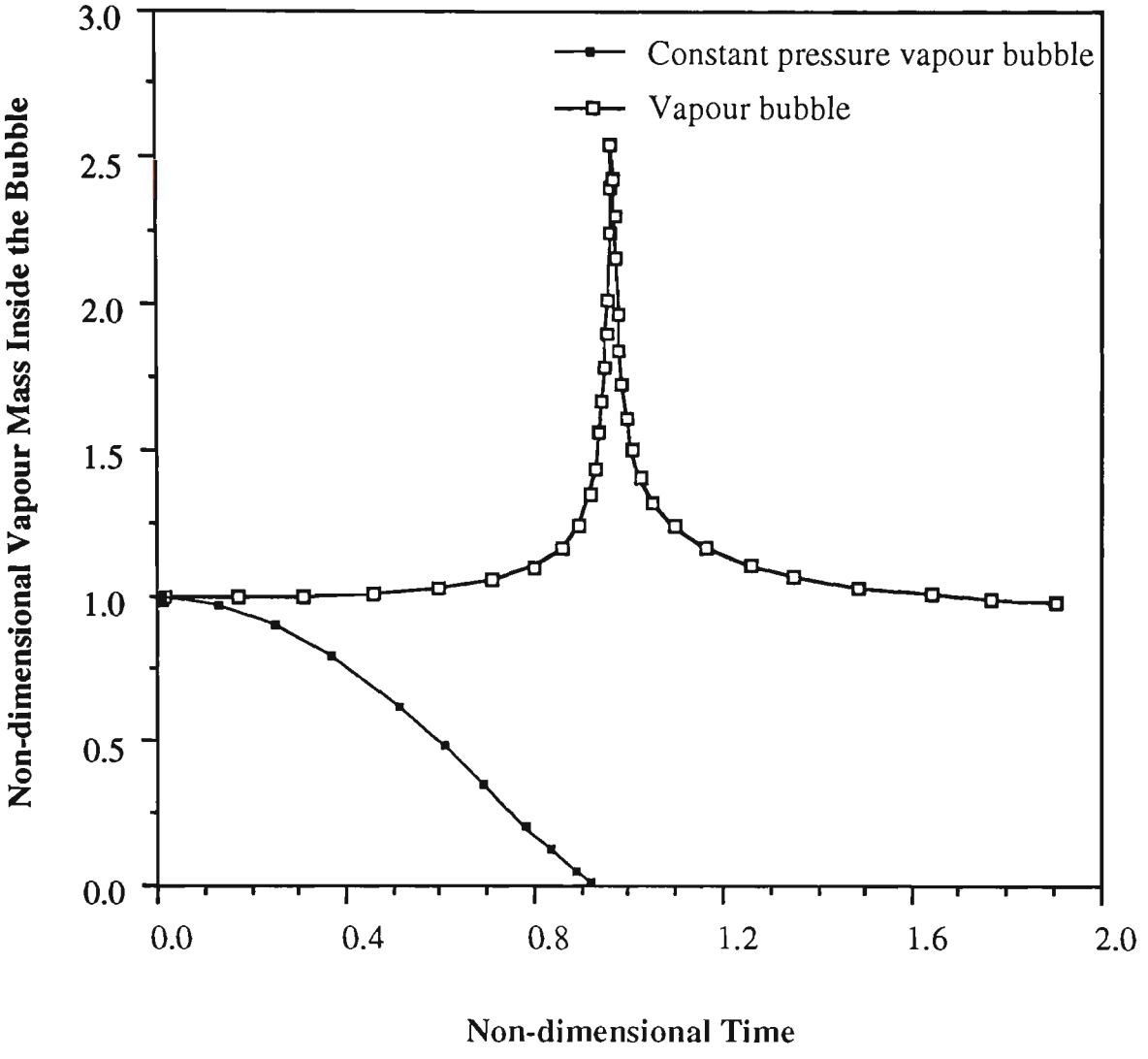

Figure 4.13 The vapour mass inside a constant pressure vapour bubble during its collapse and a vapour bubble during its collapse and rebound.

Figure 4.13 shows that the vapour mass inside a vapour bubble increases during its collapse phase and decreases during the rebound of the bubble, while in a constant pressure vapour bubble vapour mass decreases proportionally with the reduction of bubble volume during its collapse.

Figure 4.14 illustrates the pressure in the liquid domain around an ideal gas bubble in the cases of polytropic indices k=1.4, 1.2 and 1.15 and a vapour bubble at the

end of the collapse phase and just before the rebound instant. Figure 4.15 also shows the pressure inside the liquid domain around a constant pressure vapour bubble during the later stages of the bubble collapse.

As shown in Figure 4.14 the pressure developed inside the liquid domain around a constant pressure vapour bubble is much higher than the pressure developed inside the liquid domain around ideal gas bubbles and/or a vapour bubble.

Figure 4.14 also shows that the curve representing the pressure developed around a vapour bubble is located between the curves representing the pressure developed around two different cases of an ideal gas bubble with polytropic indices k of 1.2 and 1.15.

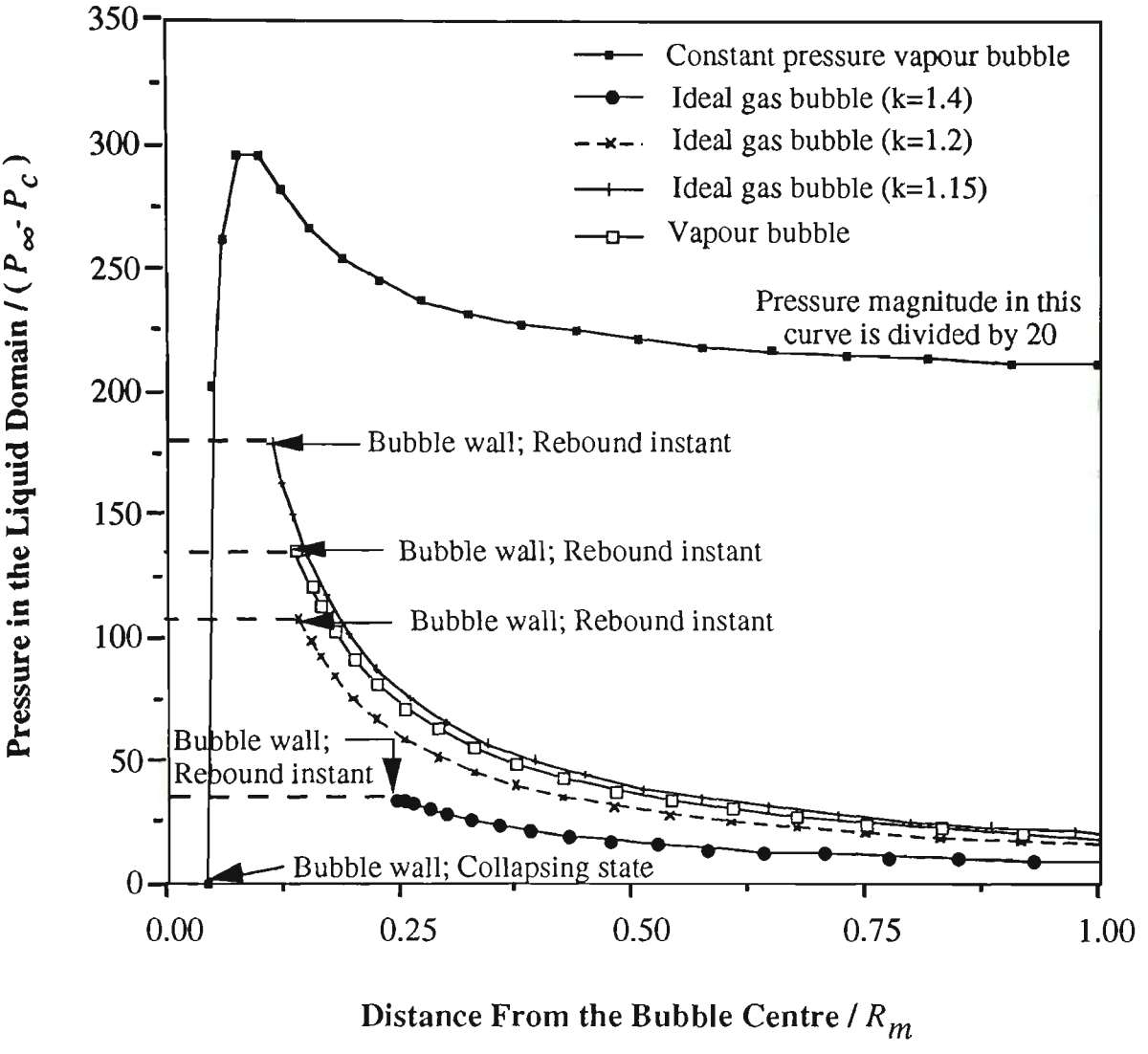

Figure 4.14 The pressure in the liquid domain around a constant pressure vapour bubble during the later stages of its collapse, ideal gas bubbles with polytropic indices k of 1.4, 1.2 and 1.15 at the rebound instant, and a vapour bubble at rebound instant.

Table 4.2 represents several dynamic characteristics of an isolated bubble in the different cases which are discussed in this chapter. In this table $\frac{V_{min}}{V_{max}}$ indicates the ratio between the bubble volume at the end of collapse phase and just before rebound while $\frac{R_{min}}{R_m}$ represents the corresponding values for the bubble radius.

Also in Table 4.2 $(P_v)_{max}$ and T_{max} represent the maximum pressure and temperature inside the bubble respectively which are obtained at the end of the collapse phase and just before the rebound in the cases of rebounding bubbles.

Table 4.2 Comparison between several dynamic characteristics of an isolated bubble in the different cases which are discussed in this chapter

	Collapse time (Time for one collapse in rebounding bubbles)	$\frac{V_{min}}{V_{max}}$	$\frac{R_{min}}{R_m}$	$\frac{(P_v)_{max}}{P_\infty - P_C}$	Maximum normal velocity of the bubble boundary during the collapse phase	$T_{max}(^oC)$
Constant pressure vapour bubble	$0.91486 R_m \left(\frac{\rho}{P_\infty - P_C}\right)^{\frac{1}{2}}$	tends to zero	tends to zero	0.099*	approaches to infinity	25.000*
Ideal gas bubble (k=1.4)	$0.96675 R_m \left(\frac{\rho}{P_\infty - P_C}\right)^{\frac{1}{2}}$	0.0150	0.2467	35.51	$2.624 \left(\frac{P_\infty - P_C}{\rho}\right)^{\frac{1}{2}}$	1327.4
Ideal gas bubble (k=1.2)	$0.95781 R_m \left(\frac{\rho}{P_\infty - P_C}\right)^{\frac{1}{2}}$	0.0029	0.1434	108.31	$4.870 \left(\frac{P_\infty - P_C}{\rho}\right)^{\frac{1}{2}}$	684.8
Ideal gas bubble (k=1.15)	$0.95455 R_m \left(\frac{\rho}{P_\infty - P_C}\right)^{\frac{1}{2}}$	0.0015	0.1140	179.12	$6.357 \left(\frac{P_\infty - P_C}{\rho}\right)^{\frac{1}{2}}$	521.3
Vapour bubble	$0.95393 R_m \left(\frac{\rho}{P_\infty - P_C}\right)^{\frac{1}{2}}$	0.0027	0.1389	136.09	$5.312 \left(\frac{P_\infty - P_C}{\rho}\right)^{\frac{1}{2}}$	254.916

* Remains constant during the lifetime of the bubble

4.13 SUMMARY AND CONCLUDING REMARKS

The boundary integral method developed throughout this research has been successfully applied in the simulation of the dynamics of an isolated bubble in the cases of

- a constant pressure vapour bubble;
- an ideal gas bubble with different polytropic indices; and
- a vapour bubble.

The numerical results show the accuracy and convergence of the solution. This can be deduced from several observations. The collapse time for a constant pressure vapour bubble obtained in this research by the boundary integral method is in a very good agreement with the collapse time according to Rayleigh. Comparison between the results of bubble radius against time obtained by the boundary integral method and by the numerical solution of the Rayleigh equation by Mathematica also shows very good agreement and indicates the accuracy of the solution.

The results also show that while a constant pressure vapour bubble collapses to zero volume, an ideal gas bubble collapses to a minimum volume and then rebounds.

It was found that energy transfer via latent heat in a vapour bubble causes the building up of pressure inside the bubble during its collapse phase and therefore causes the bubble rebound.

Through the comparisons between the results it was found that a vapour bubble (by considering energy transfer through latent heat from the point of view of pressure inside the bubble, the normal velocity of the bubble boundary and minimum

volume of the bubble) behaves as an ideal gas with a polytropic index between 1.15 and 1.2.

It is found that the maximum temperature obtained inside an ideal gas bubble which undergoes isentropic process, is much higher than the maximum temperature obtained inside ideal gas bubbles with polytropic indices of 1.2 and 1.15. It is also shown that the temperature inside a vapour bubble during its collapse and rebound is less than the temperature inside the ideal gas bubble with polytropic index of 1.15. This fact may be explained in terms of mass conservation: In a polytropic process the mass in a bubble is constant, whereas in the process modelled in *Section 4.4*, there is mass interchange between vapour and liquid during condensation and vaporisation.

The numerical results show that the vapour mass inside a vapour bubble increases during its collapse phase and decreases during the bubble rebound. Whereas the vapour mass inside a constant pressure vapour bubble increases during its collapse and vanishes at the end of the collapse phase.

Numerical calculations using the boundary integral method show that the pressure in the liquid domain around an isolated bubble increases during the bubble collapse. In the case of rebounding bubbles the pressure in the liquid domain around the bubble reaches a maximum value at the end of the collapse phase and just before the bubble rebounds, (the rebound instant), and decreases during the bubble rebound. In the case of a constant pressure vapour bubble, the pressure in the liquid domain around the bubble increases to an extremely high pressure at the later stages of the bubble collapse and approaches infinity as the volume of the bubble approaches to zero.

CHAPTER FIVE

COMPUTER MODEL FOR A PULSATING BUBBLE NEAR A RIGID BOUNDARY

5.1 INTRODUCTION

In this chapter the dynamics of a cavity vapour bubble generated in a cavitational flow or due to a high local energy input in the vicinity of a rigid boundary is investigated. The growth of the bubble is followed by its rapid collapse that generates a very high impact on rigid surfaces. This is the phenomenon that gives rise to surface damage in cavitation and underwater explosions. Experimentation has shown that when a bubble collapses near a rigid surface, a high speed water jet is developed from the side of the bubble further away from the rigid boundary. The jet pierces the bubble and impinges itself normally on the rigid surface [Gibson (1968), Lauterborn (1980), Wong *et al.* (1989) and Soh and Yu (1992)]. In the case of cavitation, the continuous impingement of the jet will eventually produce fatigue cracks in the surface and thus facilitate corrosion and destruction of the surface.

Computer models of the growth and collapse of a vapour cavity bubble will complement experimental studies by providing information that eludes direct physical observations.

In this chapter the dynamics of a bubble in the vicinity of a rigid boundary is investigated in the cases of

- a bubble which contains constant pressure vapour;
- a bubble which contains a mixture of constant pressure vapour and ideal gas;
- a bubble which contains vapour and which includes energy transfer arising from latent heat; and
- a bubble which contains ideal gas with different polytropic indices.

Necking phenomenon which occurs under some conditions and splits the vapour bubble into two parts is analysed and discussed in detail.

5.2 GEOMETRICAL DEFINITION

As it is shown in Figure 5.1 the bubble is located in the liquid domain in the vicinity of a rigid boundary. The problem is assumed to be axisymmetric while r and z are the radial and vertical axes of the cylindrical polar coordinates respectively. The radial axis is laid on the rigid boundary while the vertical axis is directed upward opposite to the direction of the gravity acceleration. Thus a bubble with positive values of z is located above the rigid boundary, whereas negative values of z indicate that the bubble is located below the rigid boundary. In Figure 5.1 S represents the surface of the bubble, n is the unit normal vector directed inside the bubble outward to the liquid domain and g is the gravity acceleration.

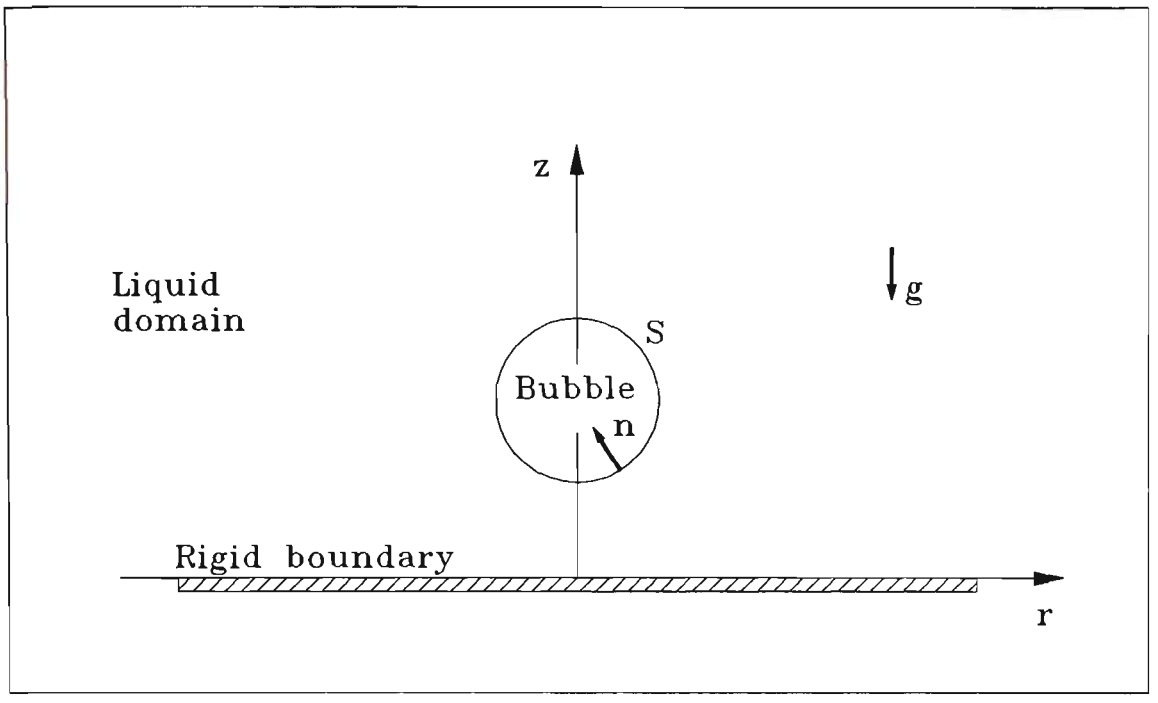

Figure 5.1 Geometrical definition for a bubble pulsating near a rigid boundary.

5.3 NON-DIMENSIONALISING

By employing the basic parameters which are defined in *Section (4.10)*, the non-dimensional form of cylindrical polar coordinates, bubble radius, time, velocity potential and velocity are introduced respectively as

$$r = \frac{r}{R_m}, \tag{5.1}$$

$$z = \frac{z}{R_m}, \tag{5.2}$$

$$R = \frac{R}{R_m}, \tag{5.3}$$

$$t = \frac{t}{R_m}\left(\frac{P_\infty - P_c}{\rho}\right)^{\frac{1}{2}}, \tag{5.4}$$

$$\Phi = \frac{\phi}{R_m}\left(\frac{\rho}{P_\infty - P_c}\right)^{\frac{1}{2}}, \tag{5.5}$$

$$\Psi = \psi\left(\frac{\rho}{P_\infty - P_c}\right)^{\frac{1}{2}}. \tag{5.6}$$

5.4 CONSTANT PRESSURE VAPOUR BUBBLE GROWING FROM AN INITIALLY MINIMUM VOLUME

The initial potential on the surface of a constant pressure vapour bubble in its minimum volume with small radius R_0 can be obtained from the Rayleigh bubble solution which is appropriately modified because of a flat rigid boundary in its neighbourhood [Taib (1985)]:

$$\phi_0(R_0, t_0) = \phi_0^R(R_0, t_0)\left(1 + \frac{R_0}{\left[(z+h)^2 + r^2\right]^{\frac{1}{2}}}\right), \tag{5.7}$$

where r and z indicate the coordinates of the bubble surface and h represents the distance of the bubble centroid from the rigid boundary. It should be noted that in Equation (5.7) $\phi_0^R(R_0, t_0)$ indicates the initial velocity potential over the surface of an isolated bubble which is given by Equation (4.1) and t_0 is the initial time that a constant pressure vapour bubble takes to grow from inception to radius R_0 and may be determined by Equation (4.2).

5.5 BUBBLE CONTAINS A MIXTURE OF CONSTANT PRESSURE VAPOUR AND IDEAL GAS

In contrast with the assumption made for the constant pressure vapour bubble that exerts a constant pressure inside the bubble throughout its lifetime, in this case it is assumed that the bubble contains a mixture of constant pressure vapour and ideal gas. This case can occur in an underwater explosion bubble which contains both vapour and the remnants of detonation which are non-condensable gases.

It is supposed that the gaseous remnants of a detonation can be described as ideal gases, and that on the time scale of the bubble oscillation the heat exchange with the surrounding liquid is negligible [see Best, (1991)]. Thus the expansions and compressions of the gaseous remnants of a detonation are assumed to be adiabatic. Herring (1949) has discussed this aspect of an explosion bubble and demonstrates that the heat transfer from the bubble to the surrounding liquid over the period of oscillation(s) of the bubble is negligible in comparison with the internal energy of the bubble contents.

By considering the gaseous contents of the bubble as an ideal gas, the partial pressure inside the bubble due to the existence the ideal gas is evaluated by:

$$P_g = P_{ig}\left(\frac{V_i}{V}\right)^k, \tag{5.8}$$

where P_g is the pressure due to the ideal gas inside the bubble during its pulsation, P_{ig} is the initial partial pressure of the ideal gas inside the bubble and V_i is the initial volume of the bubble. For a diatomic gas (air) which undergoes an isentropic process, the ratio of specific heats, k, is 1.4. It is supposed that the bubble produced by a high local energy input also contains saturated liquid

vapour with a constant vapour pressure. Thus the total pressure inside the bubble, P_b, is given by:

$$P_b = P_c + P_g, \tag{5.9}$$

or

$$P_b = P_c + P_{ig}\left(\frac{V_i}{V}\right)^k, \tag{5.10}$$

where P_c is the saturated vapour pressure of the liquid.

5.5.1 Evaluating the initial conditions for a bubble which contains a mixture of constant pressure vapour and ideal gas

Consider a bubble generated by a high local energy input in its minimum volume with a small radius, R_0. It contains highly compressed detonation products and has a high initial pressure P_i, which drives the motion, in addition to any initial radial velocity that may be imposed upon the system. According to Best (1991) such a situation inside the initial minimum volume of an explosion bubble provides the option of choosing a multitude of combinations of initial pressure and radial velocity, in addition with the assumption that the bubble is initially spherical. To obtain the initial conditions of an explosion bubble the equation which describes the motion of a spherical bubble with a constant vapour pressure inside [Rayleigh (1917)] is considered

$$R\ddot{R} + \frac{3}{2}\dot{R}^2 + \frac{\Delta P}{\rho} = 0, \tag{5.11}$$

where

$$\Delta P = P_\infty - P_c, \tag{5.12}$$

and R is the radius of the bubble, while dots denote time derivatives. Equation (5.11), which describes the purely radial motion of the bubble, is applied to the initial stages of an explosion bubble which contains a mixture of constant pressure vapour and ideal gas. The result is

$$R\ddot{R} + \frac{3}{2}\dot{R}^2 + \frac{\left(P_\infty - P_g - P_c\right)}{\rho} = 0. \tag{5.13}$$

By imposing the basic parameters which are defined for the non-dimensionalising of the solution, Equation (5.13) becomes [see *Section (5.3)*]:

$$R\ddot{R} + \frac{3}{2}\dot{R}^2 + 1 - \varepsilon\left(\frac{R_0}{R}\right)^{3k} = 0 \tag{5.14}$$

where $\varepsilon = \frac{P_{ig}}{\Delta P}$, termed the strength parameter, is a measure of the strength of the initial high pressure inside the bubble which drives the motion [Best (1991)].

Equation (5.14) describes the oscillatory motion of the bubble by assuming a non-zero radial velocity and imposing it on to the Equation (5.14) and integrating it backwards with respect to time. A new initial radius and pressure inside the bubble is obtained corresponding to a zero initial radial velocity on the surface of the bubble. Except in the case of very small amplitude radial oscillations, the initial non-zero velocity can be assumed in such a way that the time over which the above mentioned backwards integration must take place is negligible in comparison with the period of the oscillation. Thus the motion over the time of backward integration is little influenced by the presence of the rigid boundary. Therefore the initial conditions of a rebounding bubble produced by a high local energy input with an initial zero radial velocity and consequently an initial

velocity potential taken to be zero on its surface and a very high pressure inside, can be obtained by the backwards integration of Equation (5.14).

Integrating of Equation (5.14) results in:

$$\dot{R}^2 = \frac{2\varepsilon R_0^{3k}}{3(k-1)}\left(R^{-3} - R^{-3k}\right) + \frac{2}{3}\left(R^{-3} - 1\right), \qquad (5.15)$$

where $\dot{R}^2 = 0$ at $R = 1$ [see Best (1991)].

As it is mentioned above $\dot{R}$ is equal to zero at the initial volume of the bubble with the radius R_0, thus Equation (5.15) provides an equation for R_0 which can be solved by using Newton's method. From Equation (5.15) it is obvious that the value of the initial radius of the bubble is dependent upon the value of the strength parameter, ε, and with every specified value of the strength parameter a corresponding initial radius can be obtained. The values of the strength parameter and the corresponding initial radius of the bubble, determined by Equation (5.11), is given in Table 5.1.

Table 5.1 Values of the strength parameters and the corresponding initial radius of the bubble which are determined by Equation (5.11) for $k = 1.4$.

ε	R_0
10	0.3804
15	0.3266
20	0.2936
25	0.2706
30	0.2532
35	0.2392
40	0.2283
45	0.2189
50	0.2108
100	0.1651
200	0.1297
500	0.0947
1000	0.0748
2000	0.0591

5.6 VAPOUR BUBBLE

As discussed in *Section (4.4)*, in this case the bubble contains vapour and undergoes energy transfer arising from vaporisation and condensation. The pressure inside the vapour bubble during its pulsation is determined by a semi-empirical approach by using the First Law of Thermodynamics for a control mass and properties of the vapour-liquid from steam tables. The details of the thermodynamic process inside a vapour bubble is explained in *Section (4.4)*.

5.7 THE HYDRODYNAMIC EQUATION

For a bubble near a rigid surface an image bubble is considered with respect to the rigid boundary. This configuration results in zero normal velocity along the rigid surface and consequently models the dynamics of a bubble near a rigid boundary. Thus the Green's integral formula, Equation (3.3) which governs the hydrodynamics of the liquid domain, in the case of a bubble near a rigid boundary becomes:

$$C(p)\phi(p)+\int_S \phi(q)\frac{\partial}{\partial n}\left[\frac{1}{|p-q|}+\frac{1}{|p-q'|}\right]dS = \int_S \frac{\partial}{\partial n}[\phi(q)]\left(\frac{1}{|p-q|}+\frac{1}{|p-q'|}\right)dS \quad , \tag{5.16}$$

where S is the surface of bubble, p is any given point in the liquid domain, q is a point on S and q' is a point on the surface of the image of the bubble with respect to the rigid boundary.

The kinematic condition on the surface of the bubble is derived from the fact that the fluid particles remain on it. By taking the velocity of these particles as being equal to the velocity of the fluid and by using a Lagrangian description for these particles to specify the evolution of the bubble, the radial and vertical velocities of every point in the liquid domain and its boundaries are given by

$$u = \frac{\partial \phi}{\partial r}, \quad v = \frac{\partial \phi}{\partial z}. \tag{5.17}$$

The dynamic condition on the surface of the bubble is obtained by equating the dynamic pressure to the pressure inside the bubble. Then in the case of a constant pressure vapour bubble it can be shown that

$$P_c = P_\infty + \rho g z - \rho \frac{\partial \phi}{\partial t} - \frac{1}{2}\rho \left| \nabla \phi \right|^2. \tag{5.18}$$

where P_∞ is the pressure of the liquid domain at infinity and P_c is the constant pressure inside the bubble.

The non-dimensional form of Equation (5.18) can be written as

$$\frac{\partial \phi}{\partial t} = 1 + \delta^2 (z - \gamma) - \frac{1}{2} \left| \nabla \phi \right|^2, \tag{5.19}$$

where

$$\delta^2 = \frac{\rho g R_m}{P_\infty - P_c}, \tag{5.20}$$

and

$$\gamma = \frac{h}{R_m}, \tag{5.21}$$

where h is the initial distance of the bubble centroid from the rigid boundary. The non-dimensional parameters γ and δ determine the initial location of the bubble and the relative importance of the buoyancy forces respectively.

From the physical point of view δ corresponds to the ratio of the half-life of the bubble to the time that a bubble of radius R_m takes to rise the distance of one radius from rest due to buoyancy forces [see Blake *et al.* (1986)].

From Equation (5.18) the unsteady Bernoulli equation, in Lagrangian form, becomes

$$\frac{D\phi}{Dt} = \frac{P_\infty - P_c}{\rho} + \frac{1}{2}|\nabla\phi|^2 + g(z-h). \tag{5.22}$$

From Equation (5.19) the non-dimensional Lagrangian expression for the unsteady Bernoulli Equation becomes

$$\frac{D\Phi}{Dt} = 1 + \frac{1}{2}|\nabla\Phi|^2 + \delta^2(z-\gamma). \tag{5.23}$$

It is obvious that in the case of the pressure inside the bubble changing by the variation of the bubble volume, Equations (5.22) and (5.23) can be written respectively as

$$\frac{D\phi}{Dt} = \frac{P_\infty - P_V}{\rho} + \frac{1}{2}|\nabla\phi|^2 + g(z-h), \tag{5.24}$$

and

$$\frac{D\Phi}{Dt} = \frac{P_\infty - P_V}{P_\infty - P_c} + \frac{1}{2}|\nabla\Phi|^2 + \delta^2(z-\gamma), \tag{5.25}$$

where P_V is the pressure inside the bubble.

Equation (5.16) together with Equation (5.22) or Equation (5.24) form the basis of the boundary integral method used to simulate the dynamics of a bubble near a rigid boundary.

5.8 DISCRETIZED APPROXIMATION

Consider an axisymmetrical bubble as shown in Figure 5.2.

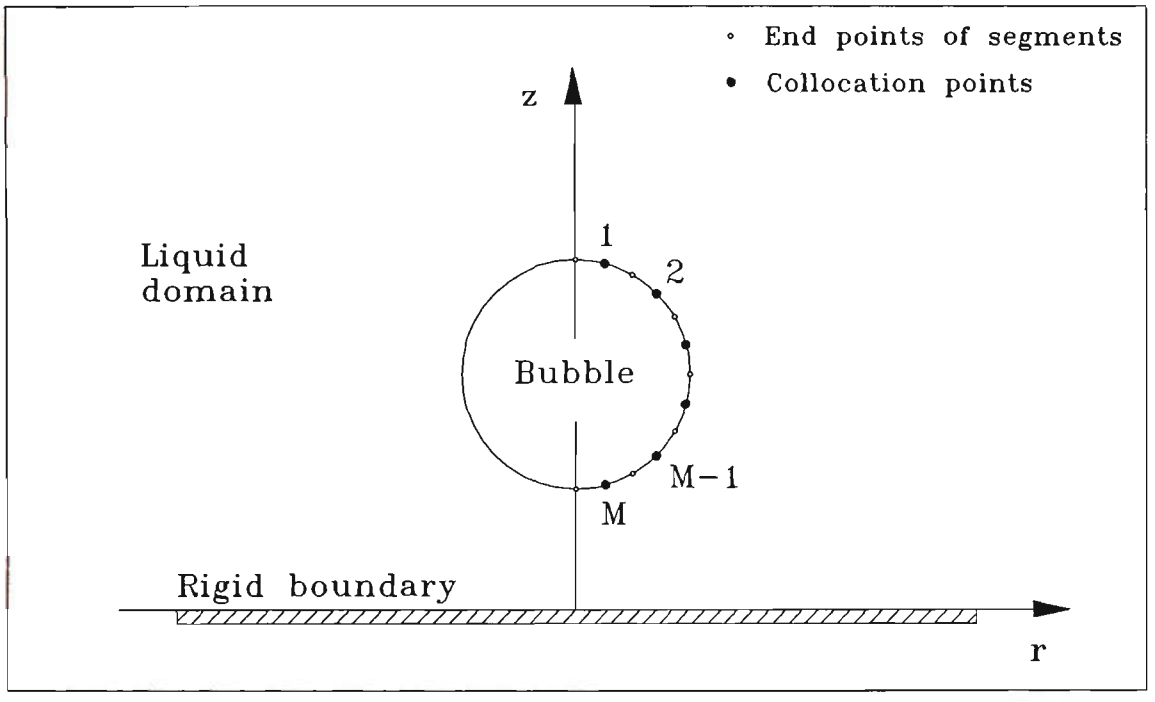

Figure 5.2 Discretization of the surface of a bubble near a rigid boundary

The surface of the bubble is discretized into M segments that are cut along planes normal to the axis of symmetry. To overcome the non-smooth nature of the piecewise linear interpolation, cubic splines are employed to approximate the surface of the bubble. Velocity potentials over the bubble surface are assumed to

be constant over each element and are located at the midpoint of elements. More details of the numerical implementation of the cubic spline approximation is discussed in *Chapter three*. Let S_j represent the j_{th} segment. Then for a point P_i on the surface of the bubble, the discretized form of Equation (5.16) is given by

$$2\pi\phi(p_i)+\sum_{j=1}^{M}\left\{\phi(q_j)\int_{S_j}\frac{\partial}{\partial n}\left[\frac{1}{|p_i-q_j|}+\frac{1}{|p_i-q_j'|}\right]dS\right\}=$$
$$\sum_{j=1}^{M}\left\{\frac{\partial}{\partial n}[\phi(q_j)]\int_{S_j}\left(\frac{1}{|p_i-q_j|}+\frac{1}{|p_i-q_j'|}\right)dS\right\}. \quad (5.26)$$

The surface integrations are carried out analytically where p, chosen as a collocation point, is located at the middle of the i_{th} segment. The term $\frac{\partial \phi}{\partial n}$ is the velocity component normal to the surface of the bubble and is denoted by ψ. It should be noted that ψ is positive when it is directed into the bubble. Thus, Equation (5.26) becomes a system of linear equations in the form of

$$2\pi\phi(p_i)+\sum_{j=1}^{M}H_{ij}\phi(q_j)=\sum_{j=1}^{M}G_{ij}\psi(q_j), \quad (5.27)$$

where H_{ij} and G_{ij} are the terms of integration in Equation (5.26) which are integrated over each segment. Thus H_{ij} and G_{ij} in the case of a bubble near a rigid boundary by considering an image of the bubble reflected about the rigid boundary, are

$$H_{ij}=\int_{S_j}\frac{\partial}{\partial n}\left[\frac{1}{|p_i-q_j|}+\frac{1}{|p_i-q_j'|}\right]dS, \quad (5.28a)$$

and

$$G_{ij} = \int_{Sj} \left(\frac{1}{|p_i - q_j|} + \frac{1}{|p_i - q_j'|} \right) dS. \tag{5.28b}$$

From a given distribution of velocity potential ϕ, the normal velocity ψ on the bubble surface is evaluated from Equation (5.27).

The tangential velocity, η, may be determined by Equation (3.31).

As discussed in Section (4.8), in the case of a rebounding bubble, the rebound instant of the bubble occurs during a large variation of normal velocity in an extremely short period of time. Thus in order to capture the rebound instant of a rebounding bubble near a rigid boundary the second order Runge-Kutta method is employed as the integration scheme.

The implementation of the second order Runge-Kutta integration is as follows. At time t the collocation point is represented by a vector p_i with cylindrical polar coordinates of r_i and z_i. The velocity potential at time t is represented by ϕ_i. Then by solving Equation (5.27) the fluid velocity at the collocation points ψ_i are determined. By denoting the radial and vertical components of the fluid velocity as (u_{i1}, v_{i1}) and the time derivative of the velocity potential as $\left[\frac{\partial \phi}{\partial t}\right]_{i1}$ the intermediate bubble geometry and the intermediate distribution of the velocity potential over the bubble surface can be written as:

$$r_{i1} = r_i(t) + u_{i1}\Delta t, \tag{5.29}$$

$$z_{i1} = z_i(t) + v_{i1}\Delta t, \tag{5.30}$$

$$\phi_{i1} = \phi_i(t) + \left[\frac{\partial \phi}{\partial t}\right]_{i1} \Delta t. \tag{5.31}$$

Equation (5.27) is solved for the intermediate geometry of the bubble and the intermediate distribution of the velocity potential over the bubble surface. Then the intermediate velocity on the bubble surface $(u_{i2},\ v_{i2})$ and the intermediate derivative of the velocity potential $\left[\frac{\partial\phi}{\partial t}\right]_{i2}$ are obtained. The evolved shape of the bubble and the distribution of the velocity potential over its surface at time $t+\Delta t$ are given by

$$r_i(t+\Delta t) = r_i(t) + \frac{1}{2}(u_{i1} + u_{i2})\Delta t + O(\Delta t^2), \tag{5.32}$$

$$z_i(t+\Delta t) = z_i(t) + \frac{1}{2}(v_{i1} + v_{i2})\Delta t + O(\Delta t^2), \tag{5.33}$$

$$\phi_i(t+\Delta t) = \phi_i(t) + \frac{1}{2}\left(\left[\frac{\partial\phi}{\partial t}\right]_{i1} + \left[\frac{\partial\phi}{\partial t}\right]_{i2}\right)\Delta t + O(\Delta t^2). \tag{5.34}$$

It should be noted that the velocity vectors (u_i, v_i), along the direction of r and z are derived from the velocity components that are normal to the bubble surface, ψ_i, and tangential to it, η_i

As discussed in *Chapter four* the discretized approximation of Equation (4.6) which governs the thermodynamic process in a vapour bubble is given by Equations (4.13), (4.14) and (4.15).

5.9 REDISCRETIZATION OF THE BOUNDARY

Since the bubble undergoes uneven deformation, the highly stretched elements on the bubble will eventually grow comparatively large and hence result in a loss of accuracy. A more serious problem with numerical stability is associated with the highly stretched elements that represent an integral with a $\frac{1}{r}$ kernel, as in

Equation (5.16). A method to overcome this problem is to rediscretize the elements into equal size. The length along the profile of the bubble is made a parameter for the velocity potential, ϕ_i and the coordinates of the collocation points p_i. The surface of the bubble is rediscretized into segments of equal size, Δl. In other words, the length parameter for the new sets of ϕ_i and p_i will be $i\Delta l$. The values for ϕ_i and p_i for the rediscretized elements are obtained by interpolation from the corresponding values that are associated with the original set of elements. Details of this process are reported by Fink and Soh (1978).

5.10 COMPUTATIONAL IMPLEMENTATION

Computations are initiated when the bubble grows from a finite but small volume. Initially the bubble has a radius, R_0, and has its centroid located at a distance h from the rigid surface. The initial velocity potential over the bubble surface is determined in such a way that the bubble will expand to a maximum volume having a non-dimensional radius of unity.

The computation begins from a small spherical bubble in which the velocity potential is known on its surface. The normal velocity, ψ, found by solving the system of equations in Equation (5.27). The tangential velocity, also initially zero, is calculated from numerical differentiation of the velocity potential, ϕ, along the surface of the bubble.

The time step, Δt, is determined by equation:

$$\Delta t = \min_i \left| \frac{\Delta\phi}{\frac{P_\infty - P_c}{\rho} + \frac{1}{2}(\psi_i^2 + \eta_i^2) + g(z_i - h)} \right|, \qquad (5.35)$$

where $\Delta\phi$ is an assigned constant which limits the velocity potential increment in each time step.

The non-dimensional form of the Equation (5.35) becomes

$$\Delta t = \min_i \left| \frac{\Delta\Phi}{1+\frac{1}{2}\left|\nabla\Phi_i\right|^2 + \delta^2(z_i - \gamma)} \right|. \tag{5.36}$$

As discussed in *Section (4.9)*, Equation (5.35) is adequate for the case of a constant pressure vapour bubble and provides an accurate and stable solution by using a simple Euler scheme. But in the case of rebounding bubbles since the later stages of the collapse are accompanied by a very high pressure inside the bubble, a modified form of Equation (5.35) is employed giving a variable time step of

$$\Delta t = \min_i \left| \frac{\Delta\phi}{\frac{P_\infty + P_V}{\rho} + \frac{1}{2}(\psi_i^2 + \eta_i^2) + g(z_i - h)} \right|, \tag{5.37}$$

where P_V indicates the pressure inside the bubble.

The non-dimensional form of Equation (5.37) can be written as

$$\Delta t = \min_i \left| \frac{\Delta\Phi}{\frac{P_\infty + P_V}{P_\infty + P_c} + \frac{1}{2}\left|\nabla\Phi_i\right|^2 + \delta^2(z_i - \gamma)} \right|. \tag{5.38}$$

The rediscretization technique is applied to readjust the elements into equal size. This completes one loop of the computation.

5.11 NUMERICAL RESULTS AND DISCUSSION

A computational study on the pulsation of a bubble near a rigid boundary is now carried out using the boundary integral method in the case of

- a bubble containing constant pressure vapour;
- a bubble containing a mixture of constant pressure vapour and ideal gas;
- a bubble containing vapour which includes energy transfer arising from latent heat; and
- bubble containing an ideal gas with different polytropic indices of 1.0, 1.1, 1.2 and 1.4.

5.11.1 The growth and collapse of a constant pressure vapour bubble near a rigid boundary

In this section the dynamics of a constant pressure vapour bubble in the vicinity of a rigid boundary are investigated by applying the boundary integral method. The influence of the buoyancy forces are included. The positive values of γ indicate that the bubble is above the rigid boundary and the buoyancy forces act in the opposite direction to the Bjerknes attraction force towards the rigid boundary. The negative values of γ indicates that the bubble is below the rigid boundary and the buoyancy forces act in the direction of the attraction force of the rigid boundary.

Figure 5.3 illustrates the dynamics of a vapour bubble above a rigid boundary with $\gamma = 1.0$ and $\delta = 0.1808$. As it is shown in Figure 5.3(a) at the latest stages

of the bubble expansion, the bottom side of the bubble close to the rigid boundary is flattened. Figure 5.3(b) shows that the bubble during its collapse phase is elongated in the direction normal to the rigid surface and migrates towards the rigid boundary. A liquid jet developed in the latest stages of the bubble collapse is directed towards the rigid boundary and directly impinges upon the surface.

Figure 5.4 shows the growth and collapse of the bubble below the rigid boundary where the buoyancy forces act in the direction of the Bjerknes attraction force, and $\gamma = -1.0$ and $\delta = 0.1808$. In this case the time that the liquid jet takes to impinge upon the rigid boundary is less than in the case of buoyancy forces acting opposite to the attraction forces.

Figure 5.5 illustrates the bubble behaviour when it is initially located above the rigid boundary with $\gamma = 1.5$ and $\delta = 0.1808$. In this case the liquid jet penetrates the opposite side of the bubble before approaching the rigid boundary and there is no direct impingement of the liquid jet on the nearby surface. It is shown that the time for the collapse of a bubble further away from the rigid boundary is less than the time for the collapse of a bubble very close to the boundary.

Figure 5.6 illustrates the dynamics of a bubble below the rigid boundary with $\gamma = -1.5$ and $\delta = 0.1808$. In this case since buoyancy forces act in the direction of the Bjerknes force, the migration of the bubble boundary towards the rigid boundary is more pronounced than in the case of the bubble above the rigid surface, and the liquid jet is broader.

Figure 5.7 shows bubble shapes during the growth and collapse phases above a rigid boundary with $\gamma = 1.0$ and $\delta = 0.2557$. This figure shows that the strong buoyancy forces in the direction opposite to the attraction force of the rigid

boundary cause elongation of the bubble in the vertical direction normal to the rigid boundary and the development of a further narrower liquid jet.

Figures 5.8 and 5.9 show the bubble profiles during the growth and collapse of the bubble above a rigid boundary with strong buoyancy forces. In Figure 5.8 the bubble with $\gamma = 1.0$ and $\delta = 0.3132$ is elongated greatly during its collapse while in Figure 5.9 the bubble with $\gamma = 1.0$ and $\delta = 0.4610$ takes on a bulb shape during the latest stages of the collapse phase which is also reported by Blake *et al.* (1986).

Figure 5.10 illustrates the behaviour of the bubble below a rigid boundary with $\gamma = -1.0$ and $\delta = 0.4610$. Figure 5.10 shows that in contrast with the case of the bubble above the rigid boundary (Figure 5.9), strong buoyancy forces in the direction of the Bjerknes force can cause the development of a strong liquid jet directed toward the rigid boundary.

It should be noted that as shown in Figures 5.3, 5.4, 5.5, 5.6, 5.7 and 5.10 the development of the high speed liquid jet takes place over a very short period of time.

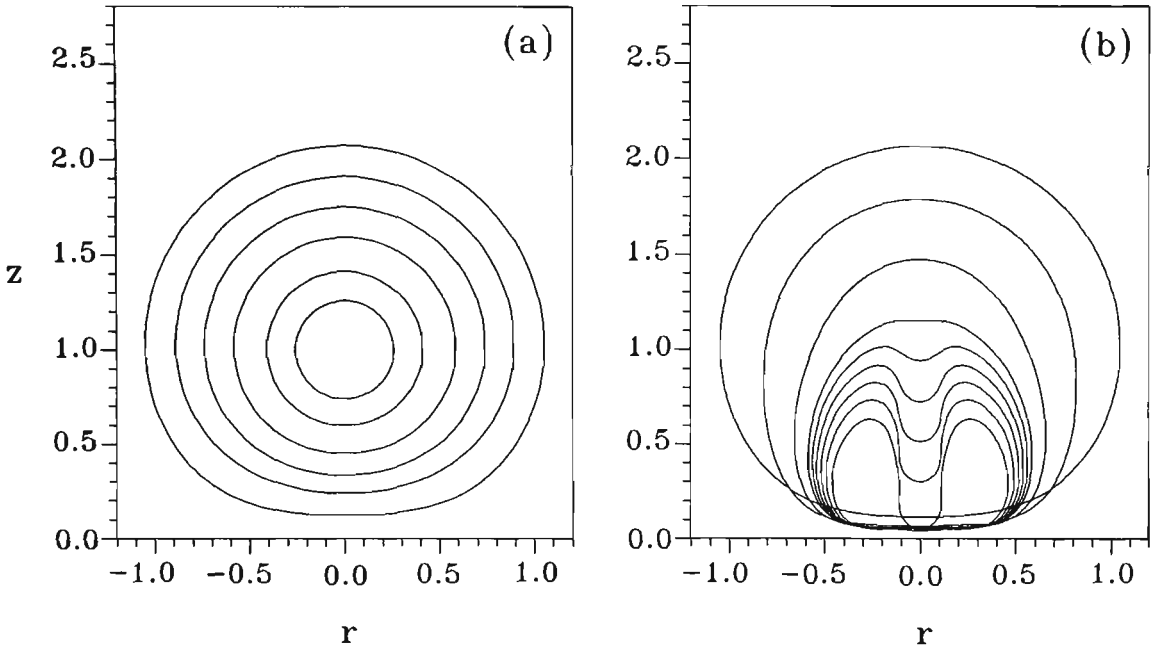

Figure 5.3 Bubble shapes for the growth (a) and collapse (b) of a constant pressure vapour bubble above a rigid boundary with $\gamma = 1.0$ and $\delta = 0.1808$. The non-dimensional times corresponding to bubble successive profiles are: (a) Growth phase: 0.0154 (innermost), 0.0487, 0.1238, 0.2403, 0.4311, 1.1154 (outermost). (b) Collapse phase: 1.1154 (outermost), 1.7825, 2.0154, 2.1067, 2.1308, 2.1517, 2.1717, 2.1922, 2.2155 (innermost).

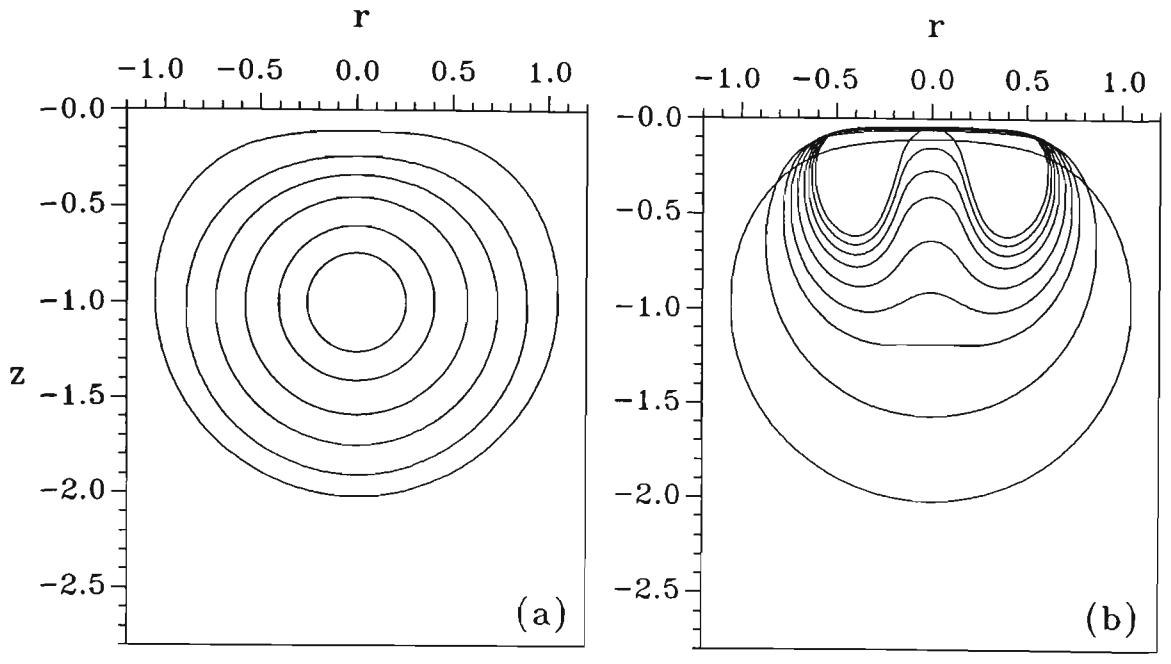

Figure 5.4 Bubble shapes for the growth (a) and collapse (b) of a constant pressure vapour bubble below a rigid boundary with $\gamma = -1.0$ and $\delta = 0.1808$. The non-dimensional times corresponding to bubble successive profiles are: (a) Growth phase: 0.0154 (innermost), 0.0484, 0.1228, 0.2387, 0.4317, 1.1135 (outermost). (b) Collapse phase: 1.1135 (outermost), 1.7927, 1.9671, 2.0312, 2.0802, 2.1216, 2.1463, 2.1671 , 2.1851 (innermost).

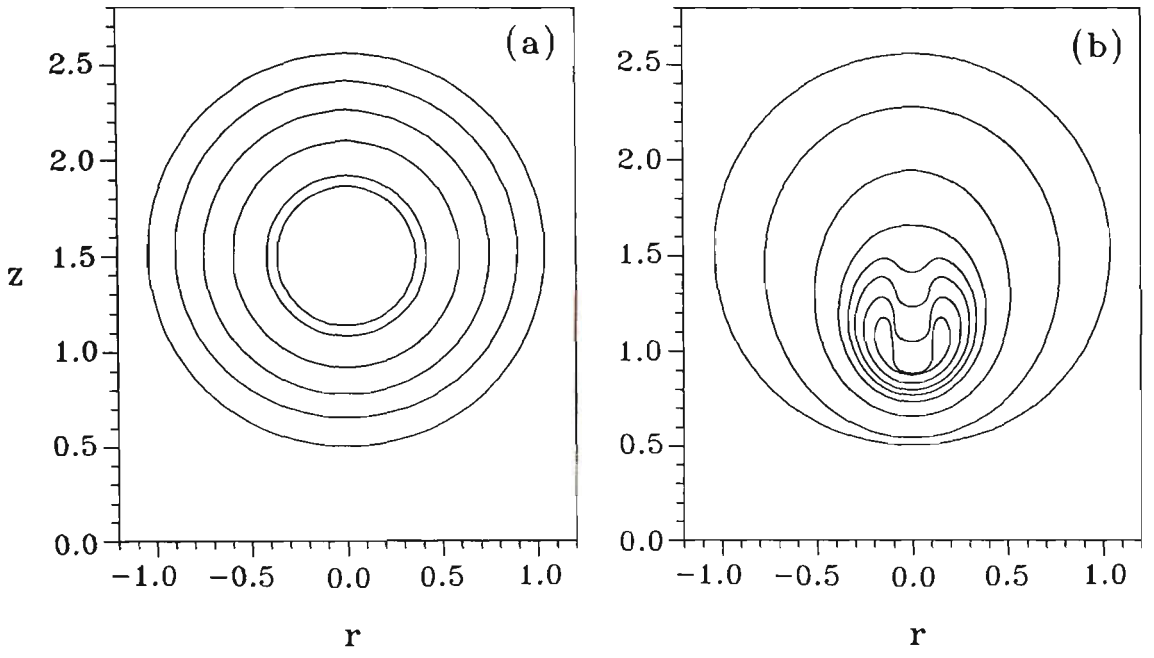

Figure 5.5 Bubble shapes for the growth (a) and collapse (b) of a constant pressure vapour bubble above a rigid boundary with $\gamma = 1.5$ and $\delta = 0.1808$. The non-dimensional times corresponding to bubble successive profiles are: (a) Growth phase: 0.0360 (innermost), 0.0520, 0.1287, 0.2486, 0.4435, 1.0782 (outermost). (b) Collapse phase: 1.0782 (outermost), 1.7785, 2.0146, 2.0868, 2.1066, 2.1186, 2.1306, 2.1412 (innermost).

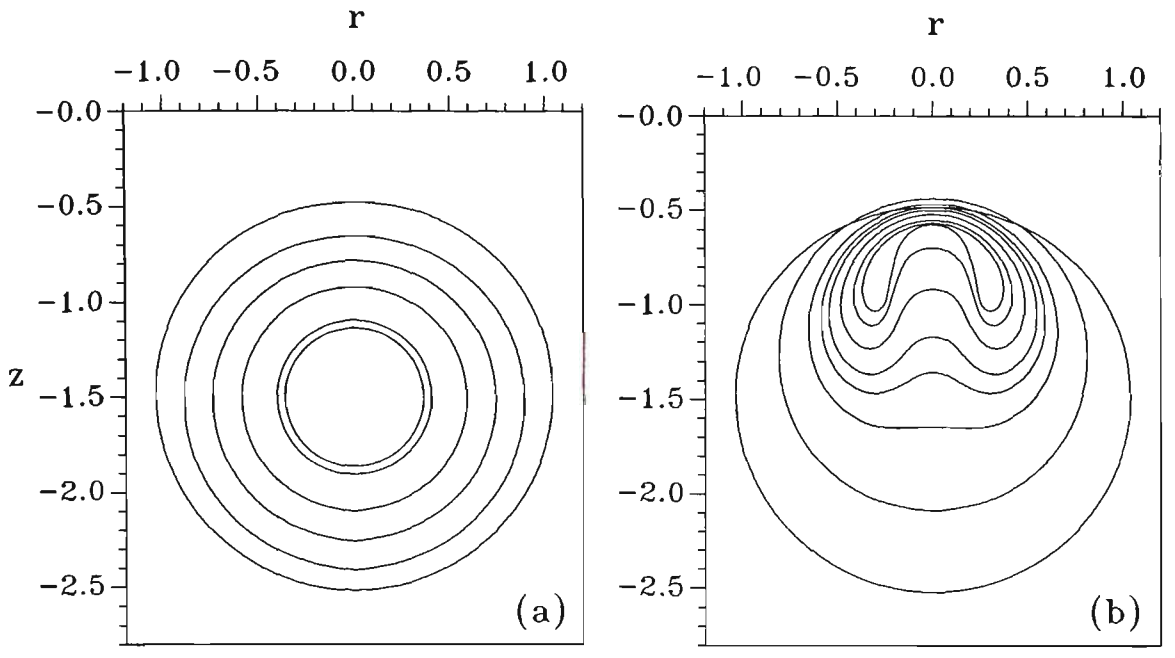

Figure 5.6 Bubble shapes for the growth (a) and collapse (b) of a constant pressure vapour bubble below a rigid boundary with $\gamma = -1.5$ and $\delta = 0.1808$. The non-dimensional times corresponding to bubble successive profiles are: (a) Growth phase: 0.0360 (innermost), 0.0473, 0.1264, 0.2417, 0.4339, 1.0679 (outermost). (b) Collapse phase: 1.0679 (outermost), 1.7790, 1.9644, 2.0217, 2.0155, 2.0533, 2.0879, 2.1066 (innermost).

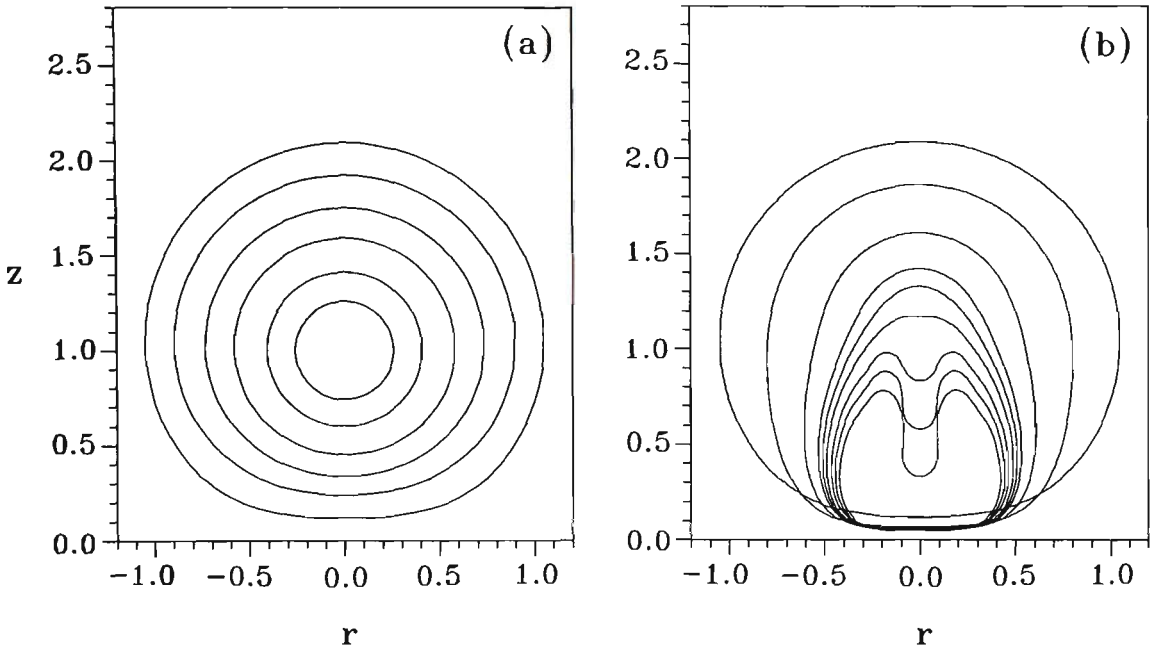

Figure 5.7 Bubble shapes for the growth (a) and collapse (b) of a constant pressure vapour bubble above a rigid boundary with $\gamma = 1.0$ and $\delta = 0.2557$. The non-dimensional times corresponding to bubble successive profiles are: (a) Growth phase: 0.0154 (innermost), 0.0484, 0.1220, 0.2350, 0.4417, 1.1090 (outermost). (b) Collapse phase: 1.1090 (outermost), 1.7853, 2.0205, 2.1017, 2.1314, 2.1516, 2.1713, 2.1858, 2.1922, 2.2028 (innermost).

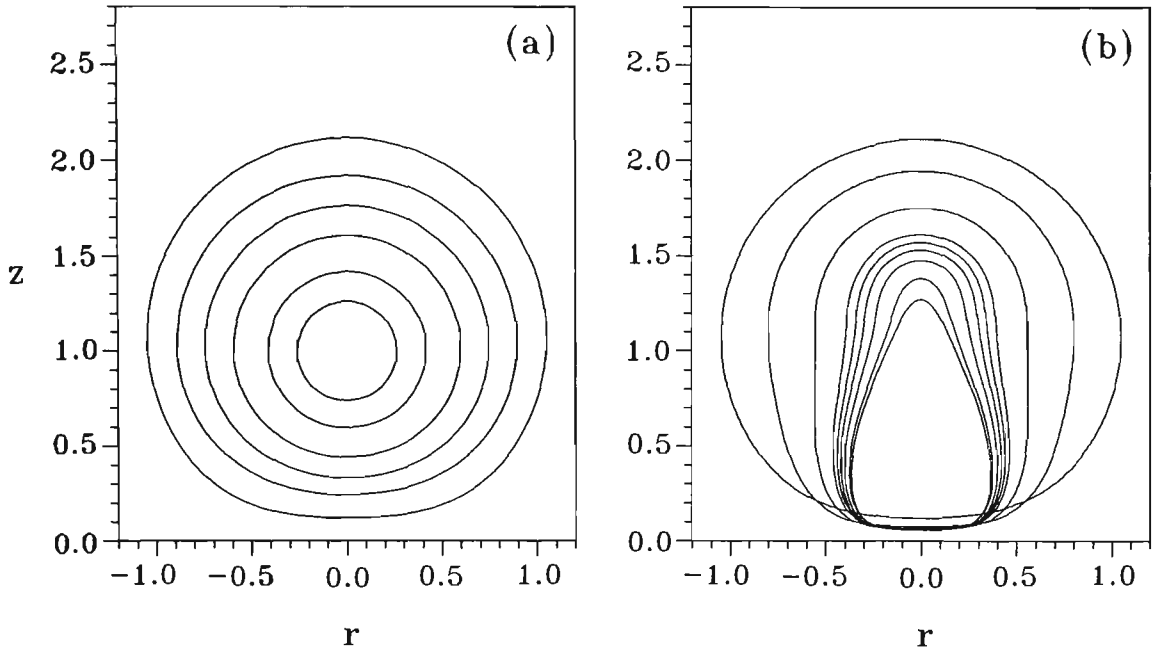

Figure 5.8 Bubble shapes for the growth (a) and collapse (b) of a constant pressure vapour bubble above a rigid boundary with $\gamma = 1.0$ and $\delta = 0.3132$. The non-dimensional times corresponding to bubble successive profiles are: (a) Growth phase: 0.0154 (innermost), 0.0488, 0.1281, 0.2412, 0.4279, 1.1157 (outermost). (b) Collapse phase: 1.1157 (outermost), 1.7740, 2.0136, 2.1121, 2.1343, 2.1518, 2.1708, 2.1921, 2.2008 (innermost).

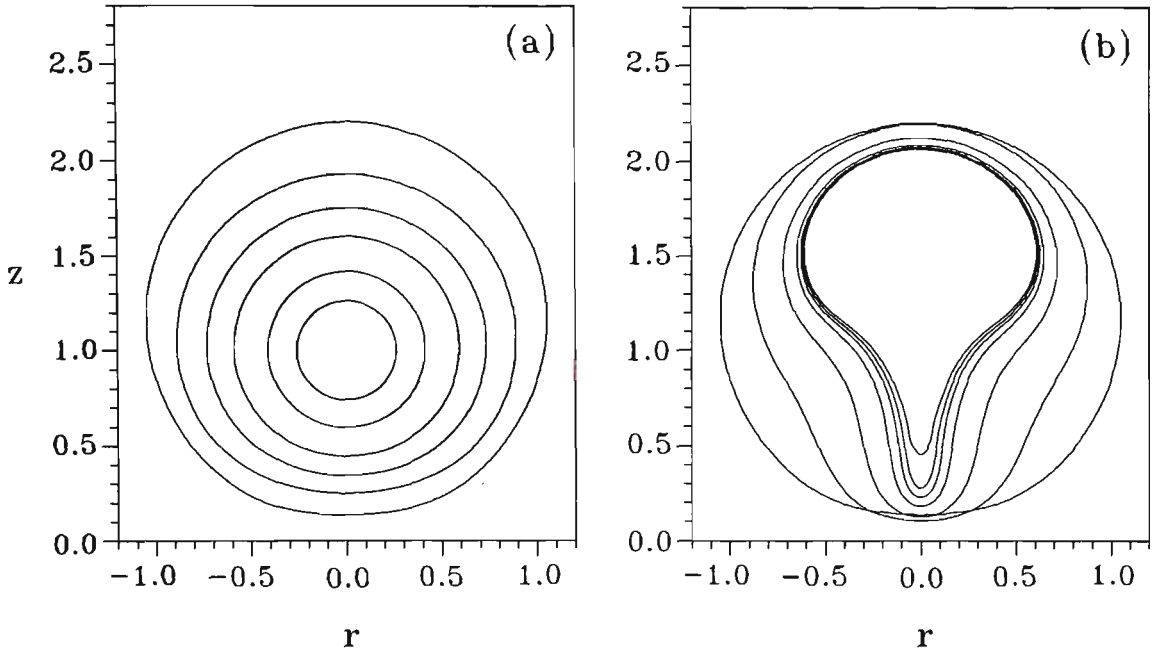

Figure 5.9 Bubble shapes for the growth (a) and collapse (b) of a constant pressure vapour bubble above a rigid boundary with $\gamma = 1.0$ and $\delta = 0.4610$. The non-dimensional times corresponding to bubble successive profiles are: (a) Growth phase: 0.0154 (innermost), 0.0486, 0.1256, 0.2316, 0.4271, 1.1511 (outermost). (b) Collapse phase: 1.1511 (outermost), 1.7690, 2.0233, 2.1113, 2.1358, 2.1518, 2.1632 (innermost).

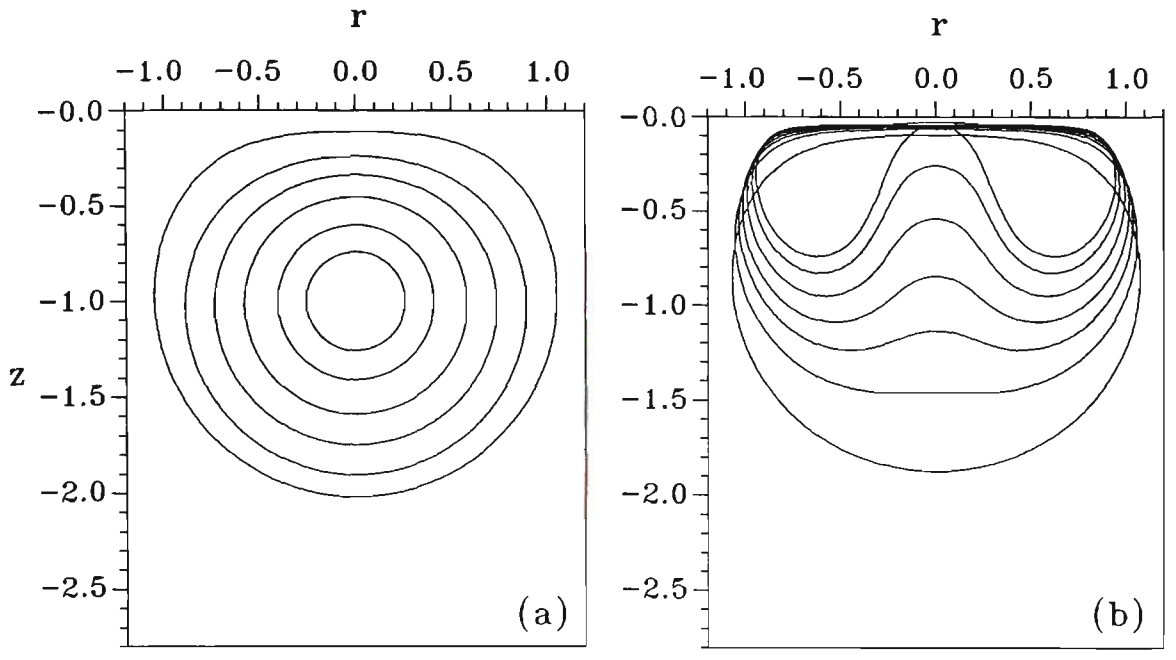

Figure 5.10 Bubble shapes for the growth (a) and collapse (b) of a constant pressure vapour bubble below a rigid boundary with $\gamma = -1.0$ and $\delta = 0.4610$. The non-dimensional times corresponding to bubble successive profiles are: (a) Growth phase: 0.0154 (innermost), 0.0482, 0.1209, 0.2334, 0.4231, 1.0956 (outermost). (b) Collapse phase: 1.0956 (outermost), 1.5214, 1.6832, 1.7913, 1.8944, 1.9871, 2.0553 (innermost).

Table 5.2 shows the direction of the liquid jet either towards the rigid boundary or away from it for a constant pressure vapour bubble collapsing near a rigid boundary with different values of γ and δ.

Table 5.2 Direction of the liquid jet or migration of the bubble in the case of a constant pressure vapour bubble above a rigid boundary

γ \ δ	0.1808	0.2557	0.2859	0.3132	0.4610
1.0	Liquid jet ↓	Liquid jet ↓	Liquid jet ↓	Migration downward ↓	Migration upward ↑
1.5	Liquid jet ↓	Migration downward ↓			
2.0	Liquid jet ↓	Liquid jet ↑	Liquid jet ↑		
2.5	Migration upward ↑				
3.0	Liquid jet ↑				

↓ Liquid jet directed towards the rigid boundary, ↑ Liquid jet directed away from the rigid boundary

Figure 5.11 illustrates that during the collapse of a constant pressure vapour bubble near a rigid boundary, the liquid jet is directed towards the rigid boundary in the cases of $\gamma\delta < 0.442$. The cases of $\gamma\delta > 0.442$ the liquid jet is directed away from the rigid boundary. Figure 5.11 indicates that the direction of the liquid jet, either towards the rigid boundary or away from it, is delineated by the critical value of $\gamma\delta = 0.442$ which was found and introduced by Blake and Ceron (1982) and Blake *et al.* (1986) for the null Kelvin-impulse. This delineation the direction of the liquid jet by the critical value of $\gamma\delta$ indicates the accuracy of the numerical technique which is employed in this research.

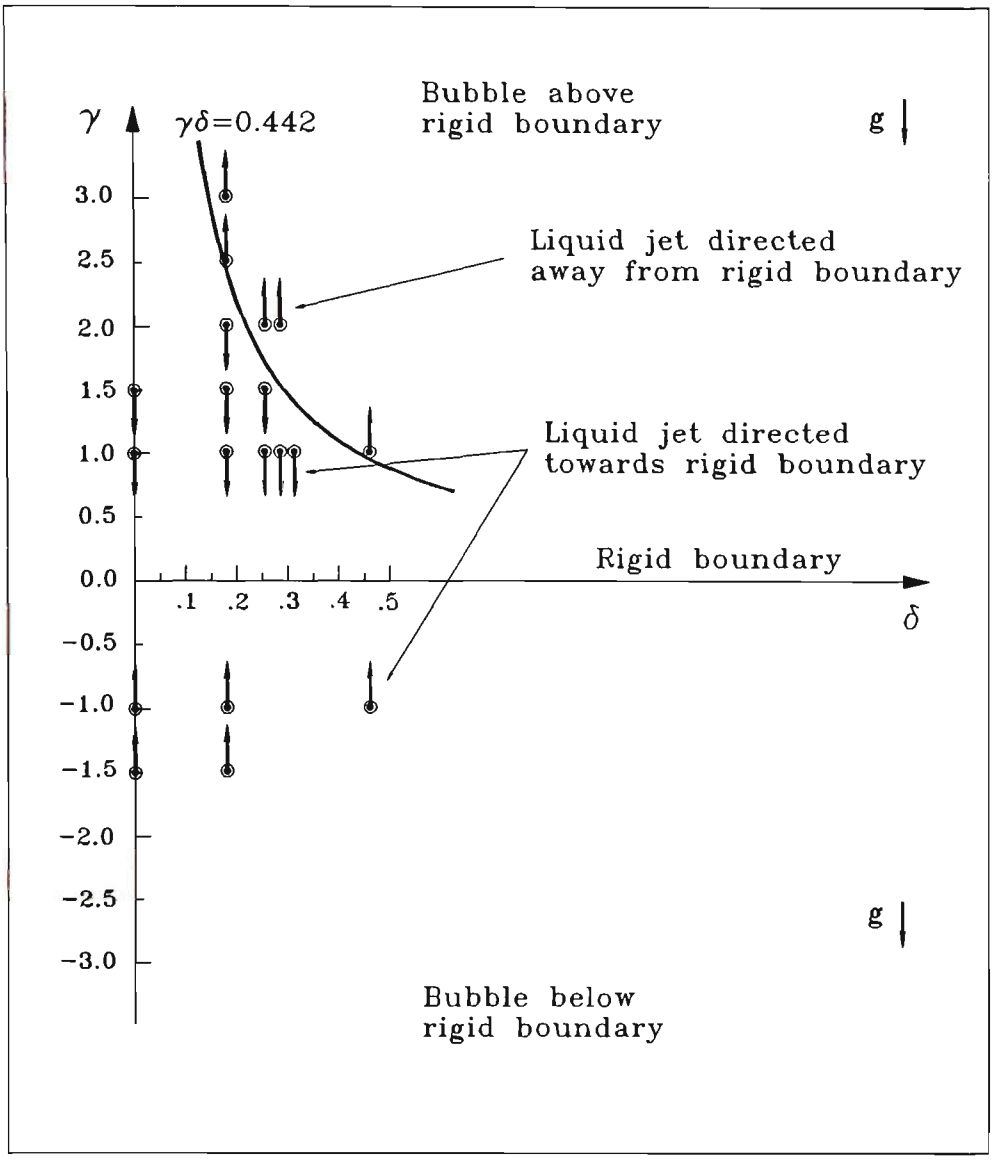

Figure 5.11 Graphical illustration of the direction of the liquid jet and the bubble migration in the case of a bubble near a rigid boundary for different values of γ and δ. The solid line represents the null Kelvin-impulse with $\gamma\delta = 0.442$.

These computational results have provided significant information on the dynamics of a constant pressure vapour bubble near a rigid boundary.

Figures 5.12(a) and (b) illustrate the collapse of a constant pressure vapour bubble from its initially spherical shape at maximum volume V_{max} in an infinite liquid domain and near a rigid boundary for the two different cases of $\gamma = 1.0$ and $\gamma = 1.5$ under the same initial conditions. In order to be able to examine the effect of the presence of a rigid boundary on the dynamics of the bubble, buoyancy forces are ignored $(\delta = 0)$. As shown in Figure 5.12(a), the collapse rate of an isolated bubble is higher than the collapse rate of a bubble near a rigid boundary. It can also be seen that the collapse rate of a bubble further away from the rigid boundary is higher than the collapse rate of a bubble located very close to the rigid boundary.

The corresponding velocity of the bubble wall in the case of an isolated bubble and velocity of the liquid jet in the case of a bubble near a rigid boundary are shown in Figure 5.12(b). This figure also shows that the radial velocity of the isolated bubble wall is higher than the velocity of the liquid jet for the case of the bubble near a rigid boundary. It is also shown that the velocity of the liquid jet in the case of a bubble further away from the rigid boundary is higher than the velocity of the liquid jet in the case of a bubble very close to the rigid boundary.

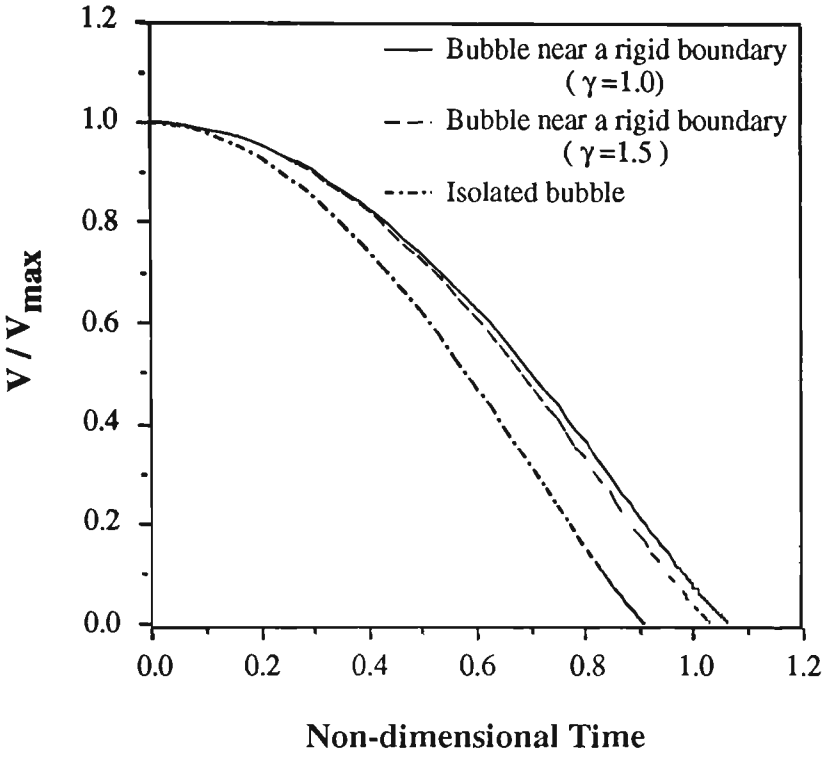

Figure 5.12(a) Collapse rate of an isolated bubble and a bubble near a rigid boundary in the cases of $\gamma = 1.0$ and $\gamma = 1.5$.

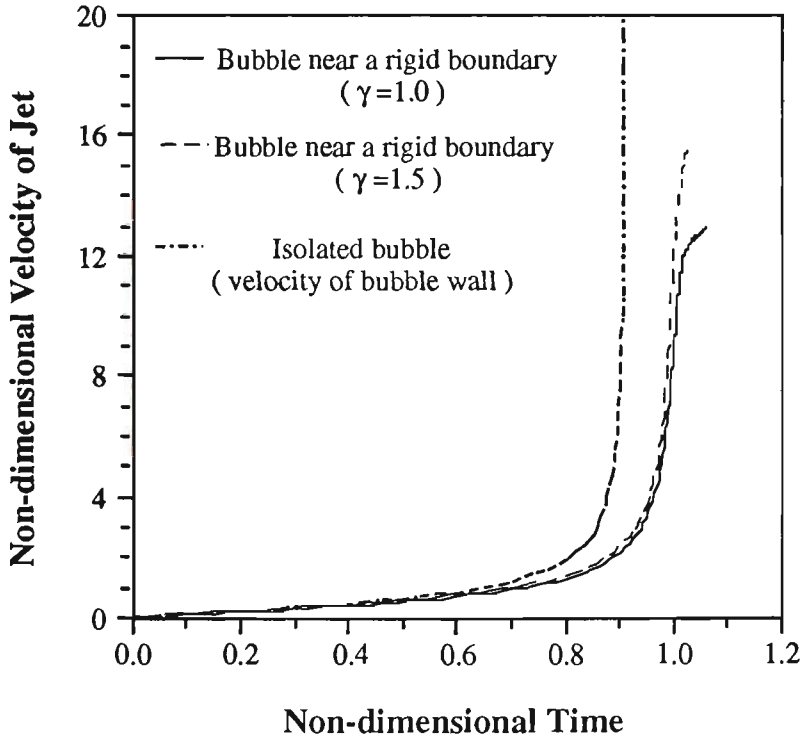

Figure 5.12(b) Velocity of an isolated bubble wall and velocity of the liquid jet for a bubble near a rigid boundary with $\gamma = 1.0$ and $\gamma = 1.5$.

Figures 5.13(a), (b), (c), and (d) illustrate the dynamic characteristics of two constant pressure vapour bubbles during their growth and collapse phases under the same initial conditions but with the two different values of $\gamma = 1.0$ and $\gamma = 1.5$.

Figure 5.13(a) shows the movement of the bubble centroid with respect to time during the growth and collapse of the bubbles. In this case the buoyancy forces are also ignored $(\delta = 0)$. It is shown that in the case of the bubble with $\gamma = 1.0$, the bubble centroid during the growth phase migrates away from the rigid boundary. However during the collapse phase the bubble centroid marginally migrates with increasing speed towards the rigid boundary. Figure 5.13(a) shows that this migration of the bubble centroid away from the rigid boundary decreases by increasing the initial distance of the bubble from the rigid boundary. The corresponding values of the liquid jet velocity is illustrated in Figure 5.13(b). It should be noted that the positive values of the velocity of the liquid jet indicate a velocity directed into the bubble. Negative values of the velocity of the liquid jet indicate a velocity directed outward from the bubble.

Figure 5.13(c) shows that the collapse rate of the bubble further away from the rigid surface is less than the collapse rate of the bubble located very close to the rigid boundary.

Figure 5.13(d) illustrates the pressure inside the liquid domain on the surface of the rigid boundary and at a given point $(r = 0,\ z = 0)$, which is denoted by P_{rozo}, during the growth and collapse of the bubble. It can be seen that the pressure on the rigid boundary at this point at the end of the collapse of the bubble with $\delta = 1.5$ is higher than in the case of the bubble with $\delta = 1.0$. It should be noted

that in the case of the bubble with $\delta = 1.0$, the liquid jet directly impinges upon the rigid surface. The water hammer pressure exerted by the impingement of the liquid jet would be extremely high. Therefore the destructive effect of the bubble collapse in the case of direct impingement of the liquid jet on the rigid boundary would be much higher than in the case of the no impingement of the liquid jet [see Gibson (1968) and Tomita and Shima (1986)]. Furthermore it should be noted that for $\delta = 1.0$ the bubble has not collapsed as far as the bubble with $\delta = 1.5$ which could account for the lower pressure on the rigid boundary. This is because of the earlier transformation of the bubble closer to the rigid boundary into a toroidal form, and thus termination of the computations. As the bubble collapses the pressure increases over a very short period of time, so the pressure on the rigid boundary may increase for the bubble with $\delta = 1.0$ if the bubble is allowed to collapse. The computational simulation of the bubble behaviour after its transformation into a toroidal form requires a special treatment [see Best (1991) and Zhang *et al.* (1993)].

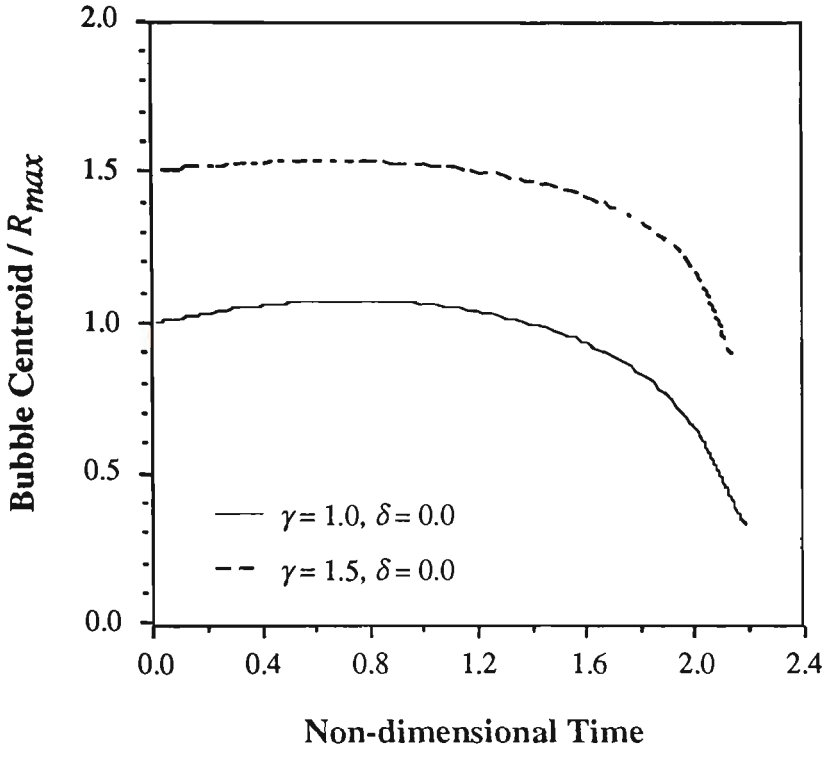

Figure 5.13(a) Migration of the bubble centroid near a rigid boundary

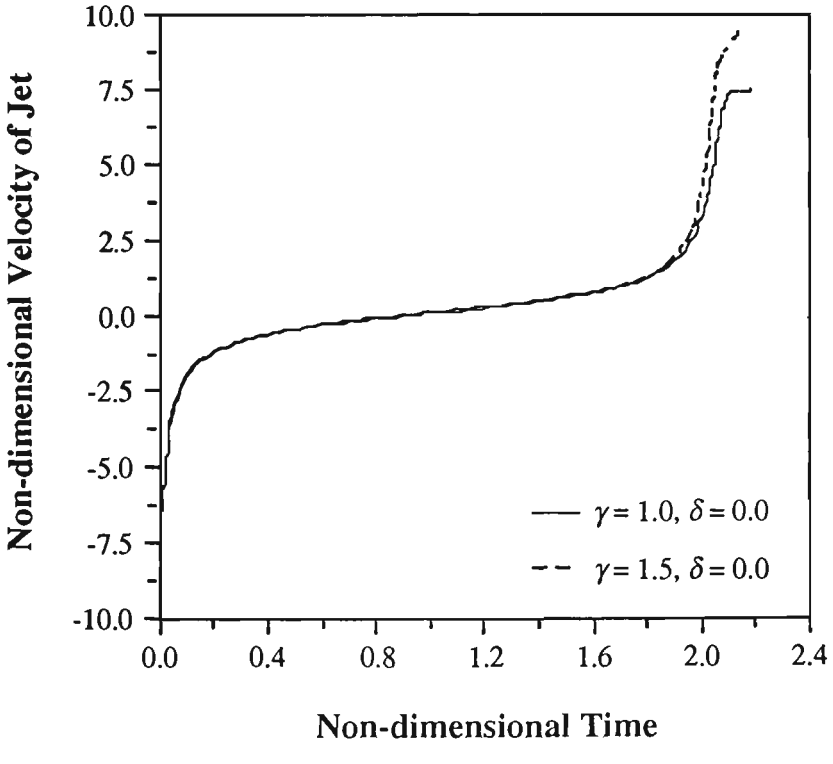

Figure 5.13(b) Velocity of the liquid jet

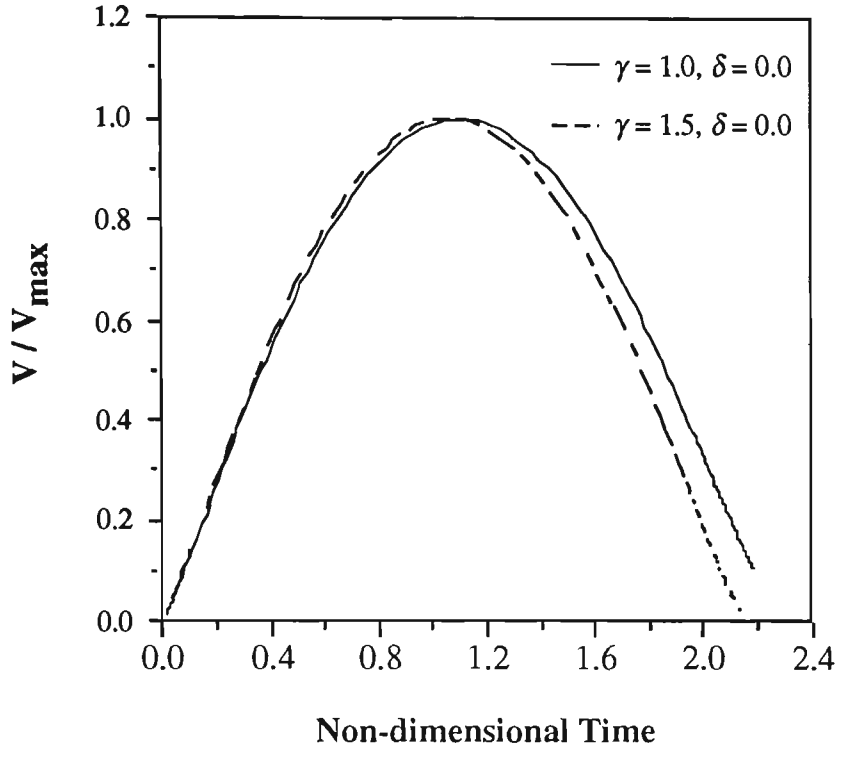

Figure 5.13(c) Variation of the bubble volume during its growth and collapse phases

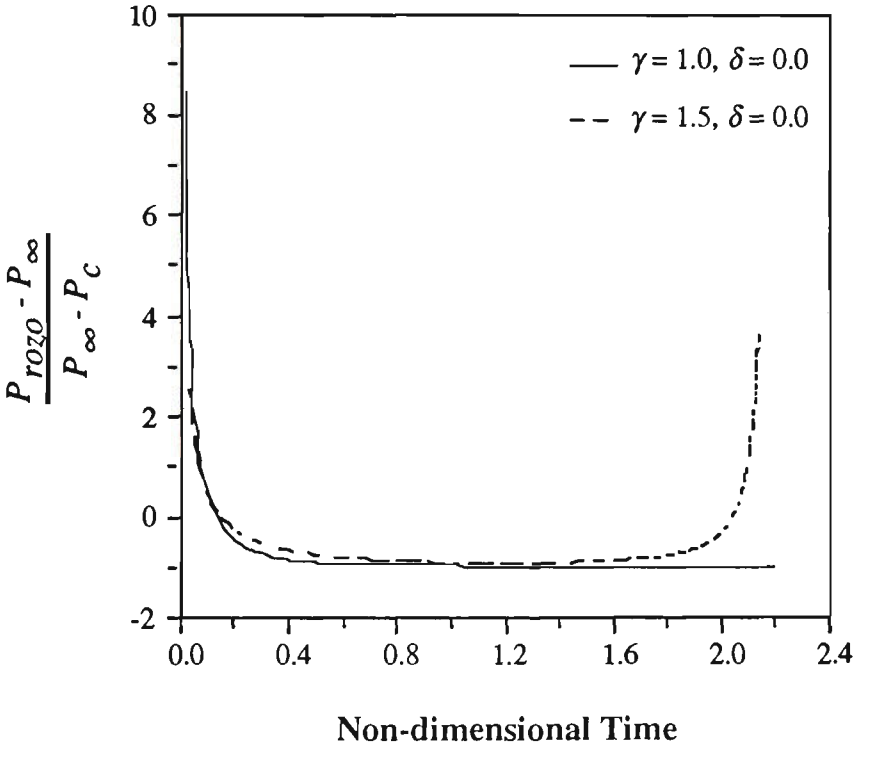

Figure 5.13(d) Pressure on the rigid boundary at $(r = 0, z = 0)$ during the growth and collapse of the bubble

Figures 14(a) and (b) indicate the effects of buoyancy forces on the dynamics of a constant pressure vapour bubble above a rigid boundary where buoyancy forces act in the opposite direction to the Bjerknes force. Figures 14(a) and (b) show the dynamic characteristics of the bubble corresponding to the bubble behaviour presented in Figures 5.3, 5.5, 5.7, 5.8 and 5.9 and the dynamic characters of a bubble with $\gamma = 0.0$ and $\delta = 1.0$.

Figure 14(a) illustrates the effect of the buoyancy forces on the migration of the bubble either towards the rigid boundary or away from it. It can be seen that the marginal movement of the bubble centroid away from the rigid boundary during the growth phase of the bubble increases by increasing the buoyancy forces. The figure also shows that in the case of higher buoyancy forces when the value of $\gamma\delta$ is greater than its critical value (0.442) for the null Kelvin-impulse, the bubble migrates away from the rigid boundary during its collapse phase. Figure 5.14(a) together with Figure 5.9 indicate that in the case of a bubble above the rigid boundary, strong buoyancy forces cause the migration of the bubble away from the rigid boundary.

Figure 14(b) shows that the buoyancy forces have a significant effect on the velocity of the liquid which is developed during the collapse phase of the bubble. Figure 5.14(b) together with Figures 5.3, 5.5 and 5.7 indicate that in the case of a bubble above a rigid boundary, increasing of the buoyancy forces within a certain limited range causes a narrower liquid jet with a higher velocity directed toward the rigid boundary.

It was found that the buoyancy forces do not have a major effect on the collapse rate of the bubble.

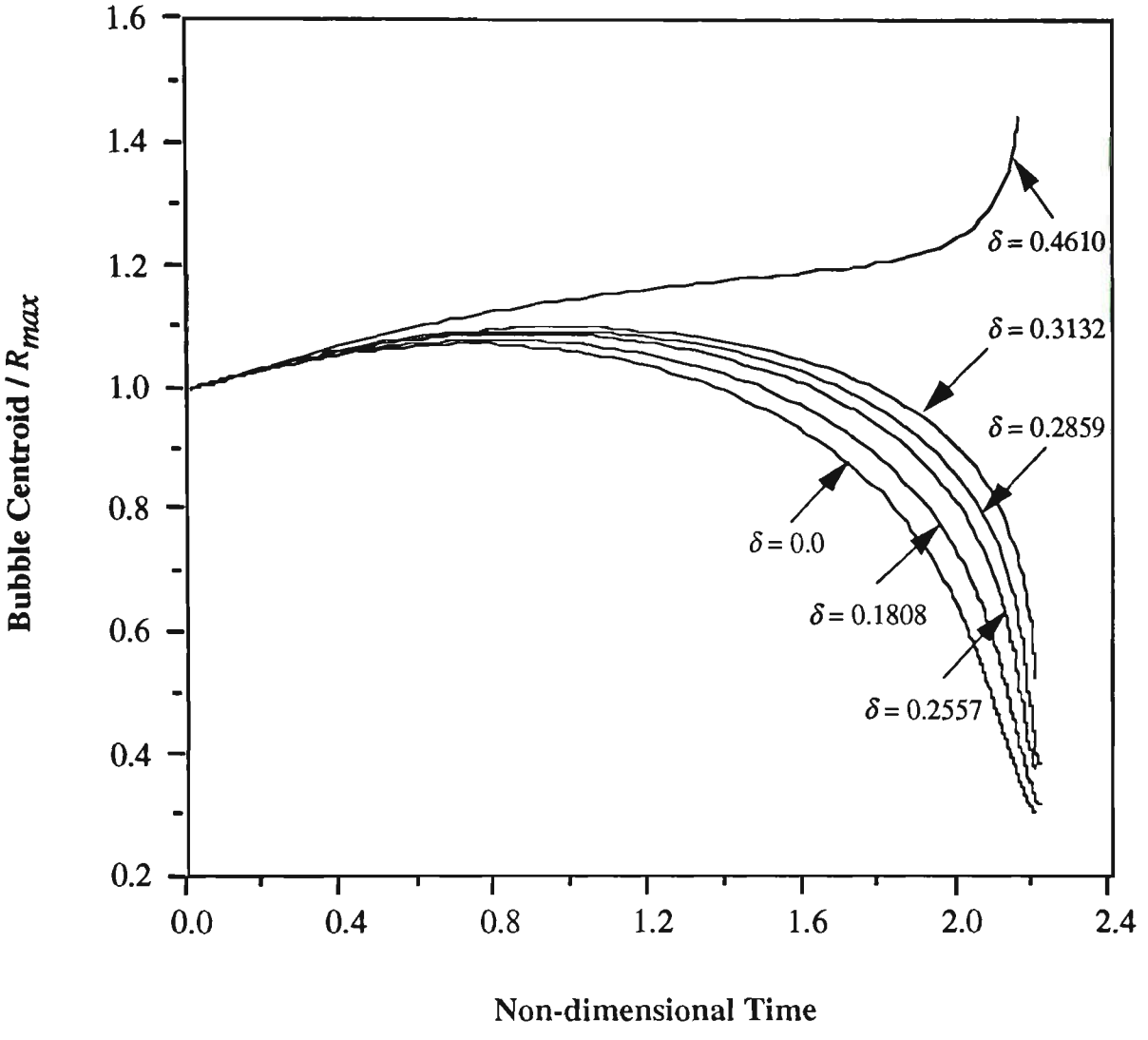

Figure 5.14(a) Migration of the bubble centroid for a bubble with $\gamma = 1.0$ and different values of buoyancy forces

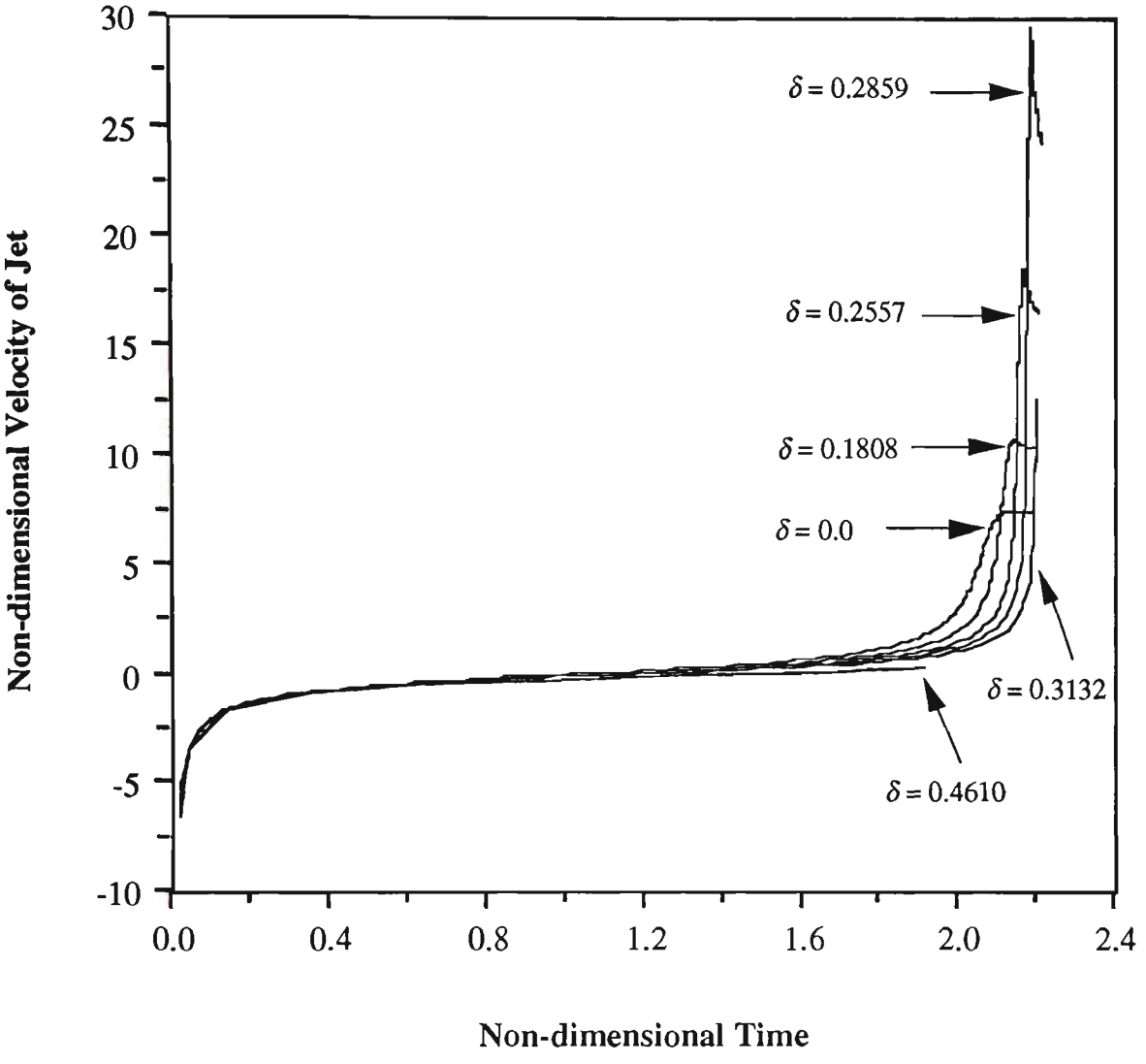

Figure 5.14(b) Velocity of the liquid jet for a bubble with $\gamma = 1.0$ and different values of buoyancy forces

In the case of the bubble below the rigid surface, where the buoyancy forces and the Bjerknes force act in the same direction, the effect of the buoyancy forces is opposite to the previous case.

Figures 5.15(a) and (b) show the dynamic characteristics of a bubble corresponding to the bubble behaviour presented in Figures 5.4 and 5.10.

Figure 5.15(a) shows that in the case of a bubble below the rigid boundary, the marginal migration of the bubble away from the rigid boundary during the bubble growth decreases by increasing the buoyancy forces.

Figure 5.15(b) indicates that the velocity of the liquid jet decreases by increasing the buoyancy forces.

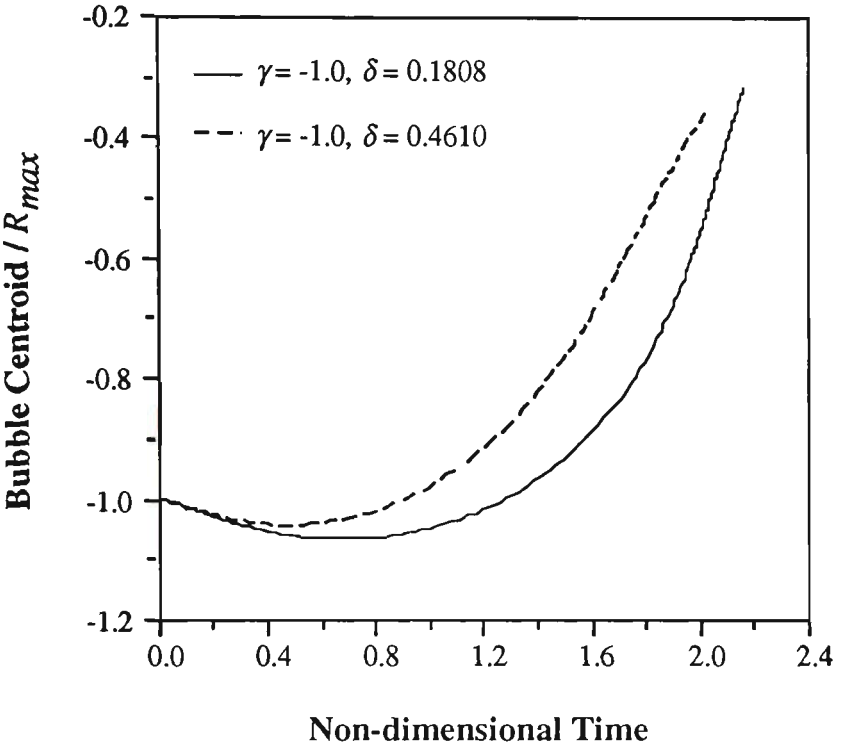

Figure 5.15(a) Migration of the bubble centroid for a bubble below a rigid boundary

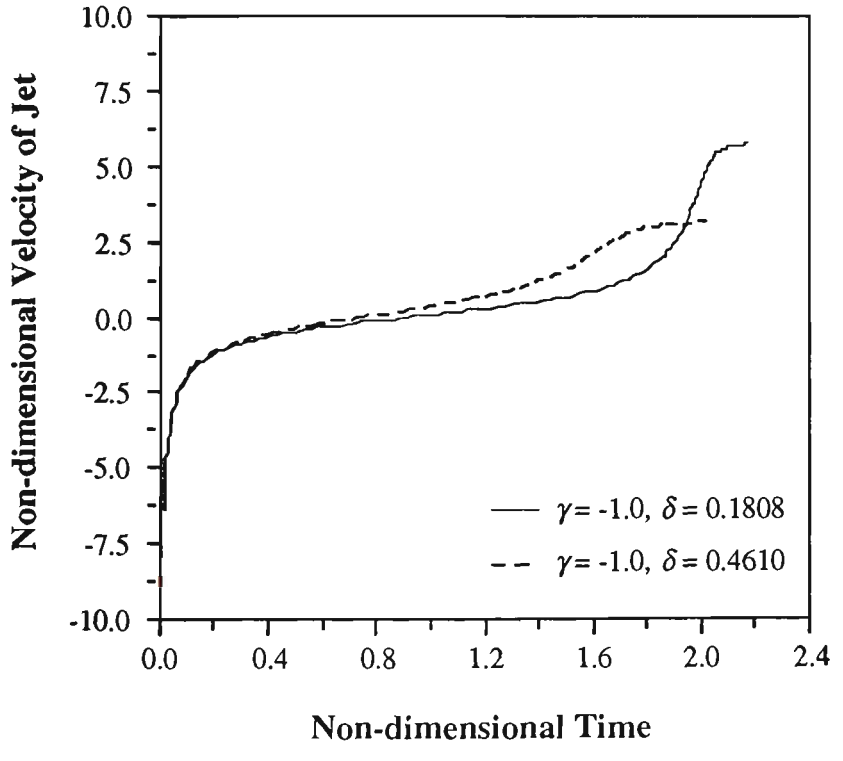

Figure 5.15(b) Velocity of the liquid jet for a bubble below a rigid boundary

5.11.2 The growth and collapse of a rebounding bubble containing a mixture of constant pressure vapour and ideal gas near a rigid boundary

In this case the growth and collapse of a rebounding gas bubble which contains a mixture of constant pressure vapour and ideal gas is investigated. As discussed in detail in *Section 5.5* the ideal gas inside the bubble undergoes an isentropic process with a polytropic index of $k = 1.4$.

Figure 5.16 shows the dynamics of the bubble above a rigid boundary with $\gamma = 0.75$, $\delta = 0.1808$ and $\varepsilon = 50$. It can be seen that the bubble during its expansion phase attaches to the rigid boundary and during the collapse phase a liquid jet is developed on the side of the bubble far from the rigid boundary and directed towards it. In this case the liquid jet impinges upon the rigid surface directly.

Figure 5.17 shows the dynamics of a bubble when it is initially located further away from the boundary with $\gamma = 1.5$, $\delta = 0.1808$ and $\varepsilon = 50$. In this case the bubble during is expansion phase remains nearly spherical. During the collapse phase a liquid jet is developed from the side of the bubble furthest from the rigid boundary and directed towards it. In this case the liquid jet penetrates the opposite side of the bubble before approaching to the rigid surface thus transforming the bubble into a toroidal shape. There is no direct impingement of the rigid boundary by the liquid jet.

Figures 5.16 and 5.17 show that the development of the high speed liquid jet occurs in a very short period of time.

Figure 5.18 illustrates the behaviour of a bubble with $\gamma = 1.25$, $\delta = 0.2557$ and $\varepsilon = 10$. In this case during the expansion phase the upper side of the bubble far

from the rigid boundary is slightly elongated in the direction of vertical axis. During the collapse phase the bubble is strongly elongated in the vertical direction. At the latest stages of the bubble collapse an interesting feature of the bubble dynamics is the development of an annular liquid jet around the bubble surface. This liquid jet causes the necking of the bubble in its middle part and splits the bubble into two parts as the bubble rebounds. The necking phenomenon during the pulsation of a bubble is discussed in detail in *Section 5.10.*

Figure 5.19 shows the dynamics of a bubble with $\gamma = 2.125$, $\delta = 0.1808$ and $\varepsilon = 10$. In this case the bubble remains nearly spherical during its expansion. During the first collapse phase of the bubble it is elongated vertically. During the rebound phase the bubble is also strongly elongated in the direction of the vertical axis. In the second collapse of the bubble two liquid jets are developed on both the top and bottom sides of the bubble on the axis of symmetry. The liquid jet on the upper side of the bubble is directed towards the rigid boundary. The liquid jet on the bottom side of the bubble is directed away from the rigid surface. It can be said that this is a critical case in that neither the Bjerknes force nor the buoyancy forces dominate the fluid motion.

Figure 5.20 illustrates the bubble behaviour for $\gamma = 2.25$, $\delta = 0.1808$ and $\varepsilon = 10$. In this case during the second collapse of the bubble a liquid jet is developed on the bottom side of the bubble close to the rigid boundary and is directed away from it.

Figure 5.21 shows the bubble behaviour with $\gamma = 2.25$, $\delta = 0.0$ and $\varepsilon = 10$. In this case at the end of the collapse phase a liquid jet is initiated on the side of the bubble far from the rigid boundary and directed towards it. The liquid jet is developed during the rebound phase of the bubble.

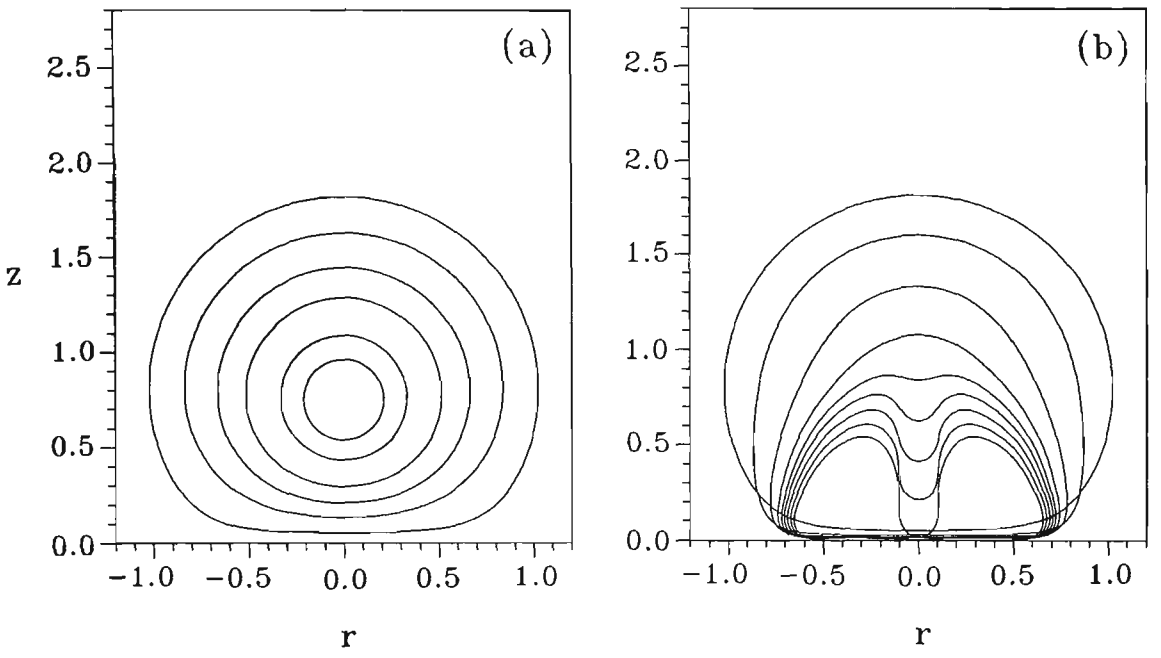

Figure 5.16 Bubble shapes for the growth (a) and collapse (b) of a bubble containing a mixture of constant pressure vapour and ideal gas above a rigid boundary with $\gamma = 0.75$, $\delta = 0.1808$ and $\varepsilon = 50$. The non-dimensional times corresponding to bubble successive profiles are: (a) Growth phase: 0.0000 (innermost), 0.0478, 0.1289, 0.2332, 0.4313, 1.1673 (outermost). (b) Collapse phase: 1.1673 (outermost), 1.7783, 2.0242, 2.1293, 2.1718, 2.1974, 2.2223, 2.2461, 2.2691 (innermost).

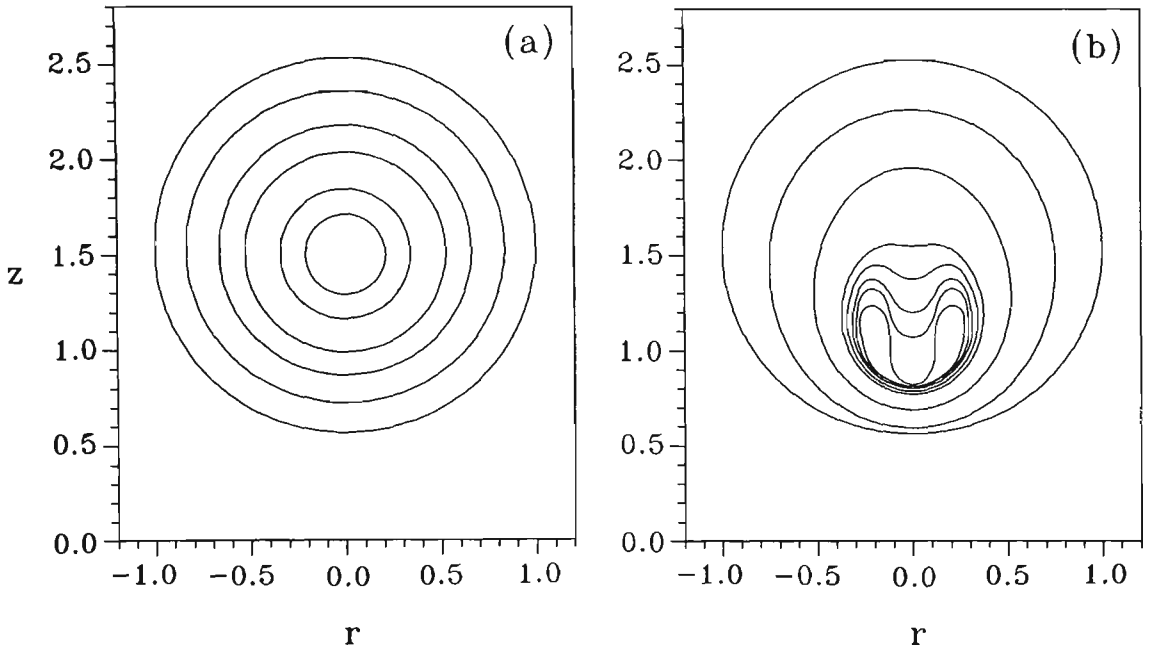

Figure 5.17 Bubble shapes for the growth (a) and collapse (b) of a bubble containing a mixture of constant pressure vapour and ideal gas above a rigid boundary with $\gamma = 1.5$, $\delta = 0.1808$ and $\varepsilon = 50$. The non-dimensional times corresponding to bubble successive profiles are: (a) Growth phase: 0.0000 (innermost), 0.0498, 0.1324, 0.2281, 0.4322, 1.0757 (outermost). (b) Collapse phase: 1.0757 (outermost), 1.7831, 2.0248, 2.1297, 2.1458, 2.1604, 2.1713, 2.1920 (innermost).

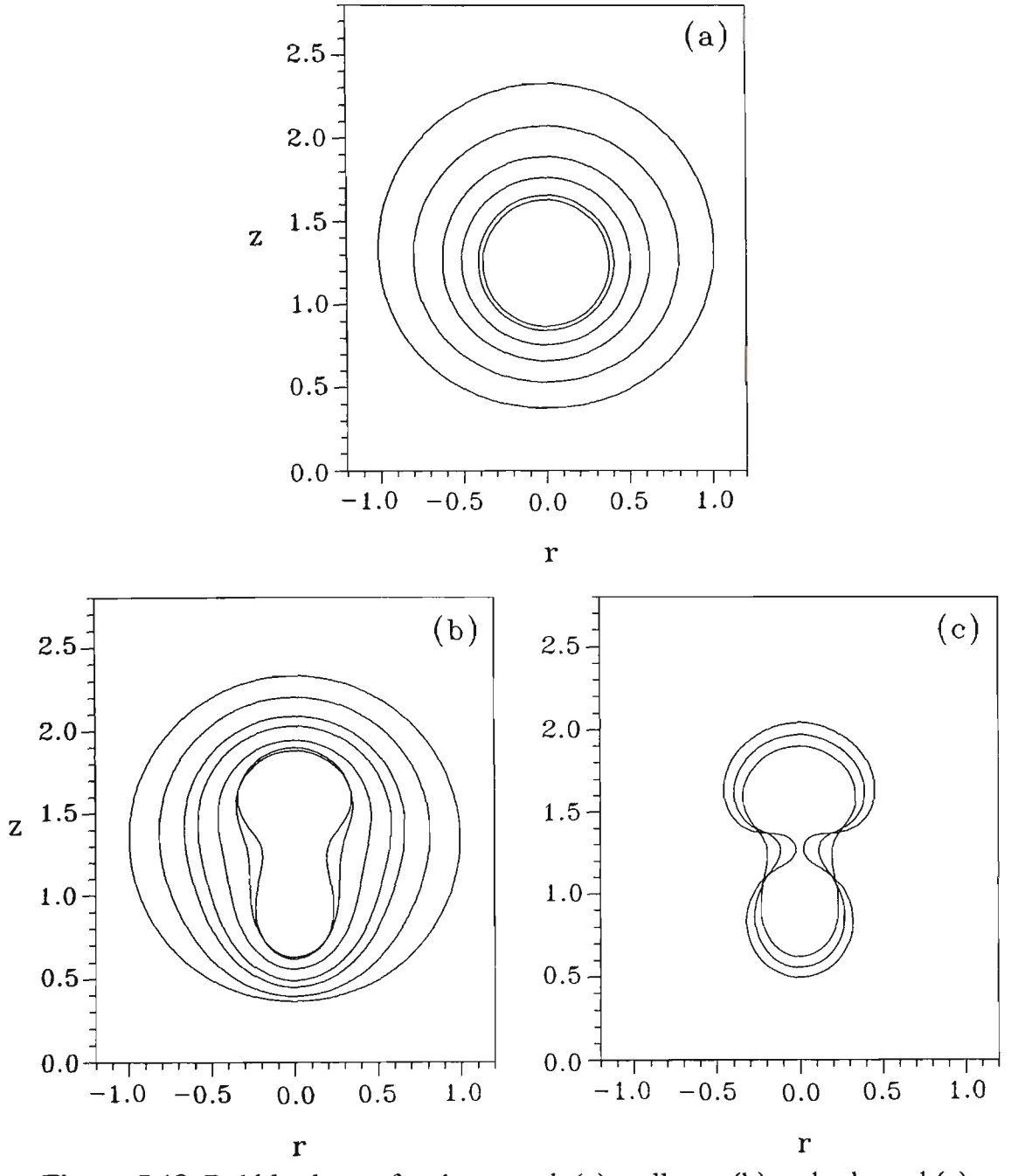

Figure 5.18 Bubble shapes for the growth (a), collapse (b) and rebound (c) of a bubble containing a mixture of constant pressure vapour and ideal gas above a rigid boundary with $\gamma = 1.25$, $\delta = 0.2557$ and $\varepsilon = 10$. The non-dimensional times corresponding to bubble successive profiles are: (a) Growth phase: 0.0000 (innermost), 0.0498, 0.1344, 0.2348, 0.4412, 1.2460 (outermost). (b) Collapse phase: 1.2460 (outermost), 1.8640, 2.0899, 2.1867, 2.3104, 2.4254, 2.4920 (innermost). (c) Rebound phase: 2.4920 (innermost), 2.5481, 2.5966 (outermost).

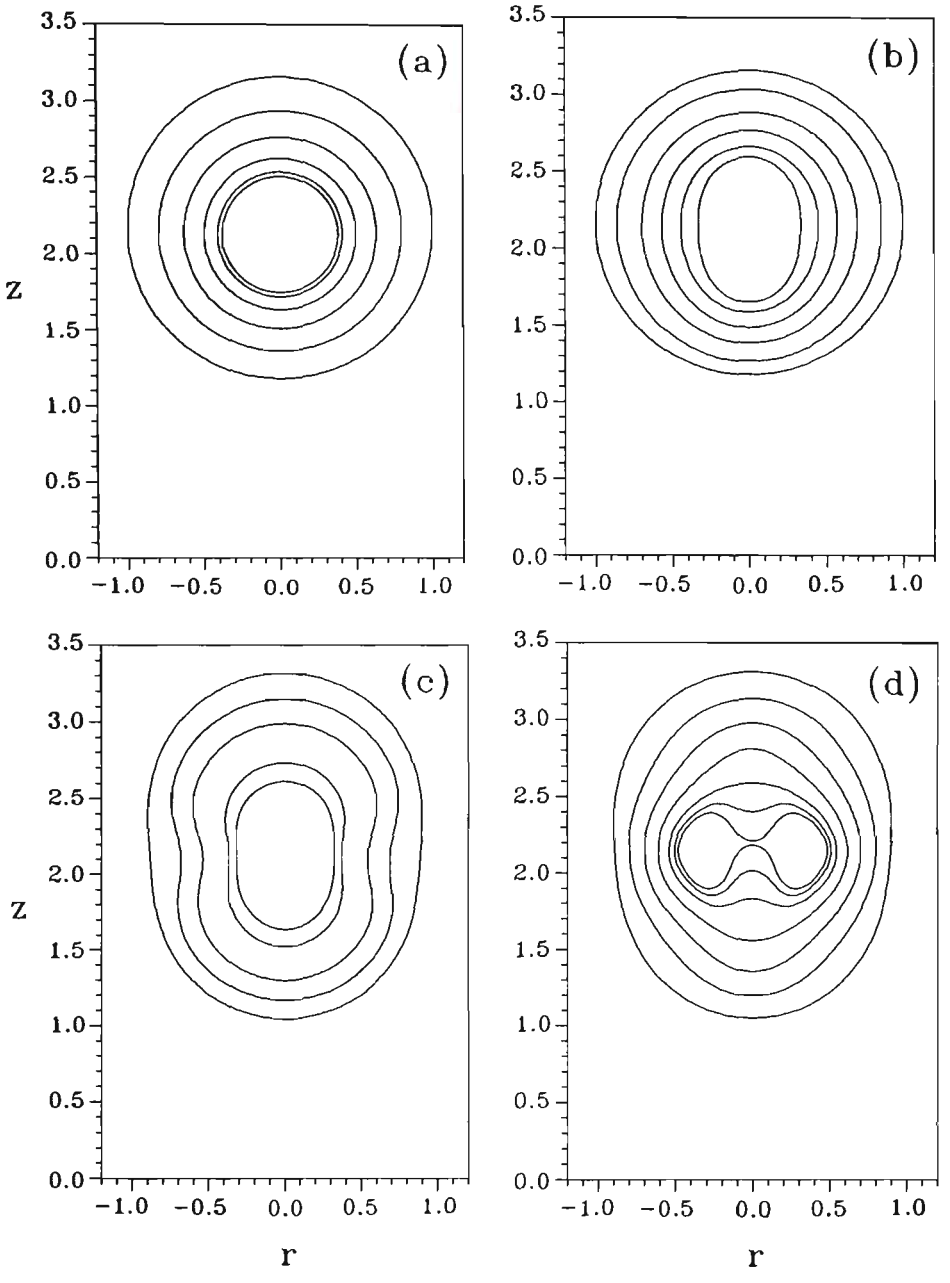

Figure 5.19 Bubble shapes for the pulsation of a bubble containing a mixture of constant pressure vapour and ideal gas above a rigid boundary with $\gamma = 2.125$, $\delta = 0.1808$ and $\varepsilon = 10$. The non-dimensional times corresponding to bubble successive profiles are: (a) Growth phase: 0.0000 (innermost), 0.0501, 0.1223, 0.2320, 0.4258, 1.1619 (outermost). (b) Collapse phase: 1.1619 (outermost), 1.7964, 2.0216, 2.1385, 2.2258, 2.3250 (innermost). (c) Rebound phase: 2.3250 (innermost), 2.4157, 2.5757, 2.7555, 3.5012 (outermost). (c) Second collapse: 3.5012 (outermost), 4.0420, 4.2578, 4.4104, 4.5123, 4.5115, 4.6087 (innermost).

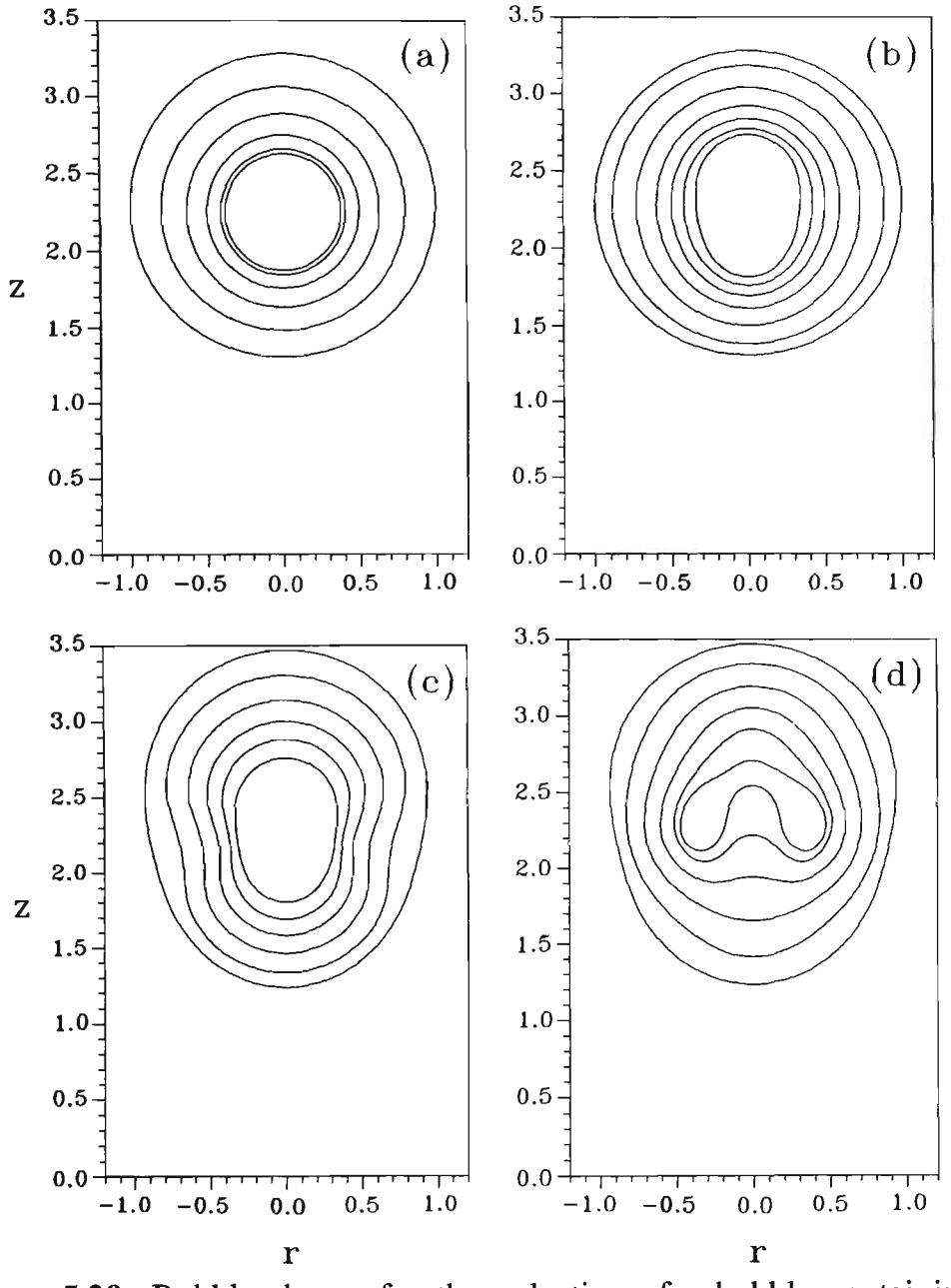

Figure 5.20 Bubble shapes for the pulsation of a bubble containing a mixture of constant pressure vapour and ideal gas above a rigid boundary with $\gamma = 2.25$, $\delta = 0.1808$ and $\varepsilon = 10$. The non-dimensional times corresponding to bubble successive profiles are: (a) Growth phase: 0.0000 (innermost), 0.0501, 0.1225, 0.2327, 0.4276, 1.1638 (outermost). (b) Collapse phase: 1.1638 (outermost), 1.7960, 2.0182, 2.1327, 2.1970, 2.2462, 2.3155 (innermost). (c) Rebound phase: 2.3155 (innermost), 2.4019, 2.4706, 2.5728, 2.7572, 3.4755 (outermost). (d) Second collapse: 3.4755 (outermost), 4.0259, 4.2654, 4.4104, 4.4117, 4.5113, 4.6269 (innermost).

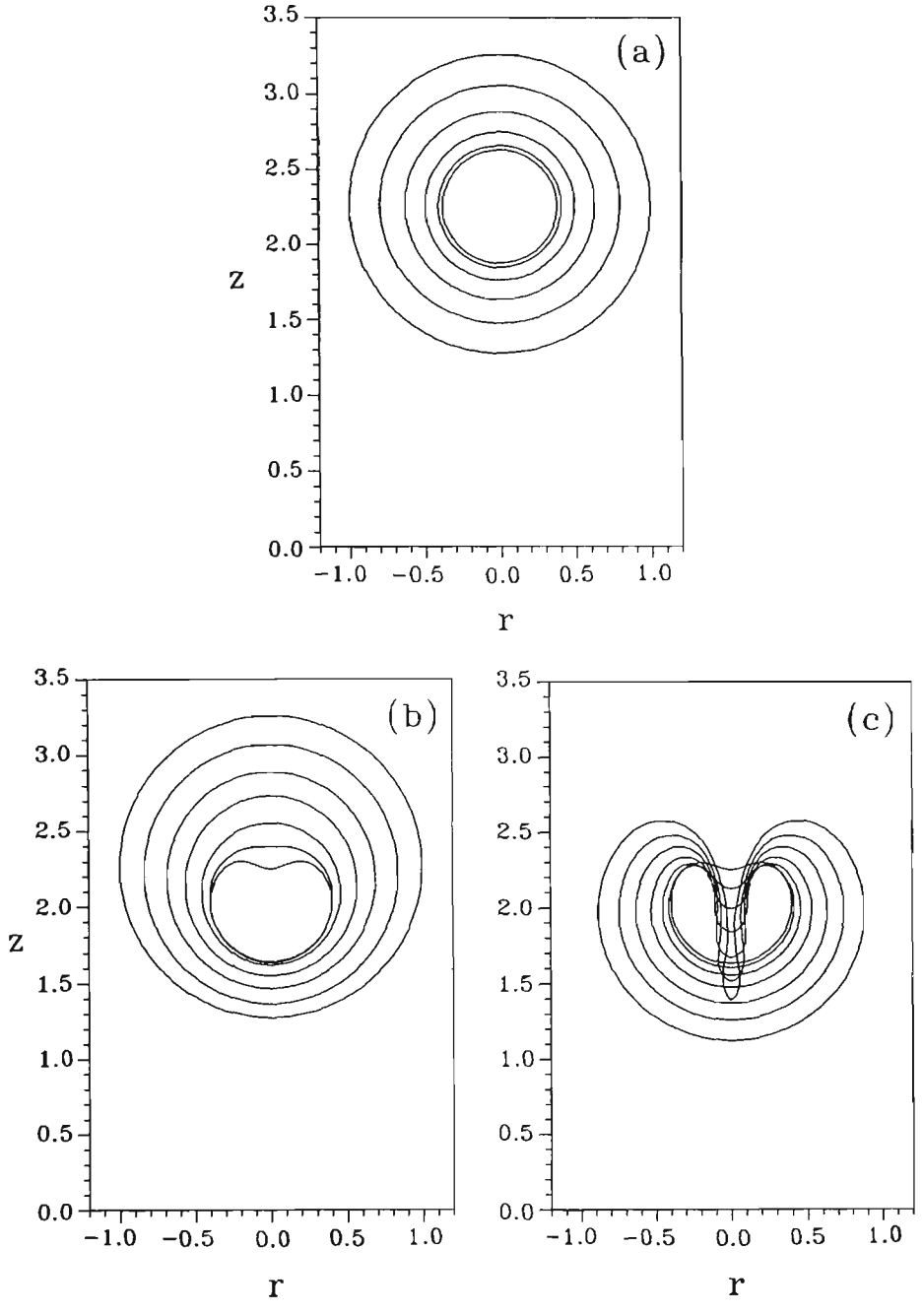

Figure 5.21 Bubble shapes for the growth (a), collapse (b) and rebound (c) of a bubble containing a mixture of constant pressure vapour and ideal gas above a rigid boundary with $\gamma = 2.25$, $\delta = 0.0$ and $\varepsilon = 10$. The non-dimensional times corresponding to bubble successive profiles are: (a) Growth phase: 0.0000 (innermost), 0.0501, 0.1225, 0.2331, 0.4309, 1.1888 (outermost). (b) Collapse phase: 1.1888 (outermost), 1.7913, 2.0195, 2.2152, 2.2638, 2.3193, 2.3597 (innermost). (c) Rebound phase: 2.3597 (innermost), 2.3939, 2.4368, 2.4993, 2.5915, 2.7160, 2.9353 (outermost).

Table 5.3 shows the direction of the liquid jet either towards the rigid boundary or away from it for a bubble containing a mixture of constant pressure vapour and ideal gas with fixed values of δ and ε and different values of γ. As shown in Table 5.3 in this case the critical value of $\gamma\delta$ obtained as a measure for the direction of the liquid jet is different from that for the case of constant pressure vapour bubble (where $\gamma\delta = 0.442$).

Table 5.3 Direction of the liquid jet in the case of a rebounding bubble containing a mixture of constant pressure vapour and ideal gas (k=1.4) for $\varepsilon = 10$ and corresponding to the different values of $\gamma\delta$

γ \ δ	0.1808
1.0	Liquid jet ↓ ($\gamma\delta = 0.1808$)
1.5	Liquid jet ↓ ($\gamma\delta = 0.2712$)
2.0	Liquid jet ↓ ($\gamma\delta = 0.3616$)
2.125	* Two liquid jets ↓↑ ($\gamma\delta = 0.3842$)
2.2	Liquid jet ↑ ($\gamma\delta = 0.3978$)
2.25	Liquid jet ↑ ($\gamma\delta = 0.4068$)
2.5	Liquid jet ↑ ($\gamma\delta = 0.4520$)

* Critical point

The dynamic characteristics of a bubble containing a mixture of constant pressure vapour and ideal gas are now investigated further.

Figures 5.22(a), (b), (c) and (d) illustrate comparisons between the dynamic characteristics of two bubbles corresponding to the bubble behaviour presented in Figures 5.16 and 5.17.

Figure 5.22(a) shows that the marginal movement of the bubble centroid away from the rigid surface during the growth phase of the bubble decreases by increasing the initial distance of the bubble centroid from the rigid boundary. In the case of smaller initial distance of the bubble centroid from the rigid surface the increasingly rapid migration of the bubble towards the rigid boundary is more pronounced.

Figure 5.22(b) shows that by increasing the initial distance of the bubble from the rigid surface, the velocity of the liquid jet increases.

Figure 5.22(c) indicates that by decreasing the initial distance of the bubble centroid from the rigid boundary, the collapse rate of the bubble decreases and consequently the collapse time of the bubble increases.

Figure 5.22(d) illustrates the pressure inside the bubbles during their growth and collapse phases. It should be noted that in both cases presented in this figure, the bubbles become toroidal before the rebound phase. Consequently, the computations are terminated. It can be seen that the internal pressure at the end of the collapse phase for the bubble further away from the rigid boundary is higher than the case for the bubble located very close to the rigid boundary. This is because the Bjerknes force exerted on the closer bubble is stronger. Thus the stronger Bjerknes force causes stronger deformation of the bubble during its

pulsation. Consequently the liquid jet initiates earlier and the volume of the bubble at the instant of its transformation to a toroidal shape is larger. It is obvious that in the case of a bubble containing a mixture of constant pressure vapour bubble and ideal gas its larger volume causes lower internal pressure.

Figure 5.22(e) shows the pressure developed inside the liquid domain on the rigid boundary at $(r = 0,\ z = 0)$ during the pulsation of the bubble. It is shown that the pressure on the rigid boundary at $(r = 0,\ z = 0)$ at the end of the bubble collapse is higher in the case of the bubble further away from the boundary. As discussed in the previous section, for the case of a bubble located close to the rigid boundary there is direct liquid jet impingement on the rigid surface, and an extremely high water hammer pressure is exerted because of this [see Gibson (1968) and Tomita and Shima (1986)]. Thus the destructive effect of the bubble collapse in the case of direct impingement of the liquid jet on the rigid surface is much higher than the case of the bubble collapse without direct impingement of the liquid jet on the rigid surface. Also, as emphasised in the previous section, because of the early transformation of the bubble closer to the rigid boundary into a toroidal form, it has not collapsed as far as the bubble further away from the rigid boundary. This could account for the lower pressure on the rigid boundary. As the bubble collapses the pressure increases over a very short period of time, so the pressure on the rigid boundary may increase for the closer bubble in its neighbourhood if the bubble is allowed to collapse further. The computational simulation of the bubble behaviour beyond its transformation into a toroidal form requires a special numerical scheme [see Best (1991) and Zhang *et al.* (1993)].

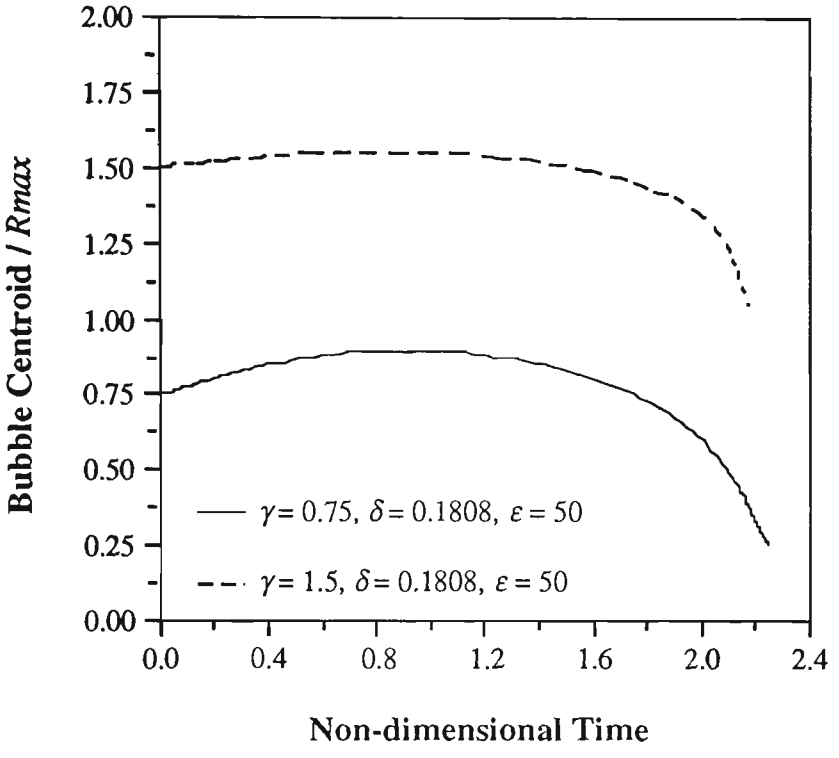

Figure 5.22(a) Migration of the bubble centroid above a rigid boundary

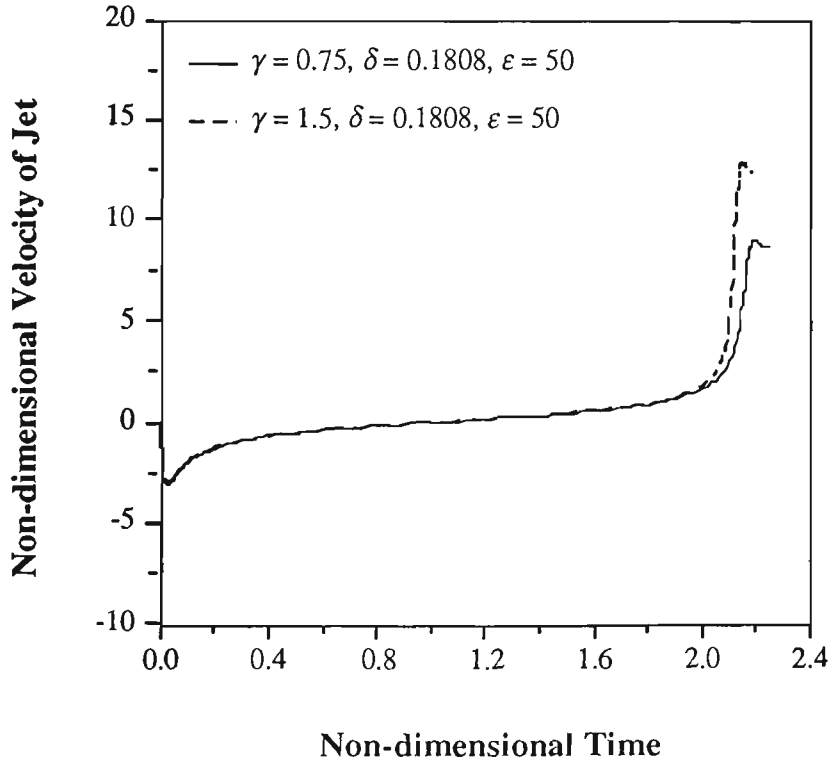

Figure 5.22(b) Velocity of the liquid jet

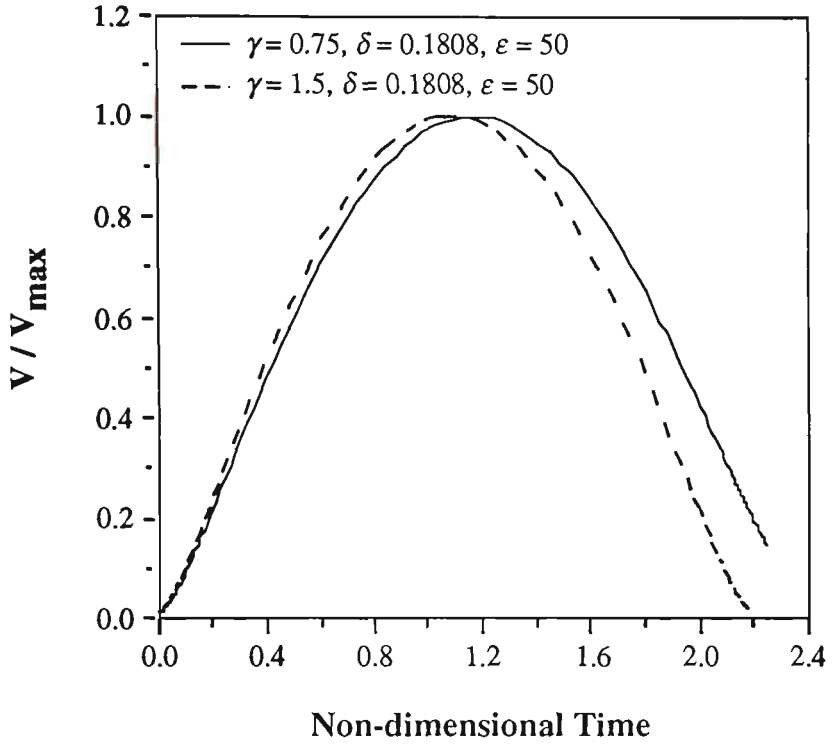

Figure 5.22(c) Variation of the bubble volume during its growth and collapse phases

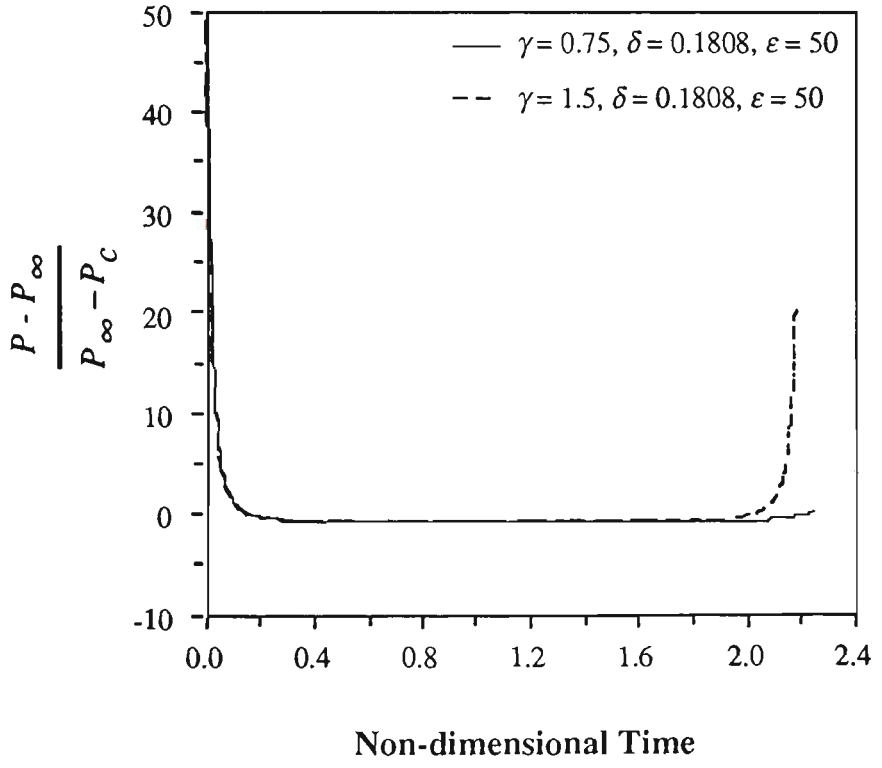

Figure 5.22(d) Pressure inside the bubble volume during its growth and collapse phases

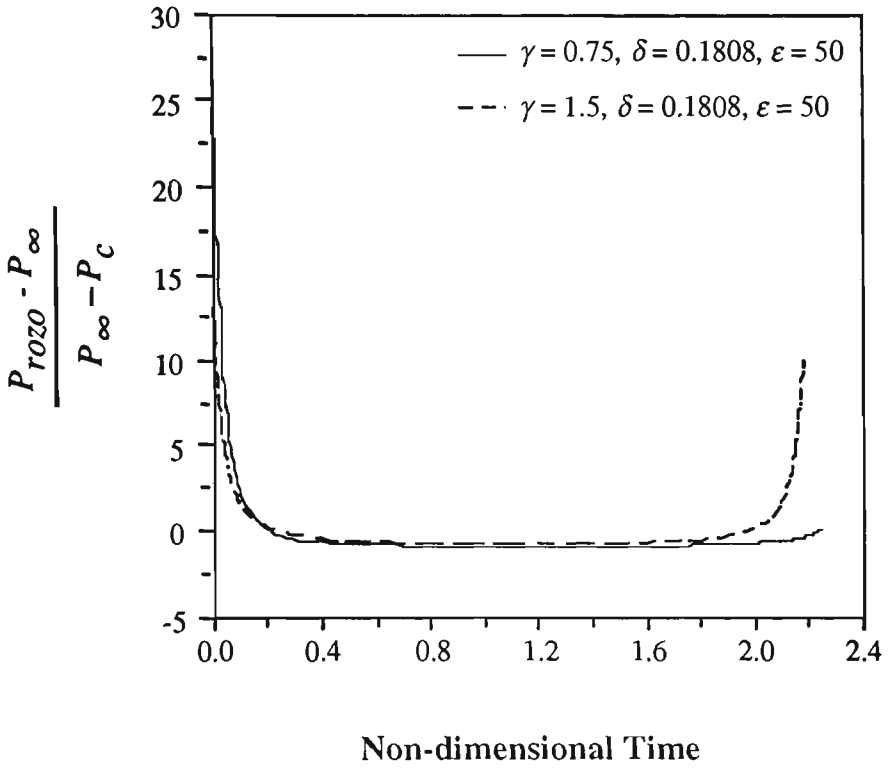

Figure 5.22(e) Pressure on the rigid boundary at $(r = 0,\ z = 0)$, P_{rozo}, during the growth and collapse of the bubble

Figures 5.23(a) and (b) illustrate the dynamic behaviour of a bubble with $\gamma = 2.25$ and $\delta = 0.0$ for the two different cases of $\delta = 0.0$ and $\delta = 0.1808$ corresponding to the bubble behaviour presented in Figures 5.20 and 5.21.

Figure 5.23(a) shows the marginal movement of the centroid of the bubble with $\delta = 0.1808$ migrating away from the rigid boundary during two complete cycles of its pulsation. In the case of the bubble without buoyancy forces the bubble centroid migrates towards the rigid boundary.

In Figure 5.23(b) the solid line represents the velocity of the liquid jet which is developed in the absence of the buoyancy forces on the side of the bubble far from the rigid boundary and directed towards it. The dashed line represents the velocity of the liquid jet in the case of buoyant bubble with $\delta = 0.1808$ which is developed on the side of the bubble close to the rigid boundary and directed away from it. As discussed previously, the positive values of the liquid jet velocity indicate a direction into the bubble, whereas the negative values indicate a velocity outward from the bubble.

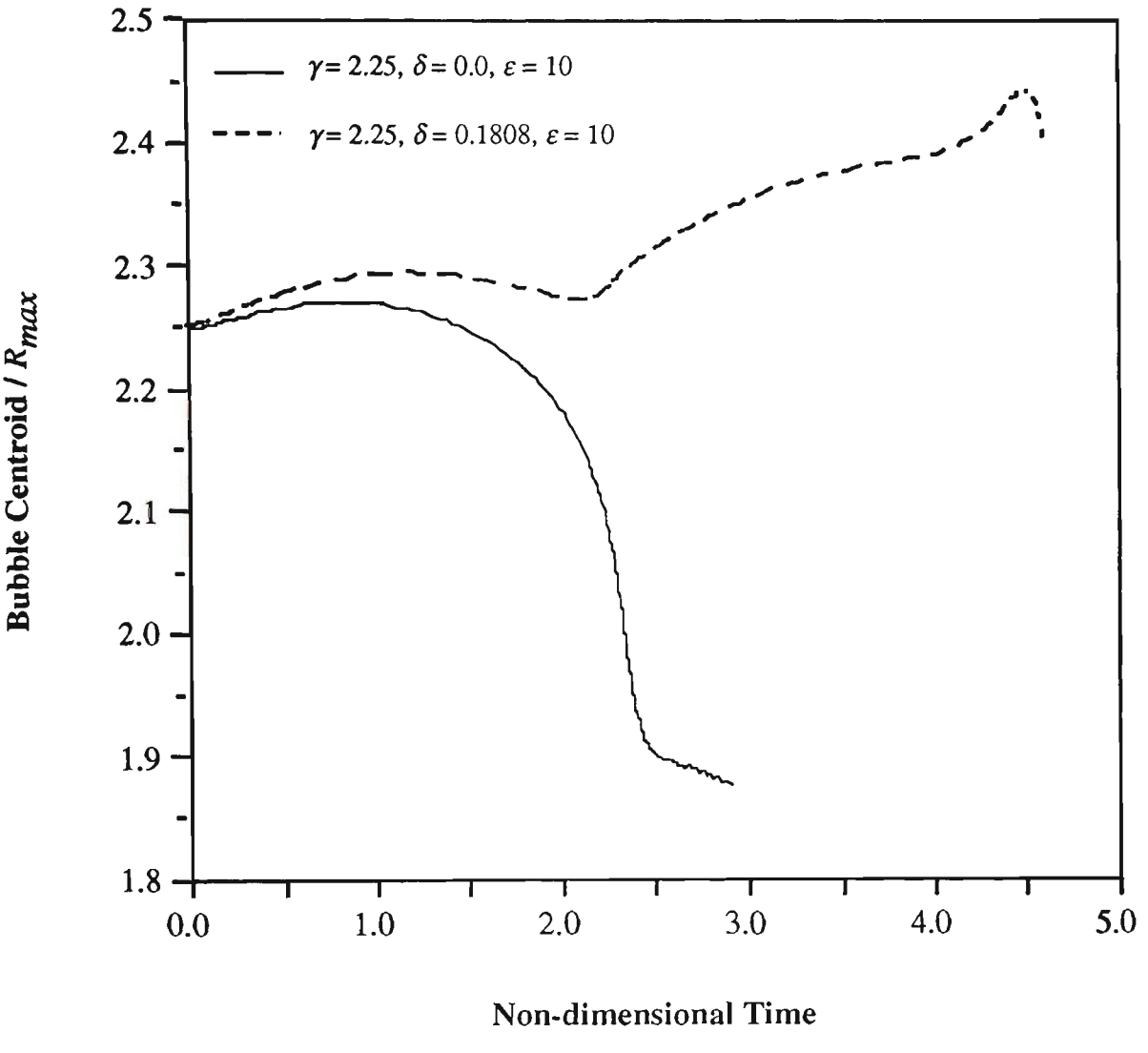

Figure 5.23(a) Migration of the bubble centroid during its pulsation for a buoyant bubble with $\gamma = 2.25$, $\delta = 0.1808$ and $\varepsilon = 10$ and for a bubble in the absence of buoyancy forces with $\gamma = 2.25$, $\delta = 0.0$ and $\varepsilon = 10$

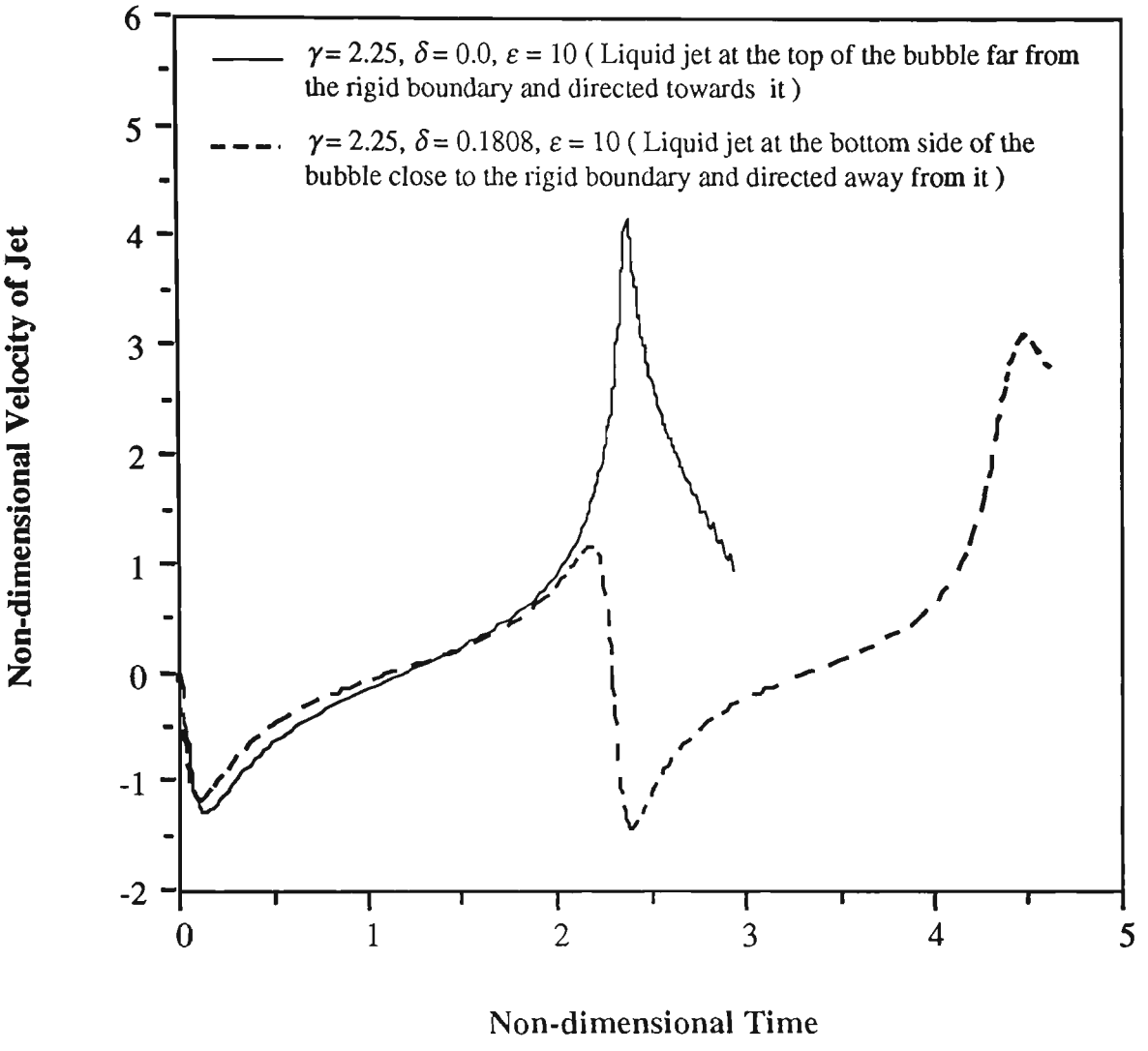

Figure 5.23(b) Velocity of the liquid jet during the pulsation of the bubble. The dashed line represents velocity of the liquid jet directed away from the rigid boundary for a buoyant bubble with $\gamma = 2.25$, $\delta = 0.1808$ and $\varepsilon = 10$ while the solid line represents the velocity of the liquid jet directed towards the rigid boundary in the absence of buoyancy forces with $\gamma = 2.25$, $\delta = 0.0$ and $\varepsilon = 10$.

Figures 5.24(a) and 5.24(b) illustrates the dynamic characteristics of the bubble in two complete cycles of its pulsation with $\gamma = 2.25$, $\delta = 0.1808$ and $\varepsilon = 10$ corresponding to the bubble behaviour presented in Figure 5.20.

Figure 5.24(a) illustrates the bubble volume and the pressure inside the bubble with respect to time during two complete cycles of the bubble pulsation. Figure 5.24(a) shows that the latest stages of the bubble collapse are accompanied by a very large variation of the pressure inside the bubble.

Figure 5.24(b) shows the corresponding values of the pressure inside the liquid domain on the rigid surface at $(r = 0,\ z = 0)$ during two complete cycles of the bubble pulsation.

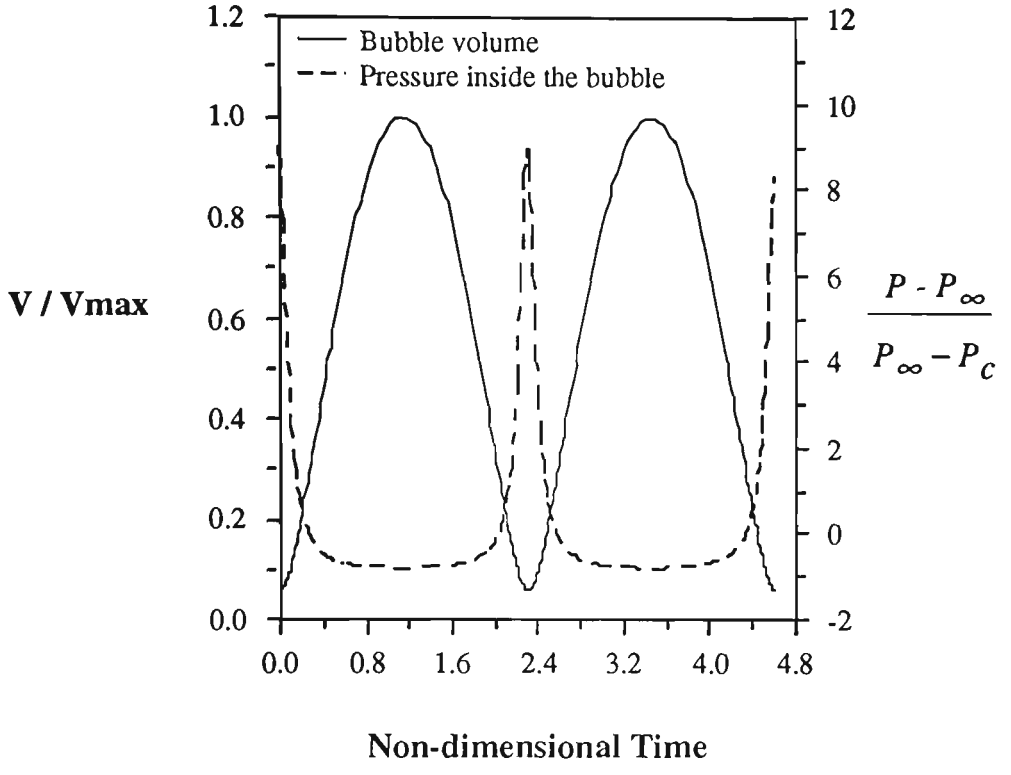

Figure 5.24(a) Variation of the volume and internal pressure during the growth and collapse of a bubble with $\gamma = 2.25$, $\delta = 0.1808$ and $\varepsilon = 10$

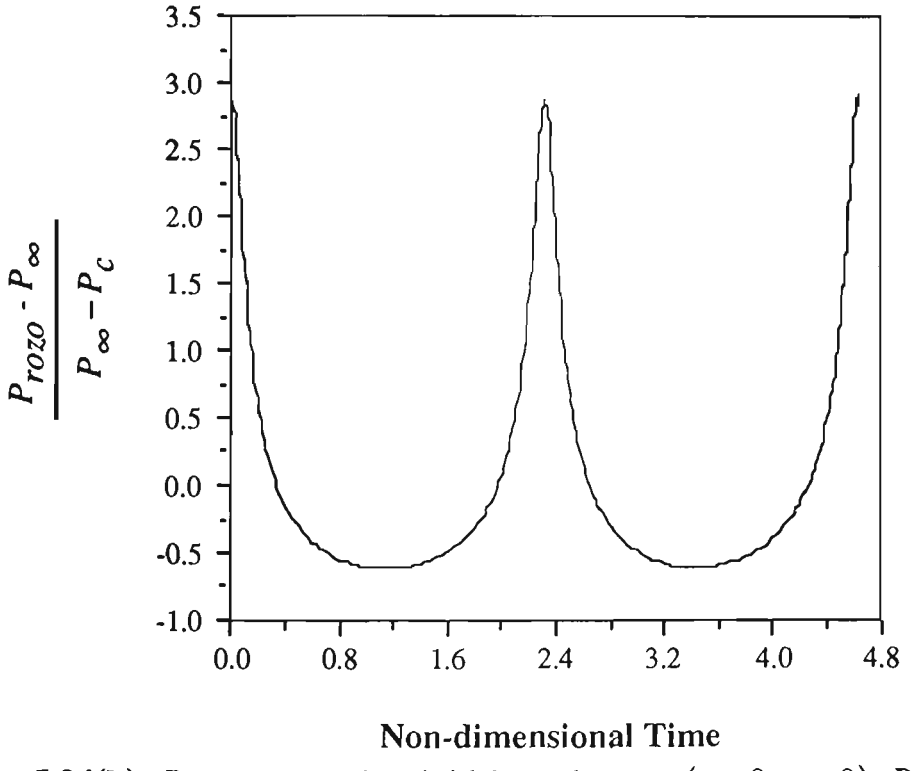

Figure 5.24(b) Pressure on the rigid boundary at $(r = 0, z = 0)$, P_{rozo}, during the growth and collapse of the bubble with $\gamma = 2.25$, $\delta = 0.1808$ and $\varepsilon = 10$.

5.11.3 Pulsations of a vapour bubble near a rigid boundary and comparisons with the pulsations of an ideal gas bubble

In this section the dynamics of a vapour bubble, which is discussed in *Sections 4.4* and *5.6*, collapsing from its initially spherical maximum volume in the vicinity of a rigid boundary, is investigated. The dynamic behaviour of an ideal gas bubble collapsing from its initially spherical maximum volume near a rigid boundary is also examined with different polytropic indices (1.0, 1.1, 1.2 and 1.4). For the vapour bubble and all cases of the ideal gas bubble γ and δ are 1.2 and 0.1505 respectively.

Comparisons are made between the dynamic behaviour of the vapour bubble and an ideal gas with different polytropic indices of 1.0, 1.1, 1.2 and 1.4.

Figure 5.25 illustrates the dynamic behaviour of a vapour bubble above a rigid boundary which undergoes two cycles of collapse and rebound. During the second rebound the liquid jet penetrates the opposite side of the bubble. It can be seen that the development of the liquid jet is a continuous process that is independent of the direction of the bubble pulsation.

Figure 5.26 illustrates the comparisons between the shapes of a vapour bubble and an ideal gas bubble having different polytropic indices of 1.0, 1.1, 1.2 and 1.4 at the end of the second collapse. As it is shown in Figure 5.26 in the case of an ideal gas bubble with polytropic index of 1.4, a liquid jet is just about to initiate at the far side of the bubble from the rigid boundary and is directed towards it. In the case of ideal gas bubbles with polytropic indices of 1.2 and 1.1 a liquid jet is developed at the at the top of each bubble, directed towards the rigid boundary. It should be noted that in the case of the ideal gas bubble with a polytropic index of

1.0, the liquid jet penetrates the opposite side of the bubble just before the end of the second collapse.

As seen in Figure 5.26 in the case of a vapour bubble pulsating near a rigid boundary the liquid jet at the end of the second collapse is located between the two cases of the ideal gas bubble having different indices of 1.1 and 1.2.

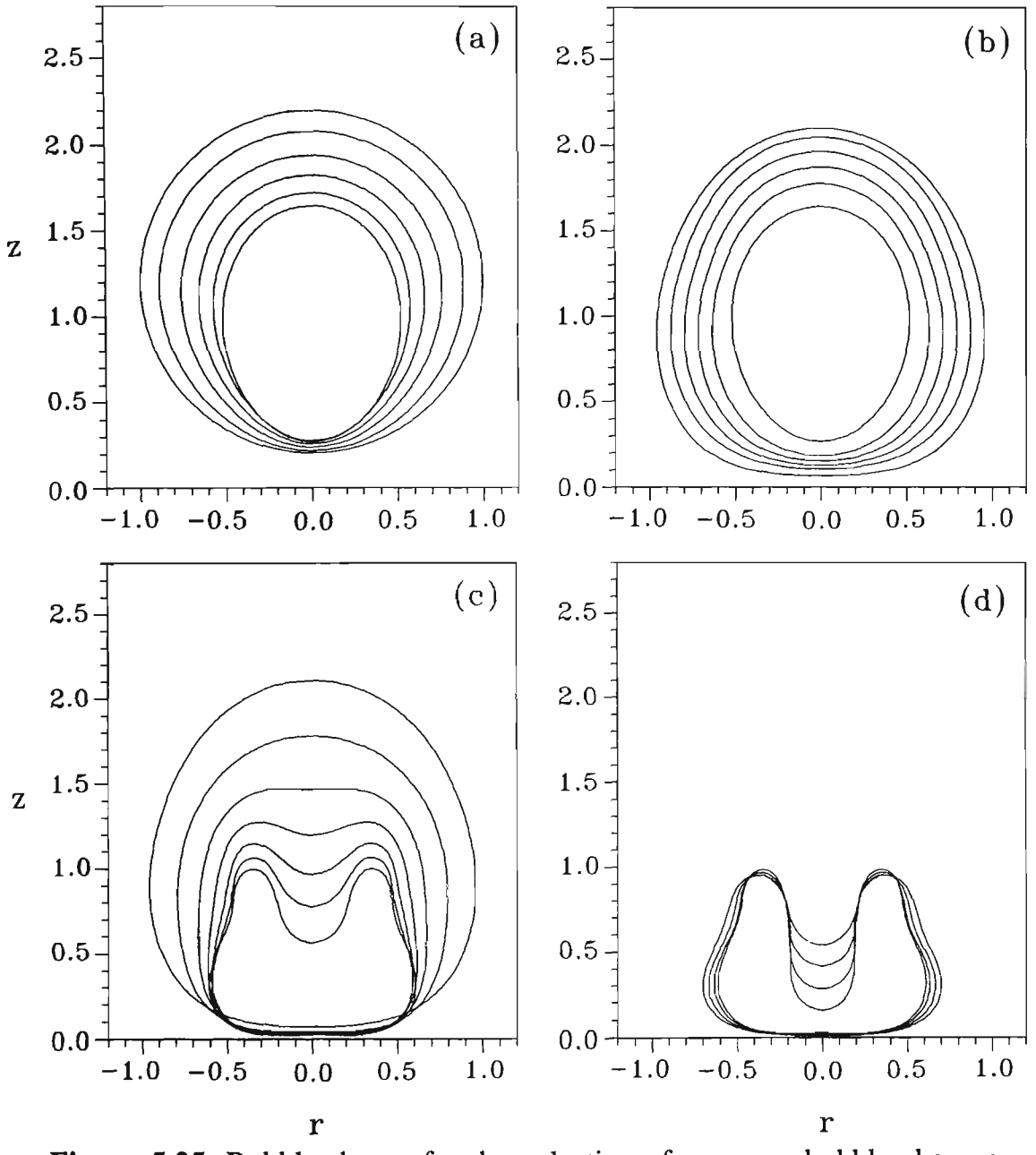

Figure 5.25 Bubble shapes for the pulsation of a vapour bubble above a rigid boundary with $\gamma = 1.2$ and $\delta = 0.1505$. The non-dimensional times corresponding to bubble successive profiles are: (a) Collapse phase: 0.0000 (outermost), 0.5005, 0.7373, 0.8868, 1.0135, 1.1752 (innermost). (b) Rebound phase: 1.1752 (innermost), 1.4208, 1.5445, 1.6818, 1.8605, 2.3577 (outermost). (c) Second collapse: 2.3577 (outermost), 2.9883, 3.2073, 3.3334, 3.4241, 3.4944, 3.5858 (innermost). (d) Second rebound: 3.5858 (innermost), 3.6197, 3.6750, 3.7284 (outermost).

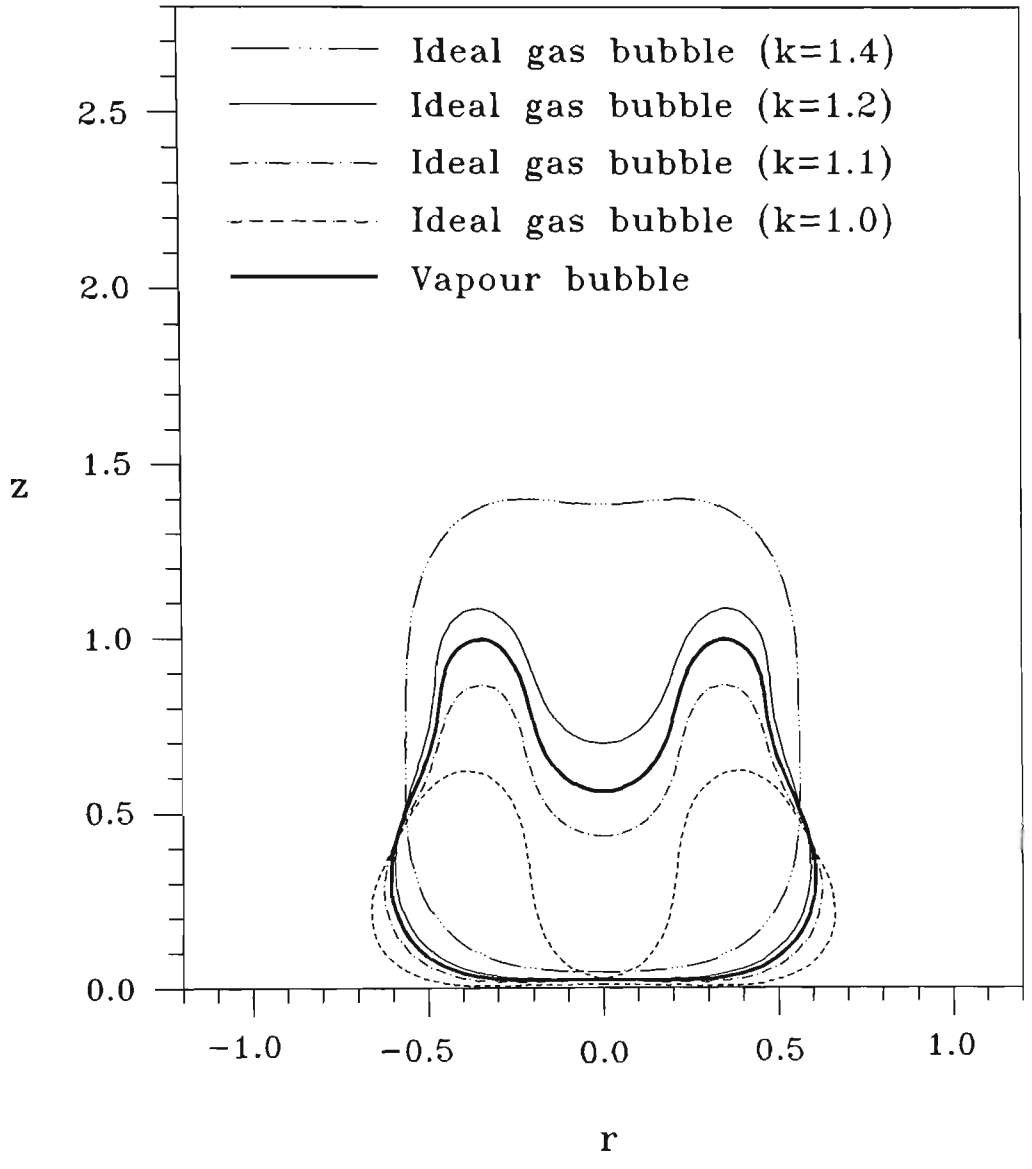

Figure 5.26 Comparisons between the bubble profiles at the end of the second collapse for a vapour bubble and ideal gas bubbles which are characterised by $\gamma = 1.2$ and $\delta = 0.1505$. In the case of the ideal gas bubble with polytropic index of 1.0 the liquid jet penetrates the opposite side of the bubble just before the second collapse. The non-dimensional time for the illustrated profile of the vapour bubble is 3.5858. Whereas the non-dimensional time for the illustrated profiles of the ideal gas bubbles with polytropic indices of 1.4, 1.2, 1.1 and 1.0 are 3.4038, 3.5495, 3.6220, and 3.7071 respectively.

Figure 5.27 illustrates the migration of the bubble centroid for a vapour bubble and ideal gas bubbles with different polytropic indices of 1.0, 1.1, 1.2 and 1.4.

Figures 5.28 and 5.29 show the variation in the volume and pressure inside the bubble in the cases of a vapour bubble and ideal gas bubbles which follow a polytropic process with polytropic indices of 1.0, 1.1, 1.2 and 1.4. This comparison indicates that an ideal gas bubble with a smaller polytropic index has a higher rate of collapse and collapses into a smaller volume and results in the higher maximum pressure at the end of the collapse phase. Figures 5.28 and 5.29 also show that the ideal gas bubble with a smaller polytropic index has a longer cycle of pulsation. It is also shown that the behaviour of vapour bubble falls between that of the ideal gas bubbles with polytropic indices of 1.1 and 1.2.

It should be noted that in the case of a rebounding isolated bubble the subsequent minimum volumes of the bubble at the end of the collapses in the absence of energy dissipation are equal. This is because of the fact that in the case of an isolated bubble at the end of a rebound or a collapse the flow of water around the bubble is stagnant. Thus the total energy of the system returns to the bubble. The pressure in the bubble is lowest at the maximum volume and highest at the minimum volume. This makes it possible for the same energy level to be stored in the state of maximum volume as well as in the state of minimum volume.

For a bubble near a rigid surface, although the energy is conserved, the maximum volumes are reduced at subsequent rebounds. On the other hand the minimum volumes are increased at subsequent collapses.

This feature is typically illustrated in Figures 5.28 and 5.29, and is due to the fact that the formation of the water jet within the bubble is associated with a portion of

kinetic energy that increases with time. This amount of energy does not return to the bubble at the ends of rebounds or collapses. As the result, at every subsequent rebounds, the maximum volume reduces, while the minimum volume increases at the end of every subsequent collapse as shown in Figure 5.28 [see Soh and Shervani-Tabar (1994)].

Figure 5.30 illustrates the velocity of the liquid jet at the top of the bubble far from the rigid surface for the cases of a vapour bubble and ideal gas bubbles having different polytropic indices of 1.0, 1.1, 1.2 and 1.4 in the vicinity of a rigid boundary.

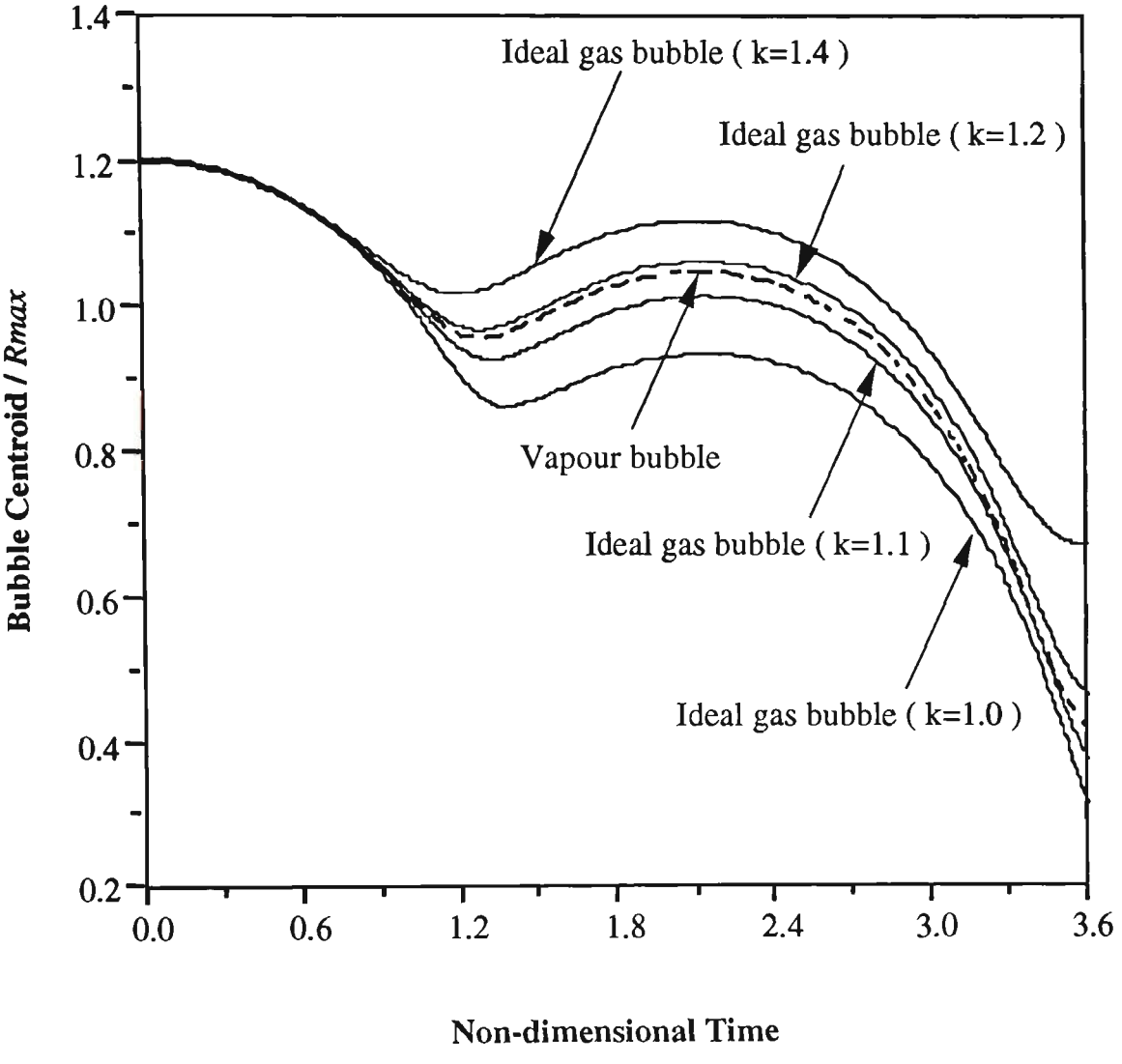

Figure 5.27 Migration of the bubble centroid of a vapour bubble and ideal gas bubbles collapsing from an initially spherical maximum volume in the vicinity of a rigid boundary. For the vapour bubble and all cases of the ideal gas bubble γ and δ are 1.2 and 0.1505 respectively.

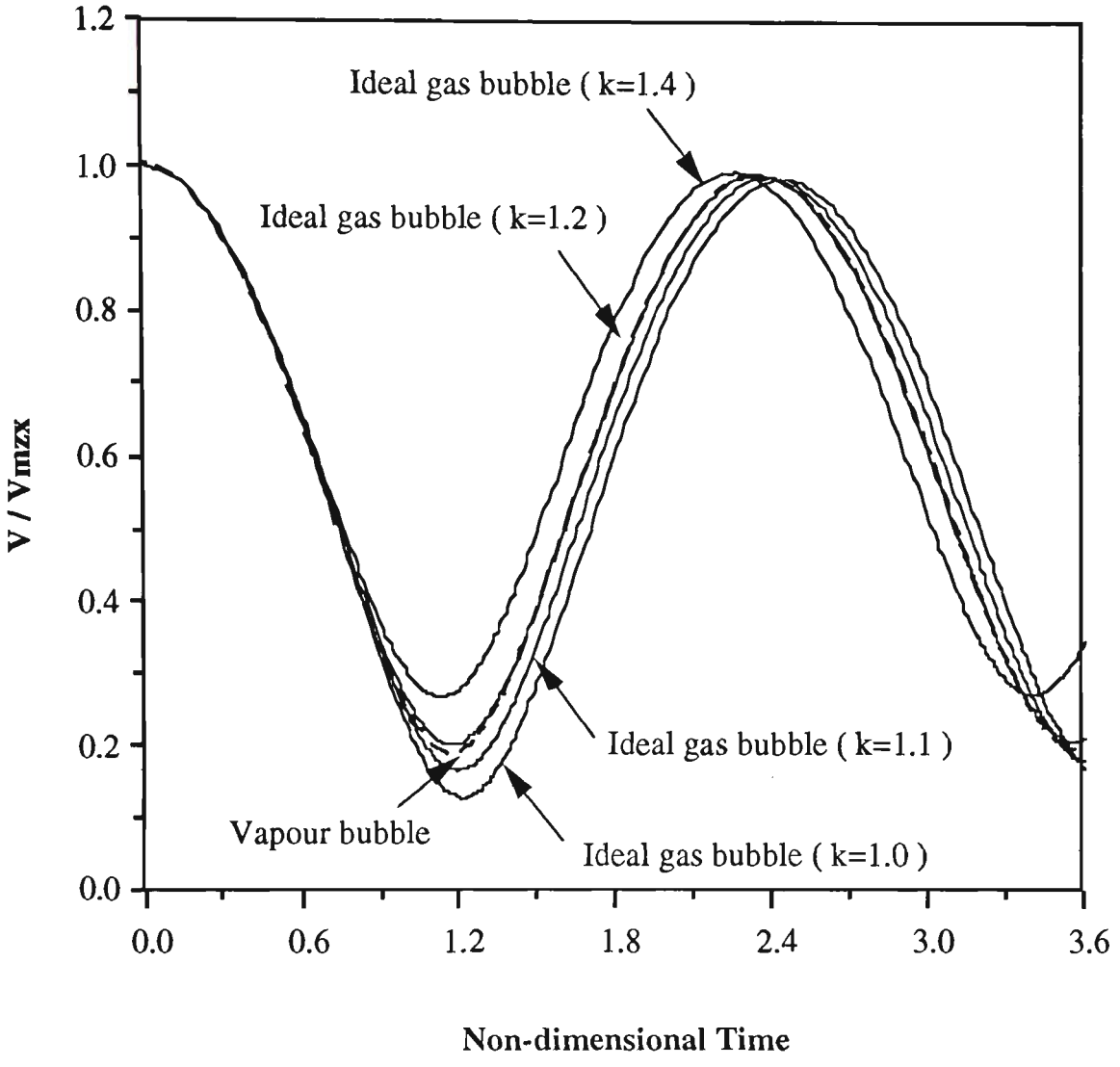

Figure 5.28 Variations of the bubble volume during its pulsation in the cases of a vapour bubble and ideal gas bubbles collapsing from an initially spherical maximum volume in the vicinity of a rigid boundary. For the vapour bubble and all cases of the ideal gas bubble γ and δ are 1.2 and 0.1505 respectively.

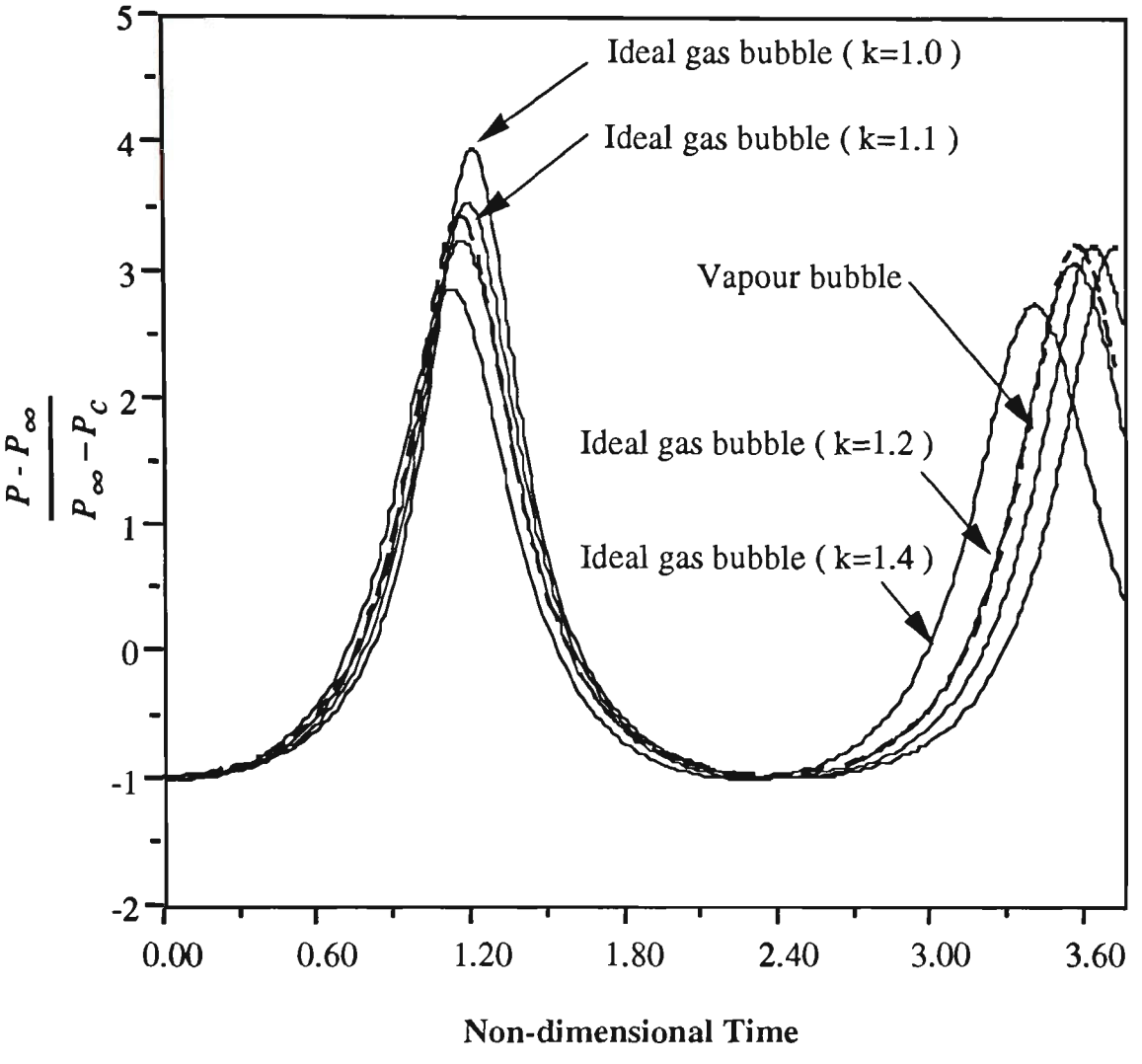

Figure 5.29 Variations of the pressure inside a bubble during its pulsation in the cases of a vapour bubble and ideal gas bubbles collapsing from an initially spherical maximum volume in the vicinity of a rigid boundary. For the vapour bubble and all cases of the ideal gas bubble γ and δ are 1.2 and 0.1505 respectively.

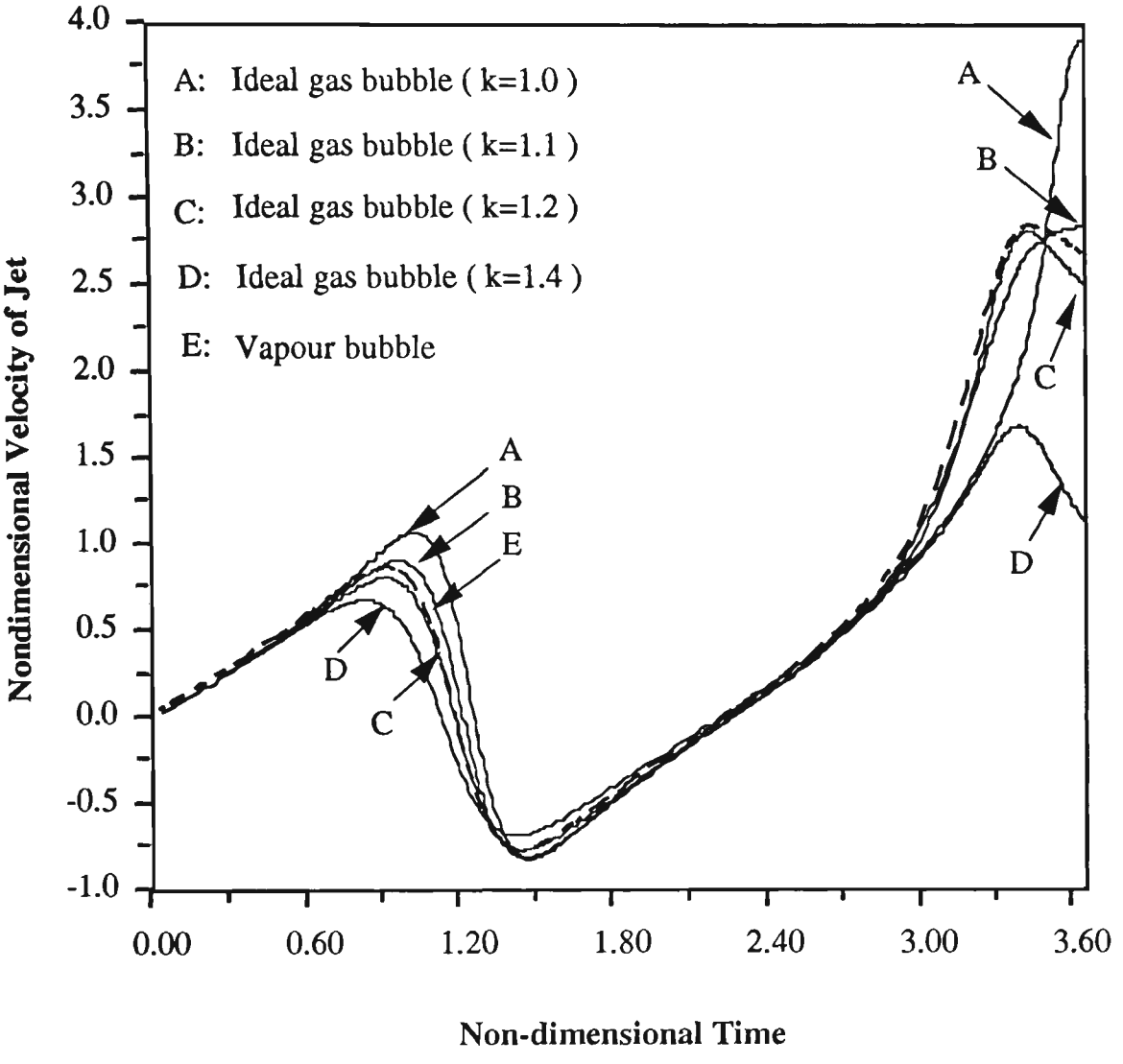

Figure 5.30 Velocity of the liquid jet for a vapour bubble and ideal gas bubbles collapsing from an initially spherical maximum volume in the vicinity of a rigid boundary. For the vapour bubble and all cases of the ideal gas bubble γ and δ are 1.2 and 0.1505 respectively.

5.12 NECKING PHENOMENON AND SPLITTING OF THE BUBBLE

The necking phenomenon occurring during the pulsation of a bubble near a rigid surface has been experimentally observed and numerically obtained by other researchers. This phenomenon occurs under certain conditions and may be thought of as the development of an annular liquid jet around the surface of the bubble, so changing the bubble into a hour-glass shape and splitting it into two parts. Taib (1985) has illustrated this necking phenomenon which occurred during the latest stages of the collapse of a constant pressure vapour bubble in a stagnation point flow near a rigid surface, with $\gamma = 2.0$, $\delta = 0.0$, $\alpha = 0.15$, where α is a measure of the stagnation point flow ($\alpha = \pm bR_m \left(\frac{\rho}{P_0 - P_c} \right)$, where b is the strength of the stagnation point flow). Blake *et al.* (1993) in their experimental and numerical study on the interaction of two bubbles near a rigid boundary observed the necking phenomenon experimentally and calculated it numerically.

It is very interesting to study the necking phenomenon and investigate the parameters that cause necking and splitting of a bubble. In this study the effects of the buoyancy forces in the necking of a bubble in the vicinity of a rigid boundary are investigated. It should be noted that the effect of the other parameters which may cause the necking of bubble such as stagnation point flow are not considered. Consequently, in order to study the influence of the Bjerknes effect through the rigid boundary and buoyancy forces on the necking of a bubble during its pulsation near a rigid surface, the dynamics of the bubble are calculated for a fixed value of δ and different values of γ.

Figure 5.31 illustrates the dynamics of a gas bubble with $\gamma = 0.75$, $\delta = 0.2557$ and $\varepsilon = 10$. In this case during the expansion of the bubble to its maximum

volume the side of the bubble close to the rigid boundary attaches to it. During the collapse phase a liquid jet is developed on the side of the bubble far from the rigid boundary and directed towards it. Thus in this case the Bjerknes attraction force of the rigid boundary completely dominates the fluid motion.

In Figure 5.32 the bubble is initially located relatively far away from the rigid boundary with $\gamma = 1.0$, $\delta = 0.2557$ and $\varepsilon = 10$. As shown in the figure during the collapse phase of the bubble an annular liquid jet is developed at the upper part of the bubble. In this case the annular liquid jet splits the bubble into two parts; a smaller upper part far from the rigid boundary and a larger lower part.

Figure 5.33 shows the dynamics of a bubble with $\gamma = 1.125$, $\delta = 0.2557$ and $\varepsilon = 10$. In this case necking occurs at about the middle part of the bubble during its collapse and splits the bubble into two parts.

Figure 5.34 illustrates the behaviour of the bubble during its growth and collapse near a rigid boundary with $\gamma = 1.6$, $\delta = 0.2557$ and $\varepsilon = 10$. In this case the liquid jet is developed at the bottom side of the bubble close to the rigid boundary and directed away from it. Thus the fluid motion, in the case of Figure 5.34, is completely dominated by the buoyancy forces.

Thus it has been found that in the case of a bubble near a rigid surface, by considering only the effects of the buoyancy forces, the necking of a bubble occurs under the conditions that the Bjerknes attraction force through the rigid boundary and buoyancy forces are comparable with respect to each other and none of them can completely dominate the fluid motion.

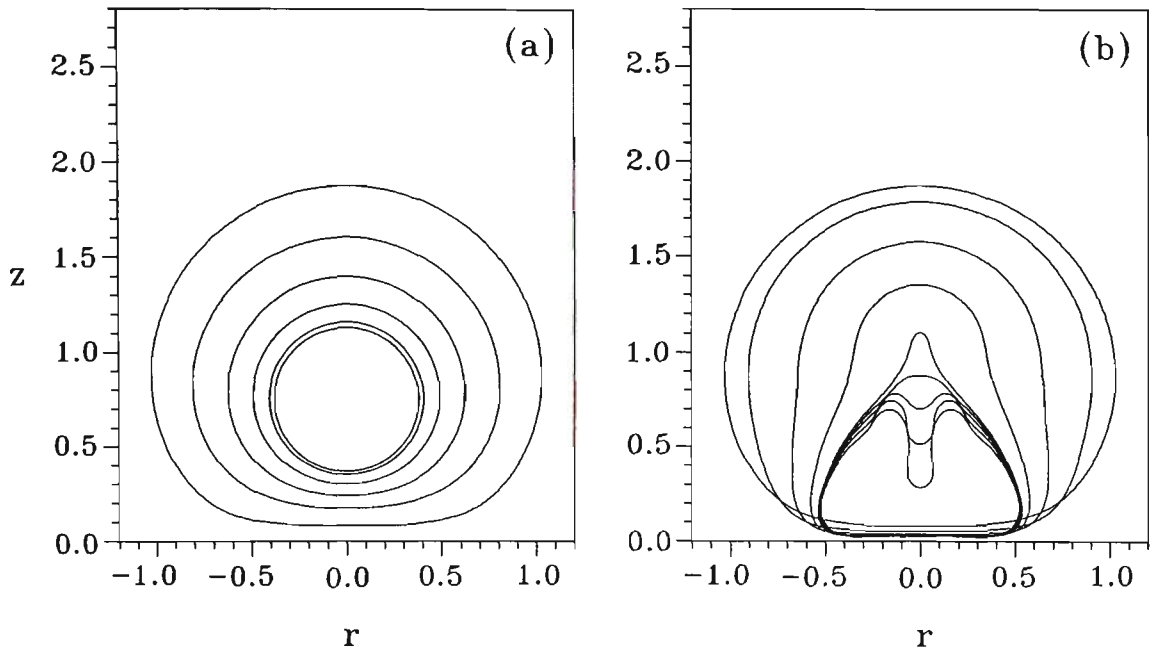

Figure 5.31 Bubble shapes for the growth (a) and collapse (b) of a bubble containing a mixture of constant pressure vapour and ideal gas above a rigid boundary with $\gamma = 0.75$, $\delta = 0.2557$ and $\varepsilon = 10$. The non-dimensional times corresponding to bubble successive profiles are: (a) Growth phase: 0.0000 (innermost), 0.0495, 0.1237, 0.2349, 0.4511, 1.2980 (outermost). (b) Collapse phase: 1.2980 (outermost), 1.7936, 2.1747, 2.3908, 2.5038, 2.5090, 2.5163, 2.5253, 2.5368 (innermost).

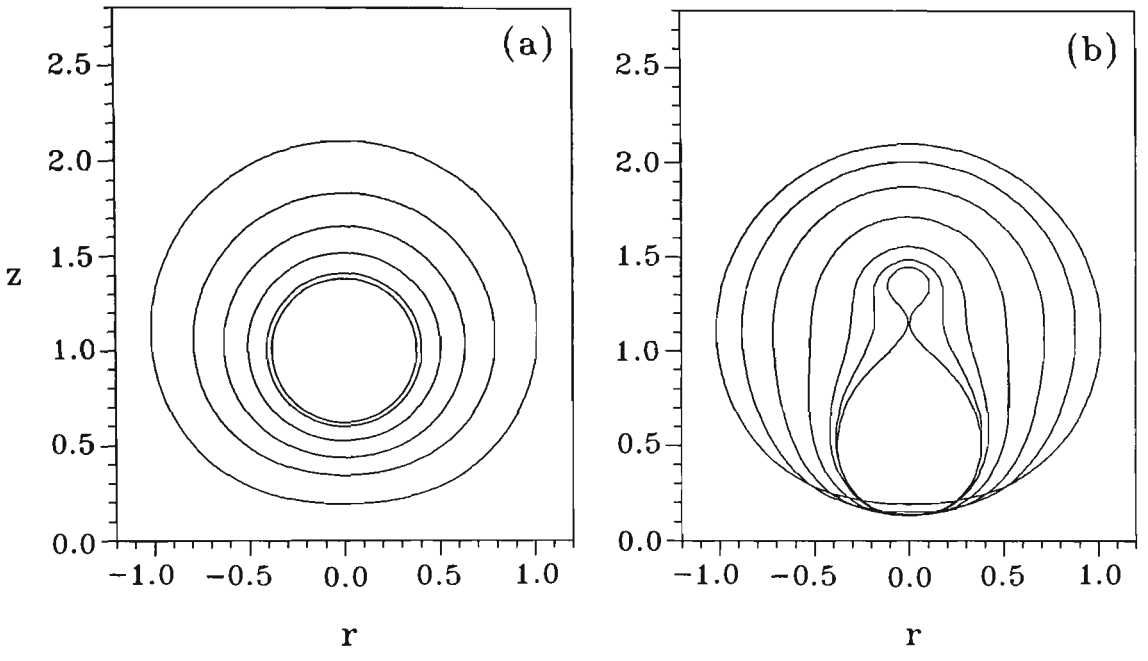

Figure 5.32 Bubble shapes for the growth (a) and collapse (b) of a bubble containing a mixture of constant pressure vapour and ideal gas above a rigid boundary with $\gamma = 1.0$, $\delta = 0.2557$ and $\varepsilon = 10$. The non-dimensional times corresponding to bubble successive profiles are: (a) Growth phase: 0.0000 (innermost), 0.0497, 0.1330, 0.2428, 0.4285, 1.2657 (outermost). (b) Collapse phase: 1.2740 (outermost), 1.2657, 1.7901, 2.0545, 2.2572, 2.3975, 2.4564, 2.5082 (innermost).

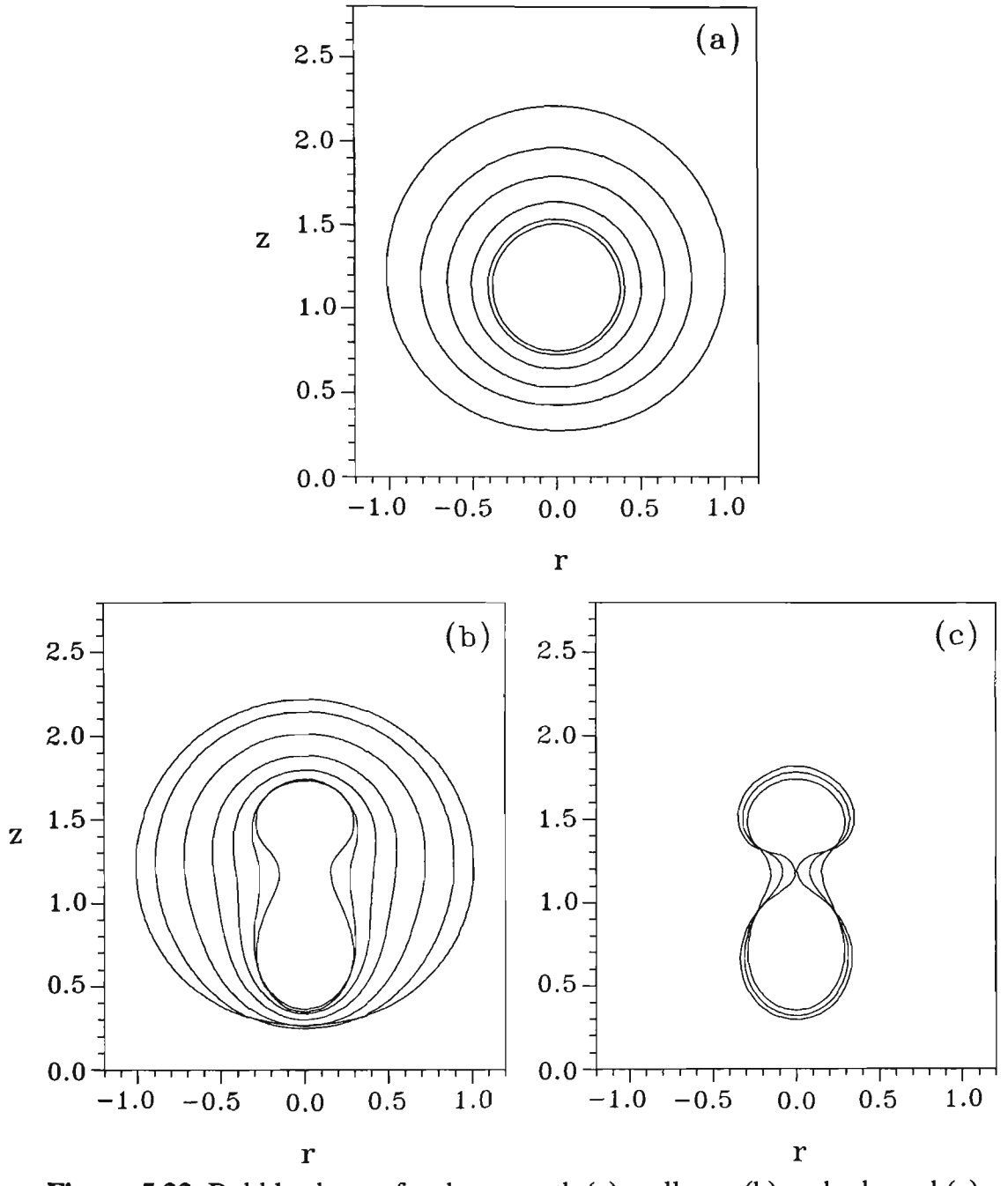

Figure 5.33 Bubble shapes for the growth (a), collapse (b) and rebound (c) of a bubble containing a mixture of constant pressure vapour and ideal gas above a rigid boundary with $\gamma = 1.125$, $\delta = 0.2557$ and $\varepsilon = 10$ The non-dimensional times corresponding to bubble successive profiles are: (a) Growth phase: 0.0000 (innermost), 0.0497, 0.1338, 0.2593, 0.4575, 1.2740 (outermost). (b) Collapse phase: 1.2740 (outermost), 1.7713, 2.0678, 2.2561, 2.3705, 2.4535, 2.5221 (innermost). (c) Rebound phase: 2.5221 (innermost), 2.5592, 2.5855 (outermost).

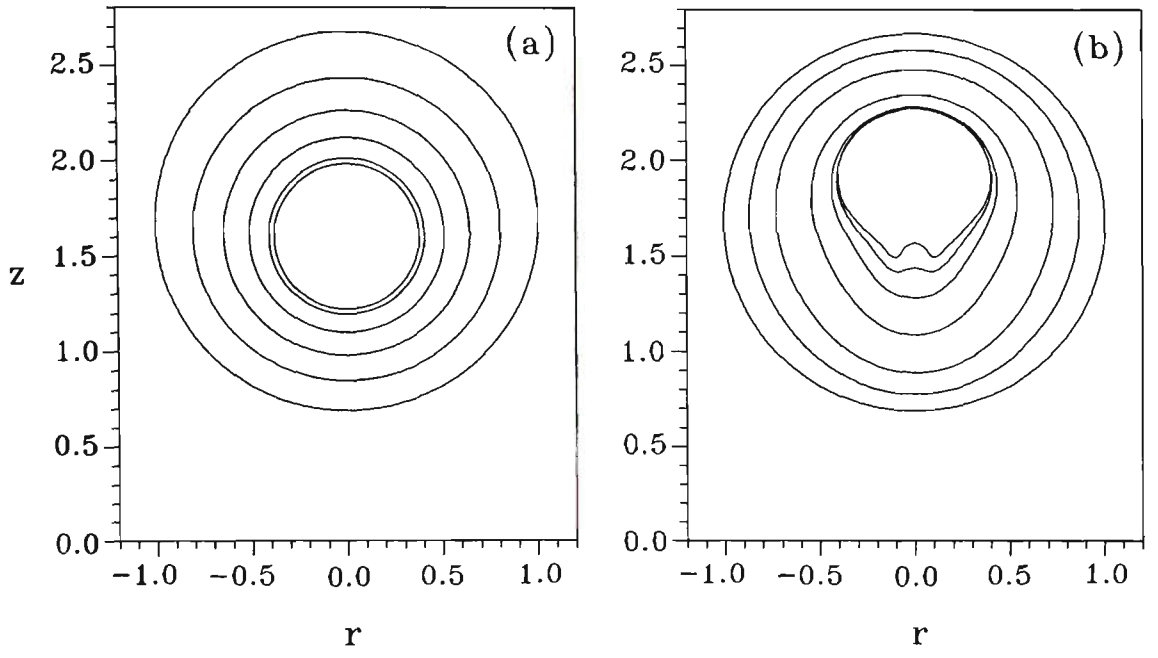

Figure 5.34 Bubble shapes for the growth (a) and collapse (b) of a bubble containing a mixture of constant pressure vapour and ideal gas above a rigid boundary with $\gamma = 1.6$, $\delta = 0.2557$ and $\varepsilon = 10$. The non-dimensional times corresponding to bubble successive profiles are: (a) Growth phase: 0.0000 (innermost), 0.0499, 0.1354, 0.2518, 0.4505, 1.2298 (outermost). (b) Collapse phase: 1.2298 (outermost), 1.8154, 2.0431, 2.2484, 2.3500, 2.3920, 2.4183, 2.5082 (innermost).

Figures 5.35(a) and (b) show the dynamic characteristics of a bubble corresponding to the case of Figure 5.31. In this case the liquid jet is directed towards the rigid boundary and the centroid of the bubble undergoes a strong migration towards the rigid boundary. The fluid motion is dominated by the Bjerknes attraction effect through the rigid boundary.

Figures 5.36(a) and (b) illustrate the dynamic characteristics of a bubble for the case of Figure 5.32. In this case the necking occurs at the upper part of the bubble and the bubble centroid also has a strong migration towards the rigid boundary.

Figures 5.37(a), (b) and (c) illustrates the dynamic characteristics of the bubble corresponding to the case of the behaviour presented in Figure 5.33. It is shown that the necking of bubble occurs in the early stages of the bubble rebound. In this case the necking occurs at about middle part of the bubble and the migration of the bubble centroid towards the rigid boundary is weak.

Figure 5.38(a) and (b) illustrate the dynamic characteristics of the bubble corresponding to the case of Figure 5.34. In this case the liquid jet is directed away from the rigid boundary and the bubble centroid has a strong migration away from the rigid surface. In this case the fluid motion is dominated by the buoyancy forces.

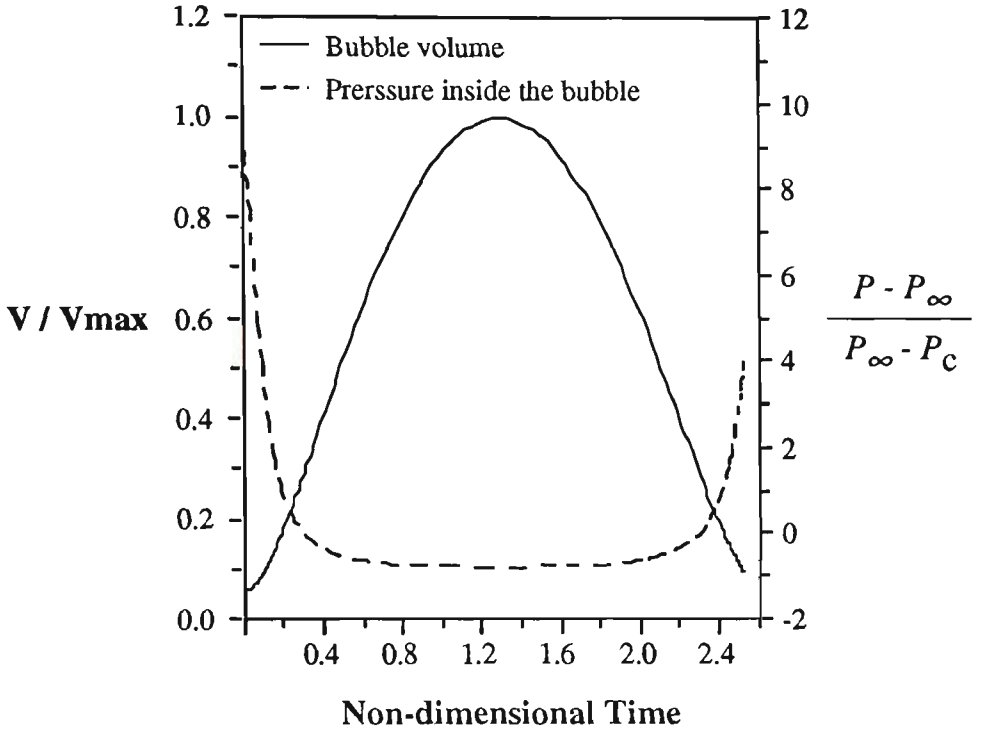

Figure 5.35(a) Variation of the bubble volume and internal pressure during its growth and collapse for $\gamma = 0.75$, $\delta = 0.2557$ and $\varepsilon = 10$.

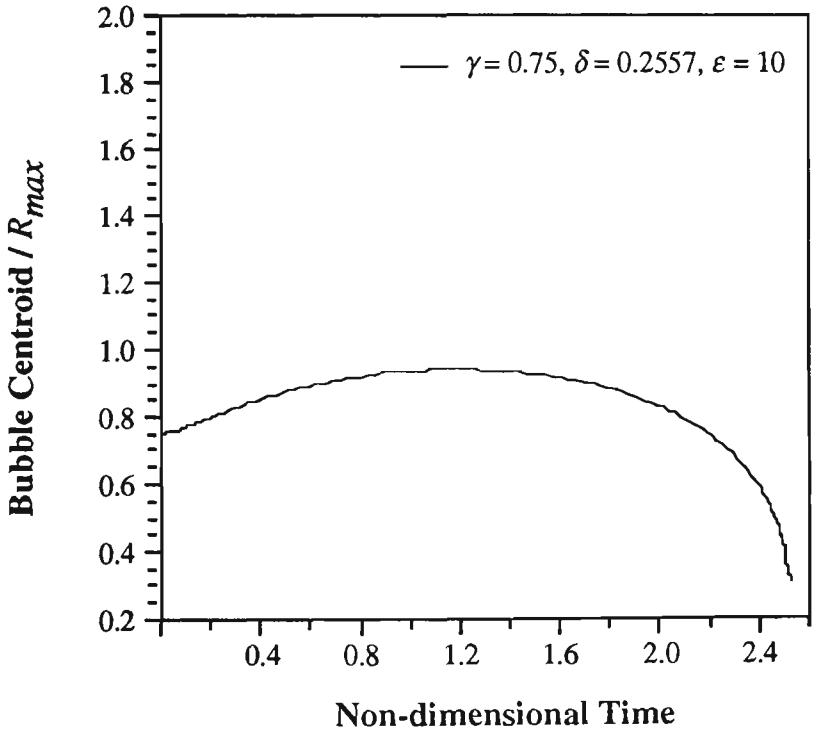

Figure 5.35(b) Migration of the bubble centroid during its growth and collapse for $\gamma = 0.75$, $\delta = 0.2557$ and $\varepsilon = 10$.

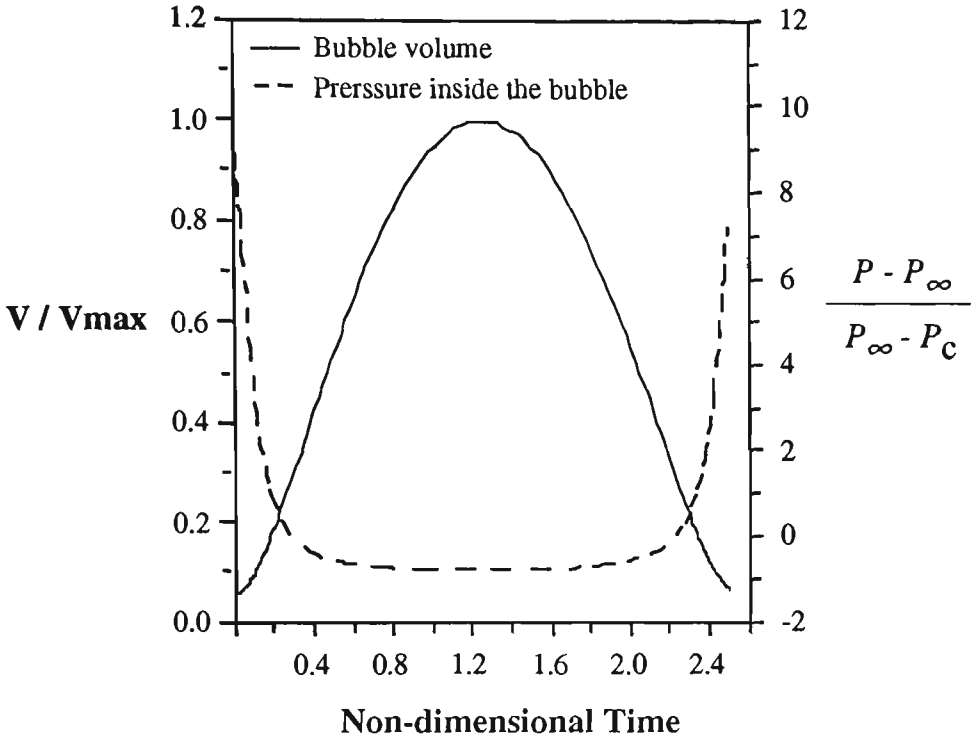

Figure 5.36(a) Variation of the bubble volume and internal pressure during its growth and collapse for $\gamma = 1.0$, $\delta = 0.2557$ and $\varepsilon = 10$

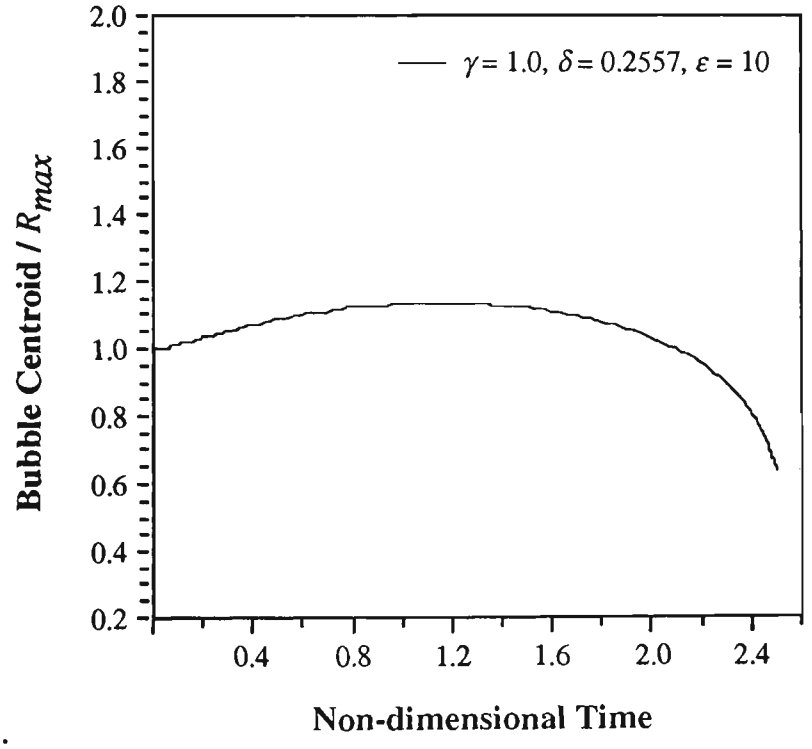

Figure 5.36(b) Migration of the bubble centroid during its growth and collapse for $\gamma = 1.0$, $\delta = 0.2557$ and $\varepsilon = 10$.

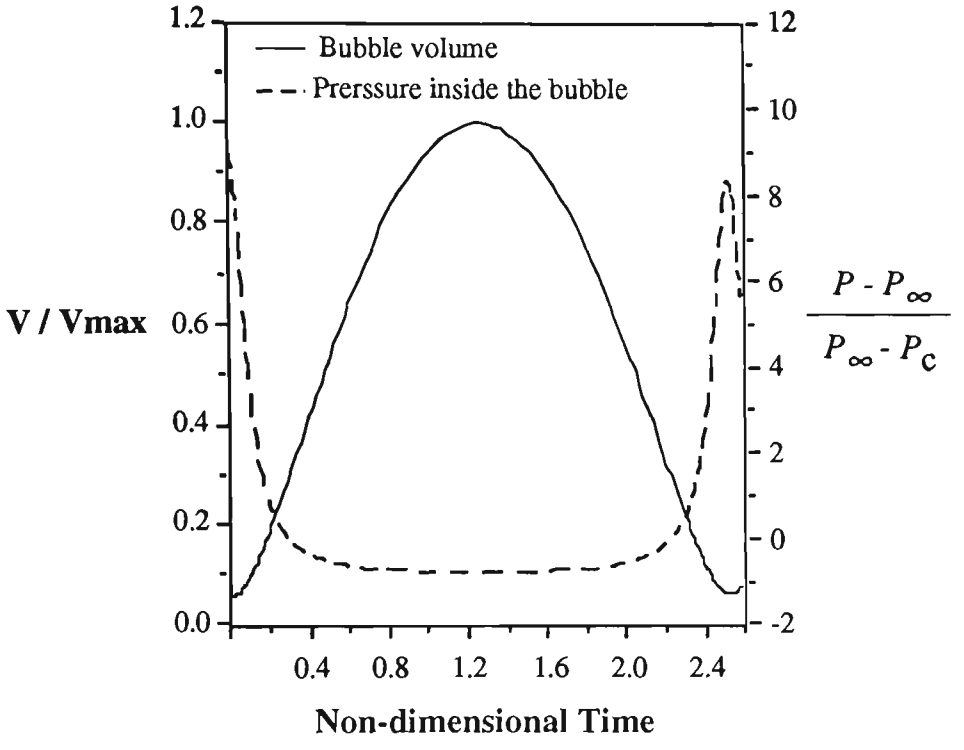

Figure 5.37(a) Variation of the bubble volume and pressure in its inside during its growth, collapse and rebound for $\gamma = 1.125$, $\delta = 0.2557$ and $\varepsilon = 10$

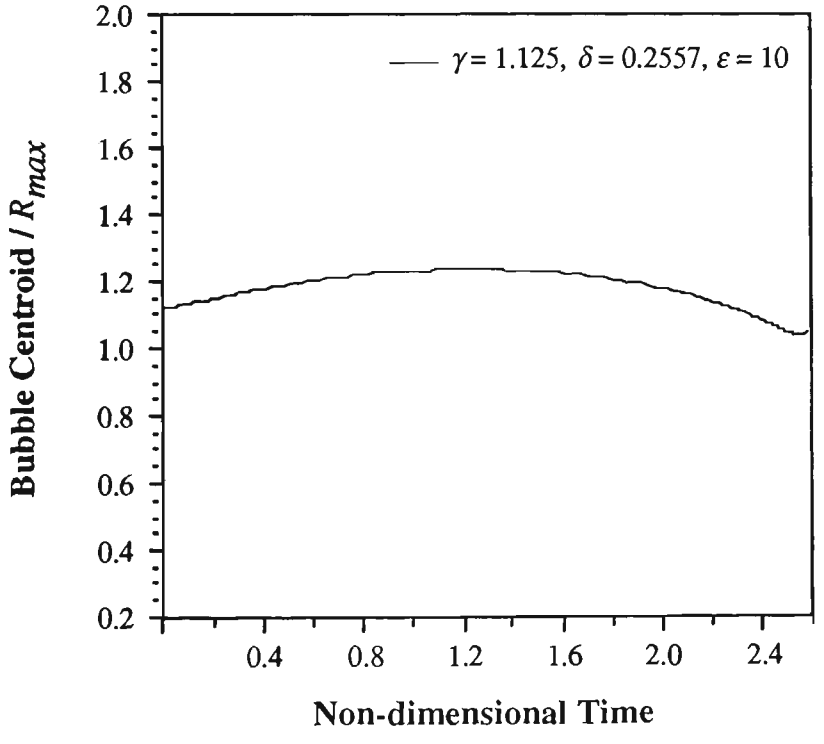

Figure 5.37(b) Migration of the bubble centroid during its growth, collapse and rebound for $\gamma = 1.125$, $\delta = 0.2557$ and $\varepsilon = 10$.

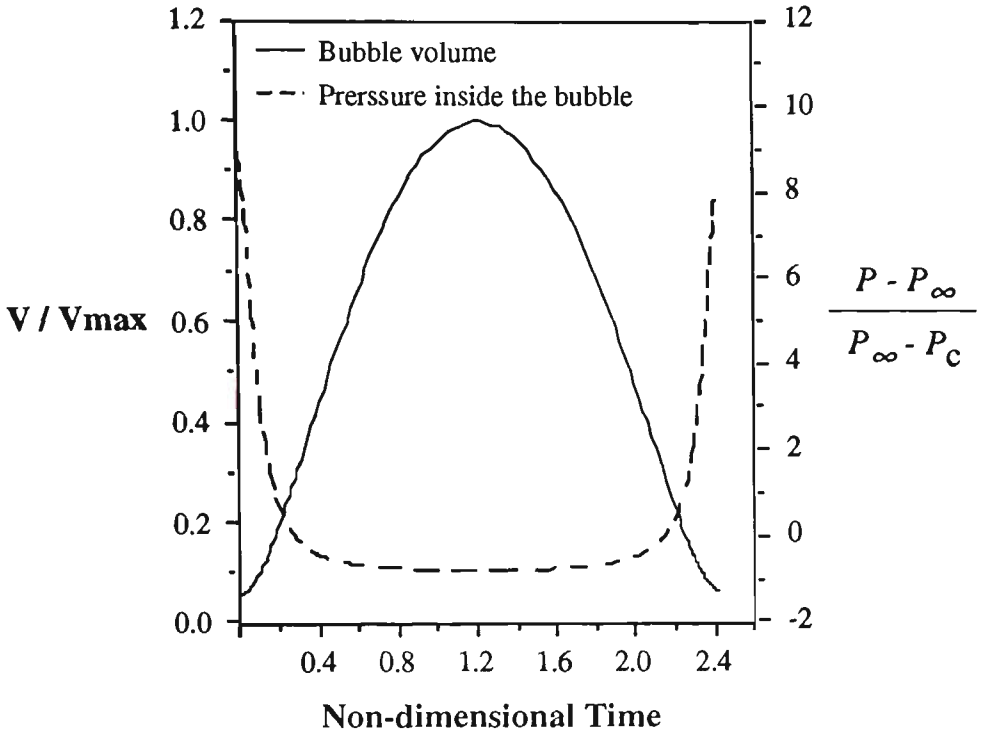

Figure 5.38(a) Variation of the bubble volume and internal pressure during its growth and collapse for $\gamma = 1.6$, $\delta = 0.2557$ and $\varepsilon = 10$

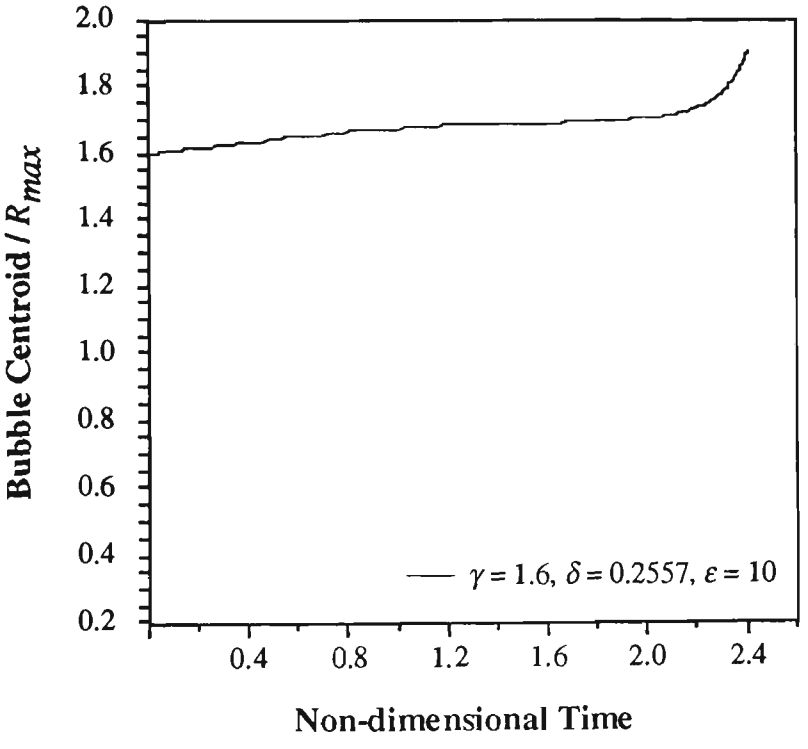

Figure 5.38(b) Migration of the bubble centroid during its growth and collapse for $\gamma = 1.6$, $\delta = 0.2557$ and $\varepsilon = 10$.

5.13 SUMMARY AND CONCLUDING REMARKS

In this chapter the dynamics of a pulsating bubble in the vicinity of a rigid boundary has been investigated by using a computer model based on the boundary integral equation. The numerical method of Cubic Spline Geometry-Constant Physical Function, which is introduced and discussed in *Chapter 3*, is used to model the bubble boundary and the distribution of the velocity potential over the bubble surface.

Results show that in the absence of buoyancy forces a high speed liquid jet is developed on the side of the bubble far from the rigid boundary and directed towards it.

It has been shown that buoyancy forces have significant effect on the dynamics of the bubble. Strong buoyancy forces acting opposite to the Bjerknes attraction effect of the rigid boundary may cause the development of a liquid jet on the side of the bubble close to the rigid boundary and directed away from it.

Results show that the development of the high speed liquid jet towards the rigid boundary occurs in a very short period of time.

It has also been found that in the case of a bubble located nearer to the rigid boundary the collapse rate of the bubble and the velocity of the liquid jet are reduced. The early initiation and development of the liquid jet in the case of the bubble nearer to the rigid boundary causes a larger bubble volume at the time of its transformation to a toroidal one which causes a broader liquid jet with a lower velocity. Early initiation and development of the liquid jet also occurs when the buoyancy forces act in the direction of the Bjerknes attraction force.

Results show that in the case of a rebounding bubble near a rigid boundary the development of the liquid jet is a continuous process that is independent of the direction of the bubble pulsation.

For a rebounding bubble generated by a high local energy input with δ=0.1808 and ε=10, it is found that the critical case for the direction of the liquid jet occurs in the case of γ=2.125. In this case in the second collapse of the bubble two liquid jets are developed on both sides of the bubble on the axis of symmetry directed to each other. In this case it is that the critical value of $\gamma\delta$ for determining the direction of the liquid jet is slightly different from the critical value which is already found for a constant pressure vapour bubble by Blake *et al.*.

Results show that in the case of a buoyant rebounding bubble generated by a high local energy input and pulsating near a rigid boundary, necking and splitting of the bubble may occur. It is found that for specified buoyancy forces the location of the necking may be controlled by variation of the Bjerknes attraction force through the rigid boundary. It is found that, by considering only the effects of the buoyancy forces, the necking of a bubble occurs under the conditions that the Bjerknes attraction effect through the rigid boundary and buoyancy forces are comparable with respect to each other. In this case none of the Bjerknes attraction force and buoyancy forces can completely dominate the fluid motion.

CHAPTER SIX

DYNAMICS OF A PULSATING BUBBLE BENEATH A FREE SURFACE

6.1 INTRODUCTION

Dynamics of a vapour bubble beneath a free surface has been one of the interesting fields in the study of the behaviour of a cavitation bubble. Chahine and Bovis (1980) investigated the dynamics of a vapour bubble beneath a two-liquid interface experimentally (i.e. bubble located in the denser liquid). They observed two different directions of bubble migration. The bubble was repelled by the two liquid interface when it was initially located closer than a critical distance from the interface. The bubble was attracted by the interface if it was further away. Blake and Gibson (1981) studied the dynamics of an electrical spark generated vapour bubble near a free surface experimentally and theoretically. They observed a liquid jet during the collapse phase of the bubble which is developed on the closest side of the bubble to the free surface and directed away from it. The results of their numerical investigations produced a very good agreement with their experimental results. They found that in the case of a bubble very close to the free surface, the free surface developed a liquid jet (spike) moving away from the bubble, with bubble collapsing producing a liquid jet directed away from the surface. The numerical investigations of Ceron and

Blake (1984) and Taib (1985) showed that in the absence of buoyancy forces, the vapour bubble beneath a free surface always collapses with a liquid jet directed away from the surface.

In the numerical studies of bubble dynamics beneath a free surface [Blake and Gibson (1981), Ceron and Blake (1984), Blake *et al.* (1984) and Taib (1985)] it is assumed that the bubble contains(ed) constant pressure vapour. Comparisons between the experimental and numerical results obtained by Blake and Gibson (1981) show very good agreement during the first cycle of bubble pulsation. Experimental observations show that an electrical spark generated bubble often pulsates through more than one cycle of growth and collapse [Gibson (1968), Lauterborn (1980), Wong *et al.* (1989) and Soh and Yu (1992)]. It should be noted that rebounding of a vapour bubble near a free surface affects the dynamic behaviour of the free surface. It is obvious that any change in the dynamic behaviour of the free surface affects the bubble dynamics.

In this chapter dynamics of a bubble beneath a free surface is investigated in the cases of

- a bubble containing constant pressure vapour,
- a bubble containing a mixture of constant pressure vapour and ideal gas.

To examine the interaction between the free surface and the bubble, the buoyancy forces are first ignored. By ignoring the buoyancy forces, the dynamics of the bubble may be calculated only under the Bjerknes force through the free surface. To investigate the interesting features of bubble dynamics under the effects of both the Bjerknes force through the free surface and the action of gravitational force, the buoyancy forces are then included.

6.2 GEOMETRICAL DEFINITION

As shown in Figure 6.1, the vapour bubble inside the liquid domain is located beneath a free surface. The problem is assumed to be axisymmetrical and r and z are the radial and vertical axes of cylindrical polar coordinates respectively. The radial axis is laid on the initial undisturbed flat free surface and the positive direction of vertical axis is towards into the liquid domain. Thus any movement of the free surface upward is in the negative direction of the vertical axis.

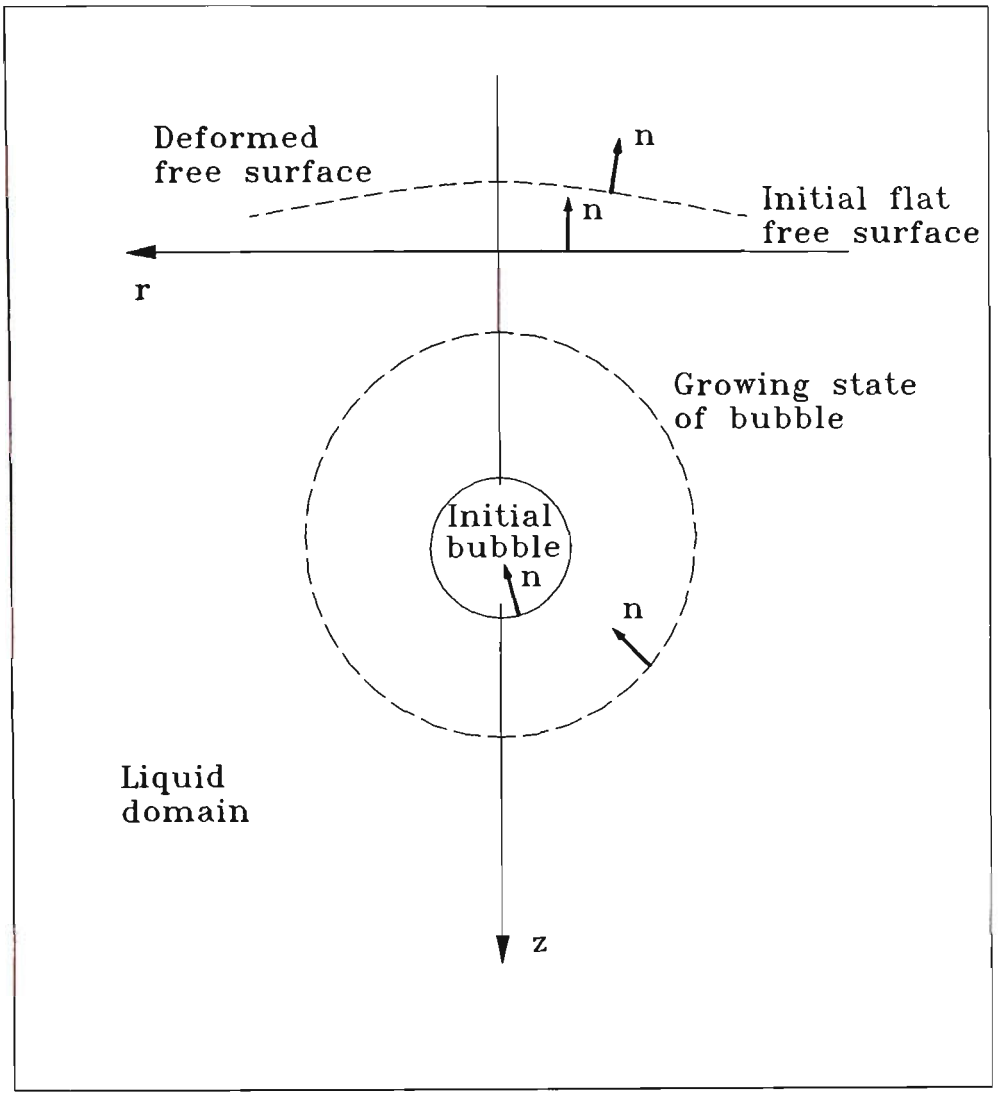

Figure 6.1 Geometry selected for modelling of the pulsation of a vapour bubble near a free surface

6.3 MATHEMATICAL MODELLING

The fluid flow is assumed to be incompressible, inviscid and irrotational and the surface tension on the bubble boundary and the free surface is neglected. Thus the liquid domain behaves in the framework of potential flow and the velocity everywhere in the liquid domain and on the bubble boundary and the free surface may be represented as the gradient of a potential which satisfies Laplace's equation.

6.3.1 Hydrodynamic equation

The free surface is assumed to lie in the horizontal plane initially, and the vapour bubble is assumed to be in its minimum spherical volume with a small radius R_0 located beneath the free surface, with a distance h between the centroid of the bubble and the free surface. Then the liquid domain is bounded by the free surface which is extended to infinity and the surface of the bubble. Thus the hydrodynamic equation to govern the dynamics of the free surface and the bubble may be written as the Green's integral formula

$$c + \int_s \left(\phi \frac{\partial G}{\partial n} - \frac{\partial \phi}{\partial n} G \right) ds = 0, \tag{6.1}$$

where S includes the surface of the bubble and the free surface, and G is Green's function and is due to a source in an infinite fluid. The coefficient $c(p)$ is 2π if the collocation point is on either the free surface or the surface of the bubble and is 4π if the collocation point is in the liquid domain. Thus Green's integral formula for the case of a bubble near a free surface becomes

$$c(p)\phi(p)+\int_{S_b+S_{fs}}\phi(q)\frac{\partial}{\partial n}\left(\frac{1}{p-q}\right)dS=\int_{S_b+S_{fs}}\frac{\partial}{\partial n}[\phi(q)]\left(\frac{1}{p-q}\right)dS, \tag{6.2}$$

where S_b indicates the surface of the bubble, S_{fs} represents the free surface, p is a collocation point which is any given point in the liquid domain, or on S, which includes S_b and S_{fs}, and q is a point on S.

6.3.2 A constant pressure vapour bubble near a free surface

The initial potential on the surface of a constant pressure vapour bubble in its minimum volume with a small radius R_0 is obtained from the Rayleigh bubble solution which is appropriately modified because of the flat free surface existing above the vapour bubble. In this case by incorporating the negative image of the bubble, the appropriately modified Rayleigh equation becomes [Blake et al. (1987)]

$$\phi_0=\phi_0^R-\left(1-\frac{R_0}{\left[(z+h)^2+r^2\right]^{\frac{1}{2}}}\right), \tag{6.3}$$

where ϕ_0^R is the velocity potential over an isolated bubble surface in its initial minimum volume, R_0 is the initial radius of the bubble, h is the initial distance of the bubble centroid from the free surface, while z and r are axial and radial cylindrical polar coordinates.

The initial potential on the flat free surface is assumed to be zero, as would occur in the linear theory, and the constant pressure on the free surface is P_0.

The kinematic condition on the surface of the bubble and free surface comes from the fact that the fluid particles remain on the surface of the bubble and on the free

surface. Then, by taking the velocity of these particles equal to the velocity of the fluid and using Lagrangian description for these particles to specify the evolution of the bubble and the free surface, the radial and vertical velocities of every point in the liquid domain and its boundaries are given by

$$u = \frac{\partial \phi}{\partial r}, \quad v = \frac{\partial \phi}{\partial z}. \tag{6.4}$$

By equating the dynamic pressure to the constant vapour pressure inside the bubble, the dynamic condition on the surface of the bubble is obtained

$$P_c = P_0 + \rho g z - \rho \frac{\partial \phi}{\partial t} - \frac{1}{2}\rho \mid \nabla \phi \mid^2. \tag{6.5}$$

By imposing the non-dimensionalising scales, which are introduced in *Section 5.3*, the non-dimensional Lagrangian form of Equation (6.5) becomes

$$\frac{D\Phi}{D\mathrm{t}} = 1 + \frac{1}{2}|\nabla\Phi|^2 + \delta^2(\mathrm{z} - \gamma). \tag{6.6}$$

The dynamic condition on the free surface is evaluated by equating the dynamic pressure to the constant pressure acting on the free surface

$$P_0 = P_0 - \rho \frac{\partial \phi}{\partial t} - \frac{1}{2}\rho \mid \nabla \phi \mid^2. \tag{6.7}$$

The non-dimensional Lagrangian form of Equation (6.7) can be written in the form of

$$\frac{D\Phi}{D\mathrm{t}} = \frac{1}{2}|\nabla\Phi|^2 + \delta^2 \mathrm{z}. \tag{6.8}$$

6.3.3 Bubble contains a mixture of constant pressure vapour and ideal gas

As it is discussed in *Section 5.5,* in this case the bubble is generated because of high local energy input and is assumed to be initiated from its minimum volume with a high internal pressure. The initial radius of the bubble and the initial high internal pressure is determined in such a way that the maximum non-dimensional radius to which the bubble expands in an infinite liquid domain is one.

6.4 DISCRETIZATION

Consider an axisymmetric bubble which is located beneath a free surface. The liquid domain is bounded by the free surface and the bubble boundary, and is extended to the infinity. As it is illustrated in Figure 6.2, the surface of the bubble is divided into M segments while the free surface is discrtized by N segments which start from the axis of symmetry. The discretization of the free surface is continued to a point on the free surface which has a negligible movement during the pulsation of the bubble. Cubic splines are employed to approximate the surface of the bubble whereas the free surface is approximated by linear segments. The collocation points are located at the mid points of each segment. By indicating S_j as the j_{th} segment, the discretized form of Equation (6.2) for a point p_i, on the surface of the bubble or on the free surface, is given by:

$$2\pi\phi(p_i)+\sum_{j=1}^{M+N}\phi(q_j)\int_{S_j}\frac{\partial}{\partial n}\left(\frac{1}{p_i-q_j}\right)dS=\sum_{j=1}^{M+N}\frac{\partial}{\partial n}\left[\phi(q_j)\right]\int_{S_j}\left(\frac{1}{p_i-q_j}\right)dS. \quad (6.9)$$

The integrations over the surface are carried out analytically, where the collocation points p_i are located at the mid of the segments. Thus Equation (6.9) becomes a system of linear equations of the following form:

$$2\pi\phi(p_i)+\sum_{j=1}^{M+N}H_{ij}\phi(q_j)=\sum_{j=1}^{M+N}G_{ij}\psi(q_j), \qquad (6.10)$$

where H_{ij} and G_{ij} are the terms with respect of integration in Equation (6.9) which are integrated over each segment.

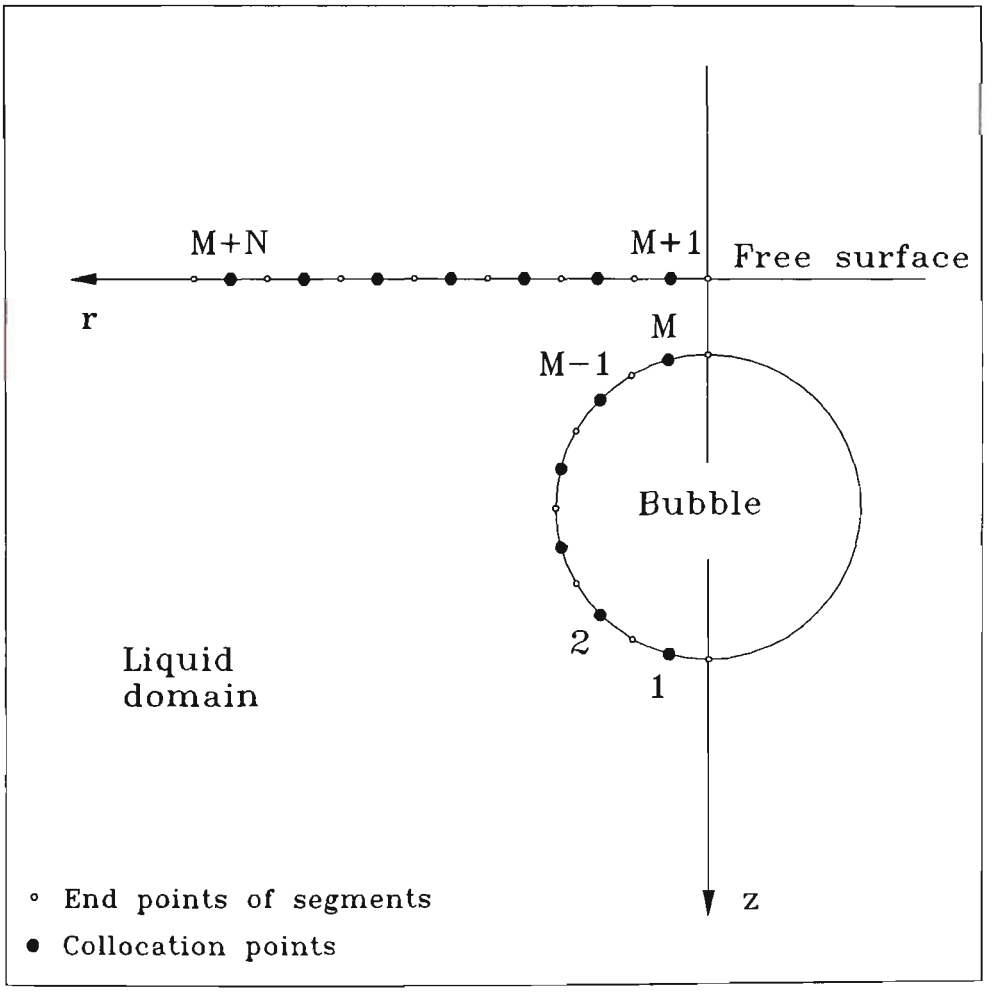

Figure 6.2 Discretization of the surface of the bubble and the free surface

6.5 COMPUTATIONAL IMPLEMENTATION

From a given distribution of velocity potential ϕ, the normal velocity ψ on the surface of the bubble and on the free surface is determined from Equation (6.10).

The tangential velocity, η, on the surface of the bubble and on the free surface may be determined by Equations (3.31) and (3.18) respectively.

The variable time step which is discussed in *Section 5.10* is used for incrementing in time.

In order to obtain an accurate solution, the Runge-Kutta method of order two is employed as the integration scheme over the time.

The implementation of the second order Runge-Kutta integration is discussed in *Section (5.8).*

6.6 NUMERICAL RESULTS AND DISCUSSION

In this section dynamics of a constant pressure vapour bubble, and also dynamics of a rebounding bubble near a free surface, are investigated by applying the boundary integral equation method.

6.6.1 The growth and collapse of a constant pressure vapour bubble beneath a free surface

In this section dynamics of a constant pressure vapour bubble beneath a free surface and the behaviour of the free surface is investigated with and also without considering the effects of the buoyancy forces on the motion of the fluid.

6.6.1.1 Dynamics of a constant pressure vapour bubble beneath a free surface without considering buoyancy forces

Figure 6.3 illustrates the shape of the bubble and the free surface at selected non-dimensional times, for $\gamma = 1.5$. It is shown that during the growth phase the bubble grows almost spherically and the free surface is pushed up by the growth of the bubble. The free surface falls with the collapse of the bubble. During the collapse phase the top side of the bubble nearer to the free surface becomes flattened and develops a broad liquid jet directed away from the free surface at the latest stages of the bubble collapse.

Figure 6.4 shows that in the case of the bubble with $\gamma = 0.98$, during the growth phase the top side of the bubble nearer to the free surface moves towards the free

surface and is elongated upward vertically. In this case the free surface moves upward and forms a substantial free-surface spike. At the latest stages of the growth phase the elongated top side of the bubble is entrained into the base of the raised free surface. During the collapse phase the bubble migrates downward with a liquid jet directed away from the free surface. Whereas the free-surface spike continues to grow along the axis of symmetry. The movement of the free surface and the top side of the bubble in the opposite directions produces a stagnation point on the axis of symmetry between the free surface and the bubble.

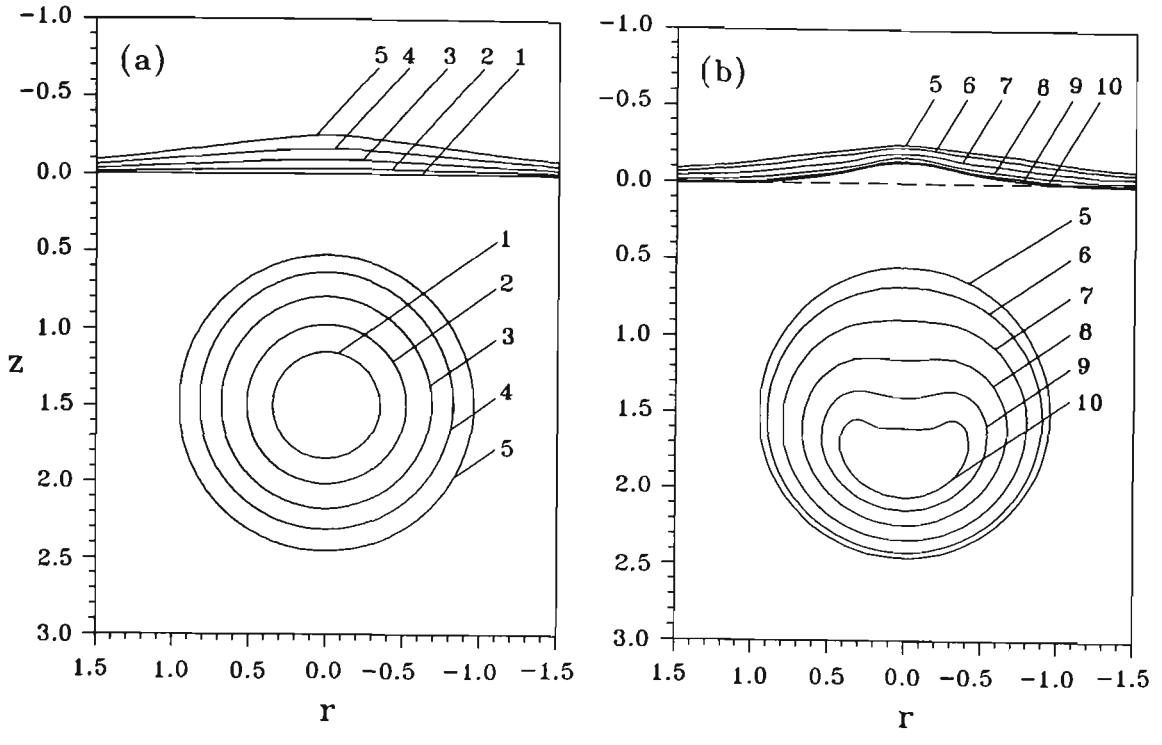

Figure 6.3 Bubble and free surface shapes for the growth (a) and collapse (b) of a constant pressure vapour bubble beneath a free surface with $\gamma = 1.5$ and $\delta = 0.0$. The non-dimensional times corresponding to bubble and free surface successive profiles are: (a) Growth phase: (1) 0.0360, (2) 0.0973, (3) 0.2033, (4) 0.3538, (5) 0.7640. (b) Collapse phase: (5) 0.7640, (6) 0.9828, (7) 1.1806, (8) 1.3310, (9) 1.4248, (10) 1.4846.

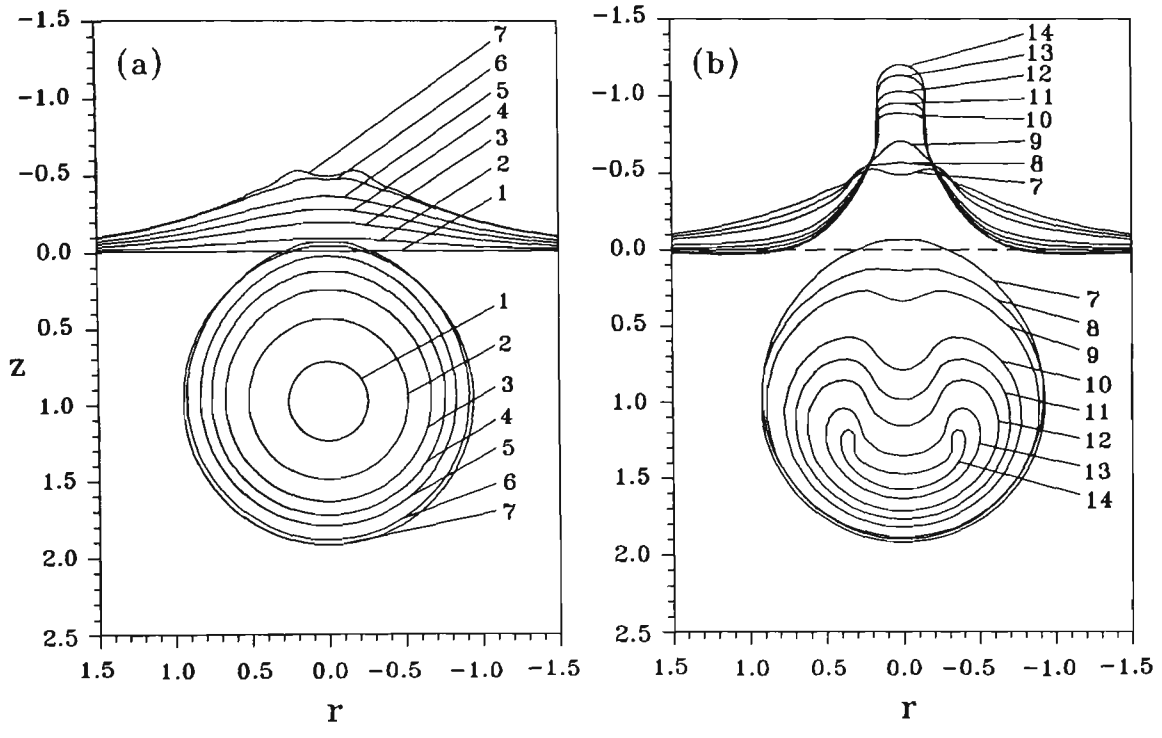

Figure 6.4 Bubble and free surface shapes for the growth (a) and collapse (b) of a constant pressure vapour bubble beneath a free surface with $\gamma = 0.98$ and $\delta = 0.0$. The non-dimensional times corresponding to bubble and free surface successive profiles are: (a) Growth phase: (1) 0.0154, (2) 0.0889, (3) 0.1768, (4) 0.2551, (5) 0.3407, (6) 0.5168, (7) 0.6804. (b) Collapse phase: (7) 0.6804, (8) 0.8631, (9) 0.9767, (10) 1.1648, (11) 1.2378, (12) 1.2992, (13) 1.3882, (14) 1.4071.

6.6.1.2 Dynamics of a buoyant constant pressure vapour bubble beneath a free surface

As shown in the previous section, in the case of a bubble near a free surface the bubble is always repelled by the free surface in the absence of buoyancy forces. This is completely in contrast with the bubble behaviour near a rigid boundary.

Numerical results show that buoyancy forces have a considerable effect on the bubble behaviour beneath a free surface.

Figure 6.5 shows the shape of the free surface and a constant pressure vapour bubble for $\gamma = 1.5$ and $\delta = 0.1808$. As illustrated in Figure 6.5, during the growth phase the bubble remains almost spherical while the free surface raises and forms a free surface-hump. During the collapse phase the bubble migrates away from the free surface and the top side of the bubble nearer to the free surface becomes flattened. A liquid jet is developed on the flattened side of the bubble and is directed away from the free surface. In this case the raised free surface collapses with the collapse of the bubble.

Figure 6.6 illustrates the shape of the free surface and the bubble for $\gamma = 1.0$ and $\delta = 0.6766$. In this case, at the latest stages of growth phase, the bubble is slightly elongated towards the free surface. During the collapse phase the bubble migrates towards the free surface and the bottom side of the bubble far from the free surface becomes flattened. At the latest stages of the collapse phase a broad liquid jet is developed at the flattened side of the bubble and directed towards the free surface. In this case the free surface collapses with the collapse of the bubble.

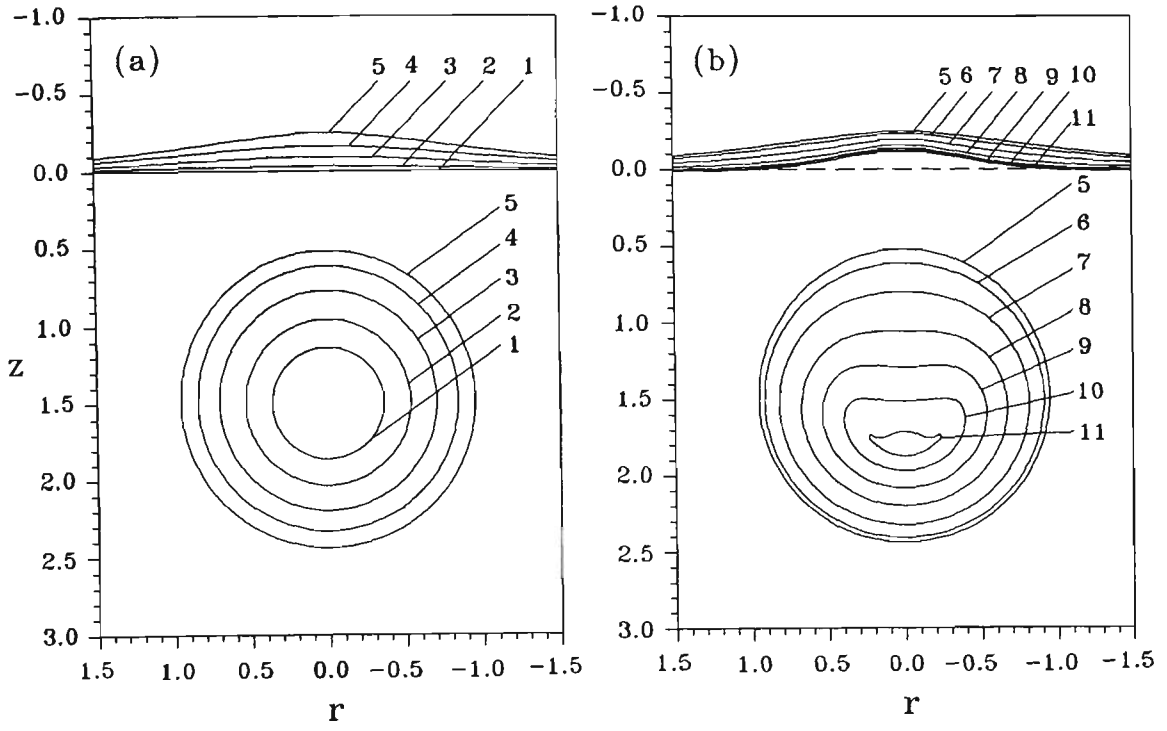

Figure 6.5 Bubble and free surface shapes for the growth (a) and collapse (b) of a constant pressure vapour bubble beneath a free surface with $\gamma = 1.5$ and $\delta = 0.1808$. The non-dimensional times corresponding to bubble and free surface successive profiles are: (a) Growth phase: (1) 0.0360, (2) 0.0980, (3) 0.2068, (4) 0.3638, (5) 0.7688. (b) Collapse phase: (5) 0.7688, (6) 0.9753, (7) 1.1743, (8) 1.3337, (9) 1.4258, (10) 1.4861, (11) 1.5190.

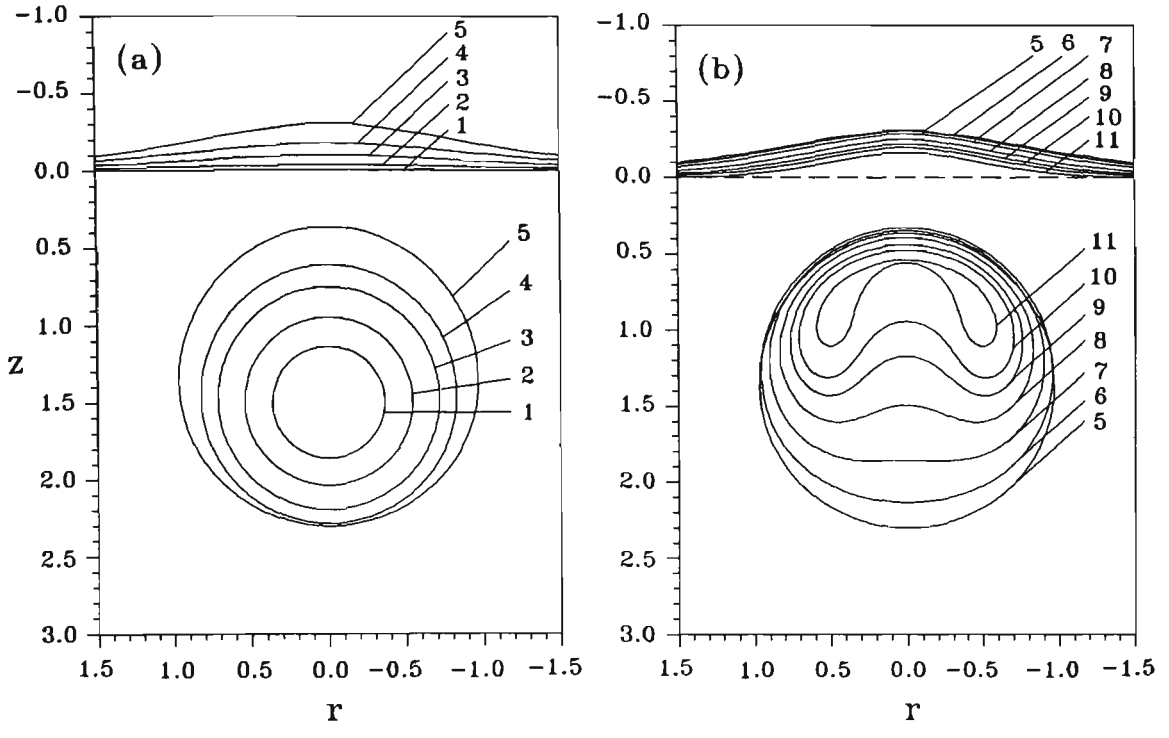

Figure 6.6 Bubble and free surface shapes for the growth (a) and collapse (b) of a constant pressure vapour bubble beneath a free surface with $\gamma = 1.5$ and $\delta = 0.6766$. The non-dimensional times corresponding to bubble and free surface successive profiles are: (a) Growth phase: (1) 0.0360, (2) 0.0998, (3) 0.2097, (4) 0.3605, (5) 0.7619. (b) Collapse phase: (5) 0.7619, (6) 0.9942, (7) 1.1748, (8) 1.3341, (9) 1.4261, (10) 1.4871, (11) 1.5741.

Figures 6.7(a) and (b) compare the dynamic characteristics of a constant pressure vapour bubble beneath a free surface in two different cases, under the same initial conditions and with two different values of $\gamma = 0.98$ and $\gamma = 1.5$.

Figure 6.7(a) illustrates the movement of the bubble centroid with respect to time during the growth and collapse phases. The buoyancy forces are ignored. In the case of $\gamma = 0.98$ during the growth phase the centroid of the bubble migrates marginally towards the free surface. Whereas during the collapse phase the bubble centroid moves increasingly rapidly away from the free surface. Figure 6.7(a) indicates that by increasing the initial distance of the bubble centroid from the free surface, the rate of migration of the bubble towards the free surface during the growth phase, and also the rapid movement of the bubble away from the free surface during the collapse phase are decreased.

Figure 7(b) shows that in the case of the bubble near a free surface, the collapse rate of the bubble increases by increasing the initial distance of the bubble centroid from the free surface. This fact is also completely opposite to the case of the bubble near a rigid boundary.

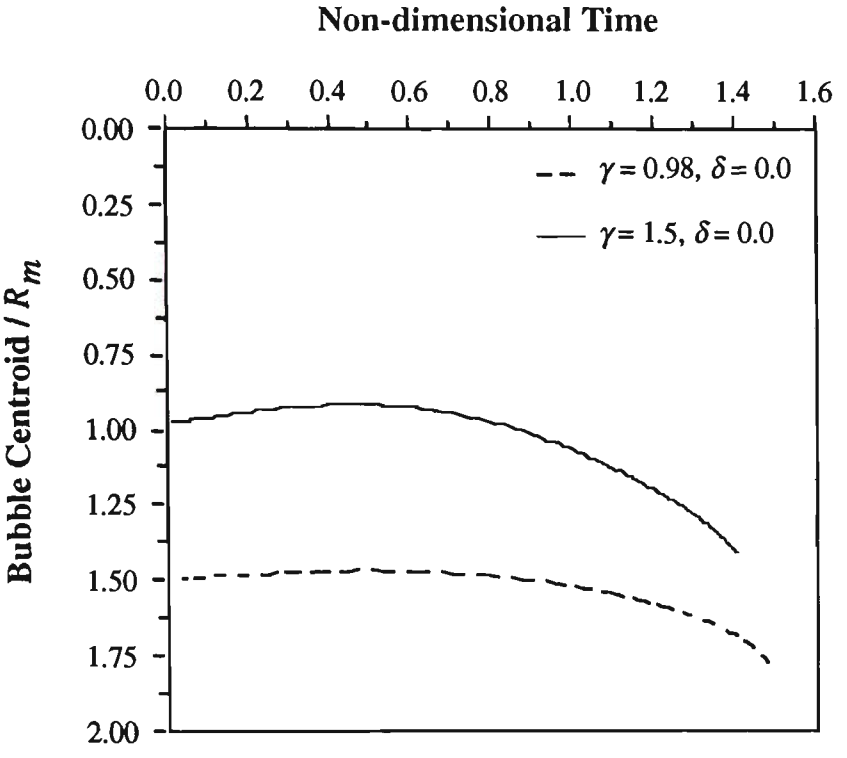

Figure 6.7(a) Migration of the bubble centroid beneath a free surface during its growth and collapse phases.

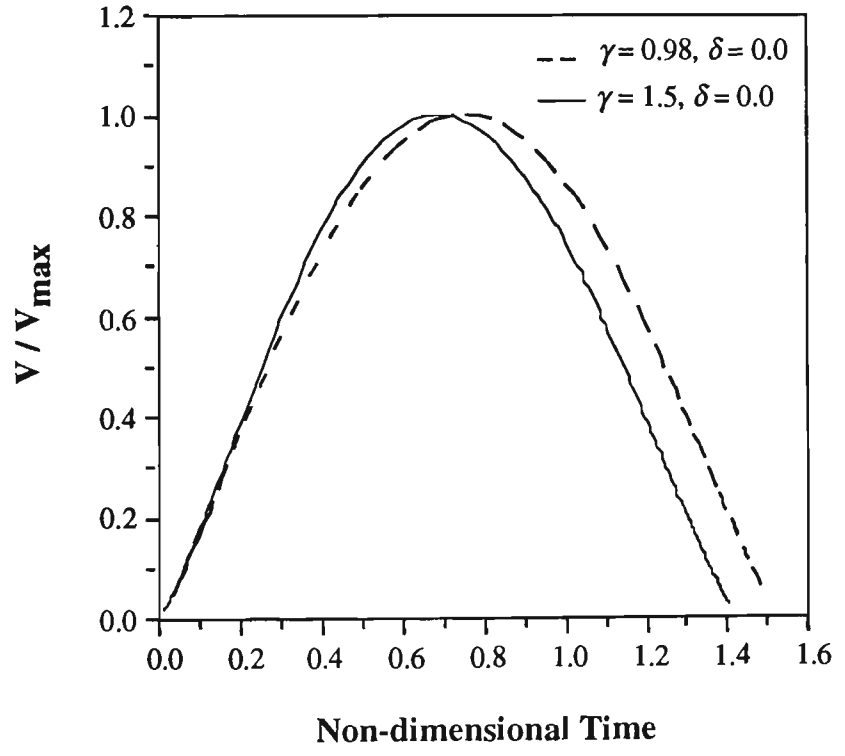

Figure 6.7(b) Variation of the bubble volume during its growth and collapse phases.

Figure 6.8 shows the effect of the buoyancy forces on the dynamics of a constant pressure vapour bubble beneath a free surface. It is shown that in the absence of the buoyancy forces the bubble centroid migrates away from the free surface. By considering the relatively weak buoyancy forces, the movement of the bubble centroid away from the free surface is decreased. Figure 6.8 indicates that strong buoyancy forces cause an increasingly rapid migration of the bubble centroid towards the free surface.

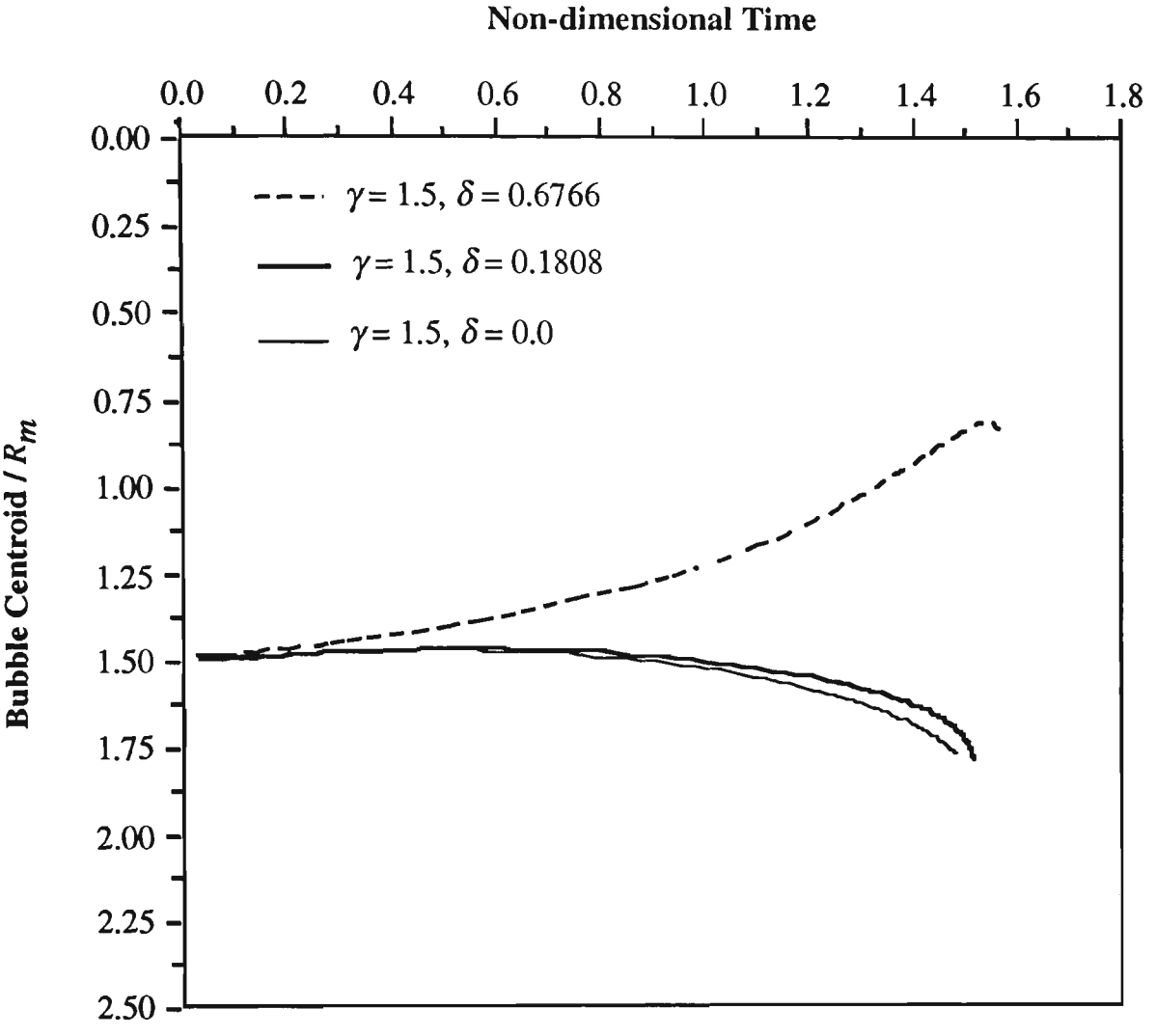

Figure 6.8 Migration of the bubble centroid beneath a free surface with $\gamma = 1.5$ and under the influence of different values of buoyancy forces.

Figure 6.9 illustrates the displacement of the mid point of the free surface located on the axis of symmetry together with the displacement of the top and the bottom points of the bubble surface located on the axis of symmetry. Figure 6.9 clearly indicates the existence of a stagnation point between the free surface and the top side of the bubble.

Figures 6.10(a) and (b) illustrate the velocity and the pressure inside the liquid domain on the axis of symmetry for a constant pressure vapour bubble near a free surface with $\gamma = 0.98$, $\delta = 0.0$ and at non-dimensional time $t = 1.2992$. It should be noted that, in Figures 6.10(a) and (b), the velocity and the pressure curves are discontinued inside the bubble and above the free surface. Figures 6.10(a) and (b) indicate the existence of a stagnation point and a point of maximum pressure between the bubble and the free surface. It is shown that the location of the stagnation point is different from the location of the maximum pressure point. The fact that, in the case of the bubble near a free surface with $\gamma = 0.98$ and $\delta = 0.0$, the stagnation point and the point of maximum pressure do not coincide, as they would in steady flow, is also reported by Ceron and Blake (1984), Taib (1985), Blake *et al.* (1987) and Dommermuth and Yue (1987).

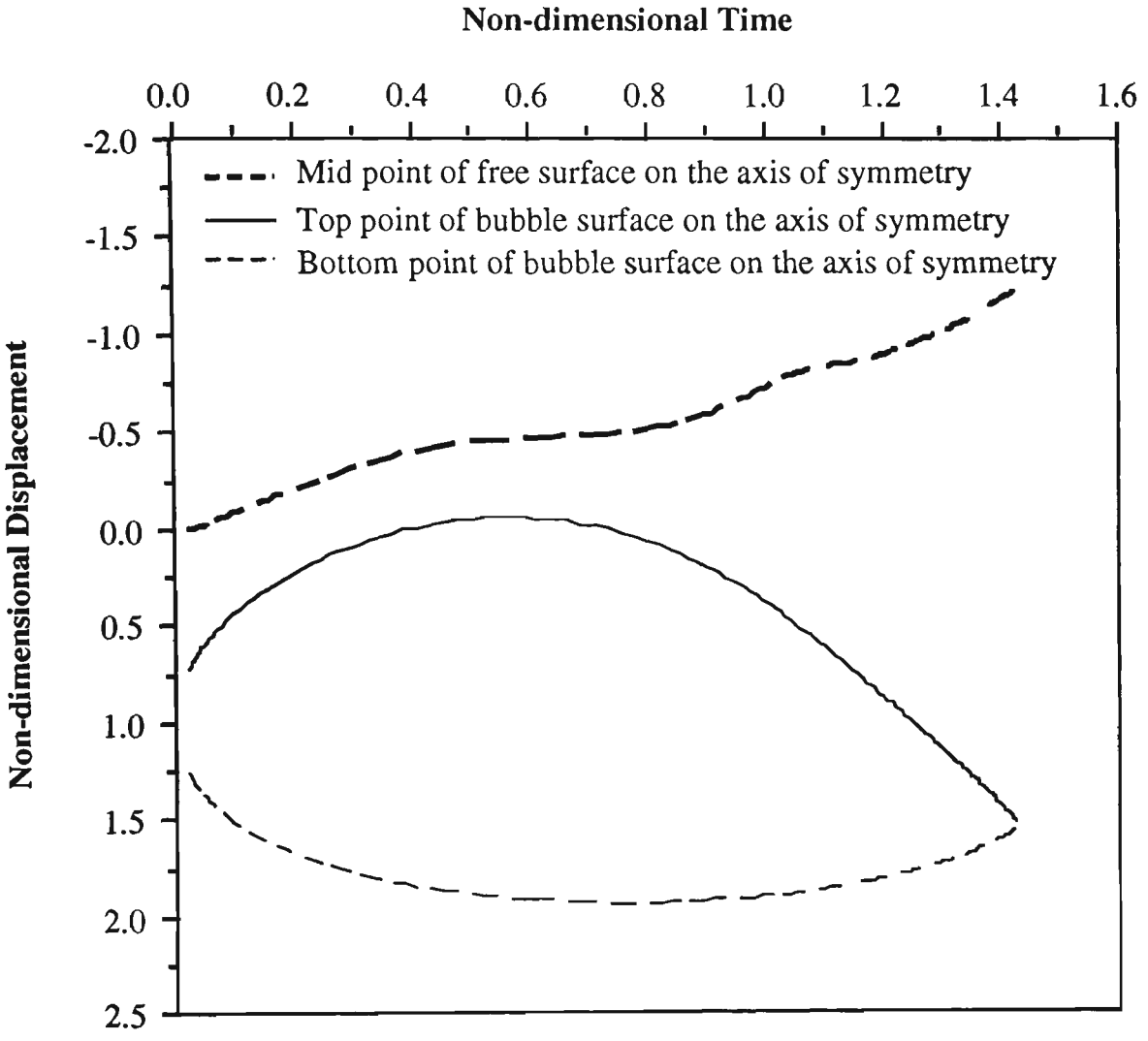

Figure 6.9 Displacement of the top and the bottom points of the bubble surface located on the axis of symmetry and displacement of the mid point of the free surface located on the axis of symmetry during the growth and collapse of a constant perssure vapour bubble with $\gamma = 0.98$ and $\delta = 0.0$.

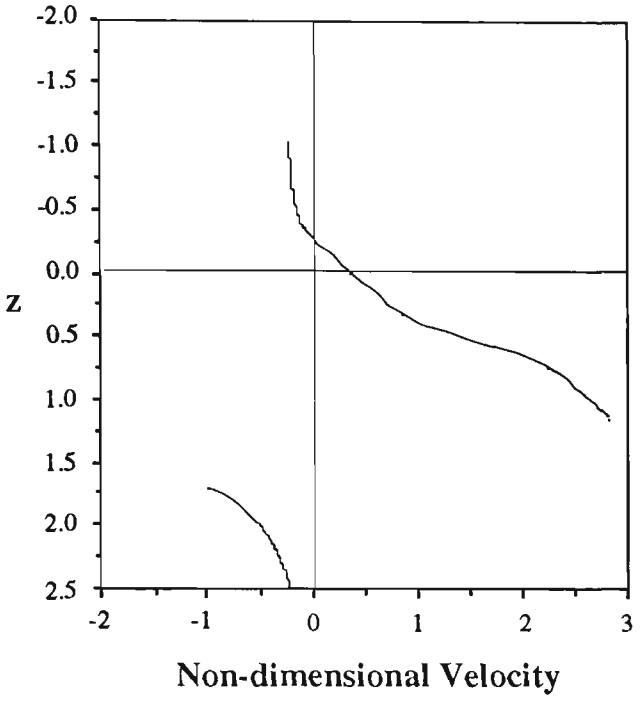

Figure 6.10(a) Velocity of the liquid on the axis of symmetry around a constant pressure vapour bubble beneath a free surface for $\gamma = 0.98$ and $\delta = 0.0$ at non-dimensional time $t = 1.2992$

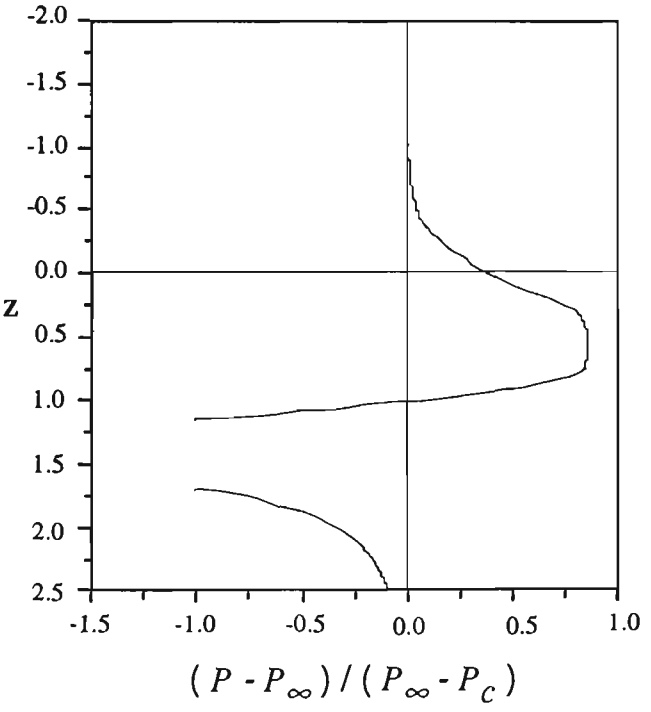

Figure 6.10(b) Pressure inside the liquid domain on the axis of symmetry around a constant pressure vapour bubble beneath a free surface for $\gamma = 0.98$ and $\delta = 0.0$ at non-dimensional time $t = 1.2992$

Figure 6.11 compares the numerical results of this research with the experimental bubble and free surface shapes reported by Blake and Gibson (1981) for $\gamma = 0.98$ and in the absence of the buoyancy forces. Experimentally, the influence of the buoyancy forces is eliminated by conducting the experiments in a falling rig. During the growth phase, the calculated shapes of the bubble and the free surface are in a very good agreement with the experimental observations. Both numerical and experimental results indicate the entrainment of the elongated top side of the bubble underneath the raised free surface at the latest stages of the growth phase. During the collapse phase there is also good agreement between the calculated shapes of the bubble and the free surface with the experimental observations. Numerical results indicate that the instant of the transformation of the bubble into a toroidal shape is corresponds to the non-dimensional time of $t = 1.420$ (the final shape of the bubble before its transformation to a toroidal form is not included in Figure (6.11). Thus it should be noted that the calculated lifetime of the bubble is about 6 percent less than the experimental measured time.

Figure 6.12 compares the movement of the bubble centroid for $\gamma = 0.98$ and in the absence of the buoyancy forces with the experimental results reported by Blake and Gibson (1981). As shown in Figure 6.12, there is a very good agreement between the numerical calculated migration of the bubble centroid with the experimental results.

a) Numerical (Non-dimensional times are (1) 0.089, (2) 0.177, (3) 0.255, (4) 0.341, (5) 0.517, (6) 0.609, (A) 0.680, (7) 0.863, (8) 0.977, (9) 1.165, (10) 1.238, (11) 1.299, (12) 1.388, (13) 1.407.)

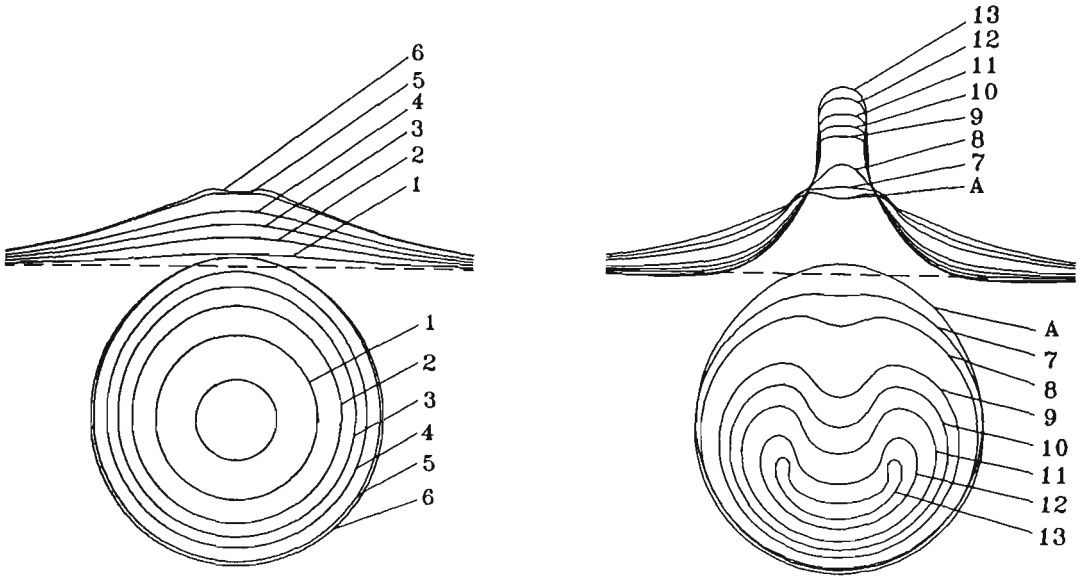

b) Experiment (Non-dimensional times are (1) 0.087, (2) 0.173, (3) 0.260, (4) 0.347, (5) 0.520, (6) 0.604, (7) 0.867, (8) 1.040, (9) 1.214, (10) 1.300, (11) 1.387, (12) 1.474, (13) 1.508.)

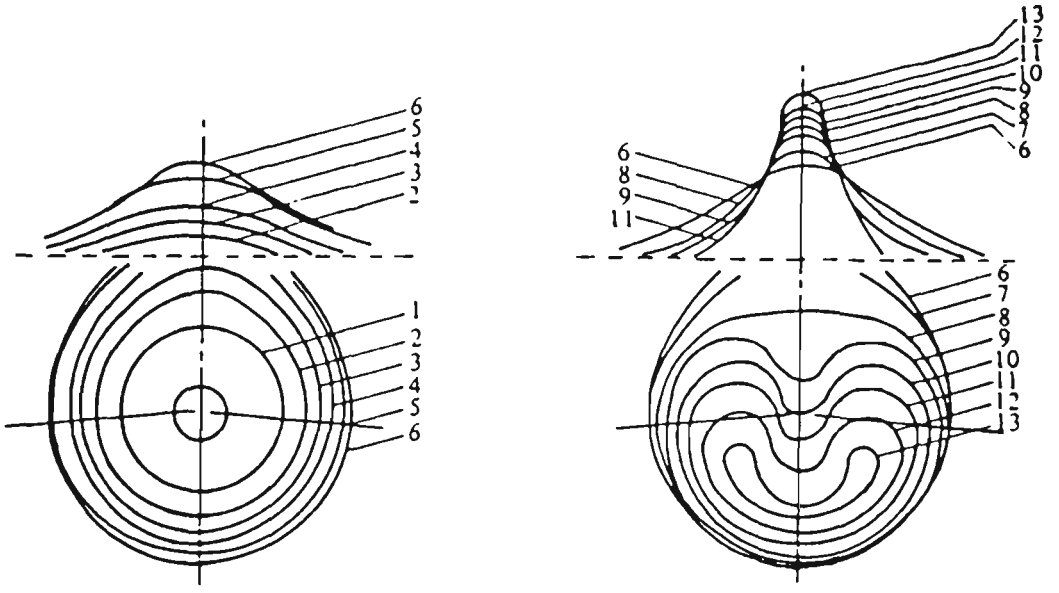

Figure 6.11 Comparison between the numerical results of this work and the experimental results of Blake and Gibson (1981) for the growth and collapse of a constant pressure vapour bubble beneath a free surface with $\gamma = 0.98$ and $\delta = 0.0$. It should be noted that, in numerical results, "A" indicates the shape of the bubble, and the free surface at the maximum volume of the bubble, which corresponds to a non-dimensional time $t = 0.680$.

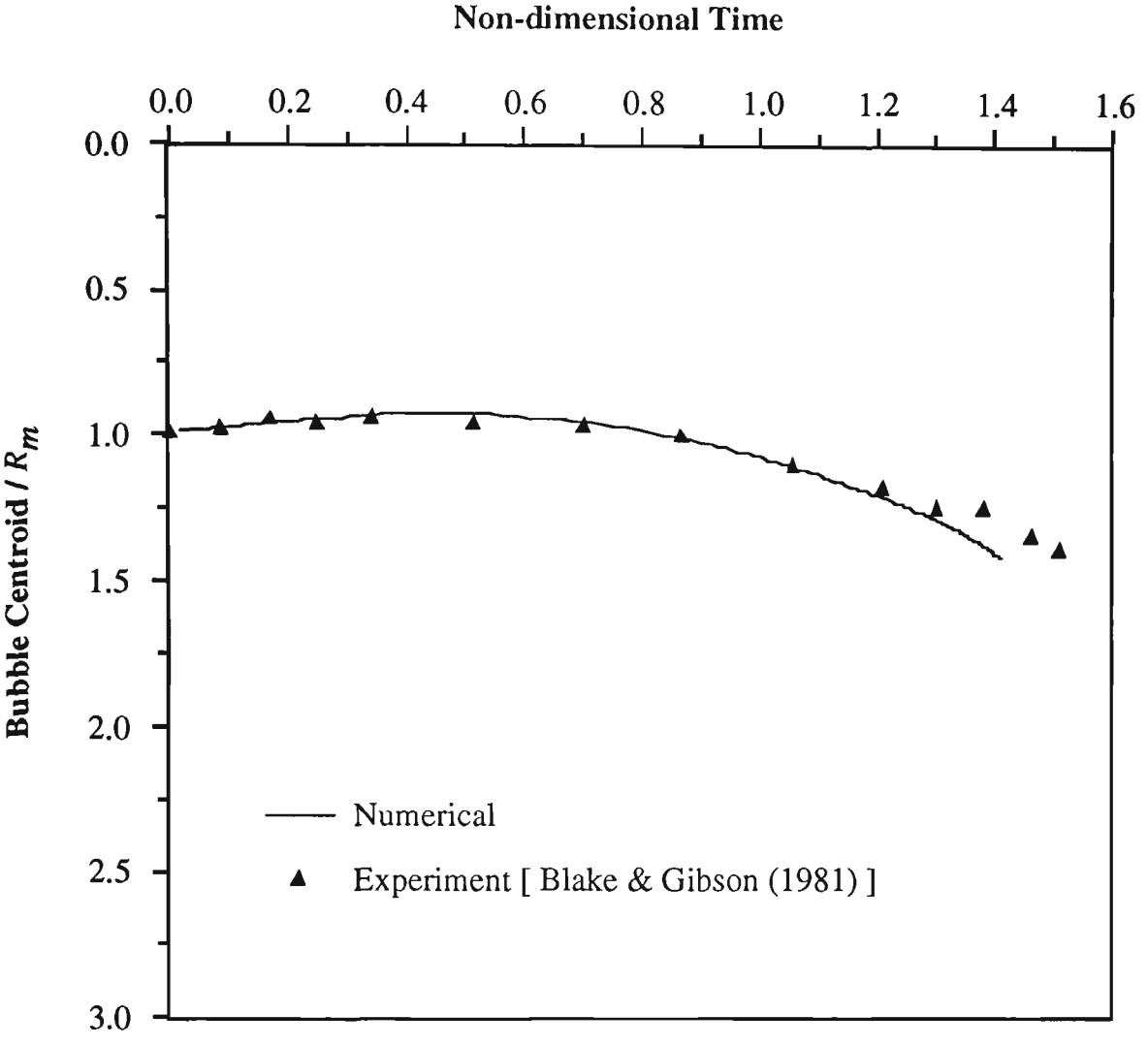

Figure 6.12 Comparison between the numerical calculated movement of the bubble centroid during the growth and collapse of a constant pressure vapour bubble beneath a free surface with experiment for $\gamma = 0.98$ and $\delta = 0.0$.

6.6.2 Pulsation of a rebounding bubble beneath a free surface

In this section pulsation of a rebounding bubble which contains a mixture of constant pressure vapour and ideal gas in the vicinity of a free surface is investigated. The bubble is initially in its minimum volume with a very high pressure inside the bubble. This situation can arise in the case of a high local energy input inside the liquid domain. The dynamics of the rebounding bubble and the free surface is investigated both with and without buoyancy forces affecting the fluid motion.

6.6.2.1 Pulsation of a rebounding bubble beneath a free surface without considering buoyancy forces

Figures 6.13(a), (b) and (c) illustrate the migration of the bubble centroid, the variation of the bubble volume and the variation of the pressure inside the bubble with respect to time for the cases of $\gamma = 1.5$ and $\gamma = 1.8$ and in the absence of the buoyancy forces.

Figure 6.13(a) shows the rate of migration of the bubble centroid towards the free surface during the growth phase of the bubble decreases by increasing the initial distance of the bubble centroid from the free surface. It is also shown that the rapid migration of the bubble centroid away from the free surface decreases by increasing the initial distance of the bubble centroid from the free surface.

Figure 6.13(b) shows that the collapse phase of the rebounding bubble beneath a free surface increases by increasing the initial distance of the bubble centroid from the free surface.

Figure 6.13(c) illustrates the pressure inside the bubble for the corresponding cases of the bubble illustrated in Figures 6.13(a) and (b). It is shown that, for the bubble further away from the free surface, the pressure inside the bubble at the end of the bubble collapse and just before the rebound phase is higher than the case of the bubble nearer to the free surface. This fact indicates that, for the bubble nearer to the free surface, the bubble volume at the end of the collapse phase is larger. The physical explanation of this fact is that in the case of the bubble nearer to the free surface the effect of the Bjerknes force through the free surface on the pulsating bubble is stronger. Thus the kinetic energy portion of the liquid domain around the bubble at the end of the collapse phase is greater. Therefore, because of the initially equal level of energy input for both the bubble located relatively nearer to the free surface and the bubble located further away from it, the greater portion of the kinetic energy for the closer bubble to the free surface results in a larger final volume for the bubble at the end of the collapse phase.

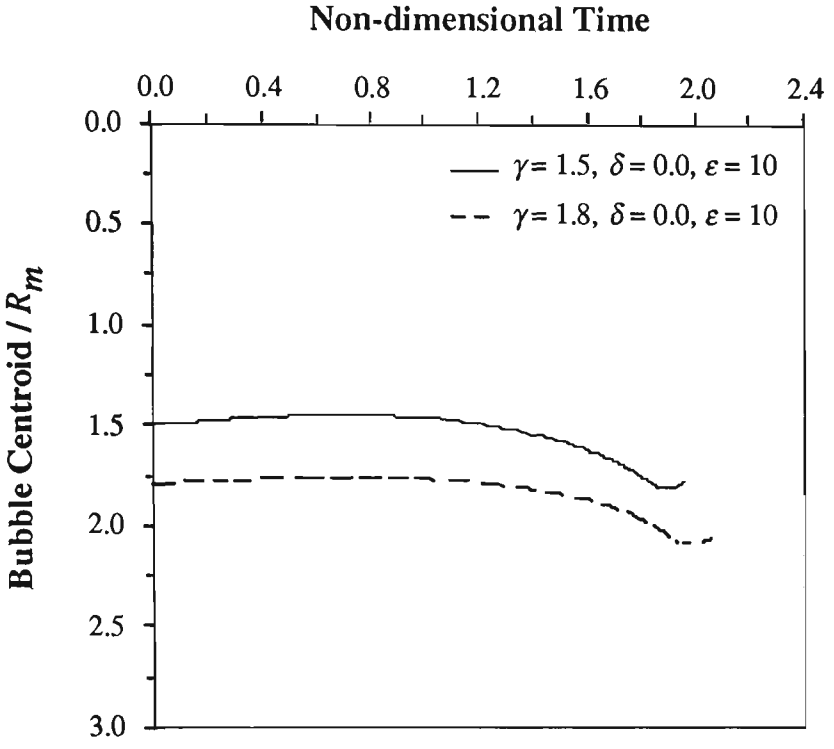

Figure 6.13(a) Migration of the bubble centroid beneath a free surface during its pulsation.

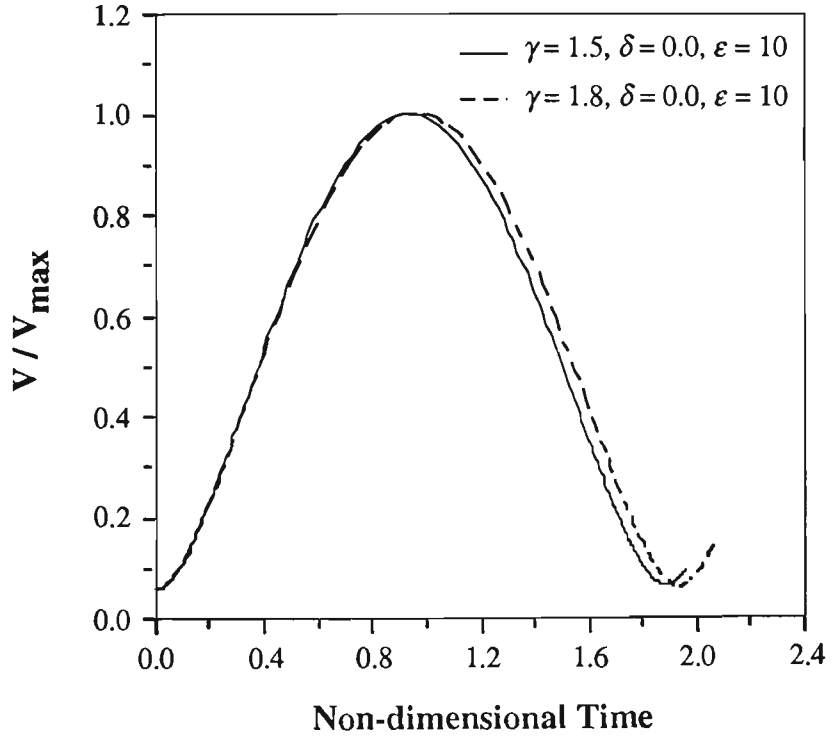

Figure 6.13(b) Variation of the bubble volume beneath a free surface during its pulsation.

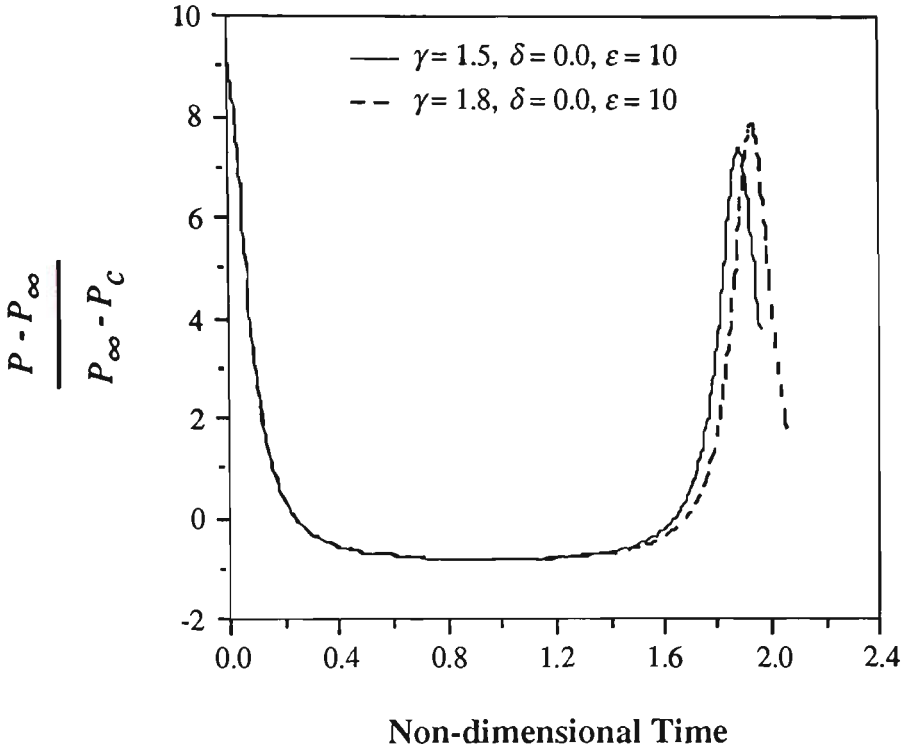

Figure 6.13(c) Variation of the pressure inside the bubble beneath a free surface during its pulsation.

Figure 6.14 compares the growth and collapse rates of a rebounding bubble in the vicinity of a rigid boundary, in an infinite liquid domain and in the neighbourhood of a free surface. The rebounding bubble is characterised by $\delta = 0.0$ and $\varepsilon = 10$, while the initial distance of the bubble centroid from the rigid boundary and also from the free surface is characterised by $\gamma = 1.5$. As shown in Figure 6.14, the collapse rate of a bubble near a rigid boundary is lower than the collapse rate of an isolated bubble. In other words, the presence of a rigid boundary causes the extension of the bubble lifetime. However Figure 6.14 indicates that in contrast to the effect of the rigid boundary on the lifetime of the bubble, the collapse rate of a bubble near a free surface is higher than the collapse rate of an isolated bubble. In other words, the free surface shortens the lifetime of the bubble.

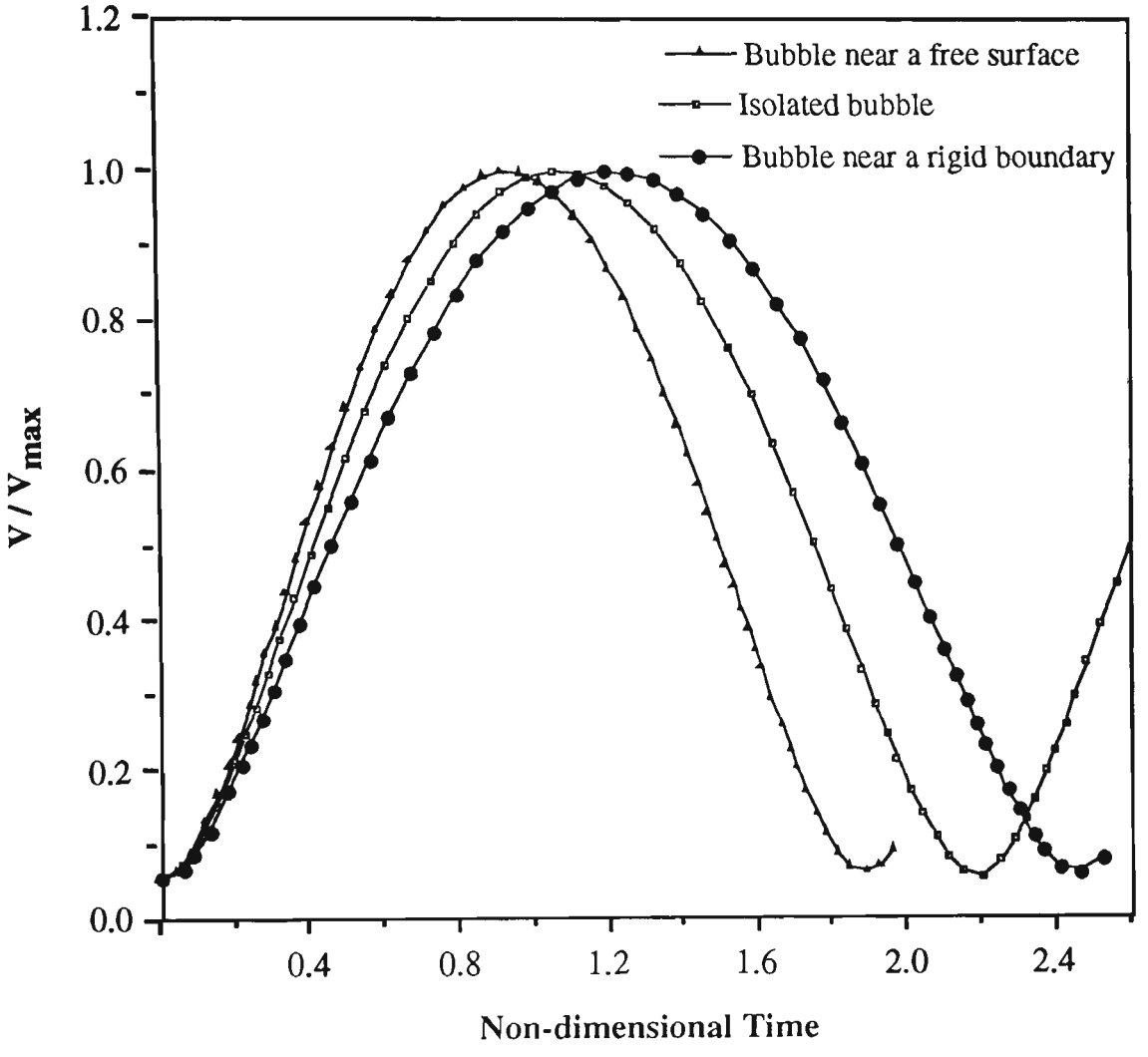

Figure 6.14 Comparison between the growth and collapse rates of a rebounding bubble in the vicinity of a rigid boundary, in an infinite liquid domain and in the neighbourhood of a free surface. The rebounding bubble is characterised by $\delta = 0.0$ and $\varepsilon = 10$, while the initial distance of the bubble centroid from the rigid boundary and also from the free surface is characterised by $\gamma = 1.5$.

6.6.2.2 Pulsation of a buoyant rebounding bubble beneath a free surface

Figure 6.15(a) illustrates shape of the free surface and a rebounding bubble in its vicinity, with $\gamma = 1.5$, $\delta = 0.1808$ and $\varepsilon = 10$. In this example, at maximum volume the bubble is slightly elongated towards the free surface. During the bubble collapse the free surface collapses and the bubble migrates away from the free surface. At the latest stages of the collapse phase a liquid jet is initiated on the side of the bubble nearer to the free surface and directed away from it. The liquid jet is developed during the rebound phase of the bubble and penetrates the opposite side of the bubble. However the collapsed free surface is pushed up by the rebound of the bubble. During the rebound phase the direction of the liquid jet away from the free surface and the movement of the free surface away from the bubble cause a stagnation point between the bubble and the free surface. The existence of a stagnation point and a point of maximum pressure between the bubble and the free surface during their rebound phase is discussed in more detail later in this section.

Figure 6.16 illustrates the shapes of the bubble and the free surface for $\gamma = 1.5$, $\delta = 0.4429$ and $\varepsilon = 10$. In this case the bubble grows almost spherically during the early stages of its growth phase. However at the latest stages of the growth phase, the top side of the bubble is attracted by the free surface and elongated in the direction of the free surface. During the collapse phase, the bottom side of the bubble further away from the free surface becomes flattened. At the latest stages of the collapse phase a liquid jet is developed at the flattened bottom side of the bubble directed towards the free surface. In this case the liquid jet penetrates the opposite side of the bubble and transforms it into a toroidal shape before the bubble rebounds.

Figure 6.17 illustrates the shape of the bubble and the free surface for $\gamma = 1.8$, $\delta = 0.6667$ and $\varepsilon = 10$. In this example at the latest stages of the growth phase, near the maximum volume, the top side of the bubble is slightly elongated towards the free surface. During the collapse phase the raised free surface collapses by the collapse of the bubble, while the bottom side of the bubble is flattened. At the latest stages of the collapse phase a liquid jet initiates on the flattened bottom side of the bubble directed towards the free surface. The liquid jet is developed during the rebound phase and penetrates the opposite side of the bubble, while the free surface rebounds upward away from the bubble. In this example, during the rebound phase the top side of the bubble nearer to the free surface moves upward while the free surface rebounds upward. Thus, because of the movement of the free surface and the top side of the bubble close to the free surface at the same direction, there is no stagnation point between the free surface and the bubble.

Figure 6.18 shows the shape of the bubble and the free surface for $\gamma = 1.5$, $\delta = 0.1808$ and $\varepsilon = 5$. In this case, during the early stages of the growth phase, the bubble grows almost spherically. At the latest stages of the growth, near the maximum volume, the top portion of the bubble is elongated towards the free surface. During the collapse phase the top side of the bubble nearer to the free surface becomes flattened. At the latest stages of the collapse phase a liquid jet is initiated on the flattened side of the bubble near the free surface and directed away from it. During the rebound phase, the liquid jet is fully developed and directed away from the free surface. Whereas the free surface rebounds upward away from the bubble. In this example a stagnation point exists between the bubble and the free surface during the rebound phase.

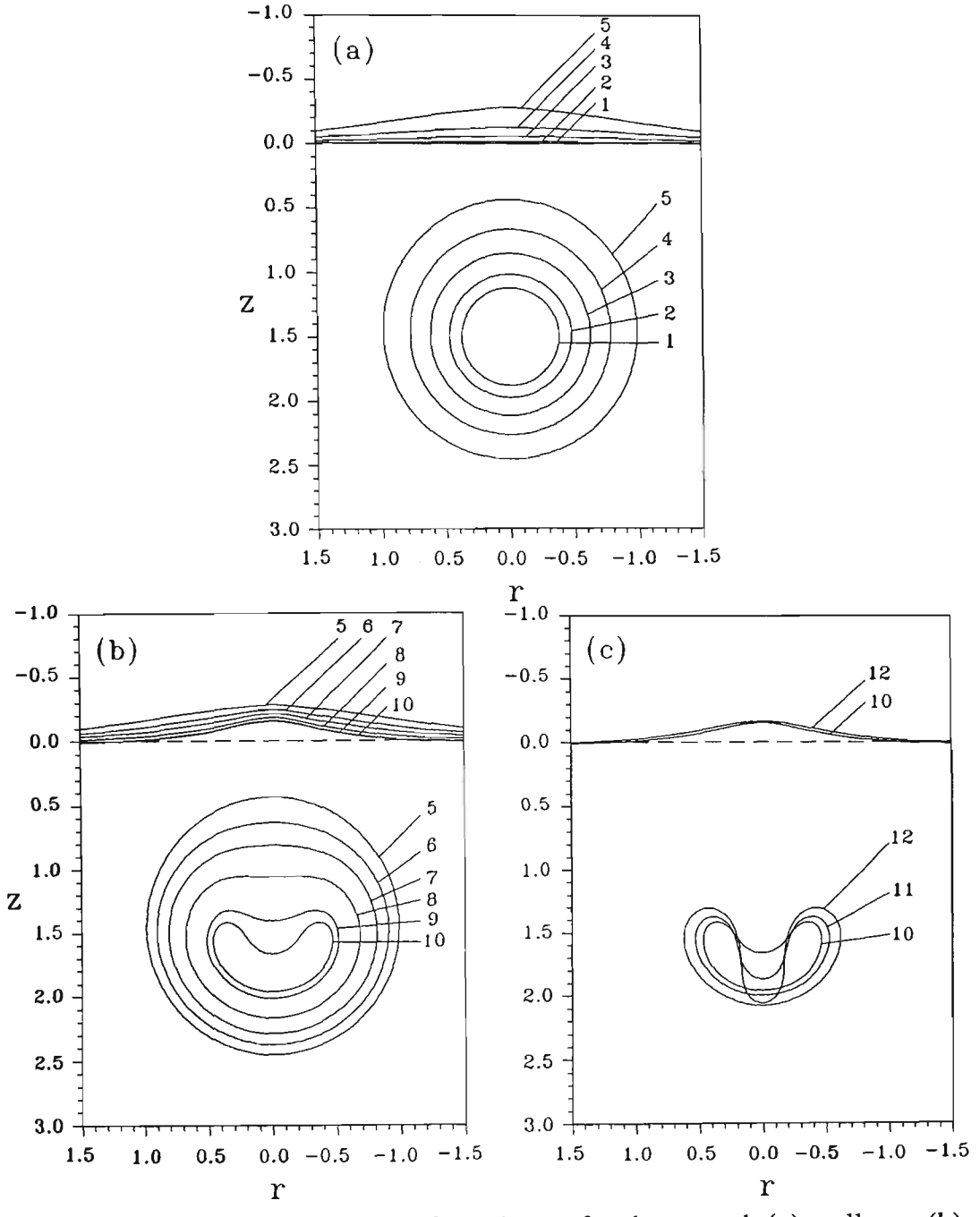

Figure 6.15 Bubble and free surface shapes for the growth (a), collapse (b) and rebound (c) of a bubble containing a mixture of constant pressure vapour and ideal gas beneath a free surface with $\gamma = 1.5$, $\delta = 0.1808$ and $\varepsilon = 10$. The non-dimensional times corresponding to bubble and free surface successive profiles are: (a) Growth phase: (1) 0.0000, (2) 0.0973, (3) 0.2041, (4) 0.3596, (5) 0.9359. (b) Collapse phase: (5) 0.9359, (6) 1.3342, (7) 1.4919, (8) 1.6445, (9) 1.7913, (10) 1.8778. (c) Rebound phase: (10) 1.8778, (11) 1.9444, (12) 2.0088.

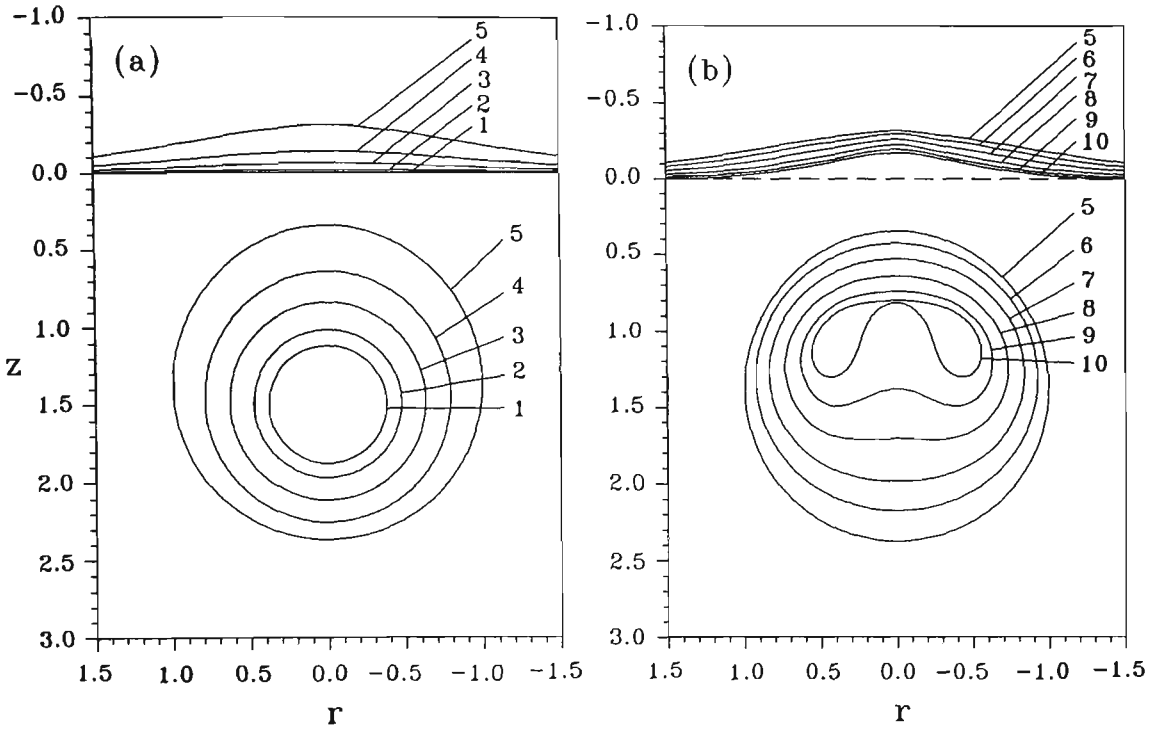

Figure 6.16 Bubble and free surface shapes for the growth (a) and collapse (b) of a bubble containing a mixture of constant pressure vapour and ideal gas beneath a free surface with $\gamma = 1.5$, $\delta = 0.4429$ and $\varepsilon = 10$. The non-dimensional times corresponding to bubble and free surface successive profiles are: (a) Growth phase: (1) 0.0000, (2) 0.0960, (3) 0.2087, (4) 0.3681, (5) 0.9333. (b) Collapse phase: (5) 0.9333, (6) 1.3368, (7) 1.5029, (8) 1.6461, (9) 1.7527, (10) 1.8943.

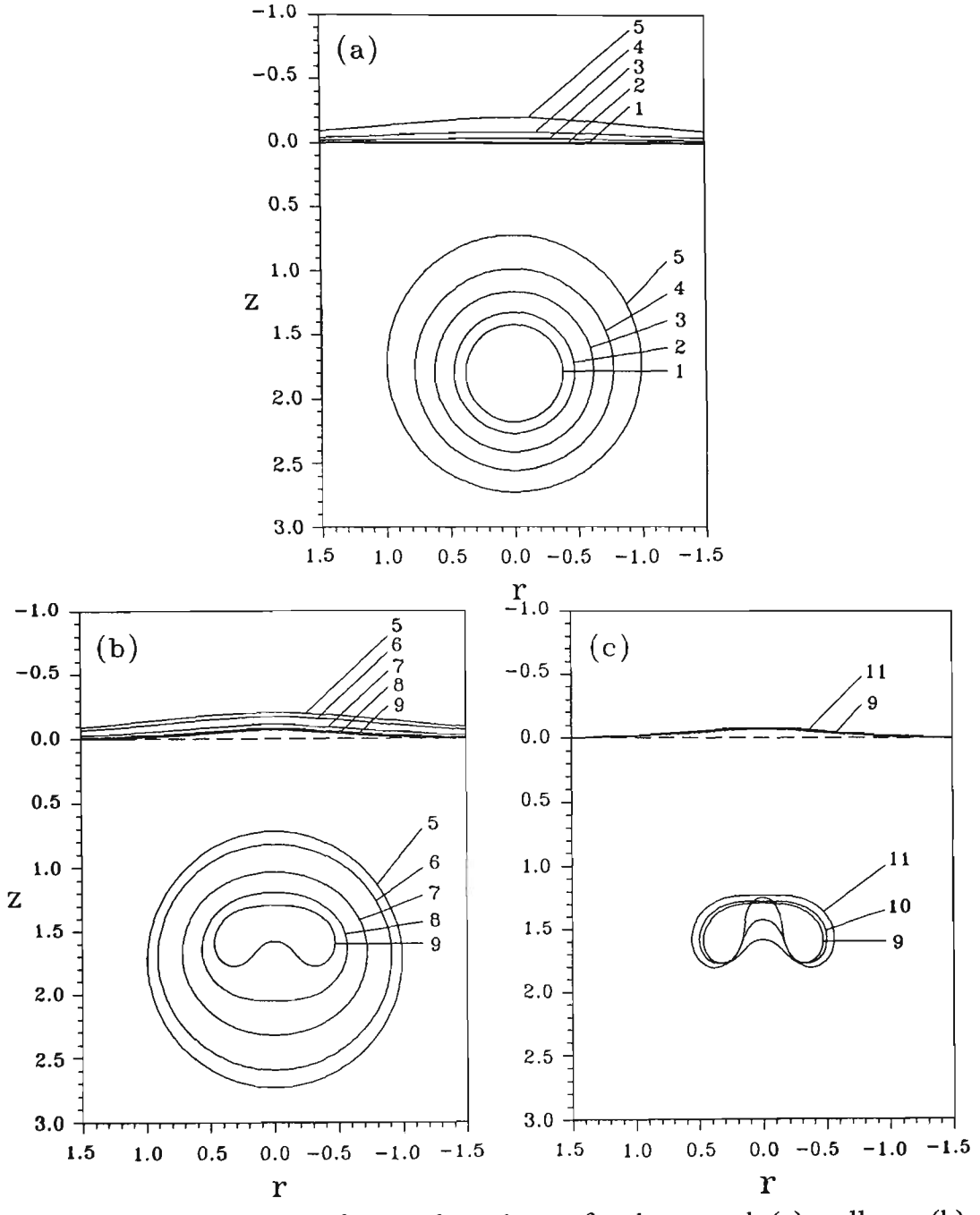

Figure 6.17 Bubble and free surface shapes for the growth (a), collapse (b) and rebound (c) of a bubble containing a mixture of constant pressure vapour and ideal gas beneath a free surface with $\gamma = 1.5$, $\delta = 0.3132$ and $\varepsilon = 10$. The non-dimensional times corresponding to bubble and free surface successive profiles are: (a) Growth phase: (1) 0.0000, (2) 0.0944, (3) 0.2038, (4) 0.3562, (5) 0.9712. (b) Collapse phase: (5) 0.9712, (6) 1.3426, (7) 1.6400, (8) 1.7925, (9) 1.9312. (c) Rebound phase: (9) 1.9312, (10) 1.9711, (11) 2.0174.

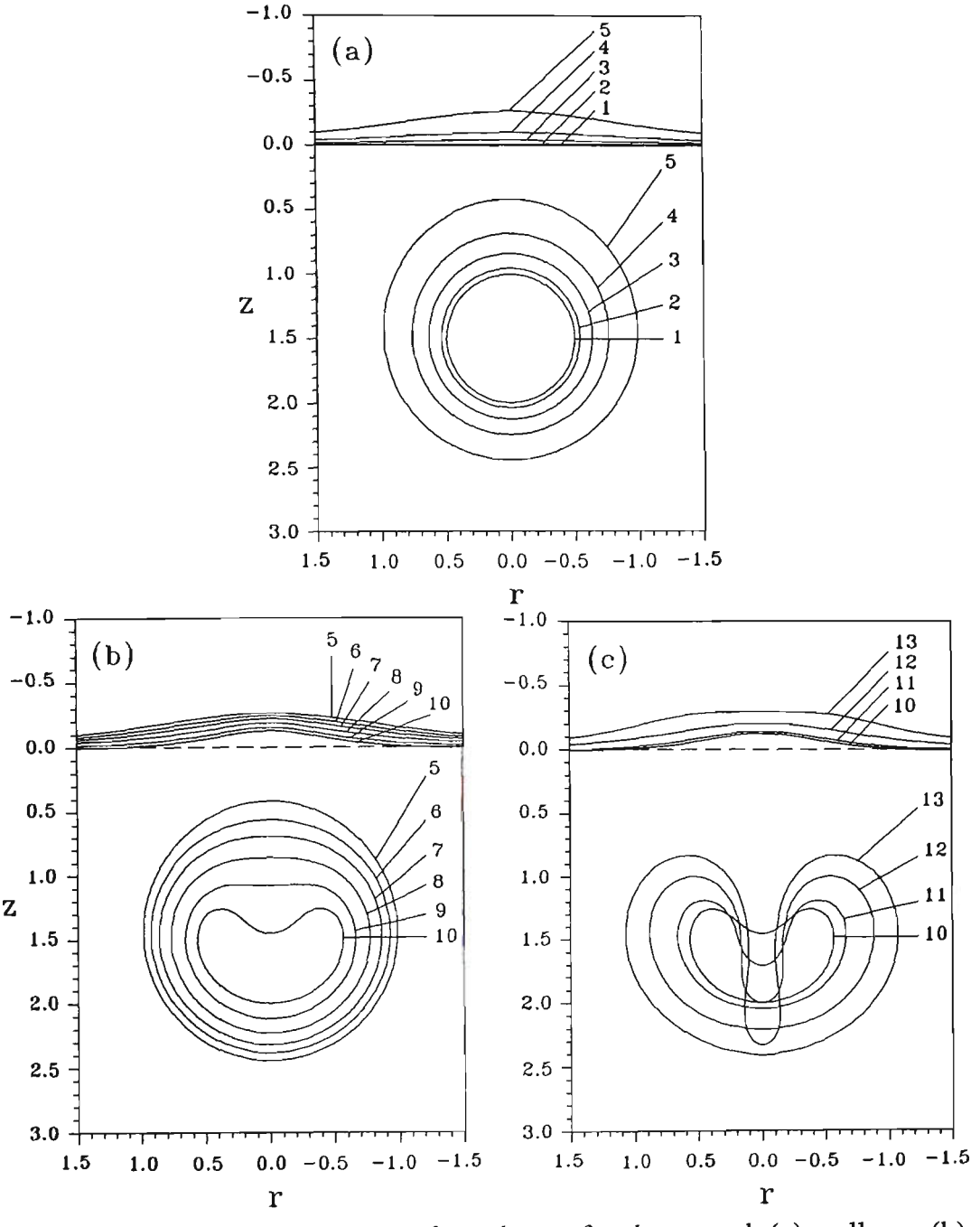

Figure 6.18 Bubble and free surface shapes for the growth (a), collapse (b) and rebound (c) of a bubble containing a mixture of constant pressure vapour and ideal gas beneath a free surface with $\gamma = 1.5$, $\delta = 0.1808$ and $\varepsilon = 5$. The non-dimensional times corresponding to bubble and free surface successive profiles are: (a) Growth phase: (1) 0.0000, (2) 0.0959, (3) 0.2068, (4) 0.3595, (5) 0.9915. (b) Collapse phase: (5) 0.9915, (6) 1.3486, (7) 1.4984, (8) 1.6476, (9) 1.7958, (10) 1.9966. (c) Rebound phase: (10) 1.9966, (11) 2.1379, (12) 2.3888, (13) 2.9883.

Figure 6.19 compares the migration of the bubble centroid for the cases of the bubble located nearer to the free surface and further away from it with $\delta = 0.1808$ and $\delta = 0.4429$ and for $\gamma = 1.5$ and $\varepsilon = 10$. This corresponds to the dynamic characteristics of the bubble and the free surface illustrated in Figures 6.15 and 6.16. Figure 6.19 indicates that in the case of relatively weak buoyancy forces the bubble is repelled by the free surface with a liquid jet directed away from it. Whereas strong buoyancy forces cause the migration of the bubble towards the free surface with a liquid jet directed towards it.

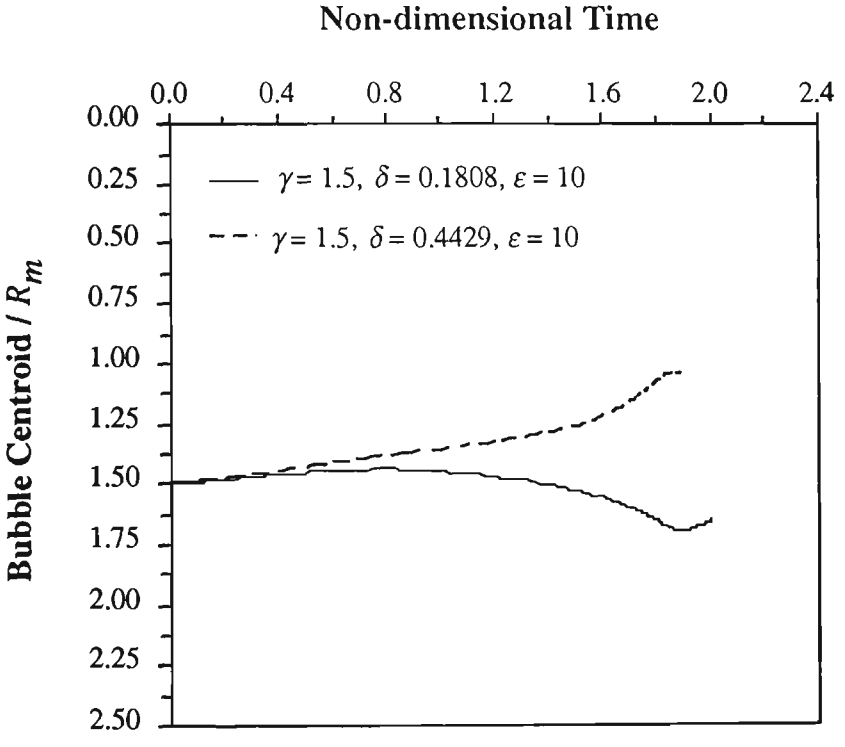

Figure 6.19 Comparison between the migration of the bubble centroid during the pulsation of a rebounding bubble beneath a free surface with $\gamma = 1.5$, $\varepsilon = 10$ and with two different values of $\delta = 0.1808$ and $\delta = 0.4429$.

Figures 6.20(a), (b) and (c) illustrate the dynamic characteristics of the bubble and the free surface corresponding to the case of the bubble and the free surface illustrated in Figure 6.18.

Figure 6.20(a) shows that during the growth phase, the bubble centroid migrates marginally towards the free surface. During the collapse phase the bubble migrates rapidly away from the free surface. It is shown that during the rebound phase the bubble centroid migrates slightly towards the free surface.

Figure 6.20(b) illustrates the variation of the bubble volume and also the variation of the pressure inside the bubble against time during the growth, collapse and rebound phases of the bubble.

Figure 6.20(c) shows the displacement of the top and bottom points on the bubble surface both located on the axis of symmetry and also the displacement of the mid point of the free surface located on the axis of symmetry with respect to time during the growth, collapse and rebound phases. Figure 6.20(c) clearly indicates the existing of a stagnation point between the bubble and the free surface during the rebound phase while the free surface and the top side of the bubble nearer to the free surface migrate in opposite directions.

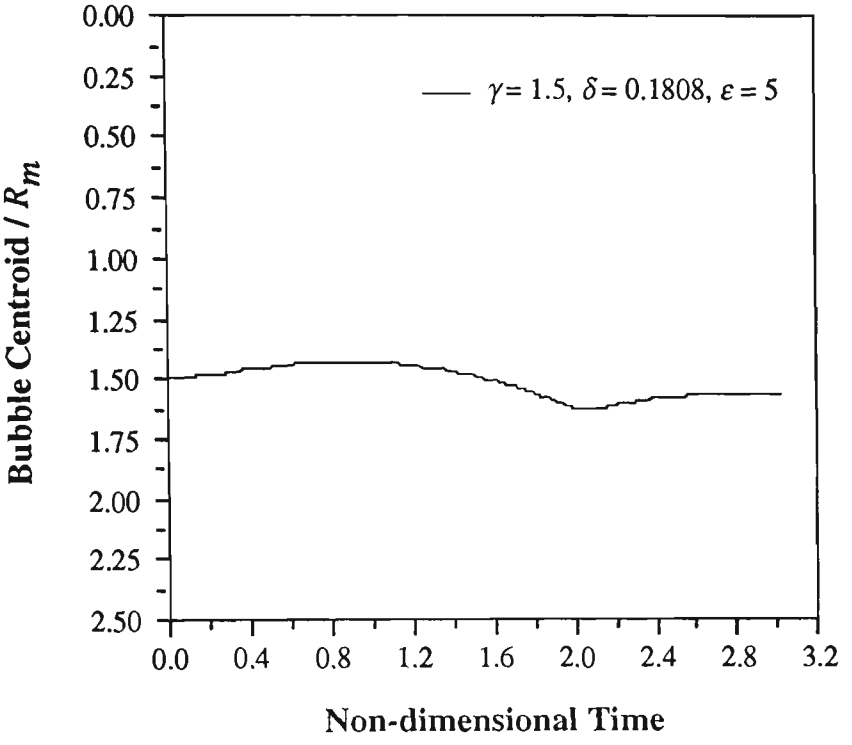

Figure 6.20(a) Migration of the bubble centroid during its pulsation beneath a free surface.

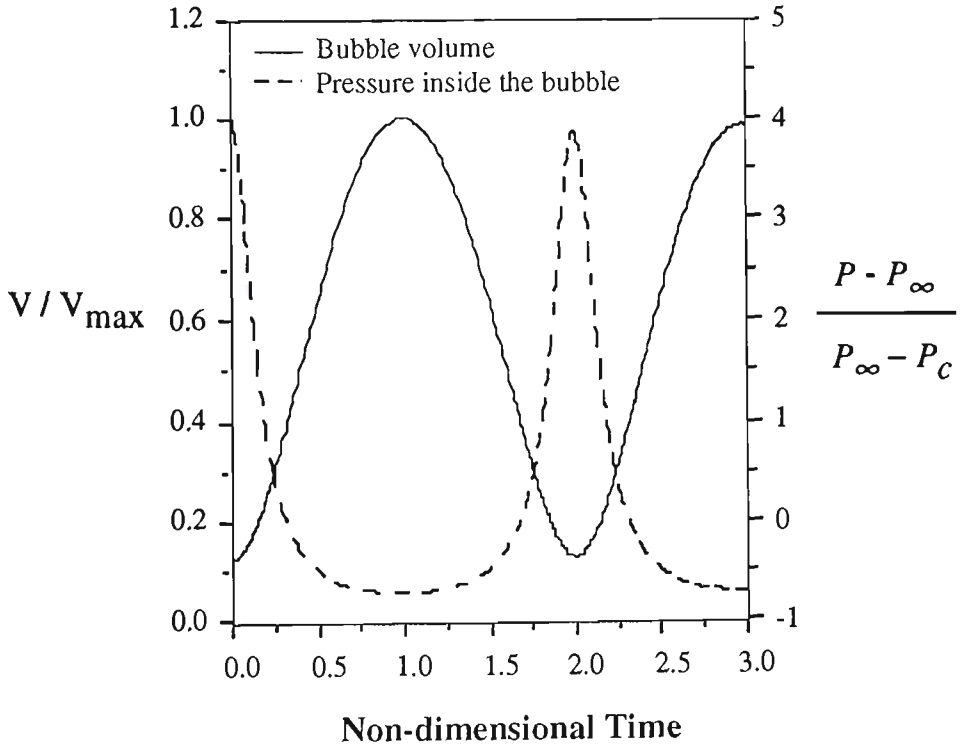

Figure 6.20(b) Variation of the bubble volume and variation of the pressure inside the bubble during the pulsation of a rebounding bubble beneath a free surface for $\gamma = 1.5$, $\delta = 0.1808$ and $\varepsilon = 5$.

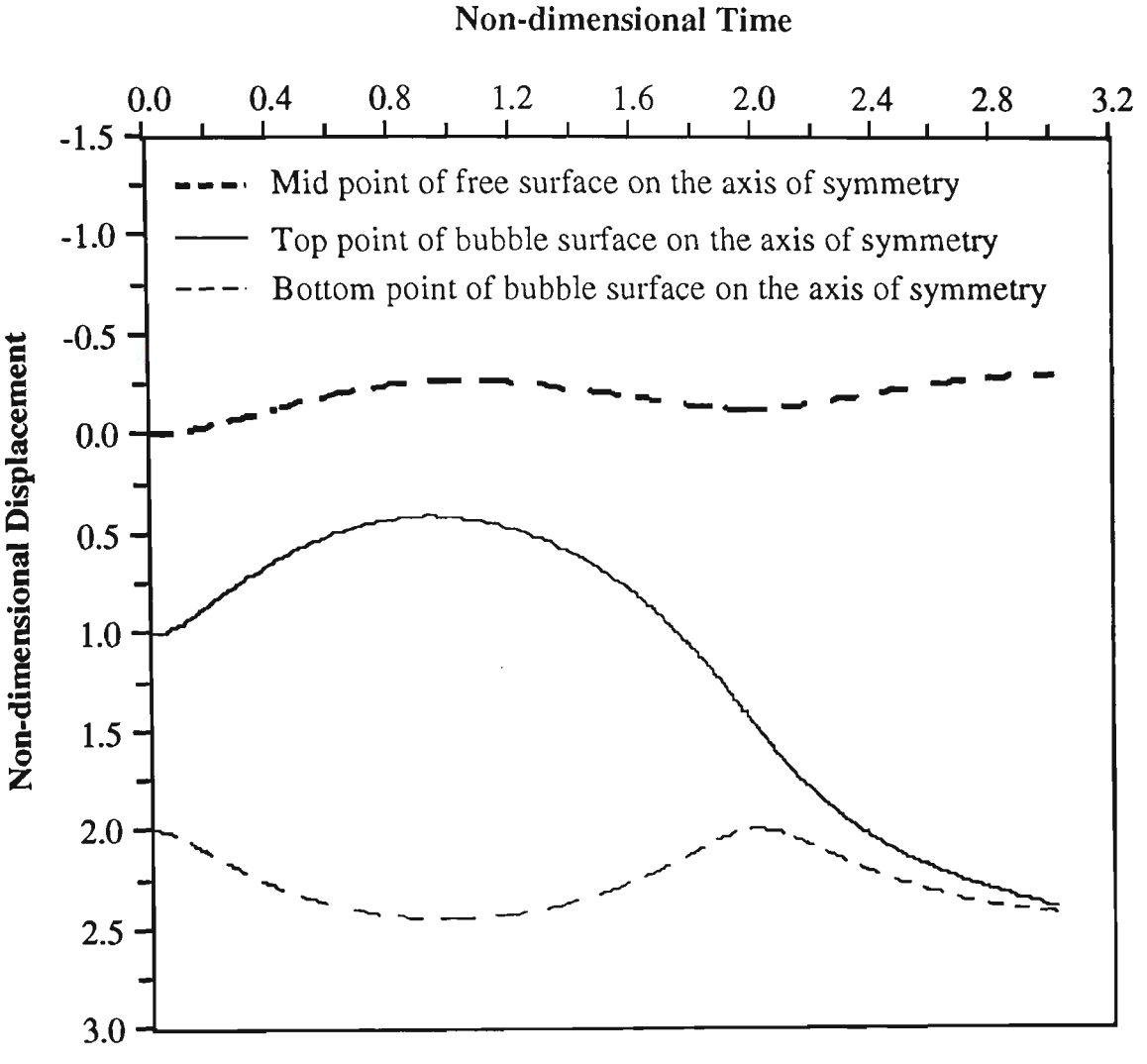

Figure 6.20(c) Displacement of the top and the bottom points of the bubble surface located on the axis of symmetry and displacement of the midpoint of the free surface located on the axis of symmetry during the growth, collapse and rebound phases of a rebounding bubble beneath a free surface with $\gamma = 1.5$, $\delta = 0.1808$ and $\varepsilon = 5$.

Figures 6.21(a) and (b) illustrate the velocity and the pressure inside the liquid domain on the axis of symmetry around the bubble beneath the free surface illustrated in Figure 6.18 during the rebound phase at non-dimensional time $t = 2.0968$. It should be noted that, in Figures 6.21(a) and (b), the velocity and the pressure curves are discontinued inside the bubble and above the free surface. Figures 6.21(a) and (b) indicate the existence of a stagnation point and a point of maximum pressure between the bubble and the free surface. It is shown that the location of the stagnation point and the point of maximum pressure do not coincide.

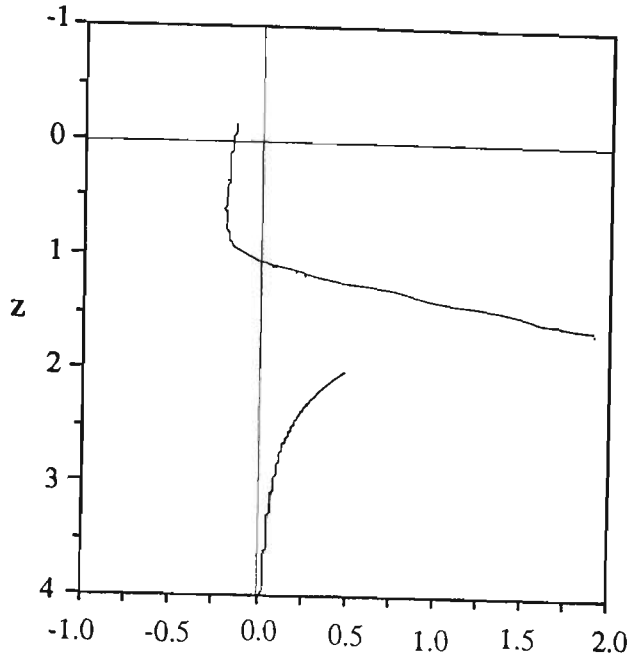

Figure 6.21(a) Velocity of the liquid domain on the axis of symmetry around a rebounding bubble beneath a free surface for $\gamma = 1.5$, $\delta = 0.1808$ and $\varepsilon = 5$ at non-dimensional time t = 2.0968

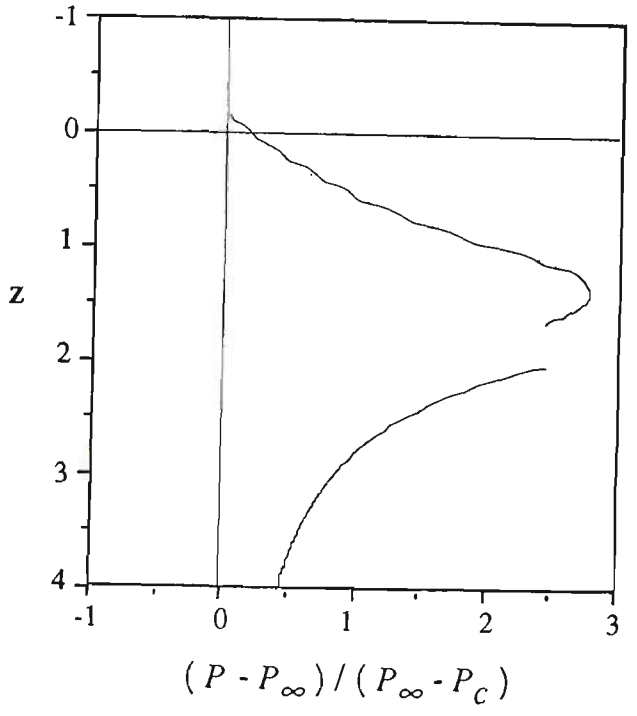

Figure 6.21(b) Pressure inside the liquid domain on the axis of symmetry around a rebounding bubble beneath a free surface for $\gamma = 1.5$, $\delta = 0.1808$ and $\varepsilon = 5$ at non-dimensional time t = 2.0968

6.7 SUMMARY AND CONCLUDING REMARKS

In this chapter the growth and collapse of a constant pressure vapour bubble and the pulsation of a rebounding bubble near a free surface is investigated. The effects of both ignoring and including of the buoyancy forces in the analysis dynamics of the bubble near a free surface is studied. Computational results show that in contrast to the case of a bubble near a rigid boundary, the Bjerknes force through the free surface repels the bubble away from it.

It is shown that considering the buoyancy forces which act in the opposite direction of the Bjerknes force have significant effect on the behaviour of the bubble and may reverse the migration of the bubble and the direction of the liquid jet.

Results show that in the case of the constant pressure vapour bubble for $\gamma \geq 1.5$ the free surface is pushed up by the growth of the bubble and collapses during the bubble collapse. Whereas for $\gamma = 0.98$ and gravity-free case the raised free surface continues its upward movement away from the bubble even during the collapse phase of the bubble and forms a high-speed spike. The movement of the free surface and the top side of the bubble near to the free surface in opposite directions leads to the existence of a stagnation point between the free surface and the bubble. In this case a maximum pressure point also exists, but in a different location from the stagnation point. Whereas the stagnation point and the maximum pressure point would coincide in steady state flow. The separate locations, of the maximum pressure point and the stagnation point is a result of the unsteady nature of the phenomenon.

It is found that while rigid boundary has an effect of slowing down the collapse rate of the bubble, the free surface causes of the collapse rate of the bubble to increase. The smaller the distance of the bubble from the free surface, the higher collapse rate of the bubble.

In the case of a rebounding bubble, results show that the collapse rate of a bubble located beneath a free surface is higher than the collapse rate of an isolated bubble. Whereas the collapse rate of an isolated bubble is higher than the collapse rate of a bubble located in the vicinity of a rigid boundary.

In the case of a rebounding bubble near a free surface, the numerical results for $\gamma \geq 1.5$ show that the free surface is pushed up during the growth of the bubble and collapses with the bubble collapse. It is found that the free surface rebounds in synchronisation with the rebound of the bubble. A very interesting phenomenon found during the rebound phase of the bubble and the free surface, is the existence of a stagnation point and a point of the maximum pressure between the rebounding bubble and the free surface when the liquid jet is directed away from the free surface.

Results show that the stagnation point and the point of maximum pressure during the rebound phase of the bubble and the free surface do not coincide, as was previously found for the case of the constant pressure vapour bubble near a free surface.

CHAPTER SEVEN

DYNAMICS OF A PULSATING BUBBLE NEAR COMPLIANT SURFACES

7.1 INTRODUCTION

As discussed in *Chapter 5*, during the collapse of a cavitation bubble or a bubble generated by a high local energy input in the vicinity of a rigid boundary, the Bjerknes force through the rigid boundary attracts the bubble. During the migration of the bubble towards the rigid boundary, a high speed liquid jet is developed on the side of the bubble far from the rigid boundary and directed towards it. In the case of a bubble located very close to the rigid boundary, the high speed liquid jet directly impacts upon the rigid boundary. The direct impingement of the high speed liquid jet on the rigid boundary causes an extremely high pressure water hammer which facilitates the destruction of the rigid surface.

In *Chapter 6* it is shown that a collapsing bubble near a free surface is repelled by the Bjerknes force through the free surface. In this case, at the latest stages of the bubble collapse, a high speed liquid jet is developed on the side of the bubble close to the free surface and directed away from it.

The behaviour of the bubble near free surfaces gives rise to the idea that some compliant surfaces may act in a similar manner to free surfaces due to bubble pulsation and thus may reduce the liquid jet damage. Several experimental investigations [Gibson and Blake (1982), and Shima *et al.* (1989)] and a few theoretical and computational studies [Duncan and Zhang (1991)] have been done to determine the dynamics of a pulsating bubble near compliant surfaces.

Blake and Gibson (1987) pointed out that a coating of soft material behaves as a layer of a compliant surface and may have the tendency of reducing the impact of the liquid jet. The effect of a compliant surface on the behaviour of a bubble is through the minute displacement of the surface that absorbs energy from the fluid flow.

Duncan and Zhang (1991) simulated the dynamic behaviour of a constant pressure vapour bubble collapsing from its initial maximum volume near a compliant wall. They modelled the compliant wall as a circular spring-backed membrane with a radius of about bubble size which is attached to a rigid boundary along its edge. They showed that a properly chosen compliant wall may repel the bubble and direct the liquid jet away from it. Duncan and Zhang (1991) pointed out that their proposed iteration scheme for determining the initial pressure distribution on the compliant wall fails in the case of a cavitation bubble growing from its minimum volume.

Throughout this work it is found that in the case of a rebounding bubble generated by a high local energy input and growing from its initial minimum volume it is possible to determine the initial pressure distribution on the compliant surface by applying the iteration scheme proposed by Duncan and Zhang (1991). It is

obvious that considering the growth phase of the bubble has significant effect on the dynamic behaviour of the bubble during its consequent collapse.

In this chapter dynamics of a bubble is carried out in the vicinity of different compliant surfaces in the cases of:

- a constant pressure vapour bubble;
- a vapour bubble by considering the effects of vaporisation and condensation; and
- a rebounding bubble generated by a high local energy input and growing from its initial minimum volume.

In the first case two areas of computation are involved: the hydrodynamics of the flow of water and the dynamics of the compliant wall. The numerical simulation of the second and third cases require the computations of three domains: the vapour or a mixture of vapour and ideal gas inside the bubble with a pressure changing by the variation of the bubble volume, the liquid around the bubble and the compliant wall.

7.2 GEOMETRICAL DEFINITION

As illustrated in Figure 7.1, the vapour bubble is located in the liquid domain in the vicinity of a circular compliant coating, which is placed in a rigid boundary. The compliant layer is modelled as a spring-backed membrane. The polar cylindrical coordinate axes are chosen with the radial axis lying along the undisturbed surface of the compliant layer and the vertical axis normal to this surface. The vertical axis pierces the centroid of the bubble and the centre of the circular compliant surface.

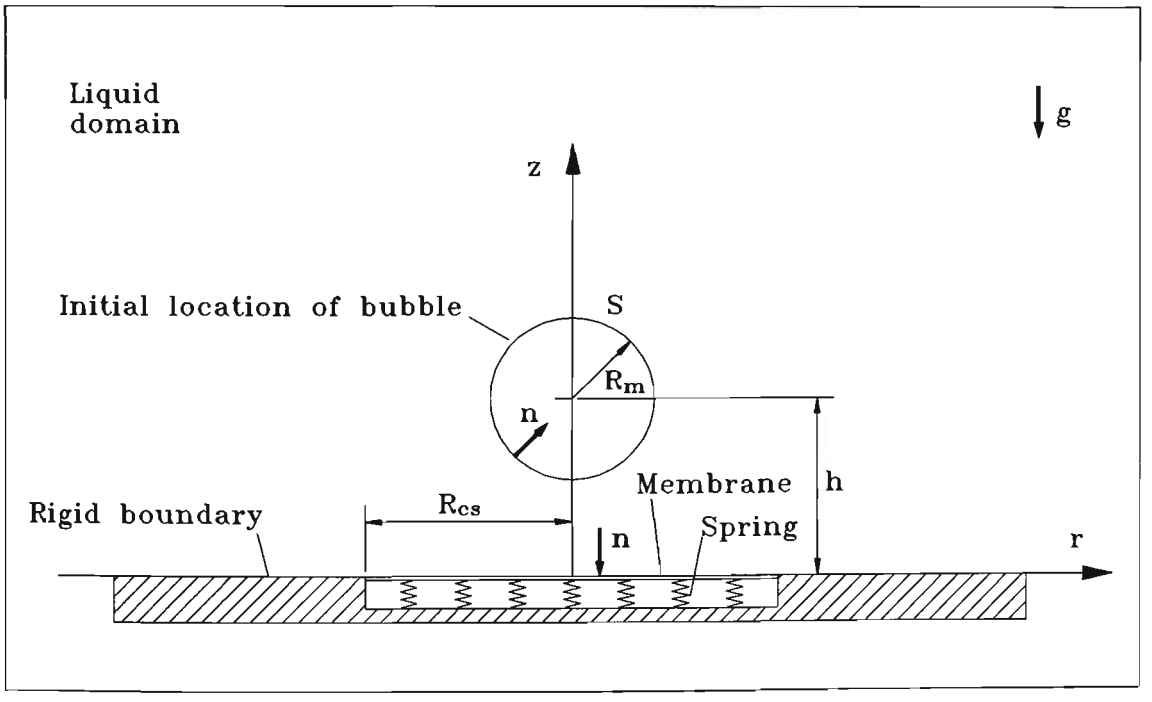

Figure 7.1 Geometrical definition for a bubble pulsating near a compliant surface.

7.3 MATHEMATICAL MODELLING

7.3.1 Hydrodynamic equation

As discussed in the previous chapters, the fluid flow is assumed to be incompressible, inviscid and irrotational and the surface tension on the bubble boundary is neglected. Thus the fluid flow behaves in the framework of potential flow and the velocity in the liquid domain and on the bubble boundary can be represented as the gradient of a potential which satisfies Laplace's equation. In this case the Green's formula may be written as:

$$c(p)\phi(p)+\int_{S_b+S_w}\phi(q)\frac{\partial}{\partial n}\left(\frac{1}{|p-q|}\right)dS=\int_{S_b+S_w}\frac{\partial}{\partial n}(\phi(q))\frac{1}{|p-q|}dS, \qquad (7.1)$$

where S_b is the surface of the bubble, S_w is the surface of the wall including compliant surface and rigid boundary, p is any given point in the liquid domain, or on S, which includes S_b and q is a point on S.

As discussed in *Section (5.7)* the unsteady Bernoulli equation, in Lagrangian form, becomes

$$\frac{D\phi}{Dt}=\frac{P_\infty-P_c}{\rho}+\frac{1}{2}|\nabla\phi|^2+g(z-h), \qquad (7.2)$$

and the non-dimensional Lagrangian expression of the unsteady Bernoulli Equation becomes

$$\frac{D\Phi}{Dt}=1+\frac{1}{2}|\nabla\Phi|^2+\delta^2(z-\gamma), \qquad (7.3)$$

where the non-dimensional variables z, t, Φ, γ and δ are defined in *Sections 5.3* and *5.7* and *7.6*.

It is obvious that in the cases that the pressure inside te bubble changes by the variation of the bubble volume, Equations (7.2) and (7.3) can be written respectively as

$$\frac{D\phi}{Dt} = \frac{P_\infty - P_V}{\rho} + \frac{1}{2}|\nabla\phi|^2 + g(z-h), \tag{7.4}$$

and

$$\frac{D\Phi}{Dt} = \frac{P_\infty - P_V}{P_\infty - P_c} + \frac{1}{2}|\nabla\Phi|^2 + \delta^2(z-\gamma), \tag{7.5}$$

where P_V is the pressure inside the bubble.

7.3.2 Compliant surface

A plate-spring backed Kramer-type compliant surface [Riley *et al.* (1988) and Carpenter and Garrad (1985)] may be represented in the form of

$$\frac{\partial^2\eta}{\partial t^2} = \frac{T}{m}\frac{\partial^2\eta}{\partial x^2} - d\frac{\partial\eta}{\partial t} - \frac{B}{m}\frac{\partial^4\eta}{\partial x^4} - \frac{K}{m}\eta + f, \tag{7.6}$$

where the coordinates are chosen with the x-axis lying the undisturbed compliant surface and the y-axis normal to this surface. Here $\eta(x,t)$ is the y-displacement of the compliant surface from its equilibrium position at time t and position x, T is the longitudinal tension and B the flexural rigidity of the plate , m is the mass per unit area, d is the damping coefficient, K is a spring constant, and f is an external forcing term. It should be noted that Equation (7.6) is for the y-component of the momentum of the compliant surface and the x-component of the momentum is usually neglected in such a model.

In this work the compliant wall is assumed to be circular sprig-backed membrane which is attached to a rigid boundary along its edge. By assuming a very thin membrane and by ignoring the effect of damping, the equation of the compliant surface in the cylindrical polar coordinates may be written in the form of [Duncan and Zhang (1991)]

$$m\frac{\partial^2\eta}{\partial t^2} - \mathrm{T}\frac{1}{r}\frac{\partial}{\partial r}\left(r\frac{\partial\eta}{\partial r}\right) + K\eta = -\left(P_w(r,t) - P_\infty\right), \tag{7.7}$$

where $\eta = \eta(r,t)$ is the vertical displacement of the compliant surface and P_w is the pressure on the compliant surface. In the absence of the bubble, for $t < 0$, the springs are compressed uniformly due to the steady uniform pressure, P_∞, exerted by the liquid domain. The displacement of the membrane at this time is taken as zero. The membrane is attached to the rigid boundary at $r = R_{cs}$ so the vertical displacement of the membrane at $r = R_{cs}$ is zero. During the collapse of the bubble, the liquid domain and the compliant surface are coupled using a linearized equation for the pressure and the velocity in both systems of the liquid domain and the compliant surface. These equations which are satisfied at the undisturbed position of the compliant surface $(z = 0)$, are:

$$\frac{\partial\eta}{\partial t} = w(r,0,t) = \frac{\partial\phi}{\partial z}, \tag{7.8}$$

$$P_w(r,t) = P(r,0,t) = -\rho\frac{\partial\phi}{\partial t} + P_\infty. \tag{7.9}$$

It should be noted that Equation (7.9) is the linearized Bernoulli equation.

7.4 DISCRETIZATION

Consider an axisymmetric bubble which is located in the vicinity of a compliant surface, Figure 7.2. The compliant surface is a spring-backed circular membrane with a radius of about bubble size. The radial axis is laid on the undisturbed compliant surface. The vertical axis is normal to the compliant surface at its centre point and penetrates the bubble through its centroid. The compliant surface is attached to a rigid boundary at $r = R_{cs}$ where R_{cs} is the radius of the compliant surface. The surface of the bubble is divided into M segments. The compliant surface is divided into M_{cs} equal segments while the rigid boundary is divided into M_{rb} segments. The lengths of the segments on the rigid boundary increase in the direction of the radial axis. Cubic splines are employed to approximate the surface of the bubble. Whereas the compliant surface and rigid boundary are approximated by linear segments. The collocation points are located at the midpoint of each segment. By indicating S_j as the *jth* segment, the discretized form of the Equation (7.1) for a point p_i on the surface of the bubble or on the surface of the compliant surface is given by:

$$2\pi\phi(p_i) + \sum_{j=1}^{M+M_w} \phi(q_j) \int_{S_j} \frac{\partial}{\partial n}\left(\frac{1}{|p_i - q_j|}\right) dS = \sum_{j=1}^{M+M_w} \frac{\partial}{\partial n}\left(\phi(q_j)\right) \int_{S_j} \frac{1}{|p_i - q_j|} dS, \qquad (7.10)$$

where $M_w = M_{cs} + M_{rb}$.

The integration over the surface of the bubble is carried out analytically, where the collocation points p_i are located at the midpoint of segments. Thus Equation (7.10) becomes a system of linear equations of the following form:

$$2\pi\phi(p_i) + \sum_{j=1}^{M+M_w} H_{ij}\phi(q_j) = \sum_{j=1}^{M+M_w} G_{ij}\psi(q_j), \qquad (7.11)$$

where *Hij* and *Gij* are the terms with respect of integration in Equation (7.11) which are integrated over each segment. The equation of the compliant surface, Equation (7.7), is decomposed into two first-order differential equations with respect to time:

$$\frac{\partial \eta}{\partial t} = \psi, \tag{7.12}$$

$$\frac{\partial \psi}{\partial t} = \frac{\mathrm{T}}{m}\frac{1}{r}\frac{\partial}{\partial r}\left(r\frac{\partial \eta}{\partial r}\right) - \frac{K}{m}\eta - \frac{P_w(r,t) - P_\infty}{m}. \tag{7.13}$$

The discretized form of Equation (7.13) can be given as:

$$\left[\frac{\partial \psi}{\partial t}\right]_i^j = \frac{\mathrm{T}}{m}\left[\frac{1}{r}\frac{\partial}{\partial r}\left(r\frac{\partial \eta}{\partial r}\right)\right]_i^j - \frac{K}{m}\eta_i^j - \frac{P_w(r_j,t_i) - P_\infty}{m}, \tag{7.14}$$

where

$$\left[\frac{1}{r}\frac{\partial}{\partial r}\left(r\frac{\partial \eta}{\partial r}\right)\right]_i^j = \left(\frac{1}{\Delta r^2} + \frac{1}{2\Delta r r^j}\right)\eta_i^{j+1} - \frac{2}{\Delta r^2}\eta_i^j + \left(\frac{1}{\Delta r^2} - \frac{1}{2\Delta r r^j}\right)\eta_i^{j-1}, \tag{7.15}$$

for $\left(0 < r^j < R_{cs}\right)$.

It should be noted that

$$\left[\frac{1}{r}\frac{\partial}{\partial r}\left(r\frac{\partial \eta}{\partial r}\right)\right]_i^j = \frac{4}{\Delta r^2}\left(\eta_i^{j+1} - \eta_i^j\right), \qquad \left(r^j = 0\right) \tag{7.16}$$

where Δr is the radial distance between the collocation points on the compliant surface. The boundary conditions are $\frac{\partial \eta}{\partial r} = 0$ at $r = 0$ and $\eta = 0$ at $r = R_{cs}$. The former boundary conditions is because of the symmetry, while the latter boundary conditions is because of the attachment of the membrane to the rigid boundary.

The discretized form of boundary conditions at the liquid domain-compliant surface interface, Equations (7.8) and (7.9), are

$$\left[\frac{\partial \eta}{\partial t}\right]_i^j = \left[\frac{\partial \phi}{\partial z}\right]_i^j = \psi_i^j, \tag{7.17}$$

$$P_{i+1}^j - P_\infty = -\rho \frac{\phi_{i+1}^j - \phi_i^j}{t_{i+1} - t_i}. \tag{7.18}$$

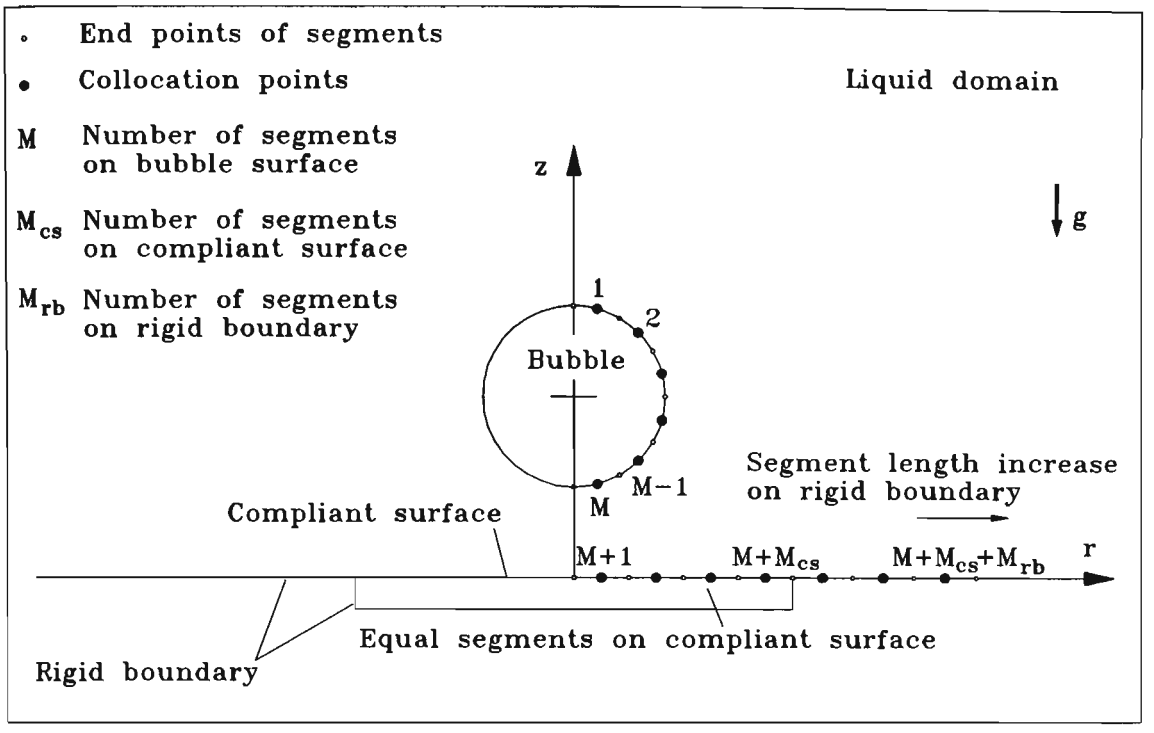

Figure 7.2 Discretization of the surface of the bubble and the compliant surface.

7.5 COMPUTATIONAL IMPLEMENTATION

A predictor-corrector scheme sometimes referred to as Heun's method [Ferziger (1981) and Duncan and Zhang (1991)] is used to integrate the boundary conditions on the bubble and the equation of the compliant surface in time. The r- and z-coordinates of the collocation points on the bubble and the corresponding values of the velocity potential, ϕ, at t_{i+1} are expressed as:

Predictor step:

$$\bar{r}_{i+1}^{j} = r_i^j + (t_{i+1} - t_i)u_i^j, \tag{7.19}$$

$$\bar{z}_{i+1}^{j} = z_i^j + (t_{i+1} - t_i)v_i^j, \tag{7.20}$$

$$\bar{\phi}_{i+1}^{j} = \phi_i^j + (t_{i+1} - t_i)\left[\frac{\partial \phi}{\partial t}\right]_i^j. \tag{7.21}$$

Corrector step:

$$r_{i+1}^{j} = r_i^j + \frac{1}{2}(t_{i+1} - t_i)(u_i^j + \bar{u}_{i+1}^j), \tag{7.22}$$

$$z_{i+1}^{j} = z_i^j + \frac{1}{2}(t_{i+1} - t_i)(v_i^j + \bar{v}_{i+1}^j), \tag{7.23}$$

$$\phi_{i+1}^{j} = \phi_i^j + \frac{1}{2}(t_{i+1} - t_i)\left(\left[\frac{\partial \phi}{\partial t}\right]_i^j + \left[\frac{\partial \bar{\phi}}{\partial t}\right]_i^j\right). \tag{7.24}$$

where the superscript refers to the collocation points ant the subscript refers to the time step.

The application of the predictor-corrector to the Equations (7.12) and (7.13) yields:

Predictor step:

$$\bar{\eta}_{i+1}^{j} = \eta_i^j + (t_{i+1} - t_i)\eta_i^j, \tag{7.25}$$

$$\bar{\psi}_{i+1}^{j} = \psi_i^j + (t_{i+1} - t_i)\left[\frac{\partial \psi}{\partial t}\right]_i^j. \tag{7.26}$$

Corrector step:

$$\eta_{i+1}^{j} = \eta_i^j + \frac{1}{2}(t_{i+1} - t_i)(\eta_i^j + \bar{\eta}_{i+1}^j), \tag{7.27}$$

$$\psi_{i+1}^{j} = \psi_i^j + \frac{1}{2}(t_{i+1} - t_i)\left(\left[\frac{\partial \psi}{\partial t}\right]_i^j + \left[\frac{\partial \bar{\psi}}{\partial t}\right]_i^j\right), \tag{7.28}$$

where $\left[\frac{\partial \psi}{\partial t}\right]_i^j$ is given by Equation (7.14).

The variable time step which is discussed in Section 5.10 is used for incrementing in time.

It should be noted that in the case of a bubble near a compliant surface there are two major starting cases:

- bubble collapses from its initial spherical maximum size; and
- bubble grows from its initial minimum size and achieves its maximum volume and then collapses.

At time t<0 the compliant surface has a horizontal flat surface which is under the hydrostatic pressure of the liquid domain, P_∞. At time $t = 0$ a spherical bubble is assumed to be located near the compliant surface and the initial pressure inside the bubble is P_i. One of the important points of the physics of the phenomenon which should be carefully considered is pressure of the liquid domain around the bubble and pressure distribution on the elastic surface at time $t = 0$.

The velocity potential on the surface of the bubble and normal velocity on the surface of the elastic layer at time $t = 0$ are equal to zero. Consequently the normal velocity on the surface of the bubble and the velocity potential on the compliant surface are zero at this time, $t = 0$. It is very important to notice that the liquid domain is unstable at this instant and the stagnant liquid domain is about to change to an unsteady fluid flow. The bubble is about to collapse and the elastic surface is about to deform. Despite the fact that normal velocity and velocity potential on the surface of the bubble and on the compliant surface at t=0 are zero, both of the surfaces have acceleration at this instant and are about to deform. This is an important point which clarifies the state of the liquid domain at $t = 0$. It means that despite the stagnant state of the liquid domain at $t = 0$, the

hydrostatic pressure not longer exists on the elastic surface and around the bubble in the liquid domain at this instant and is transferred to a hydrodynamic pressure distribution on the surface of the elastic layer and in the liquid domain around the bubble. The acceleration of the compliant surface is related to its physical properties. It is obvious that different surfaces with different physical properties under the same hydrodynamic conditions have different accelerations at $t = 0$. It is very interesting to note that the hydrodynamic pressure distribution on the surface of the elastic layer at time $t = 0$ is related to the acceleration and consequently to the physical properties of the elastic layer at this time. It is obvious that the pressure distribution on the surface of the elastic layer is also related to the pressure difference between the pressure inside the bubble and the pressure at the infinity, $\Delta P = P_\infty - P_i$, the density of water and the size and shape of the bubble. Unfortunately the pressure distribution on the compliant surface at $t = 0$ is not known. To overcome this problem the pressure distribution on the compliant surface at $t = 0$ is approximated by assuming a rigid boundary instead of the compliant surface. It is obvious that assuming a rigid boundary instead of a compliant surface at $t = 0$ will significantly affect the accuracy of the solution. To obtain an accurate initial pressure distribution on the compliant surface an iteration scheme has been proposed by Duncan and Zhang (1991) by using intermediate compliant surfaces between a specified compliant surface and rigid boundary. The iteration scheme is based on the fact that during collapsing of a bubble from its initial maximum size near a wall the pressure distribution on the surface of the wall at the early stages of the bubble collapse settles down to a distribution which is nearly constant in time. In this scheme pressure distribution on the rigid surface at time $t = 0$ is applied to a relatively stiff surface and calculations proceed a few time steps. Then the equibriliated pressure distribution

is applied to a relatively softer compliant surface and the calculations start again from time t=0 and proceed for a few time steps. This cycle repeats until reaching the desired compliant surface.

By determining the pressure distribution on the surface of the rigid boundary at time $t=0$, the calculated pressure distribution is applied to the surface of the compliant boundary to determine its acceleration at this time, $t=0$, and consequently its normal velocity at the next time step, $t=\Delta t$. Then by having velocity potential on the surface of the bubble and normal velocity on the compliant surface at $t=\Delta t$ and by applying the boundary integral method the normal velocity on the surface of the bubble and the velocity potential on the surface of the compliant surface at $t=\Delta t$ are determined. Since then the pressure distribution on the compliant surface is determined by Equation (7.18) at each time step. Having pressure distribution on the compliant surface gives the acceleration on the compliant surface and consequently normal velocity for the next time step can be determined. Then calculations proceed through the time.

It should be noted that Duncan and Zhang (1991) pointed out that their proposed iteration method could not be used to start the calculations with a growing constant pressure vapour bubble which would later reach a maximum size and then collapse. The reason for this restriction is that their proposed iteration method requires the pressure distribution on the compliant surface to be nearly constant during first ten or so time steps of the calculation. If the constant pressure bubble collapses from rest at its maximum size the pressure distribution on the wall has this property. Whereas, if the constant pressure vapour bubble is initially growing from its minimum size, the pressure distribution on the wall will

change rapidly in the early stages of the bubble growth and the iteration scheme will not work.

Throughout this research it is found that in the case of a bubble generated by a high local energy input, during the early stages of the growth phase the pressure distribution on the nearby wall changes very slowly. This is because of the fact that the velocity and consequently the velocity potential on the surface of the bubble, generated by a high local energy input, in its initially minimum volume is assumed to be zero. In this case the bubble contains a mixture of constant pressure vapour bubble and ideal gas and its governing equations are presented and discussed in *Section 5.5*. Thus it is found that the iteration scheme proposed by Duncan and Zhang (1991) can be successfully applied to the case of a growing bubble from its initial minimum volume which is generated by a high local energy input.

7.6 NUMERICAL RESULTS AND DISCUSSION

Dynamics of a bubble near compliant surfaces is a solid-liquid problem. In this problem there are a number of independent variables for the fluid including the maximum radius of the bubble, R_m, the initial distance of the centroid of the bubble from the wall, h, the pressure difference driving the bubble collapse, $\Delta P = P_\infty - P_c$, and the density of the liquid, ρ. For the compliant surface the independent variables are the mass per unit area, m, the tension, T, the spring constant, K, and the radius of the compliant surface, R_{cs}. Based on these independent variables the non-dimensional variables are defined as:

$$\mathrm{r} = \frac{r}{R_m}, \tag{7.29}$$

$$\mathrm{z} = \frac{r}{R_m}, \tag{7.30}$$

$$\mathrm{R} = \frac{R}{R_m}, \tag{7.31}$$

$$\mathrm{t} = \frac{t}{R_m}\left(\frac{P_\infty - P_c}{\rho}\right)^{\frac{1}{2}}, \tag{7.32}$$

$$\Phi = \frac{\phi}{R_m}\left(\frac{\rho}{P_\infty - P_c}\right)^{\frac{1}{2}}, \tag{7.33}$$

$$\Psi = \psi\left(\frac{\rho}{P_\infty - P_c}\right)^{\frac{1}{2}}, \tag{7.34}$$

$$\delta^2 = \frac{\rho g R_m}{P_\infty - P_c}, \tag{7.35}$$

$$\gamma = \frac{h}{R_m}, \tag{7.36}$$

$$M^* = \frac{m}{\rho R_m}, \tag{7.37}$$

$$T^* = \frac{T}{R_m \Delta P}, \tag{7.38}$$

$$K^* = \frac{K R_m}{\Delta P}, \tag{7.39}$$

and

$$R_{cs} = \frac{R_{cs}}{R_m}. \tag{7.40}$$

M^* is the ratio of the mass per unit area of membrane to an equivalent mass per unit area of the liquid based on a thickness R_m. K^* is the ratio of the spring term in the membrane equation to the pressure difference driving the collapse. T^* is the ratio of the tension term in the membrane equation to the pressure driving the collapse. The timescale for the compliant surface [Duncan and Zhang (19910] can be found by applying the Hankel-Laplace transformation techniques to Equation (7.7) in the absence of the flow. Thus it is found that

$$\left(\frac{t}{T_{cs}}\right)^2 = \frac{T^*}{M^*}\left(\frac{\lambda_n}{M^*}\right)^2 + \frac{K^*}{M^*}\left(\frac{1}{\pi}\right)^2, \tag{7.41}$$

where t is timescale for the flow which is given by Equation (7.32), T_{cs} is one-half period of free oscillation for the compliant surface and λ_n $(n = 1,2,3,...)$are the zeros of the zeroth-order Bessel function. It is obvious that for the quite small values of T^*, the spring-mass term, $\frac{K^*}{M^*}$, dominates the ratio of the flow timescale to the compliant surface timescale for the lower modes.

7.6.1 A constant pressure vapour bubble near compliant surfaces

In this section the dynamics of a constant pressure vapour bubble collapsing from its initial spherical maximum volume is carried out in the cases of the bubble near a rigid boundary and near compliant surfaces.

Figure 7.3 illustrates the collapse phase of the bubble with $\gamma = 1.5$ and $\delta = 0.1808$ above a rigid boundary. It is shown that the bubble during its collapse phase migrates towards the rigid boundary. At the latest stages of the collapse a liquid jet is developed on the far side of the bubble from the rigid boundary and directed towards it.

Figure 7.4 illustrates the collapse phase of the vapour bubble with $\gamma = 1.5$ and $\delta = 0.1808$ above a compliant surface. The compliant surface is characterised by M*=3.5, T*=0.0025, K*=3.5 and $R_{cs} = 2.5R_m$. In this case it is shown that the vapour bubble collapse is nearly spherical. At the latest stages of the collapse phase, the bottom side of the bubble close to the compliant surface becomes flattened. While the top side of the bubble far from the compliant surface is slightly pointed up away from the compliant surface. Figure 7.5 illustrates the collapse phase of the bubble characterised by $\gamma = 1.5$ and $\delta = 0.1808$ above a compliant surface. The compliant surface is characterised by M*=2.0, T*=0.0025, K*=2.0 and $R_{cs} = 2.5R_m$. In this case it is shown that the vapour bubble during its collapse phase migrates upward away from the compliant surface. At the latest stages of the collapse the bottom side of the bubble close to the compliant surface is flattened.

Figure 7.6 illustrates the collapse phase of a constant pressure vapour bubble with $\gamma = 1.5$ and $\delta = 0.1808$ above a compliant surface. The compliant surface is

characterised by M*=3.5, T*=0.0025, K*=3.5 and $R_{cs} = 2.5R_m$. In this case the vapour bubble during its collapse phase migrates rapidly upward away from the compliant surface. At the latest stages of the collapse phase the bottom side of the bubble close to the compliant surface is flattened. A broad liquid jet is developed on the flattened side of the bubble close to the compliant surface and directed away from it.

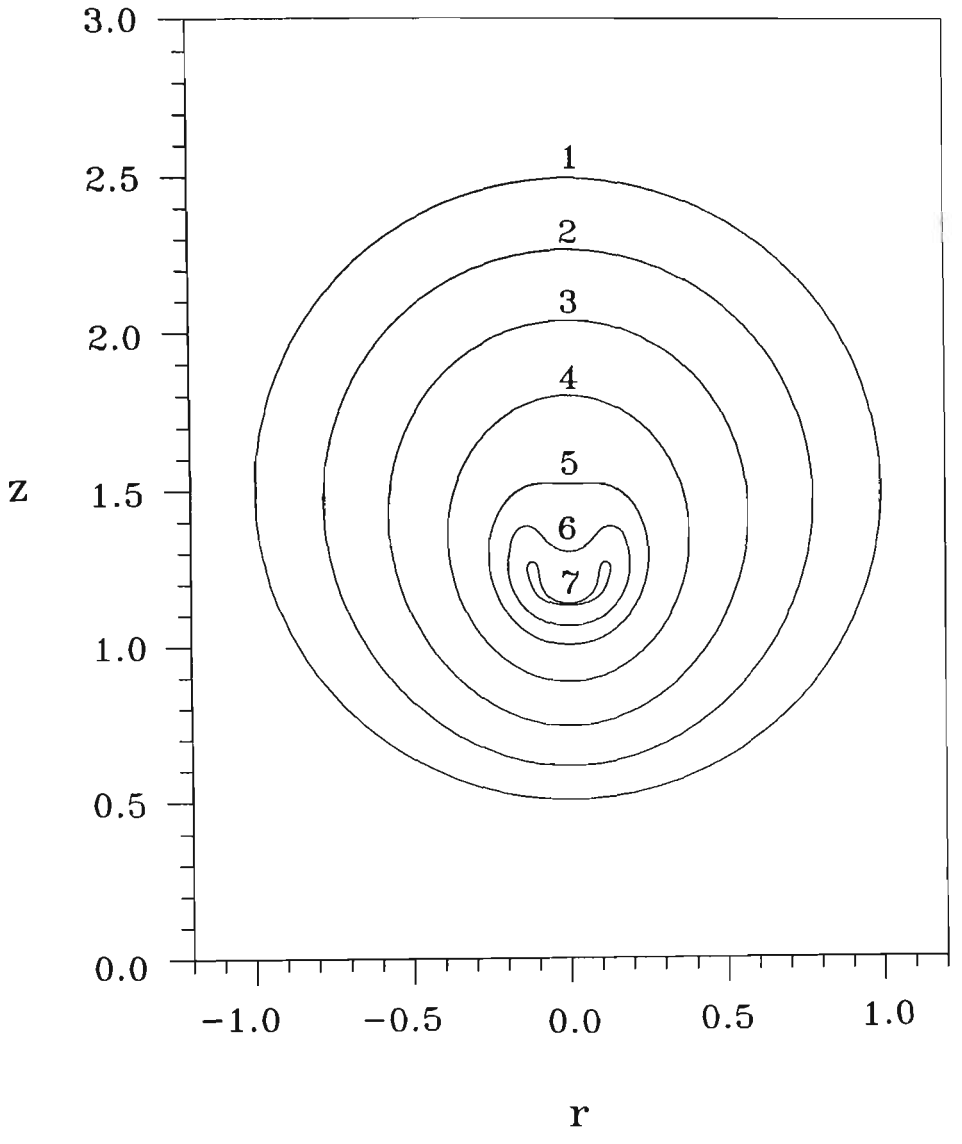

Figure 7.3 Bubble shapes for the collapse of a constant pressure vapour bubble near a rigid boundary. The bubble is characterised with $\gamma = 1.5$ and $\delta = 0.1808$. The non-dimensional times corresponding to bubble successive profiles are: 0.0000 (outermost), 0.6557, 0.8623, 0.9692, 1.0113, 1.0221, 1.0291 (innermost).

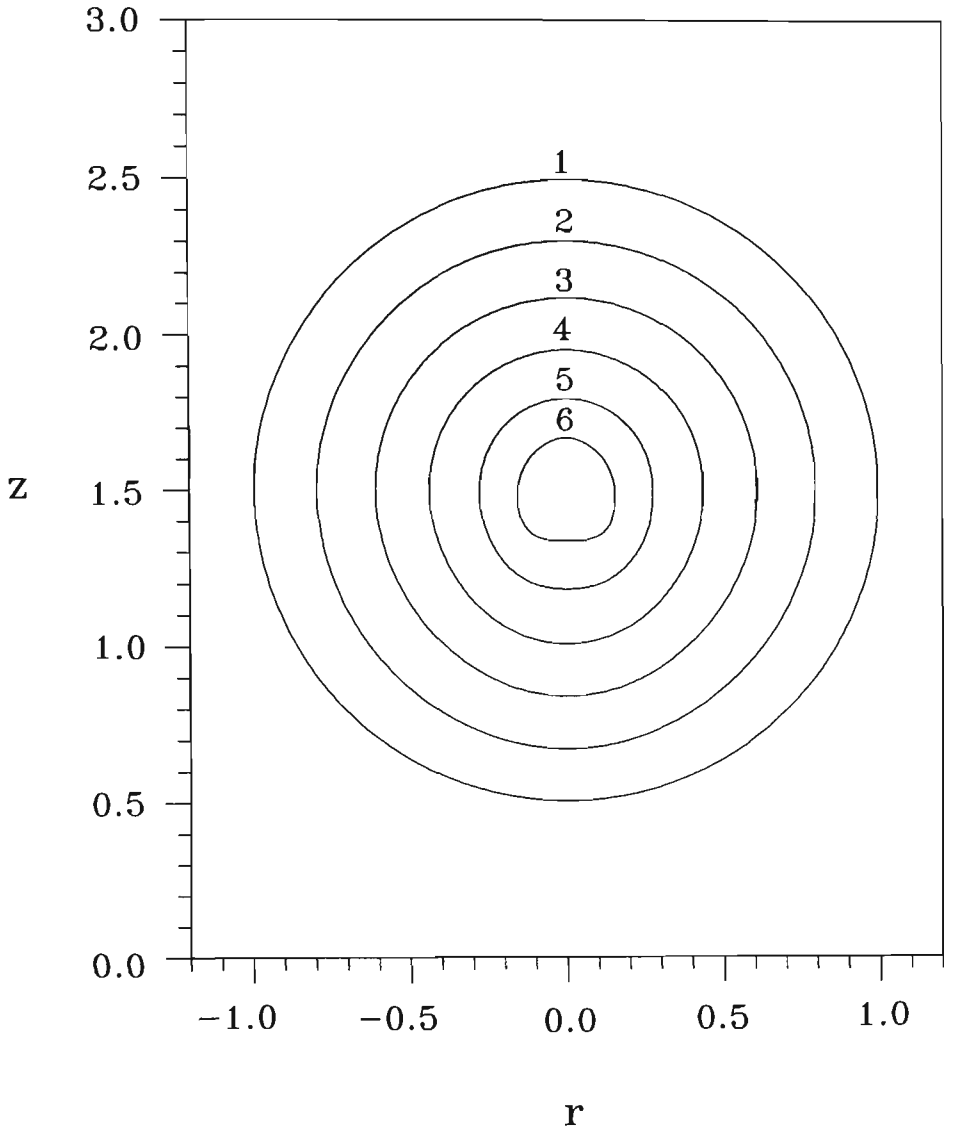

Figure 7.4 Bubble shapes for the collapse of a constant pressure vapour bubble near a compliant surface. The bubble is characterised with $\gamma = 1.5$ and $\delta = 0.1808$. The compliant surface is characterised by $M^* = 3.5$, $T^* = 0.0025$, $K^* = 3.5$ and $R_{cs} = 2.5R_m$. The non-dimensional times corresponding to bubble successive profiles are: 0.0000 (outermost), 0.6059, 0.7851, 0.8772, 0.9240, 0.9414 (innermost).

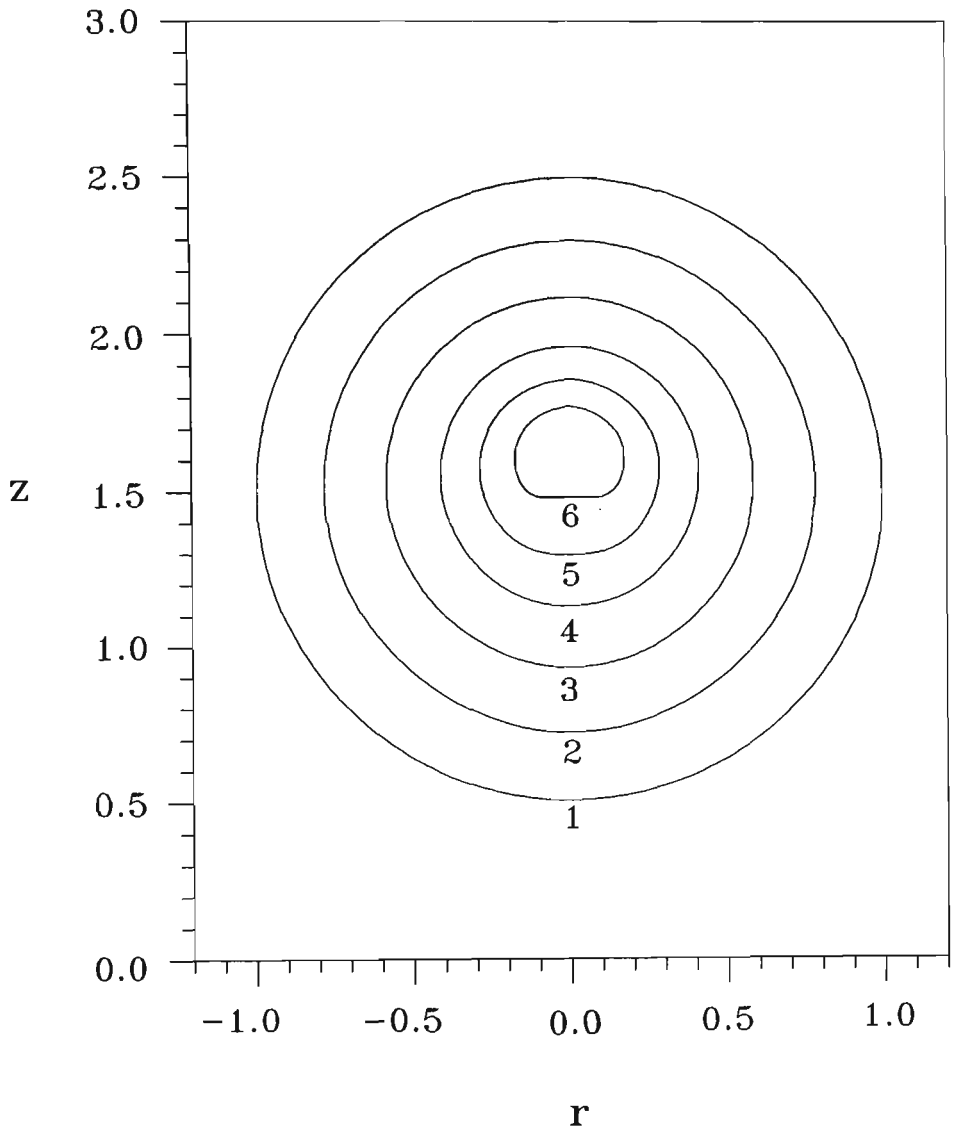

Figure 7.5 Bubble shapes for the collapse of a constant pressure vapour bubble near a compliant surface. The bubble is characterised with $\gamma = 1.5$ and $\delta = 0.1808$. The compliant surface is characterised by $M^* = 2.0$, $T^* = 0.0025$, $K^* = 2.0$ and $R_{cs} = 2.5R_m$. The non-dimensional times corresponding to bubble successive profiles are: 0.000 (outermost), 0.608, 0.779, 0.861, 0.894, 0.911 (innermost).

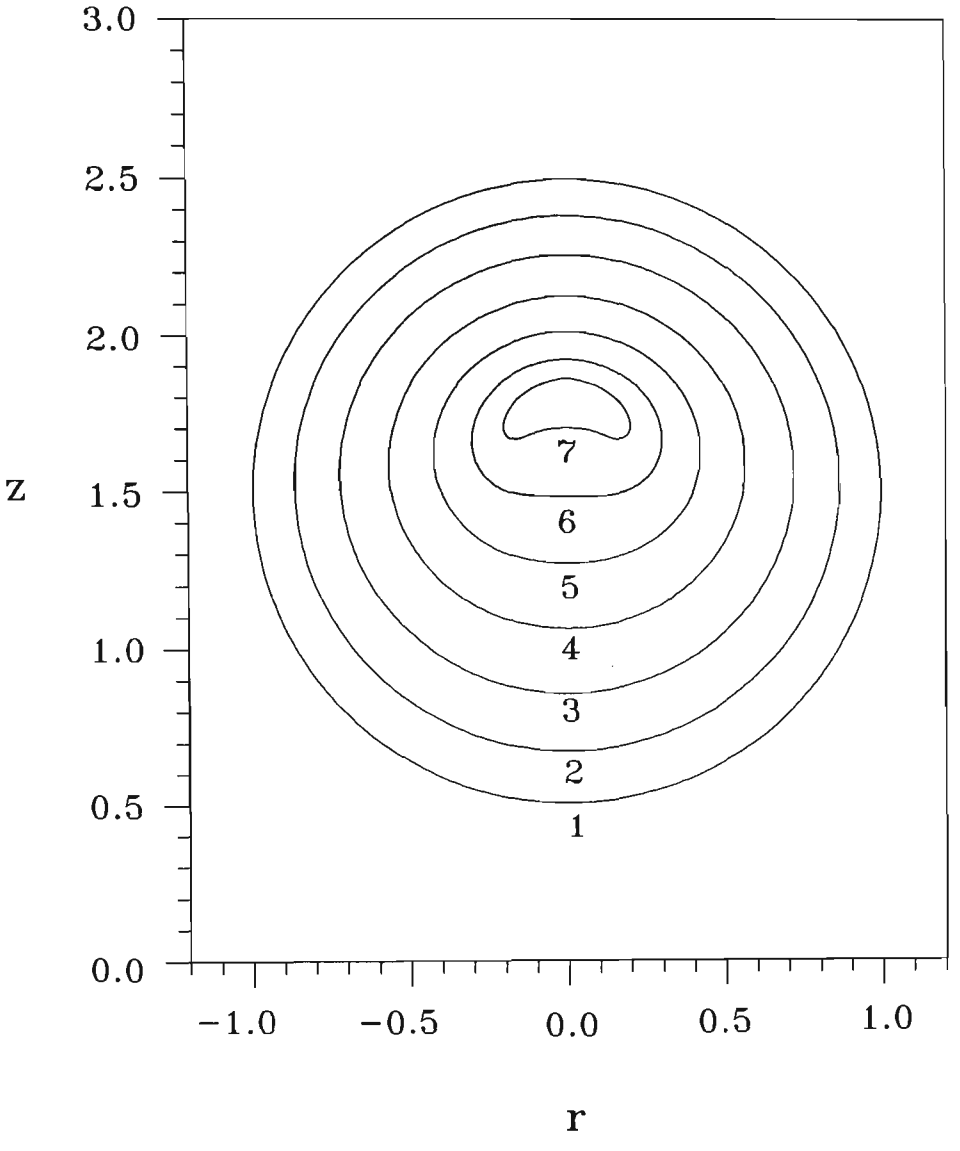

Figure 7.6 Bubble shapes for the collapse of a constant pressure vapour bubble near a compliant surface. The bubble is characterised with $\gamma = 1.5$ and $\delta = 0.1808$. The compliant surface is characterised by $M^* = 1.0$, $T^* = 0.0025$, $K^* = 1.0$ and $R_{cs} = 2.5R_m$. The non-dimensional times corresponding to bubble successive profiles are: 0.0000 (outermost), 0.4742, 0.6512, 0.7655, 0.8273, 0.8626, 0.8789 (innermost).

Figure 7.7 illustrates the initial pressure distribution on the surface of the rigid boundary and different compliant surfaces because of the pressure of the vapour bubble in its initial maximum volume. The pressure is non-dimensionalised by $\frac{P_w - P_\infty}{P_\infty - P_c}$, where P_w is the pressure on the surface of the wall, P_∞ is the pressure inside the liquid domain and on the wall in the absence of the bubble and P_c is the saturated vapour pressure of the liquid. Figure 7.7 shows that the pressure on the surface of the wall at $t = 0$ is less than the pressure of the liquid domain in the absence of the bubble. It is shown that the pressure at $r = 0$ has the lowest value when the vapour bubble starts to collapse. Figure 7.7 indicates that the initial relative negative pressure on a compliant wall is less than its corresponding value on the rigid boundary. It is also shown that for the most compliant surface the initial negative pressure on the wall has its minimum value. This fact is also found by Duncan and Zhang (1991).

Figure 7.8 shows that the collapse rate of the bubble near a rigid boundary is lower than the collapse rate of the bubble near compliant surfaces. Figure 7.8 indicates that by increasing the compliance of the surface the collapse rate of the bubble increases and consequently the lifetime of the bubble decreases. Figure 7.9 illustrates the migration of the bubble centroid with $\gamma = 1.5$ and $\delta = 0.1808$ in the cases of the bubble above a rigid boundary and the bubble above different compliant surfaces. Figure 7.9 indicates that the bubble is attracted by the rigid boundary. In the case of the bubble above a relatively stiff compliant surface the centroid of the bubble remains nearly constant. It is shown that more compliant surfaces repel the bubble and cause the migration of the bubble away from it.

Figure 7.10 illustrates the pressure generated by the bubble on the rigid boundary and on the compliant surfaces at $r = 0$. As it is shown in Figure 7.10 the pressure

on the most compliant surfaces at $r = 0$ reaches a maximum value and then rapidly drops. This exactly corresponds with the numerical results of Duncan and Zhang (1991) for the most compliant surface which repels the bubble and deflects the direction of the liquid jet away.

Figure 7.11 illustrates the velocity of the top point of the bubble on the axis of symmetry and far away from the wall. It should be noted that as discussed previously, positive values of velocity indicate a direction into the bubble, whereas negative values indicate a direction outward from the bubble.

Figure 7.12 shows the velocity of the bottom point of the bubble close to the boundary. Figure 7.12 indicates that the velocity of the bottom point of the bubble in the cases of different compliant surfaces is much higher than the case of the bubble near a rigid boundary. This is because of the fact that the compliant surfaces repel the bubble and may deflect the liquid jet away from it.

Figure 7.13 illustrates the velocity of the compliant surface at $r = 0$ during the collapse phase of a constant pressure vapour bubble collapsing from its initial spherical maximum volume. It is shown that in the early stages of the bubble collapse the velocity on the compliant surfaces at $r = 0$ is directed into the liquid domain. This is because of the negative relative pressure on the compliant surface with respect to the ambient pressure in the liquid domain. At the latest stages of the bubble collapse the velocity of the compliant surface directed into the liquid domain at $r = 0$ drops rapidly. This is because of the increasing pressure on the compliant surface generated by the bubble at the latest stages of its collapse.

Figure 7.14 illustrates the displacement of the compliant surface at $r = 0$. This figure indicates that in the case of a constant pressure vapour bubble collapsing from its initial maximum volume near a compliant surface, the compliant surface has a continuous movement into the liquid domain at $r = 0$.

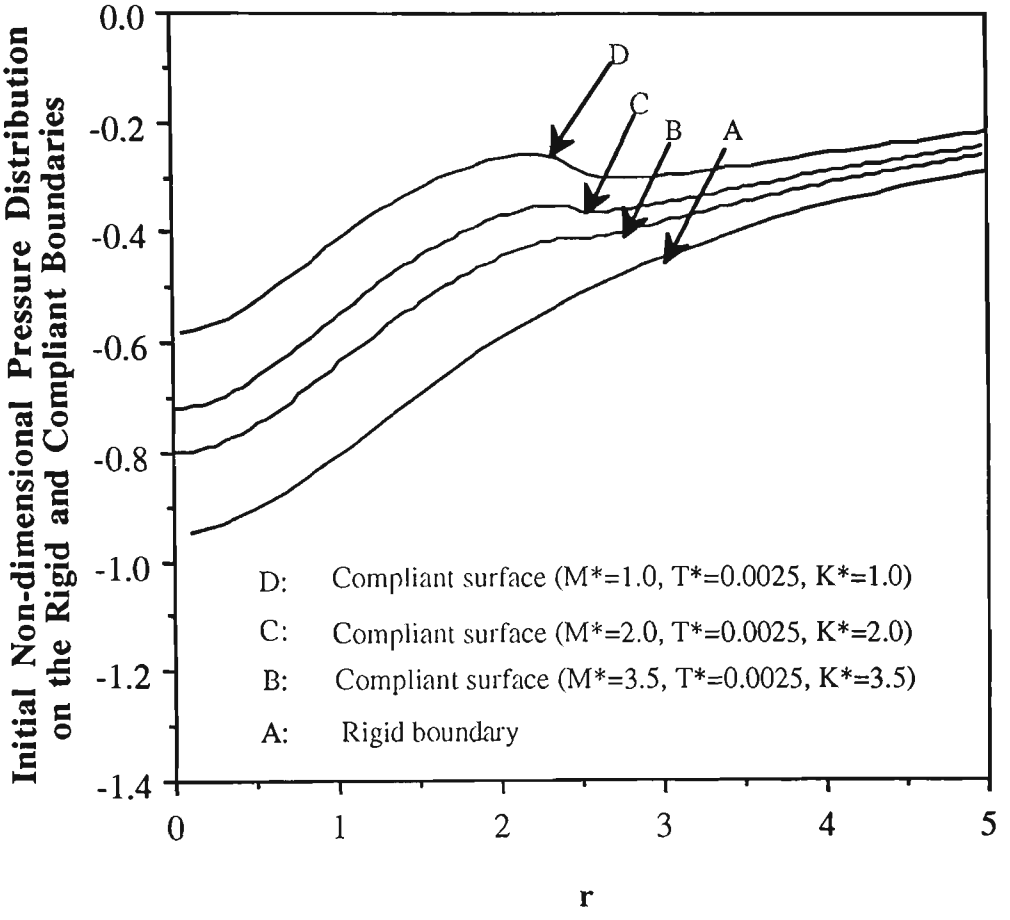

Figure 7.7 Initial pressure distribution on the rigid boundary and on the different compliant surfaces generated by the bubble in its initial maximum volume. The bubble is characterised by $\gamma = 1.5$ and $\delta = 0.1808$ and radius of the compliant surface is $R_{cs} = 2.5R_m$.

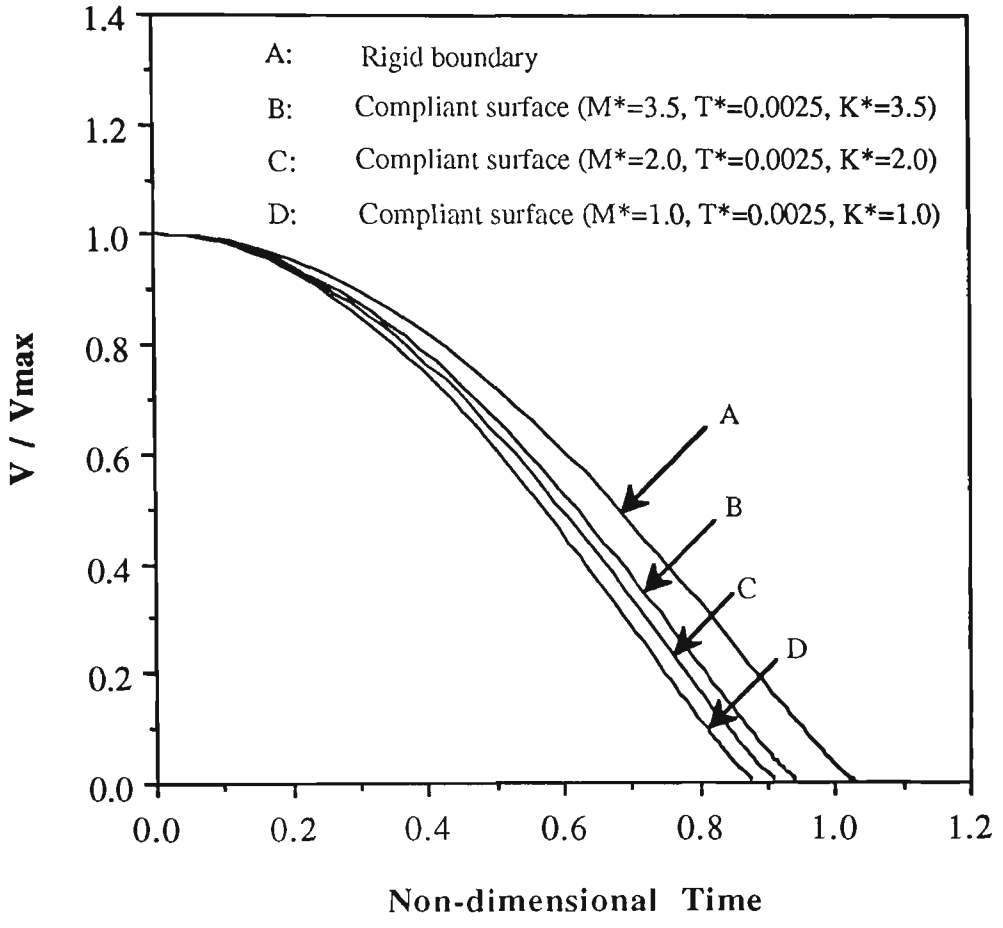

Figure 7.8 Collapse rate of a constant pressure vapour bubble collapsing from its initial maximum volume near a rigid boundary and near different compliant surfaces. The bubble is characterised by $\gamma = 1.5$ and $\delta = 0.1808$ and radius of the compliant surface is $R_{cs} = 2.5R_m$.

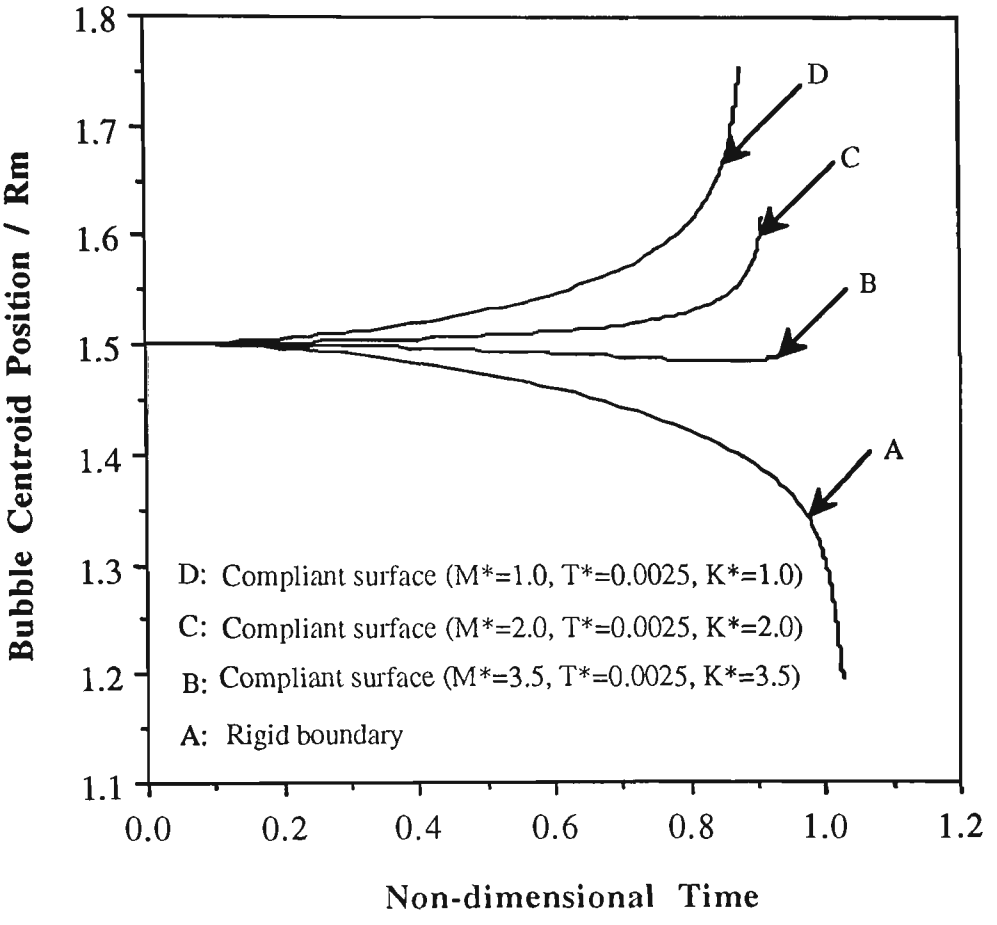

Figure 7.9 Migration of the bubble centroid during its collapse near a rigid boundary and near different compliant surfaces. The bubble is characterised by $\gamma = 1.5$ and $\delta = 0.1808$ and radius of the compliant surface is $R_{cs} = 2.5R_m$.

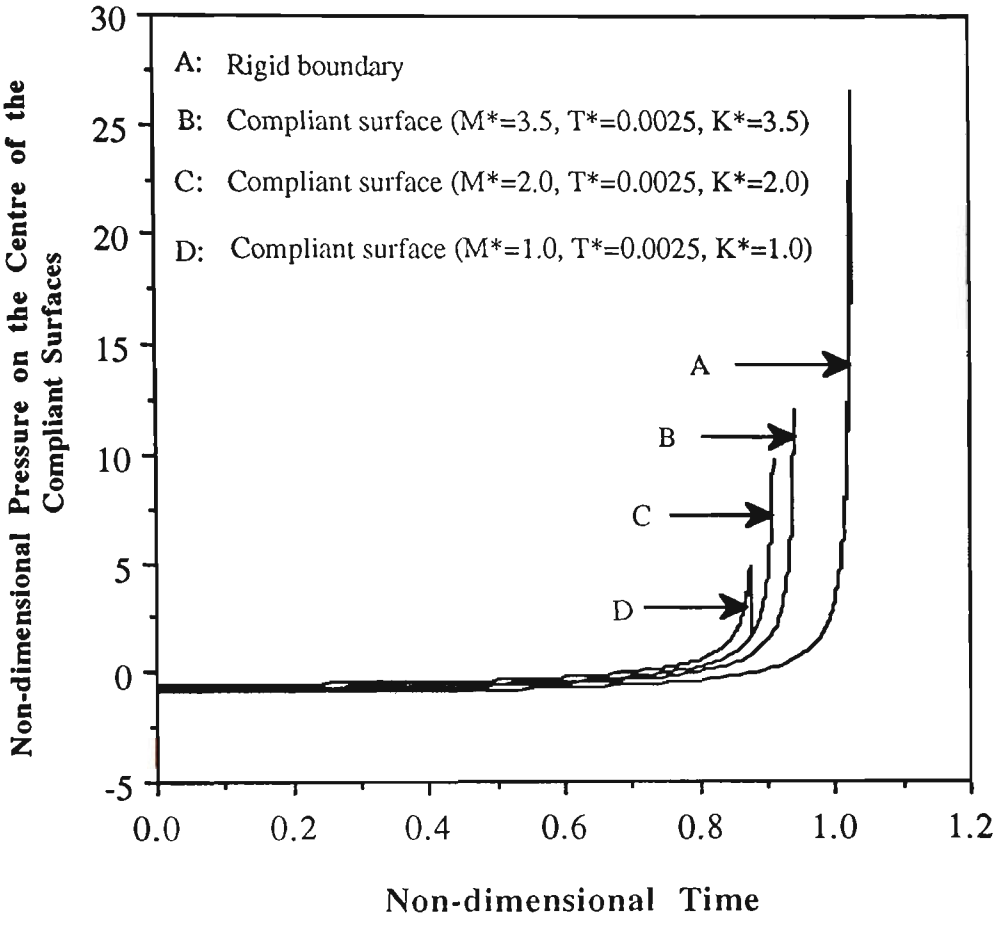

Figure 7.10 Pressure on the rigid boundary and on the different compliant surfaces at $r = 0$.

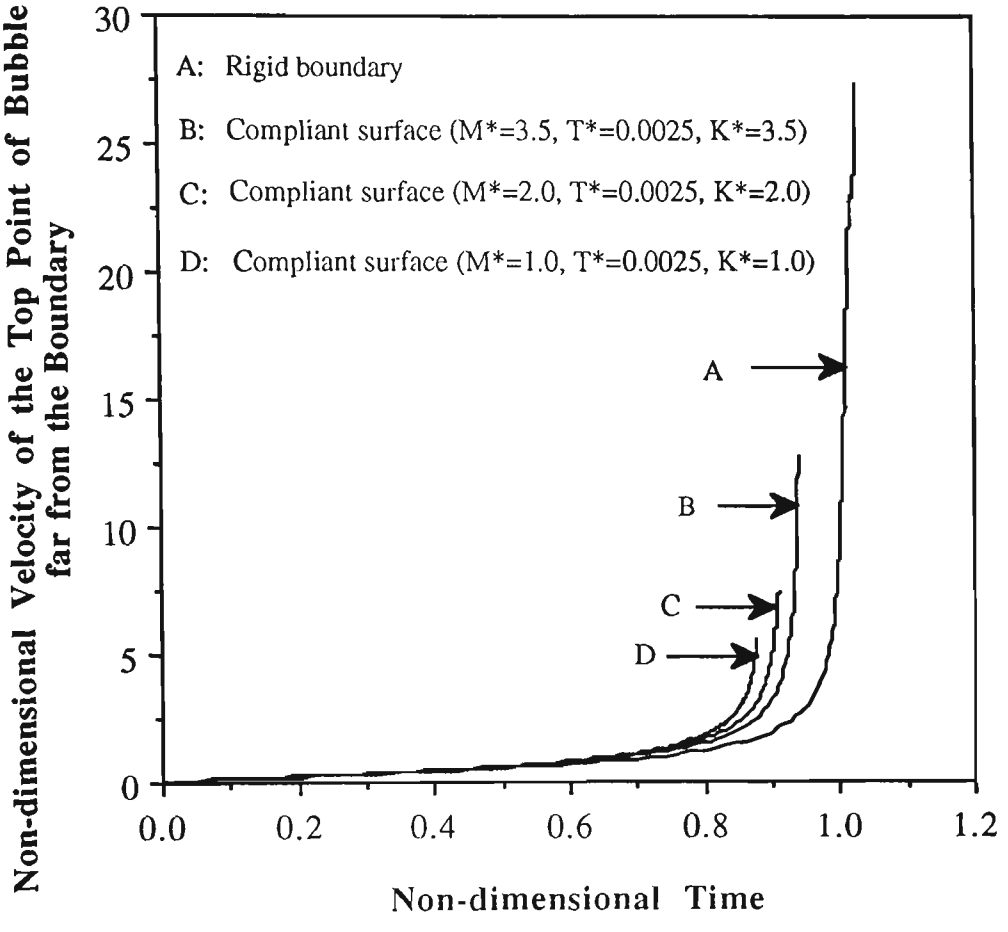

Figure 7.11 Velocity of the top point of the bubble far from the boundary in the cases of the bubble near a rigid boundary and near different compliant surfaces. The bubble is characterised by $\gamma = 1.5$ and $\delta = 0.1808$ and radius of the compliant surface is $R_{cs} = 2.5R_m$.

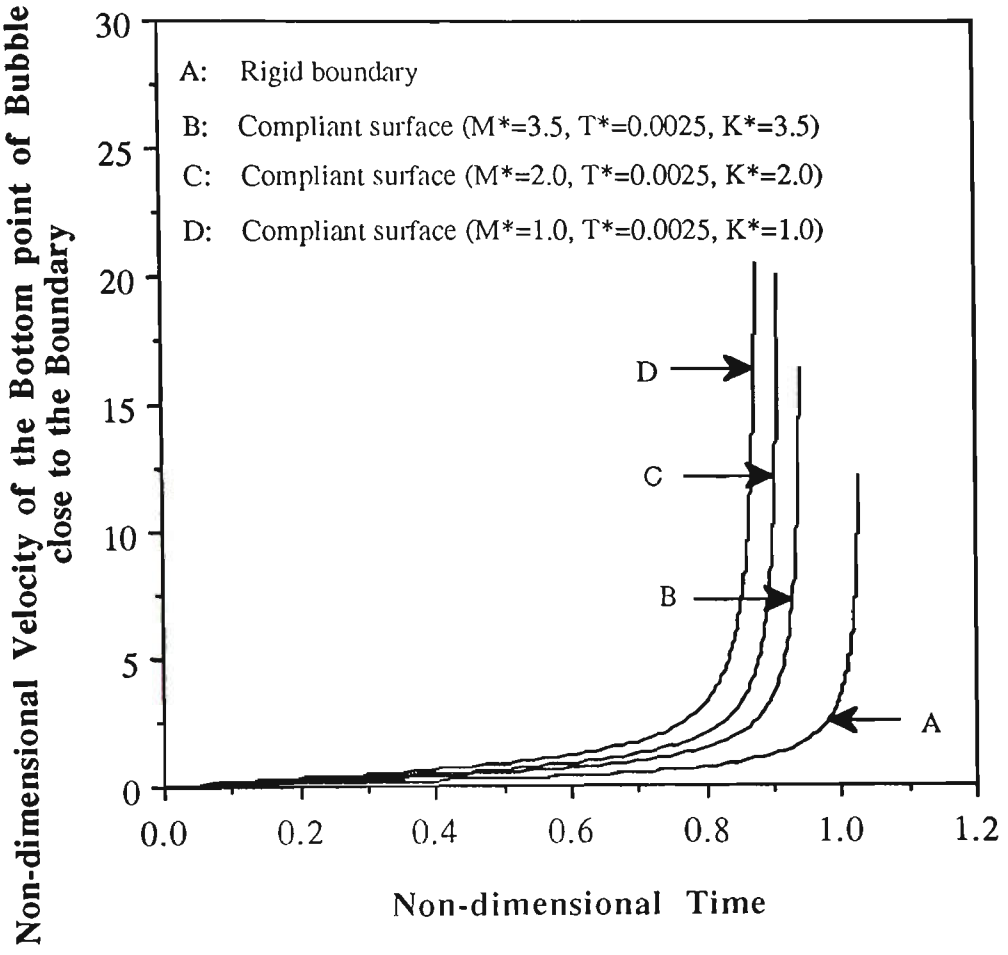

Figure 7.12 Velocity of the bottom point of the bubble close to the boundary in the cases of the bubble near a rigid boundary and near different compliant surfaces. The bubble is characterised by $\gamma = 1.5$ and $\delta = 0.1808$ and radius of the compliant surface is $R_{cs} = 2.5R_m$.

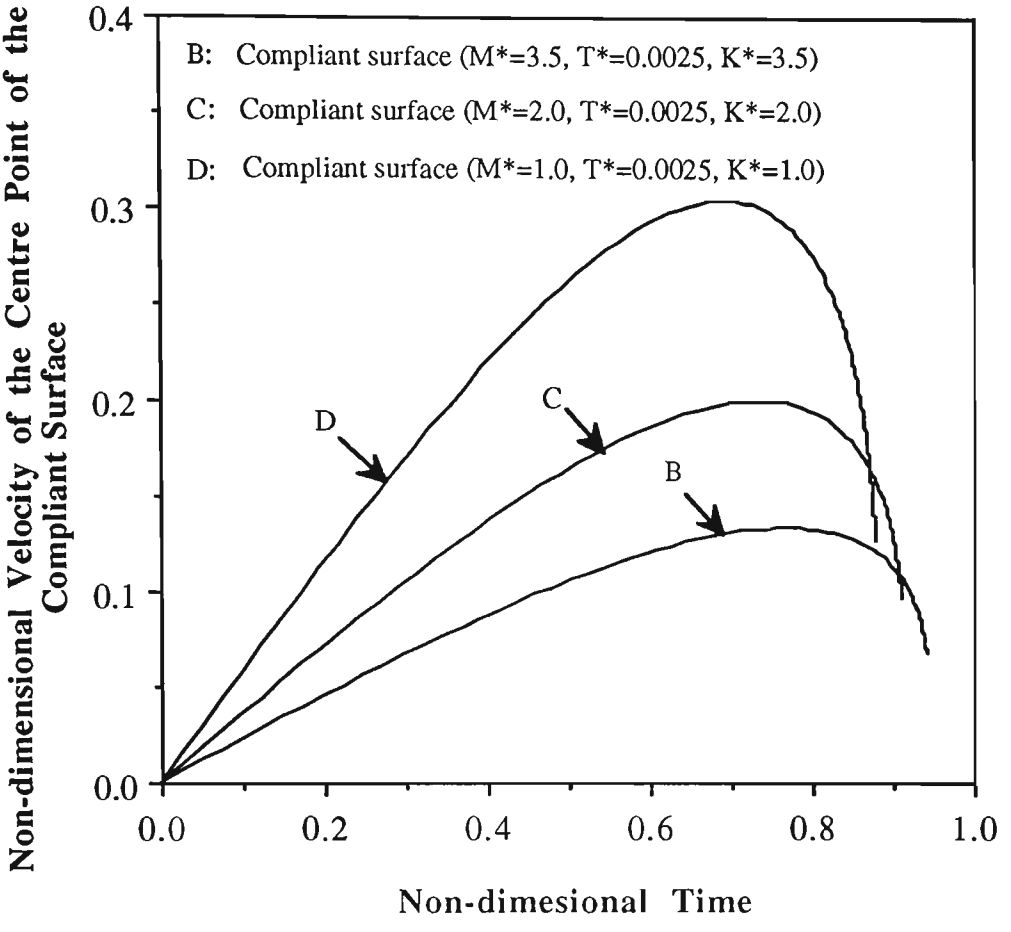

Figure 7.13 Velocity of the compliant surface during the bubble collapse at $r = 0$. The radius of the compliant surface is $R_{cs} = 2.5R_m$.

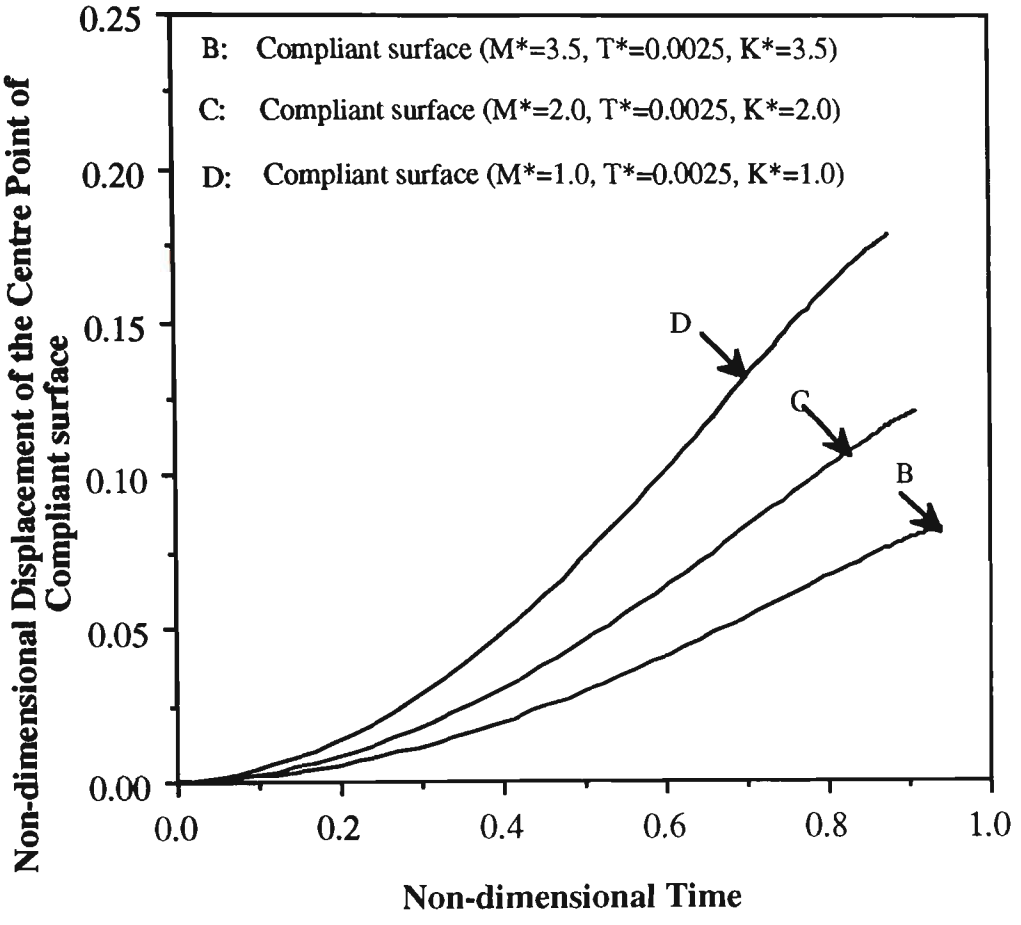

Figure 7.14 Displacement of the compliant surface during the bubble collapse at $r = 0$. The radius of the compliant surface is $R_{cs} = 2.5R_m$.

7.6.2 A rebounding vapour bubble collapsing near a compliant surface

In this section the dynamics of a rebounding vapour bubble, discussed in Sections 4.4 and 5.6, collapsing from its initially maximum volume, is investigated in the cases of the bubble near a rigid boundary and near a compliant surface.

Figure 7.15 illustrates the collapse of a vapour bubble near a rigid boundary. The vapour bubble is characterised by $\gamma = 1.5$ $\delta = 0.0$. In this case the vapour bubble collapses to its minimum volume and then rebounds. During the first collapse and rebound phases, the bubble migrates slightly towards the rigid boundary. At the latest stages of the second collapse the side of the bubble far from the rigid boundary is flattened. At the end of the second collapse phase a liquid jet is initiated and developed on the flattened side of the bubble directed towards the rigid boundary. During the early stages of the bubble rebound the liquid jet is fully developed and penetrates the opposite side of the bubble.

Figure 7.16 illustrates the vapour bubble behaviour near a compliant surface. The compliant surface is characterised by M*=1.0, T*=0.0025, K*=1.0 and $R_{cs} = 2.5R_m$. It is shown that during the first collapse and rebound phases, the vapour bubble migrates slightly away from the compliant surface. The slight migration of the bubble away from the compliant surface continues during the second collapse and rebound phases of the bubble. During the early stages of the third collapse the side of the bubble close to the compliant surface is flattened. At the latest stages of the third collapse phase of the bubble a liquid jet is initiated on the flattened side of the bubble directed away from the compliant surface. The liquid jet is fully developed during the third rebound of the bubble. At the early

stages of the fourth collapse of the bubble the liquid jet penetrates the opposite side of the bubble, and transforming it into a toroidal shape.

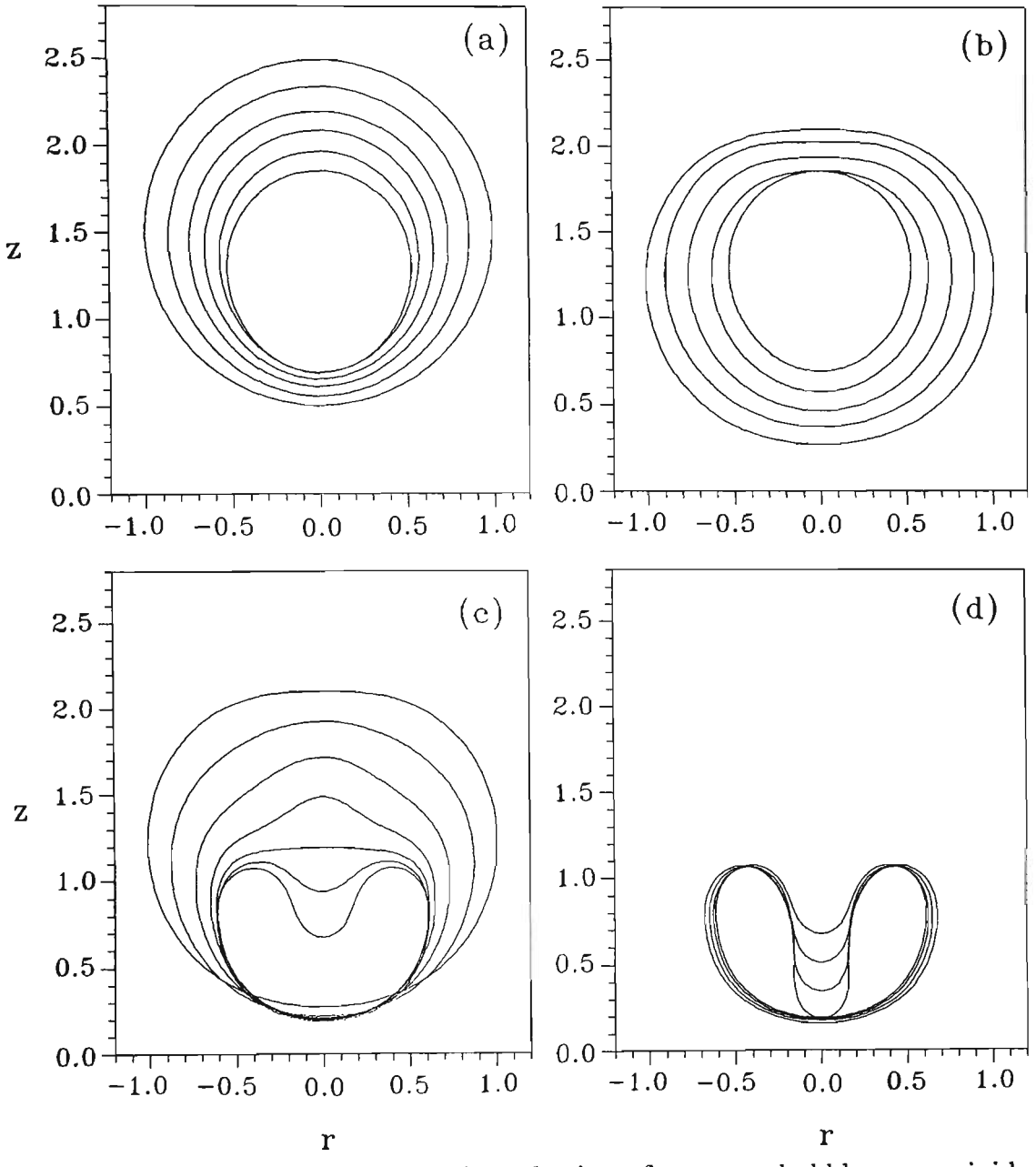

Figure 7.15 Bubble shapes for the pulsation of a vapour bubble near a rigid boundary. The bubble is characterised with $\gamma = 1.5$ and $\delta = 0$. The non-dimensional times corresponding to bubble successive profiles are: (a) Collapse phase: 0.0000 (outermost), 0.5448, 0.7505, 0.8746, 0.9983, 1.1450 (innermost). (b) Rebound phase: 1.1450 (innermost), 1.3404, 1.5241, 1.7611, 2.3042 (outermost). (c) Second collapse phase: 2.3042 (outermost), 2.8919, 3.1410, 3.2816, 3.3717, 3.4299, 3.4920 (innermost). (d) Second rebound phase: 3.4920 (innermost), 3.5368, 3.5851, 3.6323 (outermost).

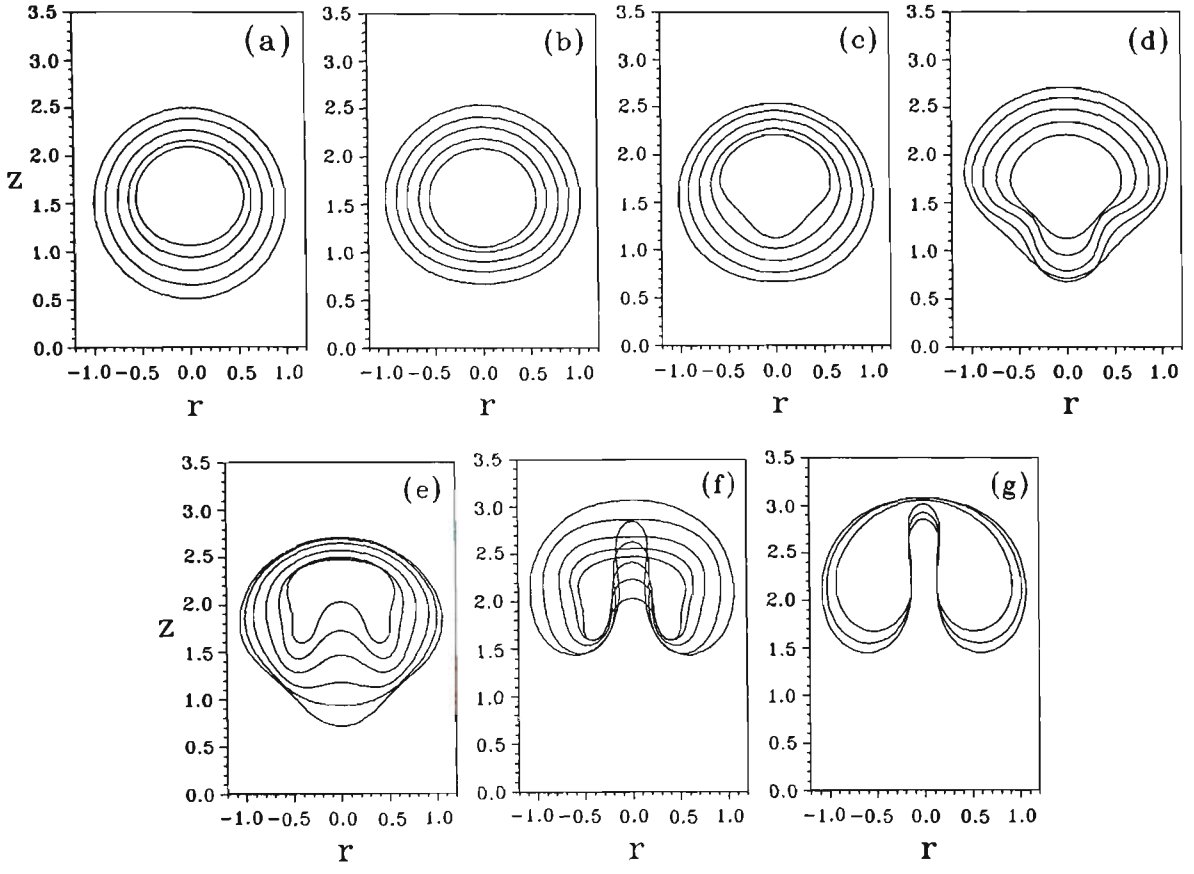

Figure 7.16 Bubble shapes for the pulsation of a vapour bubble near a compliant surface. The bubble is characterised with $\gamma = 1.5$ and $\delta = 0$. The compliant surface is characterised by $M^* = 1.0$, $T^* = 0.0025$, $K^* = 1.0$ and $R_{cs} = 2.5R_m$. The non-dimensional times corresponding to bubble successive profiles are: (a) Collapse phase: 0.0000 (outermost), 0.4610, 0.6590, 0.8032, 0.9749 (innermost). (b) Rebound phase: 0.9749 (innermost), 1.1664, 1.3185, 1.4900, 1.9502 (outermost). (c) Second collapse phase: 1.9502 (outermost), 2.3581, 2.5548, 2.7136, 2.9271 (innermost). (d) Second rebound phase: 2.9271 (innermost), 3.1284, 3.2919, 3.4680, 3.9091 (outermost). (e) Third collapse phase: 3.9091 (outermost), 4.1632, 4.3444, 4.5280, 4.6850, 4.8731 (innermost). (f) Third rebound phase: 4.8731 (innermost), 5.0061, 5.1405, 5.3658, 5.8677 (outermost). (g) Fourth collapse phase: 5.8677 (outermost), 6.1632, 6.3467 (innermost).

Figure 7.17 shows the initial pressure distribution on the rigid boundary and on the compliant surface generated by the vapour bubble at $t = 0$. The initial pressure at $r = 0$ for the case of the rigid boundary is $P_w - P_\infty = -0.927\Delta P$ and for the case of the compliant surface is $P_w - P_\infty = -0.573\Delta P$.

Figure 7.18 illustrates the variation of the volume of the rebounding vapour bubble with respect to time in the cases of the bubble near a rigid boundary and near the compliant surface. It is shown that the collapse rate of the bubble near a compliant surface of the bubble is higher than the collapse rate of the bubble near a rigid boundary.

Figure 7.19 illustrates the migration of the bubble centroid with respect to time. Figure 7.19 indicates that during the pulsation of the bubble near a rigid boundary, the vapour bubble migrates towards the rigid boundary. In the case of the bubble near the compliant surface, the vapour bubble continuously migrates away from the compliant surface.

Figure 7.20 shows the variation of the pressure inside the bubble during its pulsation near a rigid boundary and near a compliant surface.

Figure 7.21 illustrates the velocity and displacement of the compliant surface at $r = 0$ with respect to time.

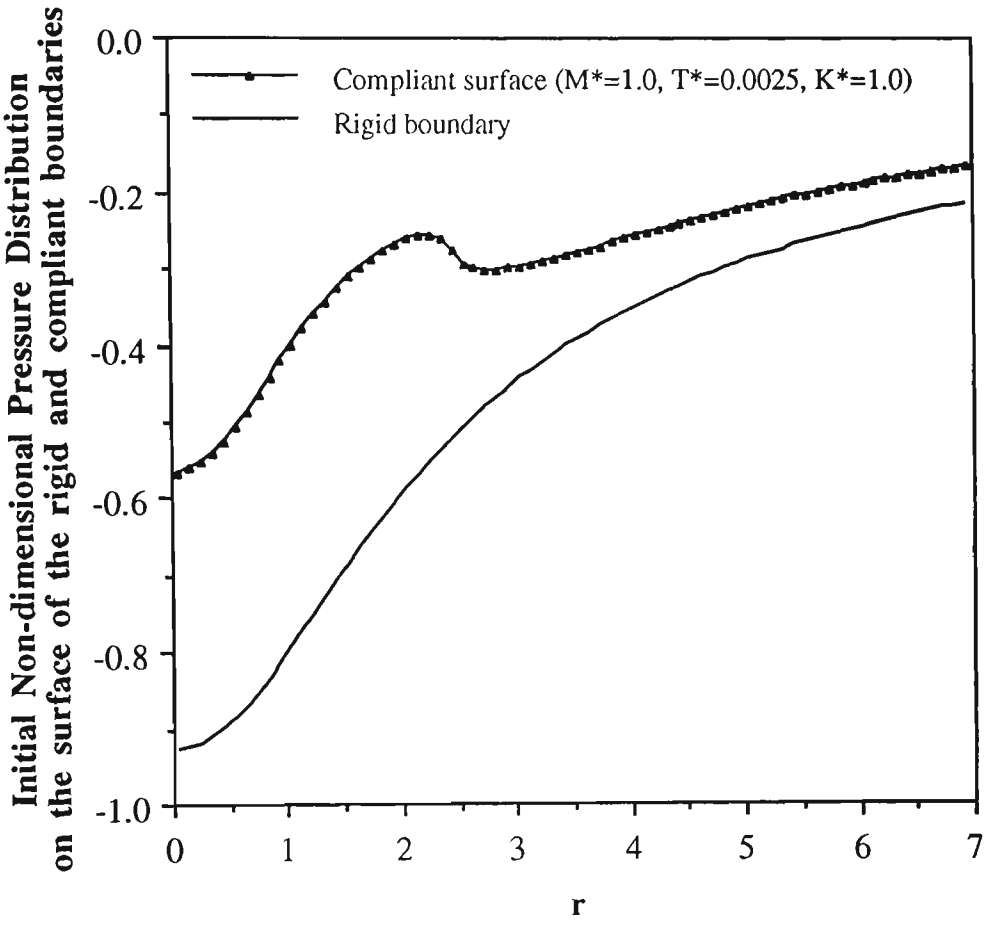

Figure 7.17 Initial pressure distribution on the rigid boundary and on the different compliant surfaces generated by a vapour bubble in its initial maximum volume. The bubble is characterised by $\gamma = 1.5$ and $\delta = 0$ and the radius of the compliant surface is $R_{cs} = 2.5R_m$.

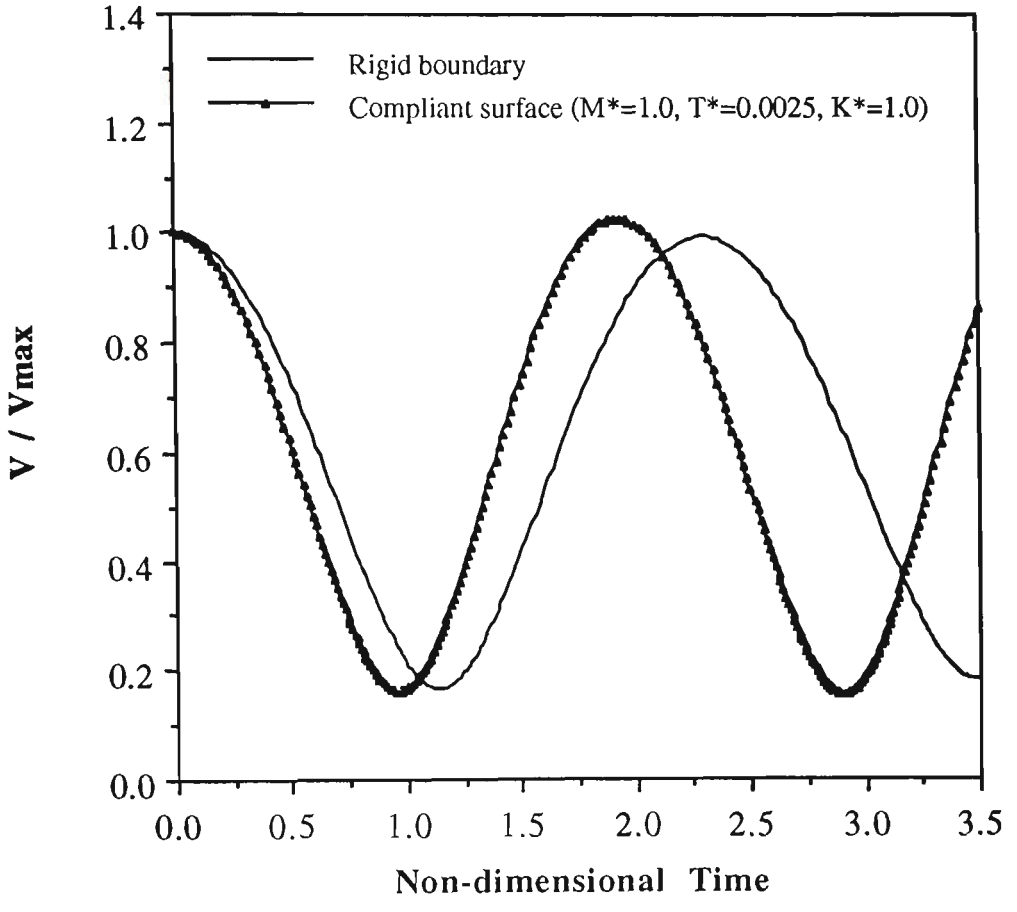

Figure 7.18 Variation of the bubble volume during its pulsation near a rigid boundary and near a compliant surface. The bubble is characterised by $\gamma = 1.5$ and $\delta = 0$ and the radius of the compliant surface is $R_{cs} = 2.5R_m$.

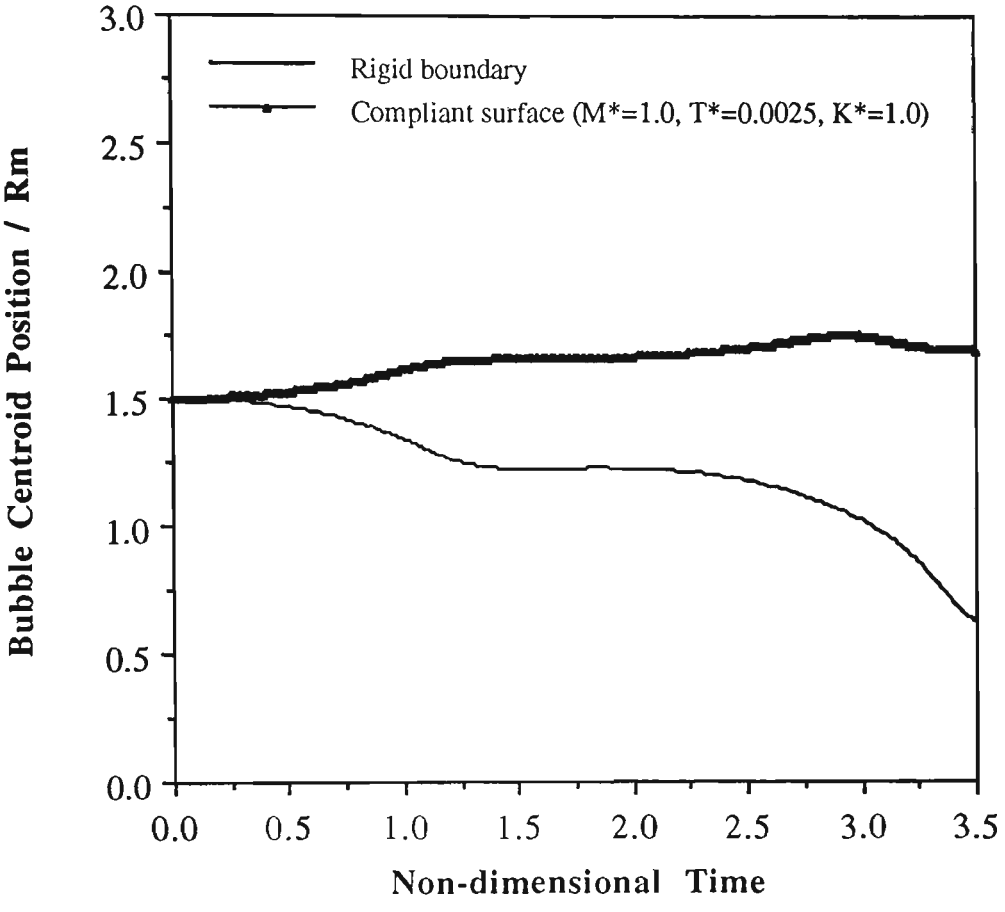

Figure 7.19 Migration of the centroid of a vapour bubble during its pulsation near a rigid boundary and near a compliant surface. The bubble is characterised by $\gamma = 1.5$ and $\delta = 0$ and the radius of the compliant surface is $R_{cs} = 2.5R_m$.

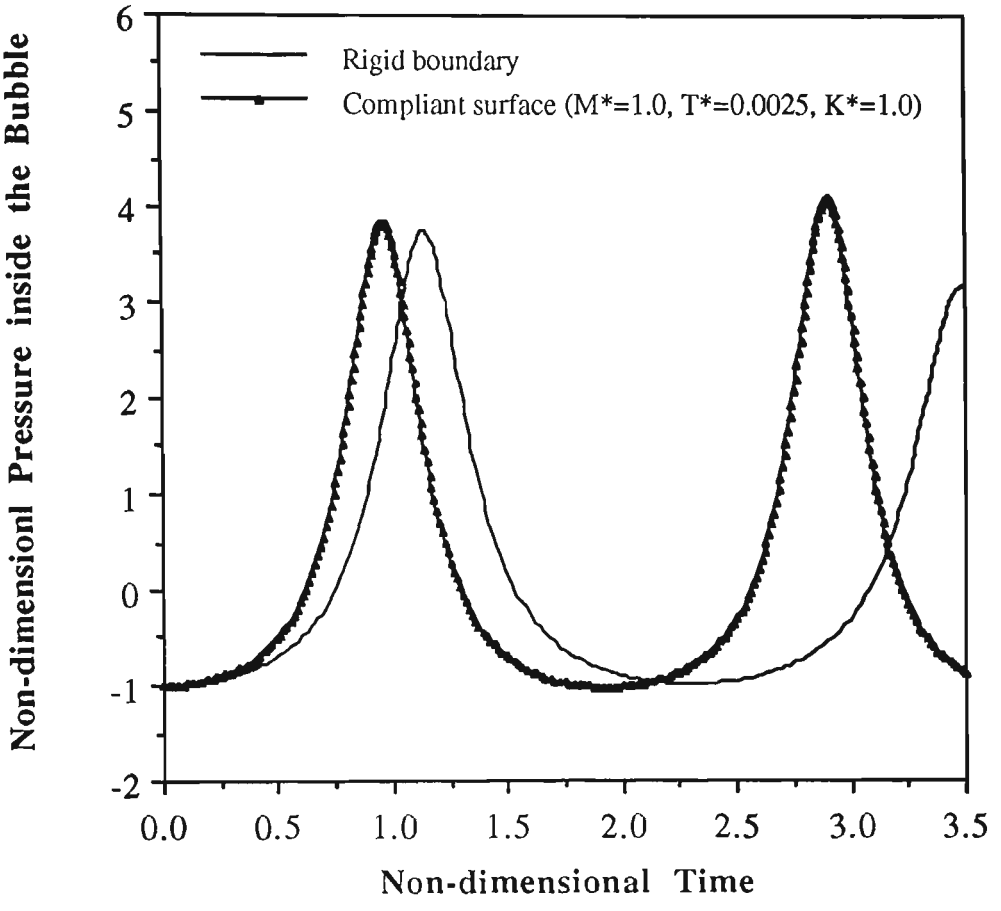

Figure 7.20 Variation of the pressure inside a vapour bubble during its pulsation near a rigid boundary and near compliant surfaces. The bubble is characterised by $\gamma = 1.5$ and $\delta = 0$ and the radius of the compliant surface is $R_{cs} = 2.5R_m$.

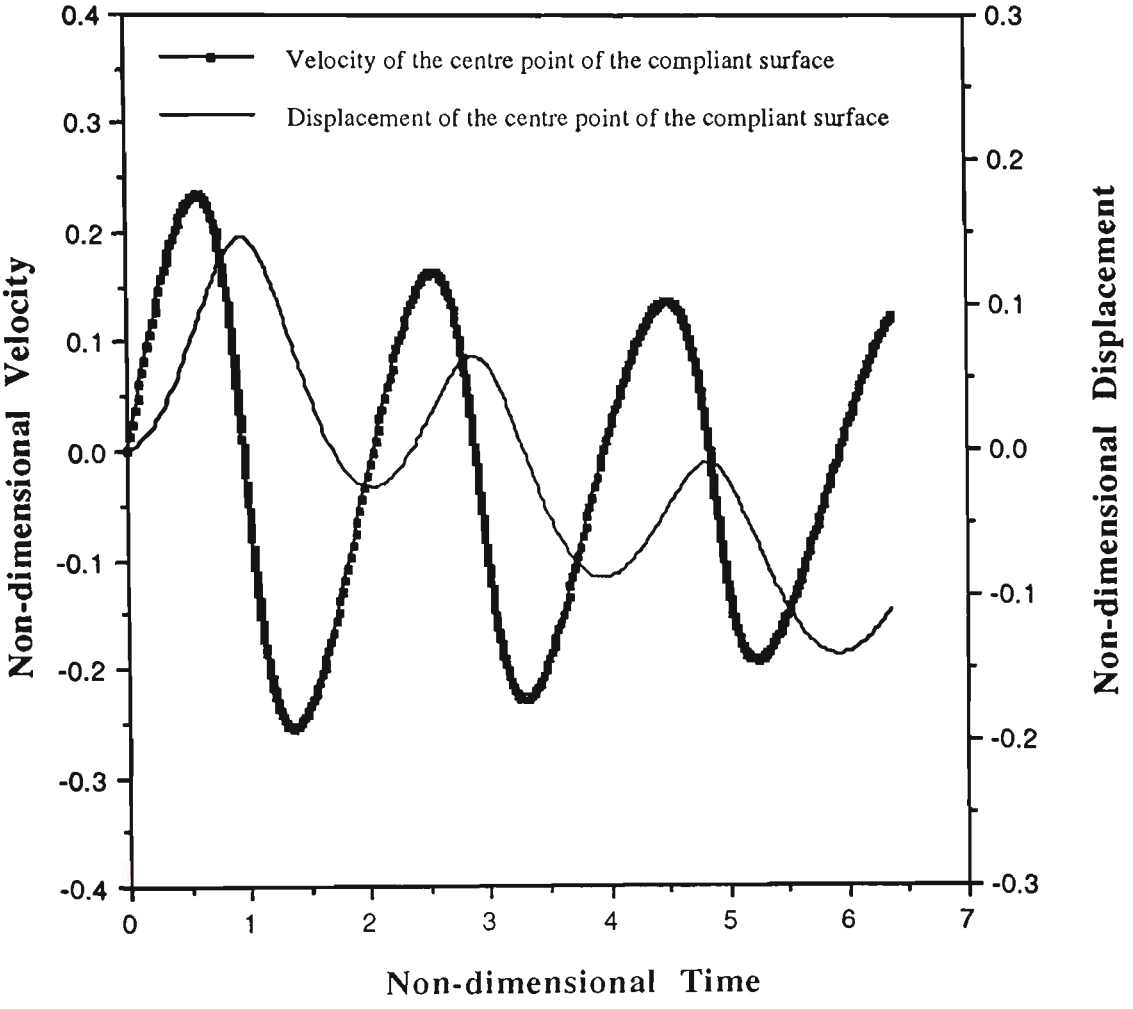

Figure 7.21 Velocity and displacement of the compliant surface at $r = 0$ during the pulsation of the vapour bubble. The bubble is characterised by $\gamma = 1.5$ and $\delta = 0$ and the radius of the compliant surface is $R_{cs} = 2.5R_m$.

7.6.3 Dynamics of a bubble generated by a high local energy input and growing from its initial minimum volume near a compliant surface

In this section the dynamics of a bubble generated by a high local energy input and growing from its initial minimum volume near a compliant surface is carried out in the cases of

- the bubble pulsating near a rigid boundary; and
- the bubble pulsating near a compliant surface.

In this case, as discussed in Section 5.5, the bubble contains a mixture of constant pressure vapour and ideal gas. The bubble is initially in its minimum volume. The initial pressure inside the bubble is very high and the initial velocity on the bubble surface and consequently the initial distribution of the velocity potential over the bubble surface are zero.

Figure 7.22 illustrates the behaviour of the rebounding bubble during its growth and collapse phases near a rigid boundary. The bubble is characterised by $\gamma = 1.5$, $\delta = 0.0$ and $\varepsilon = 40$. During the growth phase the bubble remains almost spherical. During the collapse phase the bubble is elongated in the direction of the vertical axis. At the latest stages of the collapse phase the side of the bubble far from the rigid boundary is flattened. A liquid jet is developed on the flattened side of the directed towards the rigid boundary. The liquid jet is fully developed during the latest stages of the collapse phase and penetrates the opposite side of the bubble.

Figure 7.23 shows the behaviour of the rebounding bubble near a compliant surface. The bubble is characterised by $\gamma = 1.5$, $\delta = 0.0$ and $\varepsilon = 40$. The

$R_{cs} = 2.5R_m$. Figure 7.23 indicates that the bubble expands almost spherically during its growth phase. During the collapse phase, the bubble migrates away from the compliant surface. At the latest stages of the bubble collapse the side of the bubble close to the compliant surface is flattened. At the end of the collapse phase a liquid jet is initiated at the flattened side of the bubble and is directed away from the compliant surface. It is shown that the liquid jet is fully developed during the early stages of the bubble rebound and penetrates the opposite side of the bubble.

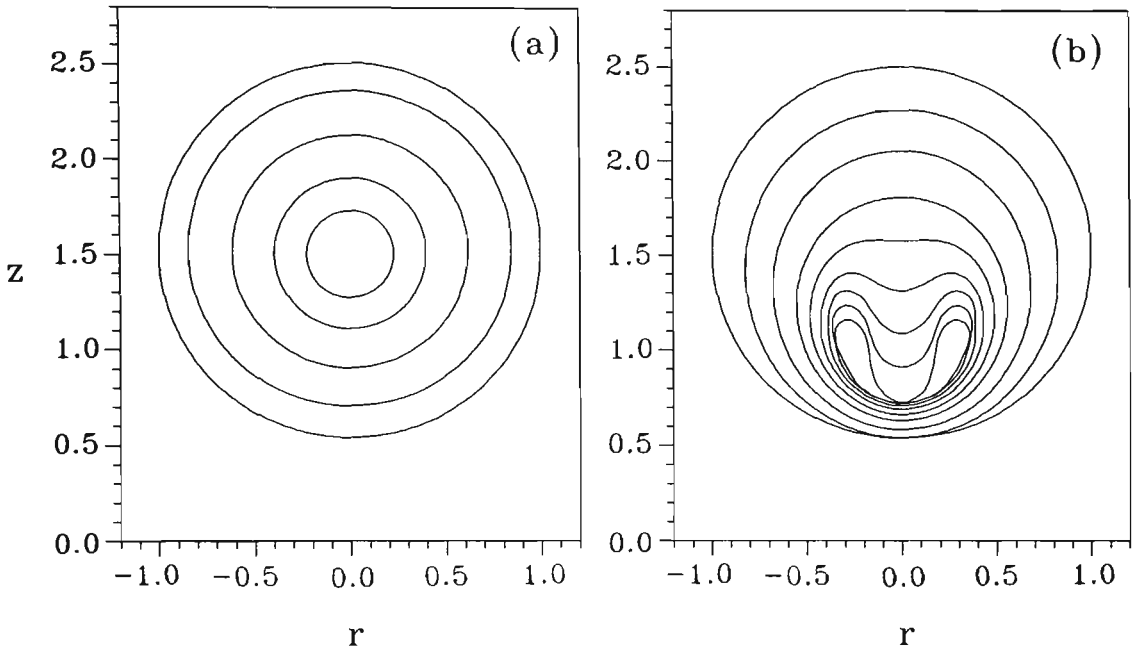

Figure 7.22 Bubble shapes for the growth (a) and collapse (b) of a bubble containing a mixture of constant pressure vapour and ideal gas near a rigid boundary. The bubble is characterised with $\gamma = 1.5$, $\delta = 0$ and $\varepsilon = 40$. The non-dimensional times corresponding to bubble successive profiles are: (a) Growth phase: 0.0000 (innermost), 0.0719, 0.1825, 0.4319, 0.1.1098 (outermost). (b) Collapse phase: 1.1098 (outermost), 1.9810, 2.1287, 2.1675, 2.1946, 2.2077, 2.2168, 2.2238, 2.2354 (innermost).

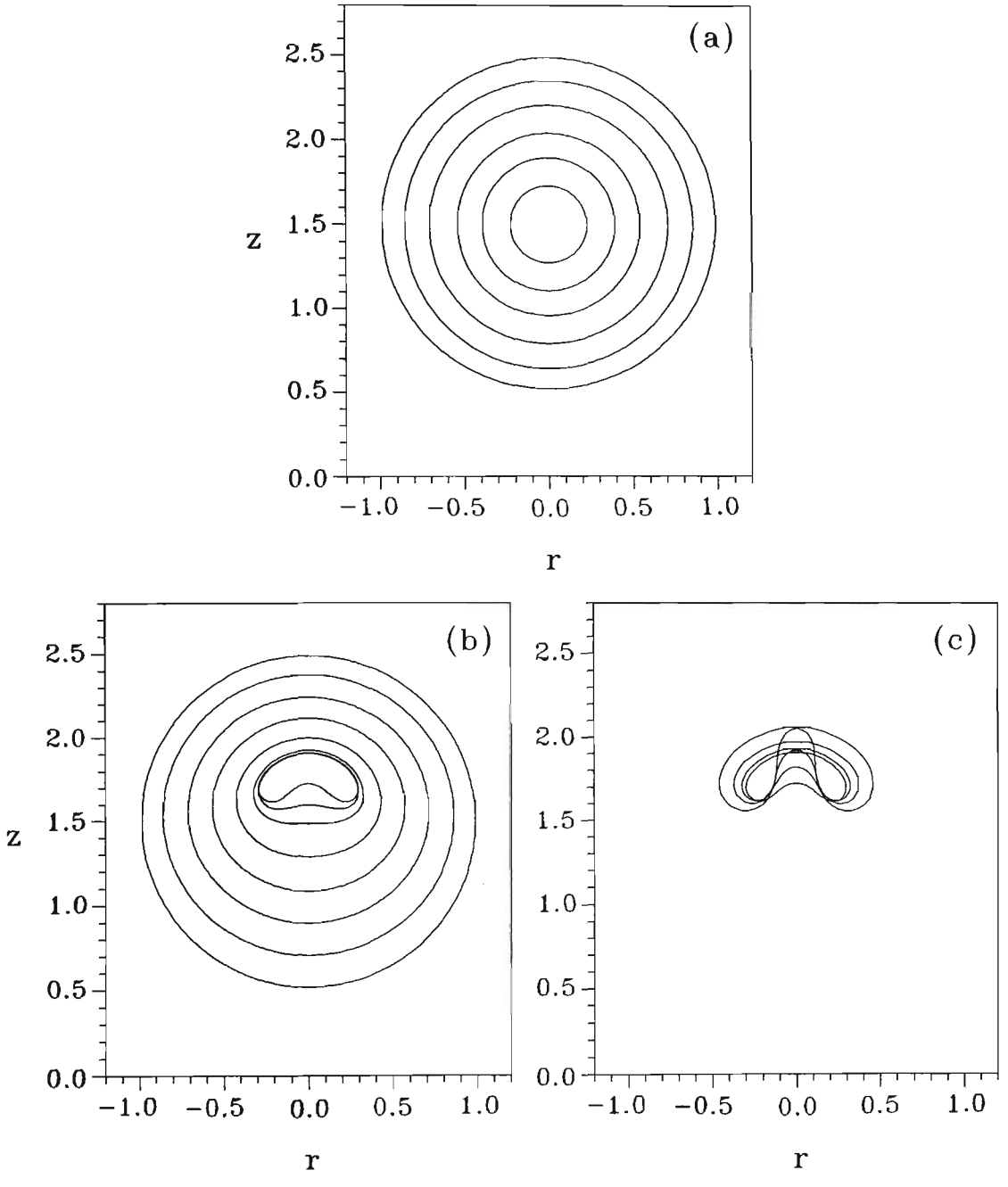

Figure 7.23 Bubble shapes for the growth (a), collapse (b) and rebound (c) of a bubble containing a mixture of constant pressure vapour and ideal gas near a compliant surface. The bubble is characterised with $\gamma = 1.5$, $\delta = 0$ and $\varepsilon = 40$. The compliant surface is characterised by $M^* = 1.5$, $T^* = 0.0025$, $K^* = 1.5$ and $R_{cs} = 2.5R_m$. The non-dimensional times corresponding to bubble successive profiles are: (a) Growth phase: 0.0000 (innermost), 0.0720, 0.1469, 0.2777, 0.4686, 0.9591 (outermost). (b) Collapse phase: 0.9591 (outermost), 1.4665, 1.7775, 1.8953, 1.9165, 1.9326 (innermost). (c) Rebound phase: 1.9326 (innermost), 1.9446, 1.9621, 1.9938 (outermost).

Figure 7.24 shows the initial pressure distribution on the rigid boundary and the compliant surface at t = 0. In this case the bubble is generated by a high local energy input and is initially in its minimum volume and the pressure inside the bubble is very high. The pressure on the rigid boundary generated by the bubble at $r=0$ is $P_w - P_\infty = 11.064\Delta P$ and at the compliant surface is $P_w - P_\infty = 5.519\Delta P$.

Figure 7.25 illustrates the variation of the bubble volume during its pulsation with respect to time in the cases of the bubble near a rigid boundary and near the compliant wall. Figure 7.25 indicates that the rate of growth and collapse of the bubble in the vicinity of the compliant surface is higher than the rate of the growth and collapse of the bubble near a rigid boundary.

Figure 7.26 shows the migration of the bubble centroid with respect to time during the pulsation of the bubble near a rigid boundary and near the compliant surface. Figure 7.26 indicates that in the case the bubble near a rigid boundary, the bubble centroid migrates marginally away from the rigid boundary during the growth phase. During the collapse phase, the bubble migrates increasingly rapidly towards the rigid boundary. Figure 7.26 illustrates an interesting feature of the bubble behaviour in the vicinity of compliant surfaces. It is shown that during the growth phase the bubble centroid migrates marginally towards the compliant surface. During the collapse and its consequent rebound phases, the bubble centroid migrates increasingly rapidly away from the compliant surface.

Figure 7.27 illustrates the variation of the pressure inside the bubble with respect to time. The pressure inside the bubble, P_b, is non-dimensionalised as $\frac{P_b - P_\infty}{P_\infty - P_c}$.

Figure 7.28 illustrates the pressure generated by the pulsation of the bubble on the rigid boundary and on the compliant surface at $r = 0$ with respect to time. As shown in Figure 7.28, the initial pressure on the compliant surface generated by bubble in its minimum volume is lower than the initial pressure on the rigid boundary at $r = 0$. This fact is already presented in Figure 7.24. Figure 7.28 also indicates that the pressure on the compliant surface at $r = 0$ at the end of the bubble collapse is lower than the pressure on the rigid boundary at $r = 0$ generated by the bubble at the end of its collapse.

Figure 7.29 illustrates the velocity of the top point of the bubble far from the boundary. Positive values of velocity indicate that the velocity is directed inside the bubble, whereas negative values indicate the outward direction from the bubble. Figure 7.29 indicates that in the case of the bubble near a rigid boundary a liquid jet is developed on the far side of the bubble from the rigid boundary and directed towards it.

Figure 7.30 shows that velocity of the bottom point of the bubble close to the boundary. Figure 7.30 indicates that in the case of the bubble near a compliant surface a liquid jet is developed on the closet side of the bubble to the compliant surface and directed away from it. In this case the maximum velocity of the liquid jet is achieved at t=1.9302 which is corresponded to the later stages of the collapse phase and just before the rebound of the bubble.

Figure 7.31 illustrates the velocity and displacement of the compliant surface at $r = 0$ with respect to time during the pulsating of the bubble. It should be noted that in the case of a bubble near a rigid boundary, the bubble is transformed into a toroidal shape before the end of the collapse phase and before the calculation is terminated.

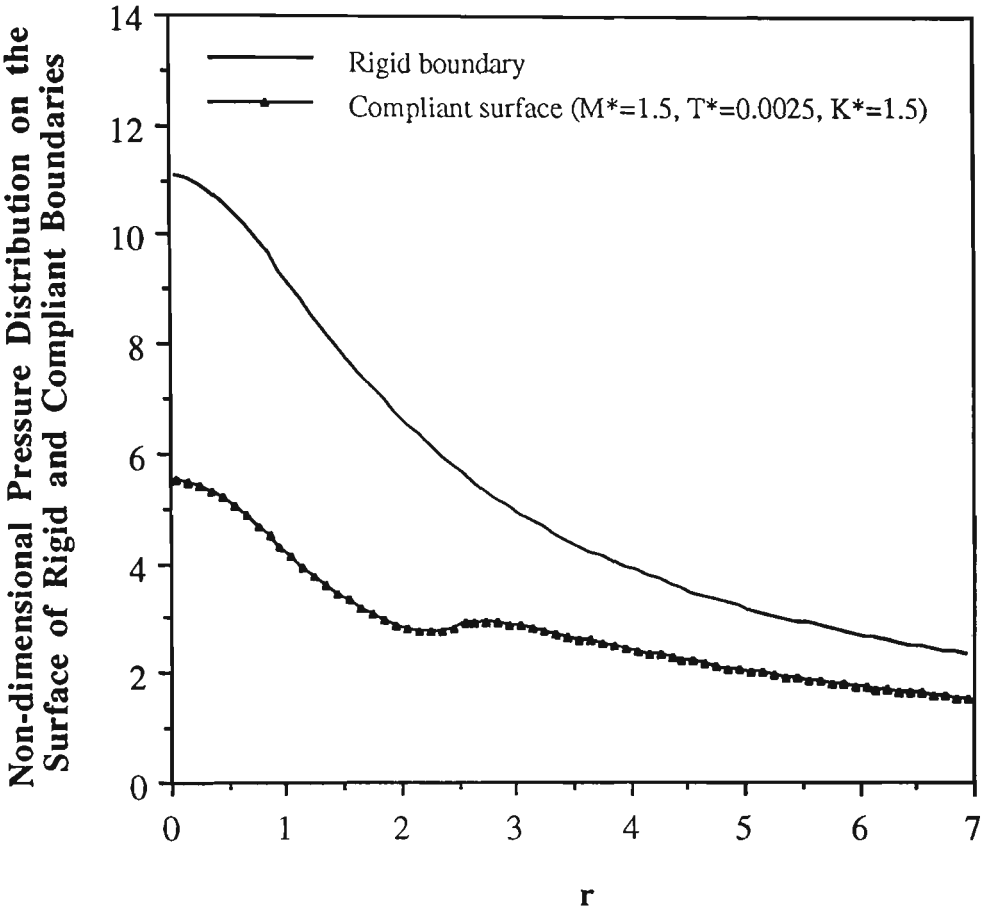

Figure 7.24 Initial pressure distribution on the rigid boundary and on the different compliant surfaces generated by a vapour bubble in its initial minimum volume. The bubble is characterised by $\gamma = 1.5$, $\delta = 0$ and $\varepsilon = 40$ and the radius of the compliant surface is $R_{cs} = 2.5R_m$.

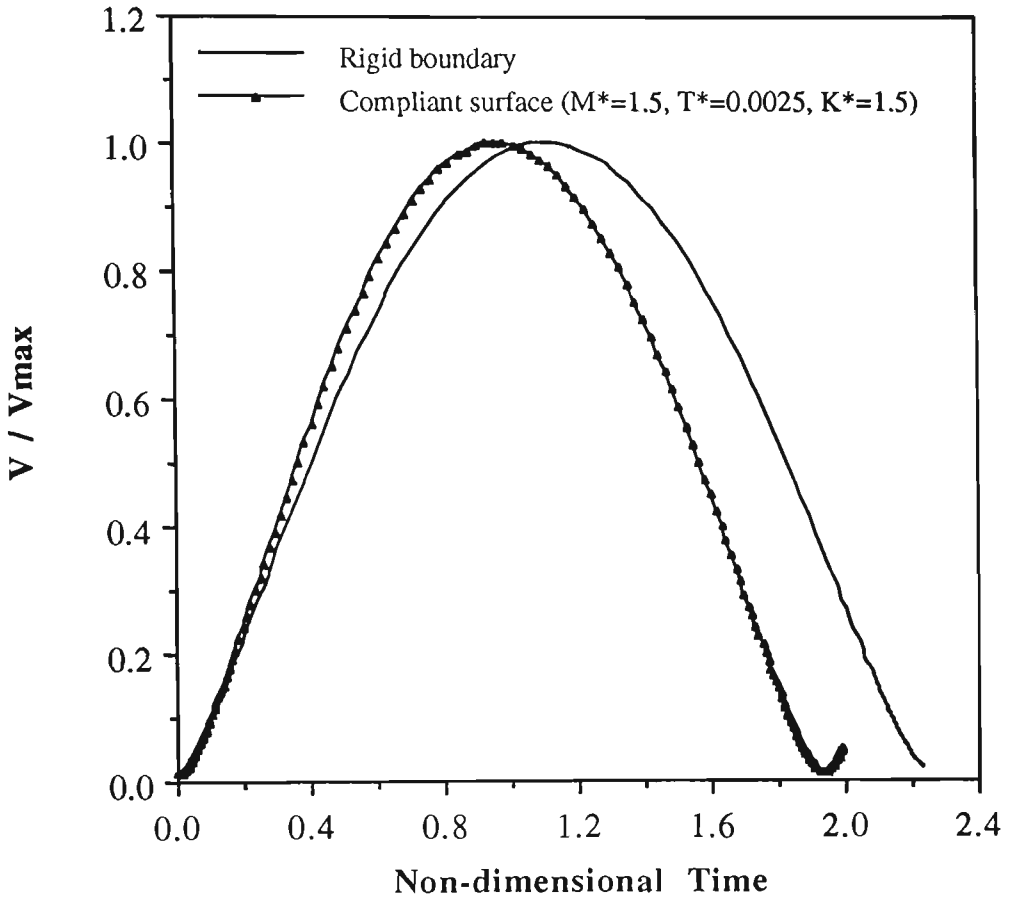

Figure 7.25 Variation of the bubble volume during its pulsation near a rigid boundary and near a compliant surface. The bubble is characterised by $\gamma = 1.5, \delta = 0$ and $\varepsilon = 40$ and the radius of the compliant surface is $R_{cs} = 2.5R_m$.

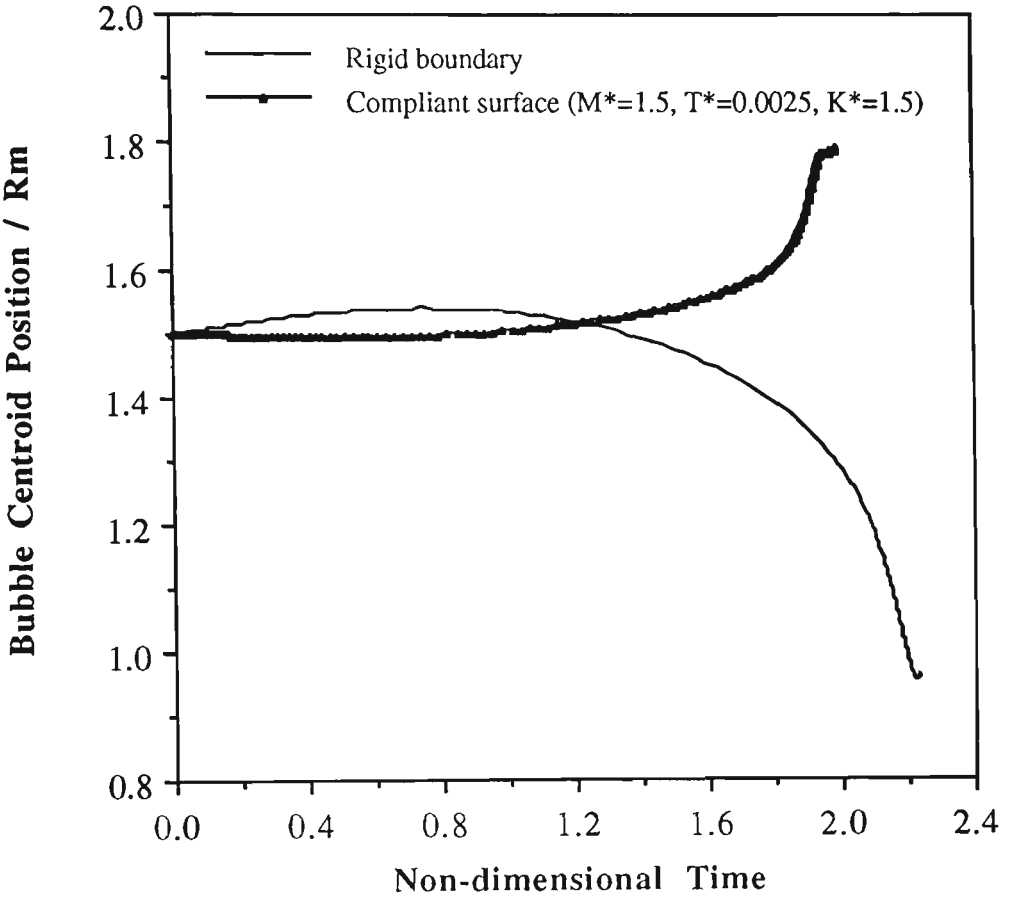

Figure 7.26 Migration of the centroid of a vapour bubble during its pulsation near a rigid boundary and near a compliant surface. The bubble is characterised by $\gamma = 1.5$ and $\delta = 0$, and $\varepsilon = 40$ and the radius of the compliant surface is $R_{cs} = 2.5R_m$.

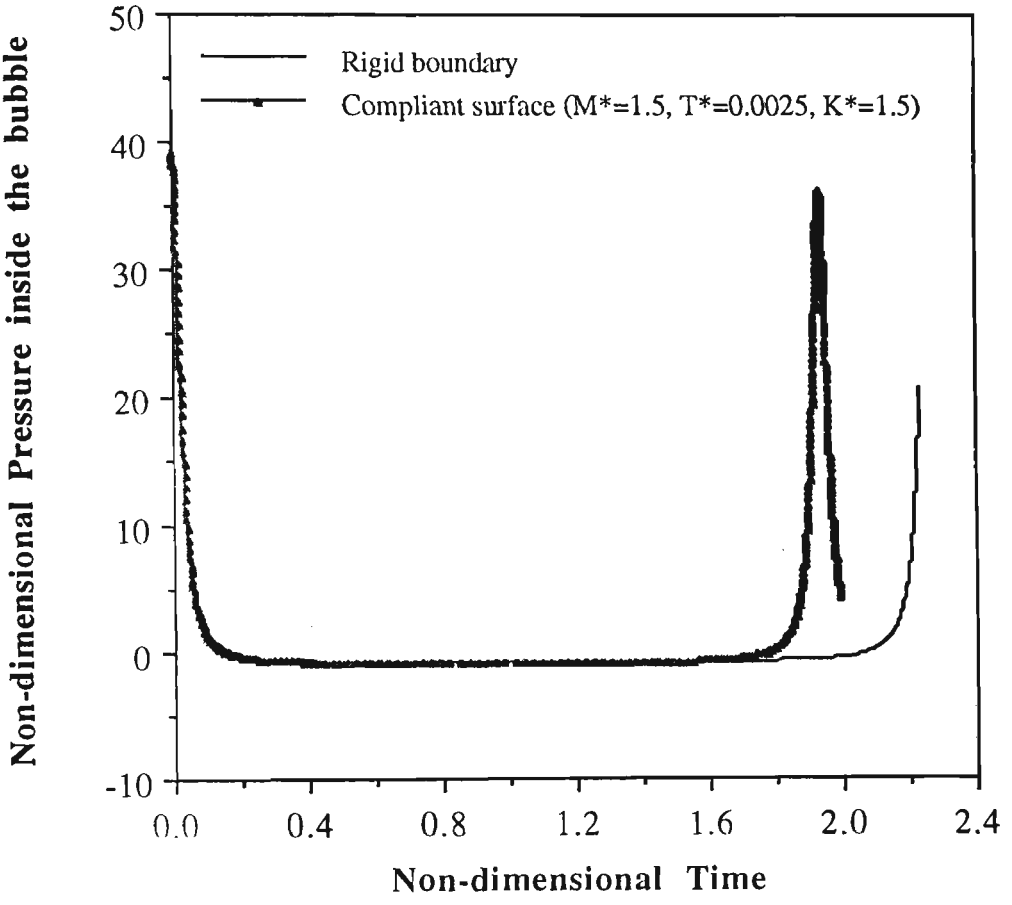

Figure 7.27 Variation of the pressure inside the bubble during its pulsation near a rigid boundary and near compliant surfaces. The bubble is characterised by $\gamma = 1.5$, $\delta = 0$ and $\varepsilon = 40$ and the radius of the compliant surface is $R_{cs} = 2.5R_m$.

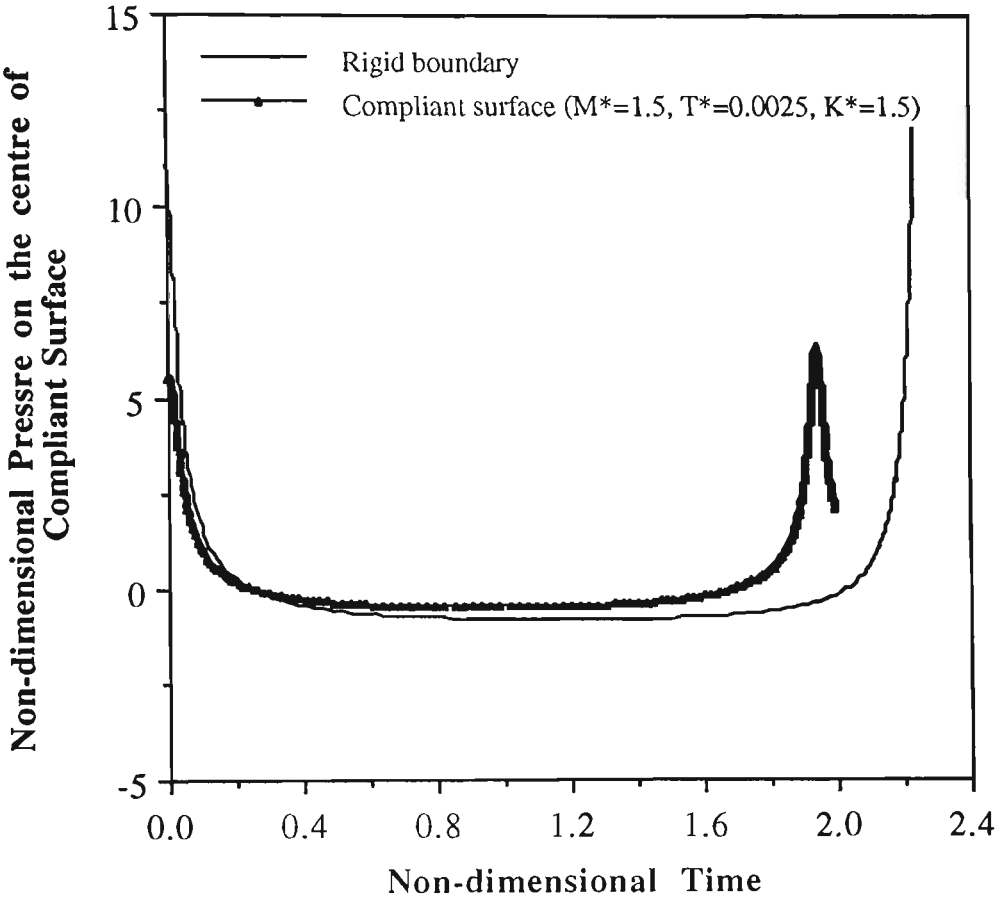

Figure 7.28 Pressure on the rigid boundary and on the compliant surface at $r = 0$ during the pulsation of the bubble. The bubble is characterised by $\gamma = 1.5$, $\delta = 0$ and $\varepsilon = 40$ and the radius of the compliant surface is $R_{cs} = 2.5R_m$.

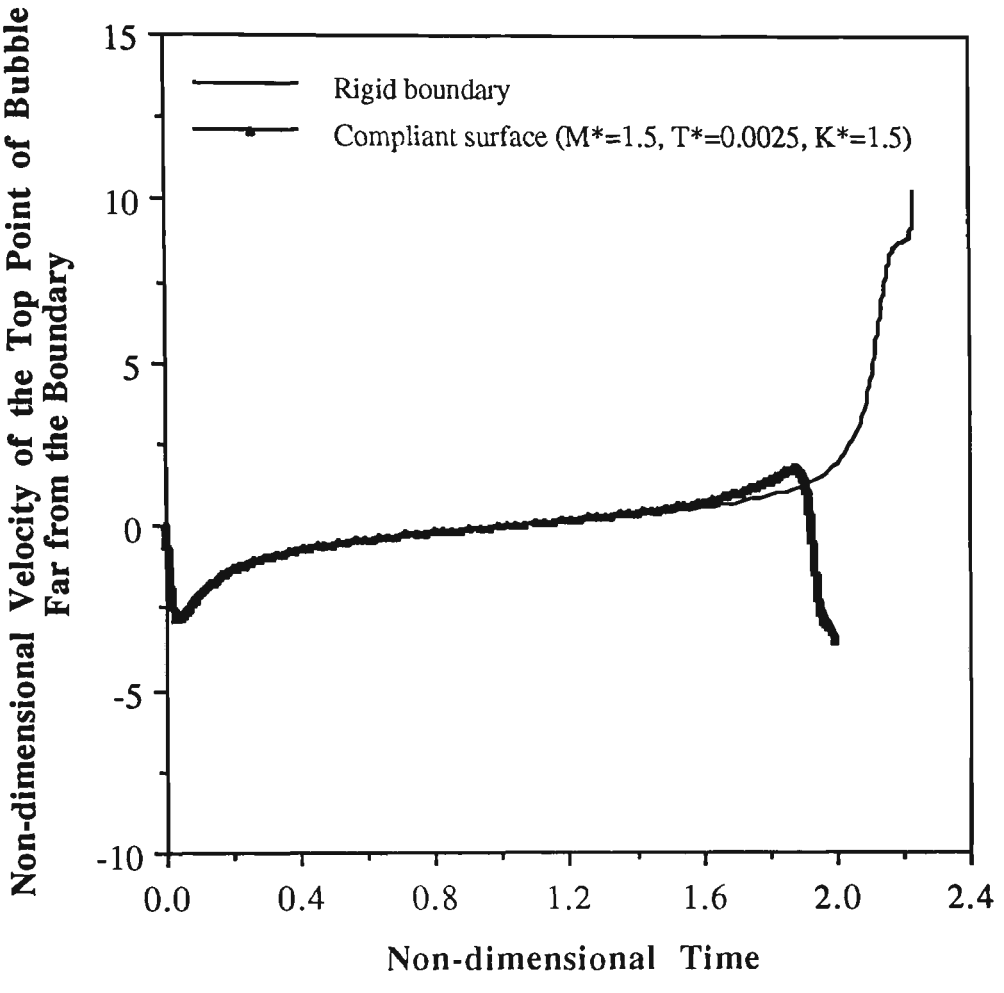

Figure 7.29 Velocity of the top point of the bubble far from the nearby boundary during its pulsation near a rigid boundary and near a compliant surface. The bubble is characterised by $\gamma = 1.5$, $\delta = 0$ and $\varepsilon = 40$ and the radius of the compliant surface is $R_{cs} = 2.5R_m$. Positive values of velocity indicate that the velocity is directed inside the bubble, whereas negative values indicate the outward direction from the bubble.

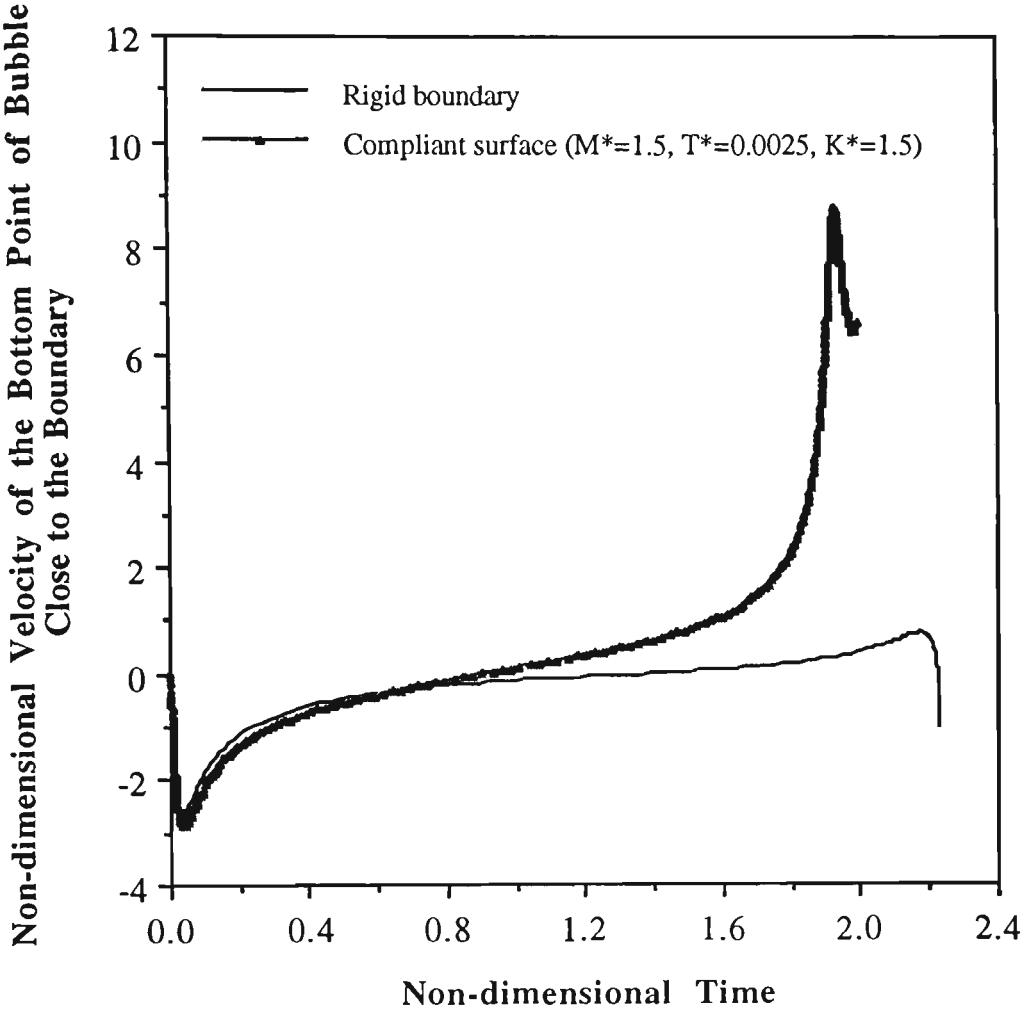

Figure 7.30 Velocity of the bottom point of the bubble close to the nearby boundary during its pulsation near a rigid boundary and near a compliant surface. The bubble is characterised by $\gamma = 1.5$, $\delta = 0$ and $\varepsilon = 40$ and the radius of the compliant surface is $R_{cs} = 2.5R_m$. Positive values of velocity indicate that the velocity is directed inside the bubble, whereas negative values indicate the outward direction from the bubble. In the case of the bubble near the compliant surface the maximum velocity of the liquid jet is achieved at t=1.9302 which is corresponded to the later stages of the collapse phase and just before the rebound of the bubble.

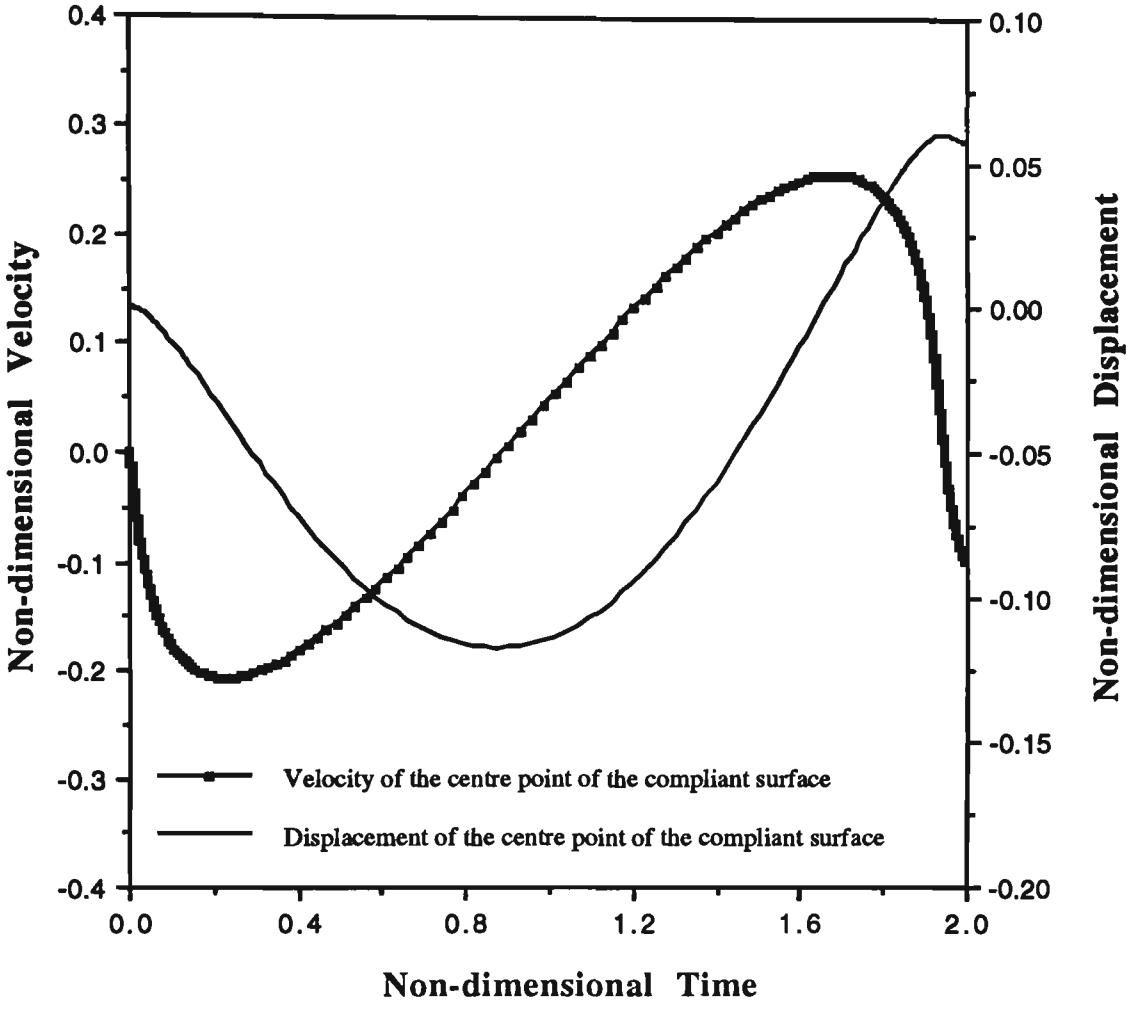

Figure 7.31 Velocity and displacement of the compliant surface at $r = 0$ during the pulsation of the bubble. The bubble is characterised by $\gamma = 1.5$, $\delta = 0$ and $\varepsilon = 40$ and the radius of the compliant surface is $R_{cs} = 2.5R_m$.

7.7 SUMMARY AND CONCLUDING REMARKS

In this chapter the dynamics of a pulsating bubble in the neighbourhood of compliant surfaces have been investigated. The compliant surface is modelled as a spring-backed membrane. The membrane is assumed to be circular with a specified radius which is attached to a rigid boundary along its edge.

Computational results show that the minute displacement of the compliant surface has significant effect on the dynamics of a pulsating bubble in its neighbourhood.

It is found that the collapse rate of the bubble in the vicinity of a compliant surface is higher than the collapse rate of the bubble near a rigid boundary. Consequently the lifetime of the bubble near a compliant surface is shorter than the period of pulsation of the bubble near a rigid boundary. The softer the surface, the higher the bubble collapse rate and consequently the shorter the period of pulsation of the bubble.

The previous numerical studies [Duncan and Zhang (1991)] on the dynamics of a constant pressure vapour bubble near compliant surfaces have considered the bubble collapsing from its initially spherical maximum volume. This is because of the fact that their proposed iteration scheme for determining the initial distribution of the pressure on the compliant surface induced by the bubble fails in the case a constant pressure vapour bubble expanding from its initial minimum volume.

In this work it is found that in the case of a rebounding bubble generated by a high local energy input, it is possible to apply the iteration scheme proposed by

Duncan and Zhang (1991) to determine the initial pressure distribution induced by the bubble in its minimum volume on the nearby compliant surface.

Results show that the pressure on the compliant surface due to the bubble collapse is lower than the corresponding pressure on the rigid boundary. This is because of the initial tendency of the compliant surface to move due to the pressure change on its surface and because of its minute movement during pulsation of the bubble and can be deduced from the linearized Bernoulli equation, Equation (7.9).

It is found that the centroid of the bubble during its growth phase migrates marginally towards the compliant surface as it was already found for a bubble near a free surface. The results show that the compliant surfaces repel the bubble during its collapse and may deflect the liquid jet away from them.

CHAPTER EIGHT

CONCLUSION AND FUTURE DIRECTIONS

8.1 CONCLUSION

The boundary integral method developed throughout this research has been successfully applied in the simulation of the dynamics of a constant pressure vapour bubble, and a rebounding bubble generated by a high local energy input in the cases of

- a bubble in an infinite liquid domain;
- a bubble in the vicinity of a rigid boundary;
- a bubble beneath a free surface; and
- a bubble near compliant surfaces.

The numerical results show the accuracy and convergence of the boundary integral method throughout this research. This can be deduced from several observations. The collapse time for a constant pressure vapour bubble in an infinite liquid domain obtained by the boundary integral method is in a very good agreement with the collapse time according to Rayleigh. Comparison between the results predicted for the collapse of an isolated bubble obtained by the

boundary integral method and by numerical solution of the Rayleigh equation using the Mathematica software package shows very good agreement and indicates the accuracy of the solution.

It was found that energy transfer via latent heat in a vapour bubble causes the build up of internal pressure within the bubble during its collapse, and consequently causes the bubble rebound.

In the case of an isolated bubble, comparisons between the results show that by considering energy transfer through latent heat, through the vaporisation and condensation, the vapour bubble behaves as an ideal gas with a polytropic index between 1.15 and 1.2.

Results also show that the maximum temperature obtained inside an ideal gas bubble during an isentropic process is much higher than the maximum temperature obtained inside ideal gas bubbles with polytropic indices of 1.2 and 1.15. It is also shown that the temperature inside a vapour bubble during its collapse and rebound is less than the temperature inside the ideal gas bubble with polytropic index of 1.15. This fact may be explained in terms of mass conservation: In a polytropic process the mass in a bubble is constant, whereas in the process modelled in *Section 4.4*, there is mass interchange between vapour and liquid during condensation and vaporisation.

In the case of the bubble in the vicinity of a rigid boundary it is found that, in the absence of buoyancy forces, a high speed liquid jet is always developed on the side of the bubble far from the rigid boundary and directed towards it. The development of the high speed liquid jet towards the rigid boundary occurs in a very short period of time.

The results show that buoyancy forces have a significant effect on the behaviour of the bubble. Strong buoyancy forces acting opposite to the Bjerknes attraction effect of the rigid boundary, may result in the development of a liquid jet on the closest side of the bubble to the rigid boundary and directed away from it.

It has also been found that the rigid boundary has the effect of slowing down the collapse rate of the bubble and reduction of the velocity of the liquid jet. The nearer the bubble is to the rigid boundary, the slower is the collapse rate of the bubble and the lower is the velocity of the liquid jet. The earlier initiation and development of the liquid jet in the case of the bubble located close to the rigid boundary causes a larger bubble volume at the instant of the transformation of the bubble to a toroidal shape and consequently results in a broader liquid jet with a lower velocity. Where the buoyancy forces act in the same direction as the Bjerknes attraction force, the initiation and development of the liquid jet occurs earlier. It should be noted that despite the lower velocity of the liquid jet in the case of the bubbles located very close to the rigid boundary, the direct impingement of the liquid jet on the rigid surface causes an extremely high pressure in water.

It is found that in case of a buoyant bubble pulsating near a rigid boundary, an annular liquid jet may develop around the bubble which causes necking and splitting of the bubble. It is shown that for specified buoyancy forces, the location of the annular jet around the bubble can be controlled by variation of the Bjerknes attraction through the rigid boundary. It has been found that for stagnation at infinity, the necking of a bubble occurs when the Bjerknes attraction force through the rigid boundary is comparable with respect to buoyancy forces, and neither of them can completely dominate the fluid motion.

Computational results show that in contrast to the case of a bubble near a rigid boundary, in the case of a bubble near a free surface, the Bjerknes force repels the bubble away from the surface. In this case, a liquid jet is developed on the closest side of the bubble to the free surface and directed away from it.

In the case of a buoyant bubble where the buoyancy forces oppose direction of the Bjerknes force, the analysis indicates significant effect on the behaviour of the bubble, possibly resulting in the reversal of the migration of the bubble and the direction of the liquid jet.

Results show that in the case of the constant pressure vapour bubble beneath a free surface, for $\gamma \geq 1.5$ the free surface is pushed up by the growth of the bubble and falls with the bubble collapse. However for $\gamma = 0.98$, and in the absence of buoyancy forces, the raised free surface continues its upward movement away from the bubble even during the bubble collapse and forms a high-speed spike.

The results indicate that rigid boundaries slow down the collapse rate of the bubble, while free surfaces cause of the collapse rate of the bubble to increase. The smaller the distance of the bubble from the free surface, the higher collapse rate of the bubble.

Results also show that in the case of a rebounding bubble, the time for one cycle of growth and collapse of the bubble in the vicinity of a free surface is shorter than the time for one cycle of growth and collapse of the bubble in an infinite liquid domain. However the time for one cycle of growth and collapse of the rebounding bubble in the vicinity of a rigid boundary is longer than the corresponding time for the bubble in an infinite liquid domain.

In the case of a rebounding bubble near a free surface, the numerical results for $\gamma \geq 1.5$ show that the free surface is also pushed up during the growth of the bubble and collapses with the bubble collapse. In this case the free surface rebounds in synchronisation with the rebound of the bubble. A very interesting phenomenon found during the rebound phase of the bubble and the free surface, is the existence of a stagnation point and a point of the maximum pressure between the rebounding bubble and the free surface when the liquid jet is directed away from the free surface.

It is found that the stagnation point and the point of maximum pressure during the rebound of the bubble and the free surface do not coincide, as was previously found for the case of the constant pressure vapour bubble near a free surface.

Computational results show that a minute displacement of a compliant surface has significant effect on the dynamics of a pulsating bubble in its neighbourhood. In this case the compliant surface is modelled as a spring-backed membrane. The membrane is assumed to be circular with a specified radius which is attached to a rigid boundary.

Results show that the collapse rate of the bubble in the vicinity of a compliant surface is higher than the collapse rate of the bubble near a rigid boundary. Consequently the lifetime of the bubble near a compliant surface is shorter than the lifetime of the bubble near a rigid boundary. The more compliant the surface, the higher the bubble collapse rate and consequently the shorter the lifetime of the bubble.

The previous numerical studies [Duncan and Zhang (1991)] on the dynamics of a constant pressure vapour bubble near compliant surfaces have considered the

bubble collapsing from its initial spherical maximum volume. This is a result of their proposed iteration scheme for determining the initial distribution of the pressure on the compliant surface induced by a bubble, which fails for the case of a constant pressure vapour bubble growing from its minimum volume.

Throughout this research it is found that in the case of a rebounding bubble generated by a high local energy input, it is possible to apply the iteration scheme proposed by Duncan and Zhang (1991) to determine the initial pressure distribution induced by the bubble in its minimum volume on the nearby compliant surface.

Results also show that the centroid of the bubble during its growth phase migrates marginally towards the compliant surface, as was previously found for a bubble near a free surface. The results show that compliant surfaces repel the bubble during its collapse phase, and may result in the deflection of the liquid jet away from the surface.

8.2 DIRECTIONS FOR FUTURE RESEARCH

More computational studies on the dynamics of a pulsating bubble in the vicinity of a wide range of compliant surfaces should be carried out by considering the damping coefficients of the surfaces. The flexural rigidity of the spring backed plates should also be included.

The effect of a cloud of bubbles on collapse characteristics should be thoroughly investigated.

Medical applications of cavitation bubbles in the disintegration of kidney stones and gallstones and in treating tumours are of great importance, and should be vigorously studied both experimentally and numerically.

REFERENCES

Abramowitz, M and Stegun, I.A. (1965), "Handbook of mathematical functions", Dover.

Barnaby, S.W. and Parsons, C.W. (1897), Trans. Inst. Naval Arch., Vol. 38, p. 232.

Barnaby, S.W. and Thornycroft, J. (1895), "Torpedo boat destroyers", Proc. Inst. Civ. Engrs., Vol. 122, p. 157.

Benjamin, T.B. and Ellis, A.T. (1966), "The collapse of cavitation bubbles and pressure thereby produced against solid boundaries", Phil. Trans. R. Soc. Lond., A Vol. 260, pp. 221-240.

Besant, W.H. (1859), "Hydrostatics and hydrodynamics", Deighton Bell, Cambridge, p. 170.

Best, J.P. (1991), "The dynamics of underwater explosions", PhD Thesis, University of Wollongong, Wollongong, Australia.

Best, J.P. (1993), "The formation of toroidal bubbles upon the collapse of transient cavities", J. Fluid Mech., Vol. 251, p. 107.

Best, J.P. and Blake, J.R. (1994), "An estimate of the Kelvin impulse of a transient cavity", J. Fluid Mech., Vol. 261, pp. 75-93.

Best, J.P., Kucera, A. and Blake J.R. (1989), "Underwater explosion bubble dynamics in the neighbourhood of boundaries", Tenth Australasian Fluid Mechanics Conference, University of Melbourne, Melbourne, Australia, 11-15 December.

Best. J.P. and Kucera, A. (1992), "A numerical investigation of non-spherical rebounding bubbles", J. Fluid Mech., Vol. 247, pp. 137-154.

Blake, J. R. and Gibson, D. C. (1987), "Cavitation bubbles near boundaries", Ann. Rev. Fluid Mech., Vol. 19, pp. 99-123.

Blake, J.R, Robinson, P.B. , Shima, A. and Tomita, Y. (1993), "Interaction of two cavitation bubbles with a rigid boundary", J. Fluid Mech., Vol. 255, pp. 707-721.

Blake, J.R. (1988), "The Kelvin impulse: Application to cavitation bubble dynamics", J. Aust. Math. Soc., Ser. B Vol. 30, pp. 127-146.

Blake, J.R. and Ceron, P. (1982), "A note on the impulse due to a vapour bubble near a boundary", J. Aust. Math. Soc. , Ser. B Vol. 23, pp. 383-393.

Blake, J.R. and Gibson, D.C. (1981), "Growth and collapse of a vapour cavity near a free surface", J. Fluid Mech., Vol. 111, pp. 123-140.

Blake, J.R. and Gibson, D.C. (1987), "Cavitation bubbles near boundaries", Ann. Rev. Fluid Mech. 19, pp. 99-123.

Blake, J.R., Ceron, P. and Gibson, D.C. (1984), "A note on the growth and collapse of buoyant vapour bubbles near a free surface", Preprint No. 9/84, Department of Mathematics, University of Wollongong, Wollongong, Australia.

Blake, J.R., Robinson, P.B., Shima, A. and Tomita, Y. (1993), "Interaction of two cavitation bubbles with a rigid boundary", J. Fluid Mech., Vol. 255, pp. 707-721.

Blake, J.R., Taib, B.B. and Doherty, G. (1986), "Transient cavities near boundaries; Part 1. Rigid boundary", J. Fluid Mech., Vol. 170, pp. 479-497.

Blake, J.R., Taib, B.B. and Doherty, G. (1987), "Transient cavities near boundaries; Part 2. Free surface", J. Fluid Mech., Vol. 181, pp. 197-212.

Brebbia, C.A. and Dominguez, J. (1989), "Boundary elements; an introductory course", McGraw-Hill Incorporated.

Brebia, C.A. (1978) , "The boundary element method for engineers", Pentech Press, London.

Brujan, E.-A., (1994), "The collapse of an initially spherical bubble between narrow parallel plates", XVII IAHR SYMPOSIUM, Beijing, China, Vol. 2, pp. 489-496.

Burden, R.L. and Fairs, J.D. (1993), "Numerical analysis", Fifth Edition, PWS Publishing Company.

Carpenter, P.W. and Garrad, A.D. (1985), "The hydrodynamic stability of flow over Kramer-type Compliant surfaces. Part 1. Tollmien-Schlichting instabilities" J. Fluid Mech., Vol. 155, pp. 465-510.

Ceron, P. and Blake, J.R. (1984), "A note on the instantaneous streamlines, pathlines and pressure contours for a cavitation bubble near a boundary", J. Aust. Math. Soc., Ser. B Vol. 26, pp. 31-44.

Chahine, G.L. and Bovis, A. (1980), "Oscillation and collapse of a cavitation bubble in the vicinity of a two-liquid interface", Cavitation and Imhomogenities in Underwater Acoustics, Proceedings of the First International Conference, Göttingen, Fed. Rep. of Germany, Lauterborn (Ed.), Springer-Verlag, pp. 23-29.

Deboor, C. (1979), "A practical guide to splines", Springer-Verlag, New York.

Dommermuth, D.G. and Yue, D.K.P. (1987), "Numerical simulations of nonlinear axisymmtric flows with a free surface", J. Fluid Mech., Vol. 187, pp. 195-219.

Duncan, J.H. and Zhang, S. (1991), "On the interaction of a collapsing cavity and a compliant wall", J. Fluid Mech., Vol. 226, pp. 401-423.

Euler, L. (1754), "Histoire de l'Academie Royale des sciences et Belle Letters", Memo. R.10, Berlin. "Classe de philosophie experimentalle", pp. 227-295; the remarks on the rupture of the liquid from the walls are made in chap. 81, pp. 266-267 (in French).

Ferziger, J.H.(1981), "Numerical methods for engineering application", John Wiley and Sons.

Fink, P.T. and Soh, W. K. (1978), "A new approach to roll-up calculations of vortex sheets", Proc. Roy. Soc. Lond. A. 362, pp. 195-209.

Forbes, L.K. (1994), "An analytical and numerical study on the forced vibration of a spherical cavity", Journal of Sound and Vibration, Vol. 172, No. 4, pp. 471-489.

Fujikawa, S. and Akamatsu, T. (1980), "Effects of non-equilibrium condensation of vapour on the pressure wave produced by the collapse of a bubble in a liquid", J. Fluid Mech., Vol. 97, Part 2, pp. 481-512.

Garcia, R. and Hammitt, F.G. (1966), "Ultrasonic-induced cavitation studies in Lead-Bismuth alloy at elevated temperature", Corrosion, Vol. 22, No. 6, pp. 157-167.

Garcia, R., Hammitt, F.G. and Nystrom, R.E. (1967), "Comprehensive cavitation damage data for water and various liquid metals including correlations with material and fluid properties", ASTM Spec. Tech. Publ., Vol. 408, pp. 239-279.

Gibson, D.C. (1968), "Cavitation adjacent to plane boundaries", Conference on Hydraulics and Fluid Mechanics, The institute of Engineers, Australia, pp. 210-214.

Gibson, D.C. and Blake, J.R. (1980), "Growth and collapse of cavitation bubbles near flexible boundaries", Proc. 7th Aust. Hydraulic and Fluid Mech. Conf., Brisbane, Australia, pp. 283-286.

Gibson, D.C. and Blake, J.R. (1982) "The growth and collapse of bubbles near deformable surfaces", Applied Scientific Research, 38, pp. 215-224.

Gipson, G.S. (1987), "Boundary elements fundamentals-basic concepts and recent developments in the poisson equation", Computational Mechanics Publications, UK.

Gracewski, S.M., Dahake, Girish, Ding, Zhong, Burns S.J. and Everbach, E Carr, (1993), "Internal strss wave measurements in solids subjeted to lithotripter pulses", J. Acoustic. Soc. Am. 94 (2) Pt. 1, August.

Hall, W.S. (1989), "Integration methods for singular boundary element integrands", Boundary Elements X, Vol. 1: Mathematical and Computational Aspects, Ed. C.A. Brebbia, pp. 219-236.

Hammitt, F.G. (1966), "Damage to solids caused by cavitation", Phil. Roy. Soc., Ser. A, Vol. 260, No. 1110, pp. 243-255.

Hammitt, F.G. (1980), "Cavitation and multiphase flow phenomena", McGraw-Hill.

Harris, P.J. (1993), "A numerical method for predicting the motion of a bubble close to a moving rigid boundary", Communications in Numerical Methods in Engineering, Vol. 9, pp. 81-86.

Harris, P.J. (1992), "A numerical model for determining the motion of a bubble close to a fixed rigid structure", Intl J. Numer. Methods Engng, Vol. 33, pp. 1813-1822.

Hayami, K. and Brebbia, C.A. (1988), "A new coordinate transformation method for singular and nearly singular integrals over general curved boundary elements", Boundary Elements IX, Vol. 1: Mathematical and Computational Aspects, Eds. C.A. Brebbia, W.L. Wendland and G. Kuhn, pp. 375-399.

Hayami, K. and Brebbia, C.A. (1989), "Quadrature methods for singular and nearly singular integrals in a 3-D boundary element method", Boundary Elements X, Vol. 1: Mathematical and Computational Aspects, Ed. C.A. Brebbia, pp. 239-264.

Herring, C. (1949), "Theory of the pulsations of the gas bubble produced by an underwater explosion", NDRC Division 6 Report C4-sr20, and in revised form, dated 1949, in Hartman and Hill, 1950.

Hirose, T., Tsuda, Y. and Kimoto, H. (1983), "An experimental study of the model microjet", Bulletin of the JSME, Vol. 26, No. 218, pp. 1340-1347.

Hutton, S.P. (1972), "The saga of the singing kettle", Inaugural Lecture, University of Southampton.

Karimi, A.A. and Soh, W.K. (1994a), "The effect of heat transfer on a pulsating bubble", XVII IAHR SYMPOSIUM, Beijing, China., Vol. 2, pp. 521-532

Karimi, A.A. and Soh, W.K. (1994b), "The application of dual reciprocity boundary element technique to the study of bubble dynamics", Computational Fluid Dynamics JOURNAL, Vol. 3, No. 3, pp. 367-378.

Kellog, O.D. (1929), "Foundations of potential theory", Springer, Berlin.

Kitayama, O., Ise, H., Sato, T. and Takayama, K. (1987)," Non-invasive gallstone disintegration by underwater shock focusing", Proceedings of 16th International Symposium on Shock Tubes and Waves, Aachen, pp. 897-903.

Knapp, R. T., Daily, J. W. and Hammitt, F. G. (1970), "Cavitation", McGraw-Hill, New York.

Kornfeld, M. and Suvrov, L. (1944), "On the destructive action of cavitation", J. Appl. Phys. Vol. 15, pp. 495-506.

Koutny, A. (1987), "Study of laws and mechanisms of combined cavitation-erosion effects in water containing hard particles and optimisation of material choice, Thesis, CVUT, Praha (in Czech).

Kucera, A. and Blake, J.R. (1988), "Computational modelling of cavitation bubbles near boundaries", Computational Techniques & Applications: CTAC-87, J. Noye & C. Fletcher(Editors), Elsevier Science Publishers B.V. (North-Holland), pp. 391-400.

Kumar, A. and Booker, J.F. (1991a), "A finite element cavitation algorithm", Transactions of the ASME, Vol. 113, pp. 276-286, April.

Kumar, A. and Booker, J.F. (1991b), "A finite element cavitation algorithm: Application/validation", Journal of Tribology, Vol. 113, pp. 255-261, April.

Kumar, S. and Brennen, C.E. (1993), "A study of pressure pulses generated by travelling bubble cavitation", J. Fluid Mech., Vol. 255, pp. 541-564.

Lauterborn, W. (1974), Acoustica, Vol. 31, p. 51.

Lauterborn, W. (1980), "Cavitation and coherent optics", Cavitation and Imhomogenities in Underwater Acoustics, Proceedings of the First International Conference, Göttingen, Fed. Rep. of Germany, Lauterborn (Ed.), Springer-Verlag, pp. 3-12.

Lauterborn, W. and Timm, R. (1980), "Bubble collapse studies at a milion frames per second", Cavitation and Imhomogenities in Underwater Acoustics, Proceedings of the First International Conference, Göttingen, Fed. Rep. of Germany, Lauterborn (Ed.), Springer-Verlag, pp. 42-46.

Lauterbrn, W. and Boll, H. (1975), "Experimental investigations of cavitation-bubble collapse in the neighbourhood of a solid boundary", J. Fluid Mech., Vol. 72, Part 2, pp. 391-399.

Lush, P.A. (1983), "Impact of a liquid mass on a prefectly plastic solid", J. Fluid Mech., Vol. 135, pp. 373-387.

Lush, P.A., Wood R.J.K. and Carpanini, L.J. (1983), Proc. 6th Int. Conf. Erosion by Liquid and Solid Impact Paper 5 (Cambridge: Cavendish Laboratory).

Matsumoto, Y. and Beylich, A.E. (1985), "Influence of homogenous condensation inside a small gas bubble on its pressure response", Journal of Fluids Engineering, June, Vol. 107, pp. 281-286.

Momose, K., Ueki, H. and Kimoto, H. (1983), "Behaviour of a bubble between parallel walls", Trans. ASME B, Vol. 49, pp. 187-197.

Naude, C.F. and Ellis, A.T. (1961), "On the mechanism of cavitation damage by non-hemispherical cavities in contact with a solid boundary", Trans. ASME, J. Basic Eng., Vol. 83, pp. 648-656.

Niessner, H. (1989), "A flexible method over cauchy singularities in boundary integral equations", Boundary Elements X, Vol. 1: Mathematical and Computational Aspects, Ed. C.A. Brebbia, pp. 265-277.

Parsons, C.A. (1906), "The steam turbine on land and at sea", Lecture to Royal Institution, 4 May.

Pearsall, I. S. (1972), "Cavitation", Mills & Boon Limited.

Philipp, A., Delius, M., Scheffczyk, C., Vogel, A. and Lauterborn, W. (1993), "Interaction of lithotripter-generated shock waves with air bubbles", J. Acoust. Soc. Am., Vol. 93 (5), May, pp. 2496-2509.

Pina, H.L.G., Fernandes, L.M. and Brebbia, C.A. (1981), "Some numerical integration formulae over triangles and squares with a $\frac{1}{R}$ singularity", Applied Math. Modelling, Vol. 5, pp. 209-211.

Plesset, M.S. and Chapman, R.B. (1971), "Collapse of an initially spherical vapour cavity in the neighbourhood of a solid boundary", J. Fluid Mech., Vol. 47, Part 2, pp. 283-290.

Plesset, M.S. and Prosperetti, A. (1977), "Bubble dynamic and cavitation", Ann. Rev. Fluid Mech., Vol. 9, pp. 145-185.

Prosperetti, A. (1982), "Bubble dynamics: a review and some recent results", Appl. Sci. Res., Vol. 38, pp. 145-164.

Prosperetti, A. (1991), "The thermal behaviour of oscillating gas bubbles", J. Fluid Mech., Vol. 222, pp. 587-616.

Prosperetti, A., (1980), "On the dynamics of non-spherical bubbbles", Cavitation and Imhomogenities in Underwater Acoustics, Proceedings of the First International Conference, Göttingen, Fed. Rep. of Germany, Lauterborn (Ed.), Springer-Verlag, pp. 13-22.

Rattray, M. (1951), "Perturbation effects in cavitation bubble dynamics", PhD Thesis, California Institute of Technology.

Rayleigh, Lord (1917), "On the pressure developed in a liquid during the collapse of a spherical void", Phil. Mag. Vol. 34, pp. 94-98.

Reynolds, O. (1973), "The cause of the racing of the engines of new screw steamers; Investigated theoretically and by experiment", Trans. Inst. Naval Arch., V14 Sci. papers, Vol. 1, pp. 56.

Riley, J.J., Gad-el-Hak, M. and Metcalfe, R.W. (1988), "Compliant coatings", Ann. Rev. Fluid Mech., Vol. 20, pp. 393-420.

Robinson, M.J. and Hammitt, F.G. (1967), "Detailed damage characteristics in a cavitating venturi", ASME, J. Basic Engr., Vol. 89, Ser. D, No. 1, March, pp. 161-173.

Sato, K., Tomita, Y. and Shima, A. (1994), "Numerical analysis of a gas bubble near a rigid boundary in an oscillatory pressure field", J. Acoust. Soc. Am., Vol. 95 (5), Pt. 1, pp. 2416-2424.

Sato, M., Yoshikoa, S., Tsukui, K. and Yuuki, R (1988), "Accurate numerical integration of singular kernels in the two-dimensional boundary element method", Boundary Elements IX, Vol. 1: Mathematical and Computational Aspects, Eds. C.A. Brebbia, W.L. Wendland and G. Kuhn, pp. 279-296.

Sedlacek, V. (1992), "Metallic surfaces, films and coatings", Translation Miroslav Rakovic, Elsevier Science Publishing, Printed in Czechoslovakia.

Shervani-Tabar, M.T. and Soh, W.K. (1993), "Dynamic loading on complint layers due to the collapse of a vapour bubble", Thirteenh Australasian Conference on the Mechanics of Structures and Materials, Wollongong, Australia, pp. 793-800, July.

Shima, A. and Nakajima, K. (1977), "The collapse of a non-spherical bubble attached to a solid wall", J. Fluid Mech., Vol. 80, part 2, pp. 369-391.

Shima, A. and Sato, Y. (1980), "The behaviour of a bubble between narrow parallel plates", Z. angew. Math. Phys., Vol. 31, pp. 691-704.

Shima, A. and Sato, Y. (1984), "The collapse of a buble between narrow parallel plates (The case where a bubble attached to a solid wall).', Rep. Inst. High speed Mech., Tohoku Univ., Vol. 49, pp. 1-21.

Shima, A., Tomita, Y., Gibson, D.C. and Blake, J.R. (1989), "The growth and collapse of cavitation bubbles near composite surfaces", J. Fluid Mech., Vol. 203, pp. 199-214.

Soh, W.K. (1990), "High speed photographic study of a cavitation bubble", SPIE, Vol. 1358, 19th International Congress on High Speed Photography and Photonics, pp. 1011-1015.

Soh, W.K. (1992), "An energy approach to cavitation bubbles near compliant surfaces", Appl. Math. Modelling, Butterworth-Heinemann, Vol. 16, pp. 263-268.

Soh, W.K. (1994), "On the thermodynamic process of a pulsating vapour bubble", To appear in Appl. Math. Modelling.

Soh, W.K. and Shervani-Tabar, M.T. (1992a), "Computer study of unsteady flow around a cavity bubble", Computational Methods in Engineering; Advances and Applications, Singapore, pp. 529-534.

Soh, W.K. and Shervani-Tabar, M.T. (1992b), "Computer study on the rebound of a vapour cavity bubble", 11th Australasian Fluid Mechanics Conference, University of Tasmania, Hobart, Australia, pp. 199-202.

Soh, W.K. and Shervani-Tabar, M.T. (1994), "Computer model for a pulsating vapour bubble near a rigid surface", Computational Fluid Dynamics JOURNAL, Vol. 3, No. 1., pp. 223-236.

Soh, W.K. and Yu, C.F. (1992), "A scale model of underwater explosion", Report to Material Research Lab., Defence Science Technology Organisation, Australia, November 1992.

Soh, W.K. and Yu, C.F. (1993), "A scale model of underwater explosion", Report to Material Research Lab., Defence Science Technology Organisation, Australia.

Stroud, A.H. and Secret, D. (1966), "Gaussian quadrature formulas", Prentice-Hall, Englewood Cliffs, N.Y.

Taib, B.B. (1985), "Boundary integral method applied to cavitation bubble dynamics", Ph.D. Thesis, University of Wollongong, Australia.

Telles, J.C.F. (1987), "A self-adaptive co-ordinate transformation for efficient numerical evaluation of general boundary element integrals", International Journal for Numerical Methods in Engineering, Vol. 24, pp. 959-973.

Thiruvengadam, A. (1965), "Intensity of cavitation damage encountered in field installations", Trans. ASME, Cavitation in Fluid Machinery, New York, pp. 32-46.

Timm, E.E. and Hammitt, F.G. (1971), "Bubble collapse adjacent to rigid wall, flexible wall and a second bubble", Cavitation Forum, ASME, pp. 18-20.

Tomita, Y. and Shima, A. (1986), "Mechanisms of impulsive pressure generation and damage pit formation by bubble collapse", J. Fluid Mech., Vol. 169, pp. 535-564.

Tomita, Y. and Shima, A. (1990), "High-speed observations of laser-induced cavitation bubbles in water", Acoustica, Vol. 71, pp. 161-171.

Trevena, D.H. (1987), "Cavitation and tension in liquids", IOP Publishing Ltd..

UK Steam Tables in SI Units (1970), United Kingdom Committee on the Properties of Steam, Edward Arnold, London.

Vakil, N., Gracewski, S.M. and Everbach, C.E. (1991), "Relationship to model stone properties to fragmetation mechnisms during lithotripsy", Journal of Lithtripsy and Stone Disease, Vol. 3, No. 4, pp. 304-310.

Vogel, A. and Lauterborn, W. (1988), "Time-resolved particle image velocimetry used in the investigation of cavitation bubble dynamics", Applied Optics, Vol. 27, No. 9, pp. 1896-1876.

Vogel, A., Lauterborn, W. and Timm, R. (1989), "Optical and acoustic investigations of the dynamics of laser-produced cavitation bubbles near a rigid boundary", J. Fluid Mech., Vol. 206, pp. 299-338.

Vokurka, K. (1985) "On the assumption of a uniform pressure field in the bubble interior", Acta Technica Csav, Vol. 30, No. 5, 585-593.

Wheeler, W.H. (1956), "Mechanism of cavitation errosion", Proc. 1955 NPL Symp. on Cavitation in Hydrodynamics, Paper 21, H.M. Stationery Office, London.

Wheeler, W.H. (1960), "Indentation of metals by cavitation", Trans. ASME, Vol. 82, Ser. D, J. Basic Engineering, pp. 184-194.

Wolframe, S. (1992), "Mathematica; a system for doing mathematics by computer", Second Edition, Addison-Wesley Publishing Company, Inc.

Wong, K.C., Soh W.K. and Blake, J.R. (1989), "High speed flow visualization of a cavitation bubble", Proceedings of The Tenth Australasian Fluid Mechanics Conference, The Institution of Engineers, Australia, Melbourne, December, pp. 227-230.

Wrobel, L.C. and Brebbia, C.A. (1981), "Axisymmetric potential problems", New Development in Boundary Element Method, Ed. Brebbia, C.A., Butterworths.

Young, R.F. (1989), "Cavitation", McGraw-hill Book Company (UK) Limited.

Yu, C.F. and Soh, W.K. (1992), "The effects of free surface and rigid boundary on a vapour cavity bubble", 11th Australasian Fluid Mechanics Conference, University of Tasmania, Hobart, Australia, pp. 91- 94.

Zhang, S. and Duncan, J.H. (1994), "On the non-spherical collapse and rebound of a cavitation bubble", Phys. Fluids, Vol. 6 (7), pp. 2352-2362.

Zhang, S., Duncan, J.H. and Chahine (1993), "The final stage of the collapse of a cavitation bubble near a rigid wall", J. Fluid Mech, Vol. 257, pp. 147 - 181.

Zhong, P. and Choung, C.J. (1993), "Propagation of shock waves in elastic solids cuased by cavitation micro jet impact. I: Theoretical formulation", J. Acoust. Soc. Am. 94 (1), pp. 19-28, July.

Zhong, P. and Choung, C.J. (1993), "Propagation of shock waves in elastic solids cuased by cavitation micro jet impact. II: Aplication in extracorporeal shock wave lithotripsy", J. Acoust. Soc. Am. 94 (1), pp. 29-36, July .

Zhong, P., Chuong, C.J. and Preminger, G.M. (1993), "Propagation of shock waves in elastic solids caused by cavitation microjet impact. I: Application in extracorporeal shock wave lithotripsy", J. Acoust. Soc. Am., Vol. 94 (1), pp. 29-36, July.